

学位論文

Production and evolution of
axion dark matter in the early universe

初期宇宙におけるアクシオン暗黒物質の生成
および発展について

平成24年12月 博士（理学）申請

東京大学大学院理学系研究科
物理学専攻

齋川 賢一

Abstract

Axion is a hypothetical particle introduced as a solution of the strong CP problem of quantum chromodynamics (QCD). Various astronomical and experimental searches imply that the axion is invisible in the sense that its interactions with ordinary matters are considerably weak. Due to this weakness of the coupling, the axion is regarded as a viable candidate of dark matter of the universe.

In this thesis, we investigate production and evolution of axion dark matter, and discuss their cosmological implications. Axions are produced non-thermally in the early universe. A well known production mechanism is so called the misalignment mechanism, where the axion field begins to coherently oscillate around the minimum of the potential at the time of QCD phase transition. This coherent oscillation of the axion field behaves as a cold matter in the universe. In addition to this coherent oscillation, however, there are other contributions, which come from the decay of topological defects such as strings and domain walls. The production mechanism due to topological defects is not understood quite well, and there is a theoretical uncertainty on the determination of the relic abundance of dark matter axions.

In order to remove this uncertainty, we analyze the spectrum of axions radiated from these string-wall systems. The evolution of topological defects related to the axion models is investigated by performing field-theoretic lattice simulations. The spectrum of radiated axions has a peak at the low frequency, which implies that axions produced by the defects are not highly relativistic. By the use of the results of numerical simulations, the relic abundance of dark matter axions is reanalyzed including all production mechanisms. It is found that the decay of domain walls produces significant amount of cold axions, which gives severe constraints on the model parameters. In particular, for the case with short-lived domain walls, the inclusion of the domain wall contribution leads to a more severe upper bound on the axion decay constant. Furthermore, models which predict long-lived domain walls are excluded because of the overproduction of cold axions, unless an unacceptable fine-tuning exists.

Contents

1	Introduction	1
1.1	Overview	1
1.2	Outline of this thesis	4
1.3	Notations	5
2	Strong CP problem and axion	6
2.1	The theta vacuum	7
2.2	The Peccei-Quinn mechanism	10
2.3	Phenomenological models of the axion	12
2.3.1	The original PQWW model	13
2.3.2	The invisible axion	14
2.4	Properties of the invisible axion	15
2.4.1	Mass and potential	15
2.4.2	Coupling with other particles	17
2.4.3	Domain wall number	18
2.5	Search for the invisible axion	19
2.5.1	Laboratory searches	19
2.5.2	Astrophysical bounds	21
2.5.3	Cosmology	22
2.5.4	Summary – The axion window	22
3	Axion cosmology	24
3.1	Thermal production	24
3.2	Non-thermal production	28
3.2.1	Evolution of the axion field	28
3.2.2	Cold dark matter abundance	30
3.3	Axion isocurvature fluctuations	32
4	Axion production from topological defects	36
4.1	Formation and evolution of topological defects	37
4.1.1	Axionic string and axionic domain wall	37
4.1.2	Domain wall problem and its solution	40
4.2	Evolution of string-wall networks	41
4.2.1	Short-lived networks	42

4.2.2	Long-lived networks	51
4.3	Axion production from strings	62
4.4	Axion production from short-lived domain walls	66
4.5	Axion production from long-lived domain walls	75
4.5.1	Production of axions	75
4.5.2	Production of gravitational waves	82
4.6	Constraints for models with $N_{\text{DW}} = 1$	85
4.7	Constraints for models with $N_{\text{DW}} > 1$	89
4.7.1	Axion cold dark matter abundance	89
4.7.2	Neutron electric dipole moment	92
4.7.3	Implication for models	93
4.7.4	Scenario with extremely small δ	93
5	Conclusions and discussion	97
A	Notes of standard cosmology	102
A.1	The Friedmann Equation	102
A.2	Thermodynamics in the expanding universe	103
A.3	Horizons	106
B	Extended field configurations	107
B.1	Classifications	107
B.2	Instantons	109
B.3	Symmetry restoration and phase transitions	114
B.4	Cosmic strings	116
B.5	Domain walls	118
C	Lattice simulation	121
C.1	Formulation	121
C.2	Identification of topological defects	122
C.2.1	Identification of strings	123
C.2.2	Identification of domain walls	123
C.2.3	Calculation of scaling parameters	125
C.3	Calculation of power spectrum of radiated axions	125
C.3.1	Energy spectrum of axions	126
C.3.2	Pseudo-power spectrum estimator	127
C.3.3	Subtraction of preexisting radiations	129
C.4	Calculation of gravitational waves	131

Chapter 1

Introduction

1.1 Overview

In the last several decades, developments of astronomical observations have provided rich information about our universe. One of the most important accomplishments is that our universe is filled by some non-baryonic energy components. Conventionally, these are categorized into two ingredients: *dark matter* and *dark energy*. Dark energy is something like the Einstein's cosmological constant, which accelerates the expansion of the present universe. Although the accelerated expansion is observationally confirmed [1, 2], the existence of constant energy density is still under debate [3]. On the other hand, the existence of dark matter is becoming more evident. The total matter density of the universe has been measured by many different kinds of methods [4], whose results are 5-6 times larger than the baryon density of the universe obtained by the observation of the light element abundance [5]. This indicates that the large fraction of the cosmic matter density is occupied by a non-baryonic component. This result is also confirmed by the recent precise measurement of cosmic microwave background (CMB) by the WMAP satellite [6]. Furthermore, the map of the gravitational potential around a cluster merger 1E0657-558, measured by means of the weak lensing, clearly shows that the matter distribution of the galaxies does not trace the distribution of the visible baryonic gas [7]. This observation strongly supports the existence of a non-baryonic matter, which interacts with ordinary matters only through the gravitational force.

The existence of the dark matter cannot be explained in the framework of the standard model of particle physics. This fact motivates us to consider some new physics beyond the standard model. Several models of the particle dark matter have been proposed so far [see e.g. [8] for reviews]. One of the well-motivated candidates is the axion [9, 10]. Axion is a hypothetical particle which arises as a consequence of the Peccei-Quinn (PQ) [11, 12] mechanism, the most attractive solution to the strong CP problem of quantum chromodynamics (QCD) [13, 14]. This mechanism introduces a global $U(1)_{\text{PQ}}$ symmetry (so called PQ symmetry) that has to be spontaneously broken at some high energy scale. The spontaneous breaking of this global symmetry predicts an existence of a (pseudo) Nambu-Goldstone boson, which we identify as the axion.

Historically, the axion was not considered as a candidate for the dark matter at the time

when it was proposed. In the original model, the axion was “visible” in the sense that it gives some predictions for laboratory experiments. Unfortunately, no signature was observed, and the prototype axion model was ruled out soon after the proposal [15]. However, it was argued that models with higher symmetry breaking scale denoted as F_a (the axion decay constant) can still avoid the experimental constraints [16, 17, 18, 19]. The essential point is that the couplings between axions and other fields are suppressed by a large factor of the symmetry breaking scale $\sim 1/F_a$. These models are called “invisible axions” because of their smallness of coupling with matter.

This invisibility leads to a cosmological consequence. It turns out that almost stable coherently oscillating axion fields play a role of the dark matter filled in the universe [20, 21, 22]. Furthermore, since these axions are produced non-thermally, they are cold in the sense that they are highly non-relativistic. This property agrees with the cold dark matter scenario motivated by the study of the large scale structure formation [23].

The behavior of dark matter axions is closely related with the history of the early universe. In particular, the cosmological phase transition associated with the spontaneous symmetry breaking gives some implications for the physics of the axion dark matter. There are two relevant phase transitions. One is the PQ phase transition corresponding to the spontaneous breaking of $U(1)_{\text{PQ}}$ symmetry, and another is the QCD phase transition corresponding to the spontaneous breaking of the chiral symmetry of quarks. Axions are produced at the PQ phase transition, then they acquire a mass due to the non-perturbative effect at the QCD phase transition. The remarkable feature of this sequence of phase transitions is that it predicts the formation of topological defects [see [24] for reviews]. When the PQ symmetry is spontaneously broken, vortex-like defects, called strings, are formed. These strings are attached by surface-like defects, called domain walls, when the QCD phase transition occurs. The cosmological evolution of these topological defects is a key to understand the physics of dark matter axions.

The structure of the domain walls is determined by an integer number N_{DW} which is referred as the “domain wall number”. The value of N_{DW} is related to the color anomaly [25, 26, 13], whose value depends on particle physics models. The cosmological history is different between the model with $N_{\text{DW}} = 1$ and that with $N_{\text{DW}} > 1$. In the model with $N_{\text{DW}} = 1$, the string-wall systems turn out to be unstable, and they collapse immediately after the formation. On the other hand, in the model with $N_{\text{DW}} > 1$, it is known that domain walls are stable and they eventually overclose the universe, which conflicts with the standard cosmology [27, 25].

One possibility to avoid the domain wall problem is to assume the occurrence of inflation, the exponentially expanding stage of the universe, after the PQ phase transition. Inflation was originally introduced in order to solve the flatness, horizon, and monopole problem of the universe [28, 29], but the same reasoning can be applied to the axionic domain wall problem. If inflation has occurred after the PQ phase transition, the cosmic density of topological defects is wiped away, and we can simply ignore them. However, in this scenario isocurvature fluctuations of the axion field gives some imprints on anisotropies of cosmic microwave background (CMB) observed today [30, 31, 32, 33, 34]. This observation gives severe constraints on axion models and requires significant amounts of fine tunings in the model parameters [35].

Another way is to introduce a small explicit symmetry breaking term, called the bias [36, 37], which lifts the vacuum degeneracy [25, 38, 39]. In this case, domain walls collapse due to the pressure force acting between different vacua [40]. It was pointed out that the bias term might be found in effects of gravity [41]. If we regard the low energy field theory as an effective theory induced by a Planck-scale physics, we expect that the global symmetry is violated by higher dimensional operators suppressed by the Planck mass M_P . This small symmetry violating operators cause the decay of domain walls. However, in the case of PQ symmetry, the situation is more complicated. It was argued that these Planck-scale induced terms easily violate the PQ symmetry and cause the CP violation [42, 43, 44, 45, 46]. In particular, the operators with dimension smaller than $d = 10$ are forbidden [44] by a requirement of CP conservation. If it is true, the biased domain walls should be long-lived, and disappear at late time due to the effect of highly suppressed operators.

Regarding these problems, we can consider several cosmological scenarios, which are summarized in Fig. 1.1. Basically, there are two possibilities.

1. For sufficiently large F_a , inflation has occurred after the PQ phase transition. Let us call it scenario I.
2. For sufficiently small F_a , inflation has occurred before the PQ phase transition. Let us call it scenario II.

Furthermore, scenario II can be divided into two cases according to the value of domain wall number N_{DW} . If $N_{\text{DW}} = 1$, domain walls quickly disappear after the formation (we call it scenario IIA). On the other hand, if $N_{\text{DW}} > 1$, domain walls are long-lived (we call it scenario IIB). These different scenarios give different predictions about the cosmological behavior of axion dark matter.

For scenario II, the total abundance of dark matter axions is given by the sum of the coherently oscillating fields [20, 21, 22] and those produced by the decay of strings [47] and domain walls [48]. Several groups have investigated the production of axions from these topological defects, and there is a controversy on the estimation of the string decay contribution. Some groups claimed that the string decay gives a significant contribution for the dark matter abundance [49, 50, 51, 52, 53], but another group disproved it [54, 55, 56]. This controversy seems to be resolved by recent extensive numerical simulations performed by [57, 58], concluding that the string decay gives a large contribution. However, we must include another contribution, which comes from the decay of domain walls. Since the fate of domain walls is relevant to the cosmological history, it is necessary to discuss the effect of dark matter axions produced from these domain walls.

The above discussions force us to reconsider the axion cosmology in a more quantitative way. In this thesis, we study these cosmological aspects of axion dark matter. The aim of this thesis is to answer the following questions:

- How axions are produced in the early universe, and how they evolved?
- Does the axion explain dark matter of the universe? If so, what class of cosmological scenario is possible?

In order to clarify these points, we develop some numerical methods to analyze cosmological evolution of the axion field.

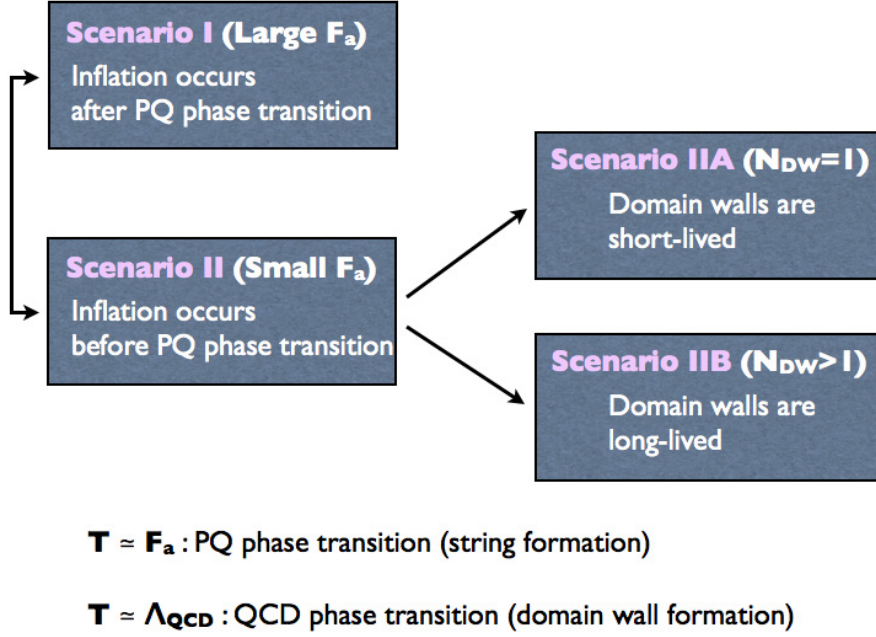


Figure 1.1: Possible cosmological scenarios in the axion models. The history of the universe differs according to the values of F_a and N_{DW} .

1.2 Outline of this thesis

The outline of this thesis is as follows.

In Chapter 2, we review the current status of the research of axion physics. The theoretical backgrounds about the QCD axion, including the theta vacuum, Peccei-Quinn mechanism, and phenomenological models are described. Then, experimental and observational constraints on the model parameters are briefly discussed.

In Chapter 3, the cosmological behavior of axions is discussed. We introduce some production mechanisms of dark matter axions. The relation with inflation is shortly discussed.

In Chapter 4, we explore the production of axions from topological defects. Cosmological evolution of topological defects is investigated by using field-theoretic lattice simulations. Based on the results of numerical simulations, we discuss the constraints on the model parameters.

Finally, we make conclusions and discussion in Chapter 5.

Some of the basic formulae relevant to cosmology are summarized in Appendix A. In Appendix B, we review field theoretical ingredients such as instantons, strings, and domain walls. The analysis methods that we used in the numerical studies are described in Appendix C.

1.3 Notations

We use the unit of $c = \hbar = k_B = 1$, unless otherwise stated. The signature of the metric in flat Minkowski spacetime is $\eta_{\mu\nu} = (-, +, +, +)$. Four-vector is represented as x^μ , where the Greek indices take $\mu = 0, 1, 2, 3$, and x^0 is the time coordinate. Some field theoretical expressions are described in Euclidean spacetime, which is obtained by replacing $x^4 = ix^0$ in Minkowski spacetime. The Euclidean action is given by multiplying i to the continuation of Minkowskion action. In the Euclidean spacetime, we do not distinguish upper and lower indices of four vector, since the sign of the metric becomes $\eta_{\mu\nu} = (+, +, +, +)$.

In the context where the cosmic expansion is taken into account, we work in spatially flat Friedmann-Robertson-Walker (FRW) universe with a metric

$$ds^2 = g_{\mu\nu} dx^\mu dx^\nu = -dt^2 + R^2(t)[dx^2 + dy^2 + dz^2],$$

where $R(t)$ is the scale factor of the universe. We denote the cosmic time as t and the conformal time as τ , where $d\tau = dt/R(t)$. A dot represents a derivative with respect to the cosmic time, while a prime represents a derivative with respect to the conformal time, i.e. $\dot{} = \partial/\partial t$, and $' = \partial/\partial \tau$. Other notations are described in Appendix A.

Chapter 2

Strong CP problem and axion

Strong CP problem is related to the non-trivial structure of the vacuum of QCD. In QCD, we can add the following term to the Lagrangian density

$$\mathcal{L}_\theta = -\frac{\bar{\theta}g^2}{64\pi^2}\epsilon^{\mu\nu\rho\sigma}G_{\mu\nu}^a G_{\rho\sigma}^a, \quad (2.1)$$

where $G_{\mu\nu}^a$ is the gluon field strength, $\epsilon^{\mu\nu\rho\sigma}$ is the totally antisymmetric tensor with $\epsilon^{0123} = +1$. This term does not affect the equation of motion and the Feynman rules since it is given by a total derivative. However, it gives physical consequences if we consider non-perturbative effects.

It is known that in 4-dimensional non-Abelian gauge theory there exist configurations which keep the action finite and are localized in spacetime, called *instantons*. Due to the existence of instanton configurations, we must consider the vacuum structure of a quantum field theory in an unusual way, which is called the theta vacuum. Historically, the instanton solutions are applied as a resolution of so called the U(1) problem of QCD [59, 60]. This resolution of the old U(1) problem creates another problem, the strong CP problem. In other words, strong CP problem is inevitable consequence of the existence of the theta vacuum.

In a theta vacuum with non-zero value of $\bar{\theta}$, we must include the term given by Eq. (2.1) in the path integral evaluation of a quantum process. This term violates discrete CP symmetry and induces neutron electric dipole moment whose magnitude is proportional to $\bar{\theta}$. However, experimental results showed that this effect is extremely small, indicating the value $\bar{\theta} \lesssim \mathcal{O}(10^{-11})$. Since $\bar{\theta}$ is a dimensionless parameter of the theory, we naively expect that its value is $\mathcal{O}(1)$. Hence we would like to explore a natural way to explain why $\bar{\theta}$ is so small. In this sense, strong CP problem is a fine-tuning problem.

The most attractive solution of the strong CP problem was proposed by Peccei and Quinn [11, 12]. The crucial point is to introduce a dynamical quantity which mimics $\bar{\theta}$ parameter and takes zero value in the low energy Lagrangian. Soon after the proposal, it was pointed out that this dynamical variable should be identified as a light spin-zero particle, called the *axion* [9, 10].

In this chapter, we review some aspects of the strong CP problem of QCD and phenomenological studies of axions. First, we describe the non-trivial structure of QCD vacua

including non-perturbative effects, and give the observational bound on the $\bar{\theta}$ parameter in Sec. 2.1. The possible solution of the strong CP problem is discussed in Sec. 2.2. Then, we briefly describe some phenomenological models of axions in Sec. 2.3, and enumerate its properties in Sec. 2.4. We also review current status of the experimental and astrophysical researches of axions in Sec. 2.5. Properties of instanton solutions are briefly described in Appendix B.3.

2.1 The theta vacuum

Because of the existence of instanton solutions in the $SU(3)$ gauge field theory, we characterize the vacuum of QCD by the Pontryagin index [see Eq. (B.25)]

$$|n\rangle, \quad n : \text{integers.} \quad (2.2)$$

The $|n\rangle$ vacuum corresponds to the instanton configuration which has the Pontryagin index $\nu = n$. It turns out that this vacuum is not invariant under the gauge transformation. For example, under a gauge transformation G_1 corresponding to the homotopy class with $\nu = 1$, the gauge field configuration with $n = 0$ transforms into that with $n = 1$

$$A_\mu|_0 \xrightarrow{G_1} -\frac{i}{g}(\partial_\mu U_1)U_1^{-1} = A_\mu|_1, \quad (2.3)$$

where $A_\mu|_0$ and $A_\mu|_1$ are gauge field configurations with $n = 0$ and $n = 1$, respectively, and U_1 is an element of the gauge group which belongs to G_1 . This feature is justified since we can continuously deform $A_\mu|_0$ into zero by using a gauge transformation corresponding to the homotopy class with $n = 0$. Equation (2.3) implies that the $|0\rangle$ vacuum changes into $|1\rangle$ under G_1 . In general, the $|n\rangle$ vacuum changes into $|n + m\rangle$ under G_m which is a gauge transformation corresponding to the homotopy class with $\nu = m$

$$|n\rangle \xrightarrow{G_m} |n + m\rangle. \quad (2.4)$$

One can show it by using the additive property of winding number given by Eq. (B.18).

Since $|n\rangle$ is not gauge invariant, we must seek a more proper vacuum. Such a vacuum can be constructed as a linear combination of $|n\rangle$ vacua

$$|\theta\rangle = \sum_{n=-\infty}^{\infty} e^{in\theta} |n\rangle, \quad (2.5)$$

which is called the *theta vacuum*. Using Eq. (2.4), we see that $|\theta\rangle$ only changes its complex phase under a gauge transformation

$$G_n|\theta\rangle = e^{-in\theta}|\theta\rangle, \quad (2.6)$$

and hence observables are gauge invariant. Note that θ is a periodic quantity

$$|\theta\rangle = |\theta + 2\pi\rangle. \quad (2.7)$$

Consider the transition amplitude between $|n\rangle$ vacua

$$\langle n|e^{-Ht}|m\rangle = \int \mathcal{D}A|_{n-m} \exp \left[- \int d^4x \mathcal{L} \right], \quad (2.8)$$

where $\mathcal{D}A|_{n-m}$ indicates a functional integration over configurations with winding number $n - m$, and the functional integral is performed in the 4-dimensional Euclidean spacetime. Using the fact that

$$\sum_{n=-\infty}^{\infty} e^{-in(\theta' - \theta)} = \delta(\theta' - \theta), \quad (2.9)$$

we obtain the transition amplitude between theta vacua

$$\begin{aligned} \langle \theta'|e^{-Ht}|\theta\rangle &= \sum_{n'} \sum_n e^{-i(n'\theta' - n\theta)} \langle n'|e^{-Ht}|n\rangle \\ &= \sum_{n'} e^{-in'(\theta' - \theta)} \sum_q \int \mathcal{D}A|_q \exp \left[-iq\theta - \int d^4x \mathcal{L} \right] \\ &= \delta(\theta' - \theta) \int \mathcal{D}A \exp \left[- \int d^4x (\mathcal{L} + \mathcal{L}_\theta) \right], \end{aligned} \quad (2.10)$$

where $q = n' - n$ and $\int d^4x \mathcal{L}_\theta = iq\theta$. Equation (2.10) indicates that there is no transition between different theta vacua and hence $|\theta\rangle$ is a good vacuum. In the Minkowski space, \mathcal{L}_θ leads the effective interaction

$$\mathcal{L}_\theta = -\theta \frac{g^2}{32\pi^2} G^{\alpha\mu\nu} \tilde{G}_{\mu\nu}^{\alpha}, \quad (2.11)$$

which follows from Eq. (B.25). Here, $\tilde{G}_{\mu\nu}^{\alpha}$ is the dual of $G_{\mu\nu}^{\alpha}$, defined by

$$\tilde{G}_{\mu\nu}^{\alpha} = \frac{1}{2} \epsilon_{\mu\nu\rho\sigma} G^{\alpha\rho\sigma}. \quad (2.12)$$

The introduction of instanton solutions solved the old U(1) problem of QCD [59, 60]. In QCD, there is global $SU(2)_L \times SU(2)_R$ flavor symmetry which arises as a consequence of the smallness of u and d quark masses. This chiral $SU(2)_L \times SU(2)_R$ symmetry is spontaneously broken due to the strong dynamics of QCD, and pions π are regarded as Goldstone bosons associated with the break down of this global symmetry. In addition to this chiral symmetry, there is $U(1)_A$ symmetry under which u and d quarks transform as

$$u \rightarrow \exp(i\gamma_5\alpha), \quad d \rightarrow \exp(i\gamma_5\alpha)d, \quad (2.13)$$

where α is an arbitral parameter. The spontaneous breaking of the $U(1)_A$ symmetry predicts another Goldstone boson, which might be identified as η' meson. Since global $SU(2)_L \times SU(2)_R$ and $U(1)_A$ symmetries become exact only in the massless quark limit, Goldstone bosons acquire small masses due to the finiteness of quark masses.

The problem is that the observed mass of the η' meson is too large if we regard it as a Goldstone boson associated with $U(1)_A$ symmetry. In particular, the explicit calculation

gives an upper bound on the η' meson mass $m_{\eta'} < \sqrt{3}m_\pi$ [61], where $m_\pi \approx 140\text{MeV}$ is the pion mass. Such a light strongly interacting particle has not been observed in any experiments.

This $U(1)$ problem can be solved if we admit the existence of instanton solutions. Under the global $U(1)_A$ transformation

$$q_f \rightarrow q'_f = \exp(i\gamma_5\alpha_f/2)q_f, \quad (2.14)$$

which acts on each of quark fields q_f with a flavor index f , the measure for path integrals over quark fields q_f changes due to the anomaly [62, 63]

$$\mathcal{D}q_f\mathcal{D}\bar{q}_f \rightarrow \mathcal{D}q_f\mathcal{D}\bar{q}_f \exp\left[-\frac{ig^2}{32\pi^2}\sum_f\alpha_f\int d^4xG^{a\mu\nu}\tilde{G}_{\mu\nu}^a\right]. \quad (2.15)$$

In the absence of instantons, the integrand $G_{\mu\nu}^a\tilde{G}_{\mu\nu}^a$ in Eq. (2.15) has no effect on observables since it is a total derivative whose integral vanishes for a trivial gauge field configuration. However, this integral does not vanish due to the existence of the instanton solution. From Eq. (B.25), we find

$$\frac{g^2}{32\pi^2}\sum_f\alpha_f\int d^4xG^{a\mu\nu}\tilde{G}_{\mu\nu}^a = \nu\sum_f\alpha_f, \quad (2.16)$$

which does not vanish for $\nu \neq 0$. In this sense, we regard that $U(1)_A$ is violated due to the anomaly. Therefore, the theory does not contain $U(1)_A$ symmetry, and there is no Goldstone boson associated with this symmetry.

Although the $U(1)$ problem was solved due to the existence of instantons, it posed another problem. Since we are living in one of the vacua parametrized by θ , as shown in Eq. (2.10), we must add a term (2.11) in the Lagrangian density, which violates a discrete CP symmetry if $\theta \neq 0$. Note that the chiral transformation (2.15) is equivalent to the shift in the value of θ

$$\theta \rightarrow \theta + \sum_f\alpha_f. \quad (2.17)$$

On the other hand, when we write down the quark mass terms

$$\mathcal{L}_m = -\frac{1}{2}\sum_f m_f\bar{q}_f(1+\gamma_5)q_f - \frac{1}{2}\sum_f m_f^*\bar{q}_f(1-\gamma_5)q_f, \quad (2.18)$$

where we assume that the quark mass matrix m_f is already diagonalized, the transformation (2.14) leads to the change in the phase of the quark mass

$$m_f \rightarrow \exp(i\alpha_f)m_f. \quad (2.19)$$

Then, the following quantity is invariant under the transformation (2.14)

$$\exp(-i\theta)\prod_f m_f. \quad (2.20)$$

Let us define the quantity

$$\bar{\theta} = \theta + \theta_{\text{weak}}, \quad (2.21)$$

where $\theta_{\text{weak}} = -\text{Arg}(\prod_f m_f)$. If we use a basis in which all quark masses are taken to be real, the CP violating effect is induced as a quantity proportional to $\bar{\theta}$, rather than θ .

The effect of CP violation would be observed as the neutron electric dipole moment (NEDM) [64]. The interaction between the spin \mathbf{S} of a non-relativistic neutron and external electromagnetic fields \mathbf{E} and \mathbf{B} can be written as

$$H = -\mu_n \mathbf{B} \cdot \frac{\mathbf{S}}{S} - d_n \mathbf{E} \cdot \frac{\mathbf{S}}{S}. \quad (2.22)$$

Since the term $\mathbf{E} \cdot \mathbf{S}$ is odd under the time-reversal symmetry T , the non-zero value of d_n implies the violation of T symmetry, or the violation of CP symmetry. The QCD θ term contributes to the NEDM, which is estimated as [14]

$$|d_n| = 4.5 \times 10^{-15} \bar{\theta} e \text{cm}. \quad (2.23)$$

On the other hand, the recent experimental bound on the NEDM gives $|d_n| < 2.9 \times 10^{-26} e \text{cm}$ [65], which requires

$$\bar{\theta} < 0.7 \times 10^{-11}. \quad (2.24)$$

It should be emphasized that the NEDM bound (2.24) constrains the magnitude of $\bar{\theta}$, rather than θ . We must require that the sum of θ and θ_{weak} is smaller than $\mathcal{O}(10^{-11})$. The origin of θ_{weak} is the phase of the quark masses. In the standard model, the quark masses are determined from the Yukawa coupling between quarks and Higgs boson when the Higgs boson acquires a vacuum expectation value and the electroweak symmetry is spontaneously broken. Hence, the value of θ_{weak} is related to the dynamics of the electroweak theory. On the other hand, the value of θ parametrizes the QCD vacua. Eqs. (2.21) and (2.24) imply that two quantities, which come from completely different physics, should cancel out in the precision of $\mathcal{O}(10^{-11})$. That is the mystery calling for an explanation.

2.2 The Peccei-Quinn mechanism

Peccei and Quinn proposed the theory which naturally explains the smallness of $\bar{\theta}$ [11, 12]. The essence of their idea is threefold: (1) Introduce a field a , which we call the axion field. (2) Assume that there exists a global $U(1)$ axial symmetry, which we call the Peccei-Quinn (PQ) symmetry $U(1)_{\text{PQ}}$, and that this $U(1)$ symmetry is spontaneously broken at some energy scale higher than the QCD scale $\Lambda_{\text{QCD}} \approx \mathcal{O}(100) \text{MeV}$. (3) Impose appropriate PQ charges into quarks so that there exists $U(1)_{\text{PQ}}\text{-}SU(3)_c\text{-}SU(3)_c$ anomaly.

The dynamical degree of freedom a can be identified as a Goldstone boson associated with the spontaneous breaking of $U(1)_{\text{PQ}}$ symmetry [9, 10]. The $U(1)_{\text{PQ}}$ symmetry acts as a shift in a field

$$U(1)_{\text{PQ}} : \quad a \rightarrow a + \epsilon \eta, \quad (2.25)$$

where ϵ is an arbitrary constant parameter, and η is the energy scale of the spontaneous $U(1)_{\text{PQ}}$ symmetry breaking. According to the assumption (3), the $U(1)_{\text{PQ}}$ current is not conserved due to the anomaly

$$\partial^\mu j_\mu^{\text{PQ}} = -\frac{g^2}{32\pi^2} A G^{a\mu\nu} \tilde{G}_{\mu\nu}^a, \quad (2.26)$$

where A is a constant determined by the charge assignment of the model. This implies that the Lagrangian should transform under (2.25) as

$$\delta\mathcal{L} = -\frac{g^2}{32\pi^2} \epsilon A G^{a\mu\nu} \tilde{G}_{\mu\nu}^a. \quad (2.27)$$

Then, the low energy effective Lagrangian can be written as

$$\mathcal{L}_{\text{eff}} = -\frac{1}{4} G^{a\mu\nu} G_{\mu\nu}^a - \frac{1}{2} \partial_\mu a \partial^\mu a - \frac{g^2}{32\pi^2} \frac{a}{F_a} G^{a\mu\nu} \tilde{G}_{\mu\nu}^a - \frac{\bar{\theta} g^2}{32\pi^2} G^{a\mu\nu} \tilde{G}_{\mu\nu}^a + \dots, \quad (2.28)$$

where dots correspond to the possible terms which contain the derivative of a , and

$$F_a = \frac{\eta}{A} \quad (2.29)$$

is called the axion decay constant. Equation (2.28) shows that the observable theta parameter $\bar{\theta}_{\text{eff}}$ is determined by the value of the axion field

$$\bar{\theta}_{\text{eff}} = \frac{a}{F_a} + \bar{\theta}. \quad (2.30)$$

If there is no CP violating term except for the term proportional to $\bar{\theta}_{\text{eff}} = a/F_a + \bar{\theta}$, the effective potential for the axion field is minimized at $\bar{\theta}_{\text{eff}} = 0$, and hence the strong CP problem is solved. We can confirm this statement by using the following arguments [66]. The effective potential $V(a)$ for the axion field is obtained by integrating out the gluon field in the path integral¹

$$\exp \left\{ - \int d^4x V(a) \right\} = \int \mathcal{D}A \exp \left\{ - \int d^4x \left[\frac{1}{4} G_{\mu\nu}^a G_{\mu\nu}^a + i \frac{g^2}{32\pi^2} \frac{a + \bar{\theta} F_a}{F_a} G_{\mu\nu}^a \tilde{G}_{\mu\nu}^a \right] \right\}, \quad (2.31)$$

where, we ignored the kinetic energy of the axion field. Using the Schwarz inequality, we find

$$\begin{aligned} \exp \left\{ - \int d^4x V(a) \right\} &= \left| \int \mathcal{D}A \exp \left\{ - \int d^4x \left[\frac{1}{4} G_{\mu\nu}^a G_{\mu\nu}^a + i \frac{g^2}{32\pi^2} \frac{a + \bar{\theta} F_a}{F_a} G_{\mu\nu}^a \tilde{G}_{\mu\nu}^a \right] \right\} \right| \\ &\leq \int \mathcal{D}A \left| \exp \left\{ - \int d^4x \left[\frac{1}{4} G_{\mu\nu}^a G_{\mu\nu}^a + i \frac{g^2}{32\pi^2} \frac{a + \bar{\theta} F_a}{F_a} G_{\mu\nu}^a \tilde{G}_{\mu\nu}^a \right] \right\} \right| \\ &= \int \mathcal{D}A \exp \left\{ - \int d^4x \frac{1}{4} G_{\mu\nu}^a G_{\mu\nu}^a \right\} \\ &= \exp \left\{ - \int d^4x V(a = -\bar{\theta} F_a) \right\}. \end{aligned}$$

¹Here, we compute the path integral in the Euclidean spacetime.

Therefore,

$$\int d^4x V(a) \geq \int d^4x V(a = -\bar{\theta}F_a). \quad (2.32)$$

We get dynamically the CP conserving value $\bar{\theta}_{\text{eff}} = a/F_a + \bar{\theta} = 0$ as a minimum of the effective potential for the axion field.

Let us redefine the axion field $a \rightarrow a + \bar{\theta}F_a$, and rewrite $\bar{\theta}_{\text{eff}}$ as $\bar{\theta}$. Then, we obtain

$$\bar{\theta} = \frac{\langle a \rangle}{F_a} = 0. \quad (2.33)$$

Since $\bar{\theta}$ has a periodicity by 2π , $\langle a \rangle = 2\pi F_a k$ (k is an integer) are also the minima of the potential. Figure 2.1 shows the form of the effective potential for the axion field. Since the potential is generated by integrating out the gluon field, the height of the potential is roughly given by the QCD scale $\sim \Lambda_{\text{QCD}}^4$. Whether the multiple vacua are identical or not is determined by the construction of the model, which will be discussed in the following sections.

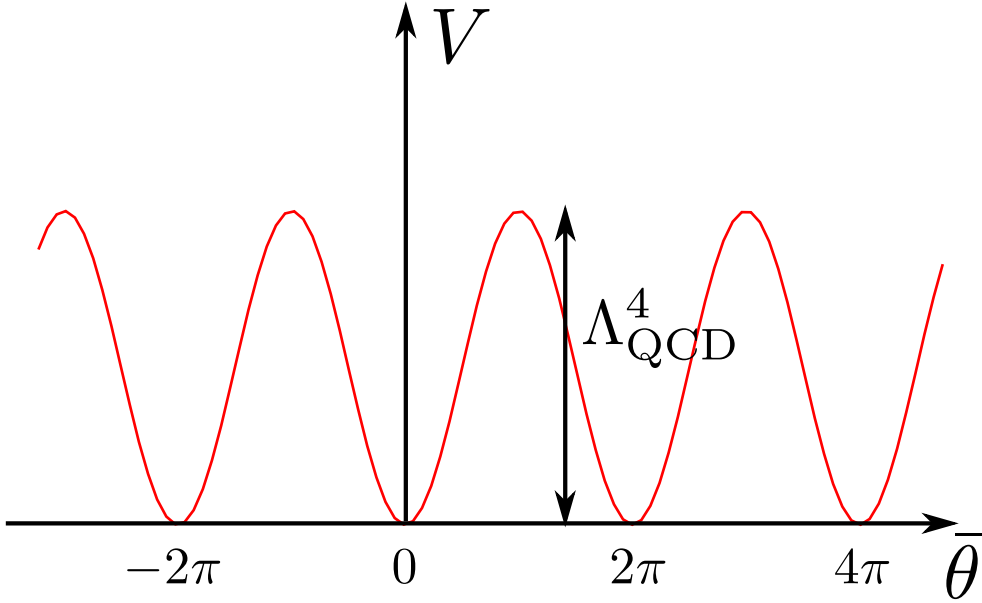


Figure 2.1: The form of the effective potential for $\bar{\theta}$.

2.3 Phenomenological models of the axion

In this section, some explicit models of the axion are shortly reviewed. As we discussed in the previous section, the presence of the QCD anomaly is necessary to induce the axion potential whose minimum is located at $\bar{\theta} = 0$. This requires some extensions of the standard model and arrangement of the $U(1)_{\text{PQ}}$ multiplet appropriately.

2.3.1 The original PQWW model

The original model of the axion was proposed by Weinberg and Wilczek [9, 10], based on the idea of Peccei and Quinn [11, 12]. This is called the Peccei-Quinn-Weinberg-Wilczek (PQWW) model, or the “visible” axion model. In this model, the axion field is identified as a phase direction of the standard model Higgs field. It is necessary to introduce two (or more) Higgs doublets, since the axion degree of freedom does not exist in the theory with single Higgs doublet.

Let us denote two Higgs doublets as φ_1 and φ_2 . We assign $U(1)_{\text{PQ}}$ charges Γ_1 and Γ_2 to Higgs doublets and quarks such that

$$\begin{aligned}
 U(1)_{\text{PQ}} : \\
 \varphi_1 &\rightarrow e^{i\epsilon\Gamma_1}\varphi_1, & \varphi_2 &\rightarrow e^{i\epsilon\Gamma_2}\varphi_2, \\
 u_L &\rightarrow e^{i\epsilon\Gamma_2/2}u_L, & u_R &\rightarrow e^{-i\epsilon\Gamma_2/2}u_R, \\
 d_L &\rightarrow e^{i\epsilon\Gamma_1/2}d_L, & d_R &\rightarrow e^{-i\epsilon\Gamma_1/2}d_R,
 \end{aligned} \tag{2.34}$$

where ϵ is an arbitrary constant parameter. The Yukawa couplings for quarks become

$$\mathcal{L}_y = -y_u\bar{q}_L\varphi_2u_R - y_d\bar{q}_L\varphi_1d_R + \text{h.c.} \tag{2.35}$$

Both PQ symmetry and electroweak symmetry are spontaneously broken when two Higgs doublets acquire the vacuum expectation values

$$\langle\varphi_1^0\rangle = v_1, \quad \langle\varphi_2^0\rangle = v_2, \quad v = \sqrt{v_1^2 + v_2^2} = 247\text{GeV}, \tag{2.36}$$

where φ_1^0 and φ_2^0 are the neutral component of φ_1 and φ_2 , respectively. One of two linear combinations of the phases becomes a degree of freedom h which is absorbed by Z boson, and another degree of freedom becomes the axion

$$\varphi_1^0 = v_1 \exp\left(x\frac{a}{v} - \frac{1}{x}\frac{h}{v}\right), \quad \varphi_2^0 = v_2 \exp\left(\frac{1}{x}\frac{a}{v} + x\frac{h}{v}\right), \tag{2.37}$$

$$x \equiv v_2/v_1 = (\Gamma_1/\Gamma_2)^{1/2}. \tag{2.38}$$

The mass of the axion was estimated by using current algebra [67], and chiral Lagrangian approach [68]. Here, we quote their result,

$$m_a = N_g \left(\frac{1}{x} + x\right) \frac{\sqrt{Z} F_\pi m_\pi}{1 + Z} \simeq 74 \left(\frac{1}{x} + x\right) \text{keV}, \tag{2.39}$$

where N_g is the number of quark generations, $F_\pi \simeq 93\text{MeV}$ is the pion decay constant, and $Z = m_u/m_d$ is the ratio between the up quark mass and the down quark mass. We used $N_g = 3$ and $Z \simeq 0.48$ [14] in the last equality.

The PQWW axion is visible, in the sense that it predicts observable signatures in the laboratory experiments. However, the theoretical predictions of the PQWW axion contradict with experimental limits on the branching ratio of J/Ψ and Υ decay [69], and K^+

decay [70]. Some other experiments such as nuclear deexcitations, reactor experiments, beam dump experiments also disfavored the prediction of the PQWW model [15]. These results seemed to rule out the original PQWW model. Later, some variant models which avoid J/Ψ and Υ decay constraints were proposed [71, 72], but these models were also excluded by the π^+ decay experiments [73] and the electron beam dump experiments [74].

2.3.2 The invisible axion

It was pointed out that the problem of the original PQWW model can be avoided, if the PQ symmetry is broken at some energy scale η , which is higher than the electroweak scale $v = 247\text{GeV}$, since the couplings of axions with other particles are suppressed by $1/\eta$ [16]. This fact motivates the “invisible” axion model. In this model, the axion is not the phase direction of the standard model Higgs doublet. We must introduce a $SU(2)_L \times U(1)_Y$ singlet scalar field, whose phase would be identified as the axion.

Let us denote the $SU(2)_L \times U(1)_Y$ singlet scalar field as Φ , and call it the Peccei-Quinn field. Under the $U(1)_{\text{PQ}}$ transformation, it changes as ²

$$U(1)_{\text{PQ}} : \\ \Phi \rightarrow e^{i\epsilon} \Phi. \quad (2.40)$$

If we impose the potential for Φ

$$V(\Phi) = \frac{\lambda}{4} (|\Phi|^2 - \eta^2)^2, \quad (2.41)$$

the PQ field acquires the vacuum expectation value $|\langle \Phi \rangle| = \eta$, and the axion field is identified as a phase direction $\Phi \propto \exp(ia/\eta)$. Experimental constraints can be avoided if η is sufficiently larger than the electroweak scale.

The PQ field Φ cannot have direct couplings with standard model quarks, since they become heavy when Φ acquires the vacuum expectation value. In order to obtain the QCD anomaly, we must introduce additional fields to the standard model sector. Here, we enumerate two known examples.

The KSVZ model

In the Kim-Shifman-Vainshtein-Zakharov (KSVZ) model [16, 17], the QCD anomaly is obtained by introducing a heavy quark Q , which has a Yukawa coupling with the PQ field

$$\mathcal{L}_Q = -y_Q \bar{Q}_L \Phi Q_R + \text{h.c.} \quad (2.42)$$

Under the $U(1)_{\text{PQ}}$ symmetry, the heavy quark transforms as

$$U(1)_{\text{PQ}} : \\ Q_L \rightarrow e^{+i\epsilon/2} Q_L, \quad Q_R \rightarrow e^{-i\epsilon/2} Q_R. \quad (2.43)$$

In this model, only Φ and Q are charged under $U(1)_{\text{PQ}}$. In particular, the axion does not interact with electrons. Such a model is called the “hadronic axion” model [75].

²Here, we choose the PQ charge of Φ to be unity. Alternatively, one can assign the PQ charge Q_Φ such that $\Phi \rightarrow e^{iQ_\Phi \epsilon} \Phi$, $a \rightarrow a + F_a \epsilon$, and $F_a = Q_\Phi \eta$.

The DFSZ model

The Dine-Fischler-Srednicki-Zhitnisky (DFSZ) model [18, 19] realizes the QCD anomaly without introducing a heavy quark. The trick is to assume two standard model Higgs doublets φ_1 and φ_2 . Light quarks directly couple to φ_1 and φ_2 through the Yukawa terms (2.35), but do not to the PQ field Φ . The PQ field couples with two Higgs doublets through the scalar potential

$$V(\varphi_1, \varphi_2, \Phi) = \frac{\lambda_1}{4}(\varphi_1^\dagger \varphi_1 - v_1^2)^2 + \frac{\lambda_2}{4}(\varphi_2^\dagger \varphi_2 - v_2^2)^2 + \frac{\lambda}{4}(|\Phi|^2 - \eta^2)^2 \\ + (a\varphi_1^\dagger \varphi_1 + b\varphi_2^\dagger \varphi_2)|\Phi|^2 + c(\varphi_1 \cdot \varphi_2 \Phi^2 + \text{h.c.}) + d|\varphi_1 \cdot \varphi_2|^2 + e|\varphi_1^\dagger \varphi_2|^2. \quad (2.44)$$

The Lagrangian is invariant under the PQ symmetry transformation

$$U(1)_{\text{PQ}} : \\ \varphi_1 \rightarrow e^{-i\epsilon} \varphi_1, \quad \varphi_2 \rightarrow e^{-i\epsilon} \varphi_2, \\ u_L \rightarrow u_L, \quad u_R \rightarrow e^{+i\epsilon} u_R, \\ d_L \rightarrow d_L, \quad d_R \rightarrow e^{+i\epsilon} d_R, \quad (2.45)$$

together with (2.40). The axion field is a linear combination of the phases of three scalar fields φ_1^0 , φ_2^0 and Φ .

2.4 Properties of the invisible axion

Since the PQWW model was experimentally ruled out, hereafter we will concentrate on invisible axions. In this section, we quote some formulae which describe properties of the invisible axion.

2.4.1 Mass and potential

The standard Bardeen-Tye estimation for the axion mass (2.39) is also applicable to the invisible axion

$$m_a = \frac{\sqrt{Z}}{1+Z} \frac{F_\pi m_\pi}{F_a} \simeq 6 \times 10^{-6} \text{eV} \left(\frac{10^{12} \text{GeV}}{F_a} \right), \quad (2.46)$$

where we used $m_\pi \simeq 140 \text{MeV}$, $F_\pi \simeq 93 \text{MeV}$, and $Z \simeq 0.48$. As we will see in the next section, astrophysical and cosmological observations imply $F_a \sim 10^9 - 10^{12} \text{GeV}$. Hence, the axion has a tiny mass $m_a \sim 10^{-6} - 10^{-3} \text{eV}$.

In Sec. 2.2, we see that the axion potential (or mass) is generated due to the QCD effect. This means that the axion becomes massless in the limit where the QCD effect becomes negligible, or in other words, the chiral symmetry is restored. This occurs when the temperature of the universe exceeds the QCD scale $\sim \Lambda_{\text{QCD}} \simeq \mathcal{O}(100) \text{MeV}$. Hence, the axion mass depends on the temperature T , if the temperature is sufficiently high ($T \gtrsim \Lambda_{\text{QCD}}$). In

order to estimate the finite temperature axion mass, it is necessary to investigate the non-perturbative effect of QCD in the quark-gluon plasma with finite temperature. This subject has been discussed by several authors [76, 77, 78]. Recently, Wantz and Shellard [79] presented the temperature dependence of m_a which is valid at all temperatures within the interacting instanton liquid model (IILM) [80]. Fitting the numerical result, they obtained the power-law expression for $m_a(T)$

$$m_a(T)^2 = c_T \frac{\Lambda_{\text{QCD}}^4}{F_a^2} \left(\frac{T}{\Lambda_{\text{QCD}}} \right)^{-n}, \quad (2.47)$$

where $n = 6.68$, $c_T = 1.68 \times 10^{-7}$. Here, Λ_{QCD} is determined by solving the self-consistency relation for the chiral condensate $\langle \bar{q}q \rangle$ in the IILM [81]. This procedure gives $\Lambda_{\text{QCD}} \approx 400\text{MeV}$ with an overall error of 44MeV . The fitting formula (2.47) is obtained for $\Lambda_{\text{QCD}} = 400\text{MeV}$. The power-law expression (2.47) should be cut off by hand once it exceeds the zero-temperature value $m_a(T = 0)$, where

$$m_a(0)^2 = c_0 \frac{\Lambda_{\text{QCD}}^4}{F_a^2}, \quad (2.48)$$

and $c_0 = 1.46 \times 10^{-3}$. In this thesis, we use Eqs. (2.47) and (2.48) as the expression for the axion mass.

Let us comment on the form of the potential for the axion field. As described in Eq. (2.31), the effective potential for the axion field is given by the functional integral

$$Z = \exp \{-V_4 V(a)\} = \int \mathcal{D}A \det(\gamma_\mu D_\mu + m) \exp(-S_g - S_{a-g}), \quad (2.49)$$

where V_4 is the volume of 4-dimensional Euclidean spacetime, γ_μ is Dirac matrices, D_μ is the gauge covariant derivative acting on the quark fields, and S_g and S_{a-g} are actions for gluon fields and axion-gluon interaction term, respectively. Here, we included the quark determinant $\det(\gamma_\mu D_\mu + m)$ which was dropped in Eq. (2.31) for simplicity. Then, the axion mass is defined by

$$m_a^2 \equiv \left. \frac{\partial^2 V(a)}{\partial a^2} \right|_{a=0}. \quad (2.50)$$

At zero temperature, the partition function (2.49) can be computed analytically through the dilute gas approximation [59]

$$Z = \sum_{n, \bar{n}} \frac{1}{n! \bar{n}!} V_4^{n+\bar{n}} Z_I^{n+\bar{n}} \exp(i\bar{\theta}(n - \bar{n})), \quad (2.51)$$

where $\bar{\theta} = a/F_a$, and Z_I is the contribution from single instanton configuration

$$Z_I = \int d\rho n(\rho), \quad (2.52)$$

$$n(\rho) = \rho^{b-5} \Lambda_{\text{QCD}}^b \left(\frac{8\pi^2}{g^2} \right)^{2N_c} C_{N_c} \prod_{f=1}^{N_F} \det(\gamma_\mu D_\mu + m_f), \quad (2.53)$$

$$b = \frac{11}{3} N_c - \frac{2}{3} N_F, \quad C_{N_c} = \frac{0.466 \exp(-1.679 N_c)}{(N_c - 1)! (N_c - 2)!}. \quad (2.54)$$

Here, N_c is the color number, and N_F is the number of fermions. From Eq. (2.51), it is straightforward to obtain the potential for the axion field

$$V(a) = -2 \int d\rho n(\rho) \cos\left(\frac{a}{F_a}\right). \quad (2.55)$$

Combined with Eq. (2.50), we can write it as

$$V(a) = m_a^2 F_a^2 \left\{ 1 - \cos\left(\frac{a}{F_a}\right) \right\}, \quad (2.56)$$

where we redefined the vacuum such that $V(a) = 0$ at $a = 0$.

The dilute gas approximation can also be used at high temperature $T \gg \Lambda_{\text{QCD}}$ where perturbative calculation remains valid, and one can derive cosine type potential (2.55) multiplied by the temperature dependent correction factor [76]. However, it is non-trivial to calculate the form of $V(a)$ in the intermediate regime, where the perturbative calculation cannot be applied. In principle, it is possible to obtain exact form of $V(a)$ by computing (2.49) in the lattice, but there are technical difficulties to execute it. For now, we simply use the axion potential at finite temperature by replacing m_a^2 in Eq. (2.56) with $m_a(T)^2$ given by Eq. (2.47). This approximation is not out of touch with reality, at least for the estimation of the height of the potential, since the formula (2.47) is motivated by the IILM, which holds in the intermediate regime between zero temperature and high temperature.

If there exist other CP violating terms in the Lagrangian, the form of the potential would be modified. Indeed, weak interactions slightly violate CP [82], which shifts the value of $\bar{\theta}$ from zero. However, it was argued that this effect is extremely small compared with the bound on $\bar{\theta}$ given by Eq. (2.24) [83]. Therefore we can safely neglect the weak CP violating contribution for the potential $V(a)$.

Other possible source of the CP violation is the contribution from gravity. It was pointed out that the gravitational effect coming from Planck scale physics easily violates CP symmetry [42, 43, 44, 46, 45]. Taking account of this contribution, we express the full potential for the axion field as

$$V_{\text{full}}(a) = V_{\text{QCD}}(a) + V_{\text{grav}}(a), \quad (2.57)$$

where $V_{\text{QCD}}(a)$ is given by Eq. (2.56). The form of $V_{\text{grav}}(a)$ is unknown, as we might not have a comprehensive theory to deal with Planck scale physics. Here, we just assume that $V_{\text{grav}}(a)$ is negligible compared with $V_{\text{QCD}}(a)$ so that the axion mass is determined by $V_{\text{QCD}}(a)$.³ However, the existence of $V_{\text{grav}}(a)$ would play a role in cosmology, and we can constrain the magnitude of $V_{\text{grav}}(a)$ by cosmological consideration, which will be discussed in Chapter 4.

2.4.2 Coupling with other particles

The interactions of the invisible axion with other particles were discussed in detail in [75, 85]. Axions interact with photons due to the coupling

$$\mathcal{L}_{a\gamma\gamma} = -\frac{g_{a\gamma\gamma}}{4} a F^{\mu\nu} \tilde{F}_{\mu\nu}, \quad (2.58)$$

³Some mechanisms to suppress $V_{\text{grav}}(a)$ were discussed in [84].

where $F^{\mu\nu}$ is the photon field strength, $\tilde{F}_{\mu\nu} \equiv \frac{1}{2}\epsilon_{\mu\nu\lambda\sigma}F^{\lambda\sigma}$ is the dual of it. The magnitude of the axion-photon coupling is parametrized by

$$g_{a\gamma\gamma} \equiv \frac{\alpha}{2\pi F_a} c_{a\gamma\gamma}, \quad (2.59)$$

where $\alpha = e^2/4\pi$ is the fine structure constant. The numerical coefficient $c_{a\gamma\gamma}$ is given by

$$c_{a\gamma\gamma} = \frac{E}{A} - \frac{2}{3} \frac{4+Z}{1+Z}, \quad (2.60)$$

where A is the color anomaly appearing in Eq. (2.26), and E is the electromagnetic anomaly. $E/A = 0$ in the KSVZ model, while E/A depends on the charge assignment of leptons in the DFSZ model [86].

Axions also have interactions with fermions

$$\mathcal{L}_{ajj} = -i \frac{C_j m_j}{F_a} a \bar{\psi}_j \gamma_5 \psi_j, \quad (2.61)$$

where ψ_j is the fermion field, m_j is its mass, and C_j is a numerical coefficient whose value depends on models. In hadronic axion models such as KSVZ model, axions do not have tree level couplings to leptons. On the other hand, in DFSZ model, axions interact with electrons so that $C_e = \cos^2 \beta / N_g$, where $\tan \beta = v_1/v_2$ is the ratio of two Higgs vacuum expectation values, and N_g is the number of generations ($N_g = 3$ for the standard model). The interaction coefficient with proton C_p and neutron C_n are calculated in [87, 88], but they contain some uncertainties which mainly come from the estimation of the quark masses.

Due to the coupling with photons, the axion would decay into two photons with a rate

$$\begin{aligned} \Gamma_\gamma &= \frac{g_{a\gamma\gamma}^2 m_a^3}{64\pi} = \frac{\alpha^2}{256\pi^3} c_{a\gamma\gamma}^2 \frac{m_a^3}{F_a^2} \\ &\simeq 2.2 \times 10^{-51} \text{sec}^{-1} \left(\frac{10^{12} \text{GeV}}{F_a} \right)^5, \end{aligned} \quad (2.62)$$

where we used Eq. (2.46) and $c_{a\gamma\gamma} = 1$ for simplicity. The lifetime of the axion exceeds the age of the universe $t_0 \simeq 10^{17} \text{sec}$ for $F_a \gtrsim 10^5 \text{GeV}$. Hence the invisible axion is almost stable, which motivates us to consider it as the dark matter of the universe.

2.4.3 Domain wall number

In Sec. 2.2, we showed that the potential for the axion field has minima at $\bar{\theta} = a/F_a = 2\pi k$, where k is an integer. This occurs because of the periodicity of $\bar{\theta}$, but the observed value of $\bar{\theta}$ vanishes at each minimum since the period of $\bar{\theta}$ is 2π . On the other hand, in general the field a itself can have a periodicity greater than $2\pi F_a$. If a has a periodicity $2\pi N_{\text{DW}} F_a$, where N_{DW} is an integer, there exist N_{DW} degenerate vacua in the theory. In other words, the degeneracy of vacua is defined as

$$N_{\text{DW}} \equiv \frac{(\text{periodicity of } a)}{2\pi F_a}. \quad (2.63)$$

If N_{DW} is greater than unity, the theory has $Z_{N_{\text{DW}}}$ discrete symmetry, in which the axion field transforms as

$$a \rightarrow a + 2\pi k F_a, \quad k = 0, 1, \dots, N_{\text{DW}} - 1. \quad (2.64)$$

This $Z_{N_{\text{DW}}}$ symmetry is spontaneously broken when the axion field acquires the vacuum expectation value, leading to the formation of domain walls (see Appendix B.5). In this sense, we call N_{DW} the *domain wall number*.

For the class of invisible axion models with single $SU(2)_L \times U(1)_Y$ singlet scalar field, the value of N_{DW} is easily obtained. Since the axion field a is identified as the phase direction of the complex scalar field Φ such that

$$\Phi = \eta \exp\left(\frac{ia}{\eta}\right), \quad (2.65)$$

a has a periodicity $2\pi\eta$. Hence, from Eqs. (2.29) and (2.63), we see that the domain wall number is determined by the color anomaly [25, 26, 13]

$$\begin{aligned} N_{\text{DW}} &= \frac{\eta}{F_a} = A \\ &= \left| 2 \sum_{i=L} \text{Tr} Q_{\text{PQ}}(q_i) T_a^2(q_i) - 2 \sum_{i=R} \text{Tr} Q_{\text{PQ}}(q_i) T_a^2(q_i) \right|, \end{aligned} \quad (2.66)$$

where $Q_{\text{PQ}}(q_i)$ is the $U(1)_{\text{PQ}}$ charge for quark species q_i , $\sum_{i=L(R)}$ represents the sum over the left(right)-handed fermions, and T_a are the generators of $SU(3)_c$ normalized such that $\text{Tr} T_a T_b = I \delta_{ab}$ where $I = 1/2$ for fundamental representation of $SU(3)_c$. In the KSVZ model we obtain $N_{\text{DW}} = 1$ if there is single heavy quark Q , while in the DFSZ model it is predicted that $N_{\text{DW}} = 2N_g$ where N_g is the number of generations.

As we discuss in Chapter 3 and 4, the cosmological scenario is different between models with $N_{\text{DW}} = 1$ and $N_{\text{DW}} > 1$. We will see that the model with $N_{\text{DW}} > 1$ is more harmful than that with $N_{\text{DW}} = 1$.

2.5 Search for the invisible axion

There are three ways to search for the invisible axion. The first way is to directly detect it by means of the laboratory experiments. The second way is to indirectly observe it in the astronomical objects. The third way is to constrain its properties from cosmology. Although the main topic of this thesis is cosmological aspects of the axion (the third one), we briefly summarize the constraints obtained in other research activities.

2.5.1 Laboratory searches

Axion helioscopes

Axion produced in the sun would be directly detected by the axion ‘‘helioscopes’’. Due to the axion-photon coupling (2.58), axions can convert into photon in the presence of the

strong magnetic field. This gives a signal in the X-ray detector, or the null detection gives a bound on the axion-photon coupling $g_{a\gamma\gamma}$. The Tokyo Axion Helioscope [89] gives a bound $g_{a\gamma\gamma} < 6 \times 10^{-10}$ for $m_a < 0.03\text{eV}$. Recently, it is improved to obtain a bound $g_{a\gamma\gamma} < (5.6\text{--}13.4) \times 10^{-10}\text{GeV}^{-1}$ in the mass region $0.84\text{eV} < m_a < 1.00\text{eV}$ [90]. Phase I of the CERN Axion Solar Telescope (CAST) [91] gives $g_{a\gamma\gamma} < 8.8 \times 10^{-11}\text{GeV}^{-1}$ for $m_a \lesssim 0.02\text{eV}$. It is improved in Phase II [92] as $g_{a\gamma\gamma} < 2.2 \times 10^{-10}\text{GeV}^{-1}$ for $m_a \lesssim 0.4\text{eV}$. The sensitivity is expected to be improved up to $g_{a\gamma\gamma} < \text{few} \times 10^{-12}\text{GeV}^{-1}$ in the next generation helioscopes [93, 94].

Microwave receiver detectors

Sikivie [95, 96] proposed the experimental methods to detect axions distributed in the galactic halo (the axion ‘‘haloscopes’’). The detection of galactic halo axions is possible by means of the resonant signal in the microwave cavity [97]. Using this technique, the Axion Dark Matter Experiment (ADMX) at Lawrence Livermore National Laboratory (LLNL) excludes KSVZ axions in the mass range $1.9 \times 10^{-6}\text{eV} < m_a < 3.53 \times 10^{-6}\text{eV}$ [98]. However, it was also pointed out that this exclusion limit would be avoided due to the uncertainty in the value of $Z = m_u/m_d$ [99].

Bragg diffraction scattering

Another technique to detect solar axions was proposed by [100]. This uses the crystal, in which axions convert into X-rays due to the atomic electric field. If the scattering angle of X-ray photon satisfies the Bragg’s condition, the signal would be enhanced enough to observe. Some groups give constraints on the axion-photon coupling by using this detection technique. COSME [101] uses germanium detectors and gives a bound $g_{a\gamma\gamma} < 2.78 \times 10^{-9}\text{GeV}^{-1}$. SOLAX [102] also uses germanium detectors and gives $g_{a\gamma\gamma} < 2.7 \times 10^{-9}\text{GeV}^{-1}$. TEXONO [103] uses germanium detectors, but the nuclear power reactor as a source of axions. They give $g_{a\gamma\gamma}g_{aNN}^1 < 7.7 \times 10^{-9}\text{GeV}^{-2}$ for $m_a \lesssim 10^5\text{eV}$, where g_{aNN}^1 is the isovector axion-nucleon coupling. DAMA [104] uses NaI detectors and gives a bound $g_{a\gamma\gamma} < 1.7 \times 10^{-9}\text{GeV}^{-1}$.

Photon regeneration

Photon regeneration experiments [105] also constrain the axion-photon coupling. These experiments are based on the light signal propagating toward the absorber wall. Some photons convert into axions due to the external magnetic field, passing through the wall. These axions reconvert into photons after passing the wall, making a signal in the detector. Recently, several groups have started this kind of experiments. PVLAS reported some signatures [106], but they are excluded by subsequent experiments. The null detection of the signal gives an upper bound on the axion-photon coupling. The BMV experiment [107] gives a bound $g_{a\gamma\gamma} < 1.6 \times 10^{-6}\text{GeV}^{-1}$. The GammeV experiment [108] improves this bound up to $g_{a\gamma\gamma} < 3.5 \times 10^{-7}\text{GeV}^{-1}$. Finally, ALPS [109] reports a constraint $g_{a\gamma\gamma} < (6 - 7) \times 10^{-8}\text{GeV}^{-1}$. These constraints are applicable to axion mass $m_a \lesssim 10^{-3}\text{eV}$.

2.5.2 Astrophysical bounds

The sun

The energy loss arguments in the sun give some constraints on the axion coupling parameters. The energy loss by solar axion emission requires enhanced nuclear burning and increases solar ^8B neutrino flux. The observation of ^8B neutrino flux gives a bound $g_{a\gamma\gamma} \lesssim 7 \times 10^{-10} \text{GeV}^{-1}$ [110, 111]. The solar neutrino flux constraint can also be applied to the axion-electron coupling, giving $g_{aee} < 2.8 \times 10^{-11}$, where $g_{aee} \equiv C_e m_e / F_a$, and m_e is the electron mass.

Globular cluster

The observations of globular clusters give another bound. The helium-burning lifetimes of horizontal branch (HB) stars give a bound for axion-photon coupling $g_{a\gamma\gamma} \lesssim 0.6 \times 10^{-10} \text{GeV}^{-1}$ [112]. Furthermore, the delay of helium ignition in red-giant branch (RGB) stars due to the axion cooling gives $g_{aee} < 2.5 \times 10^{-13}$ [113].

Supernova 1987A

From the energy loss rate of the supernova (SN) 1987A [114], one can constrain the axion-nucleon coupling. For a small value of the coupling, the mean free path of axions becomes larger than the size of the SN core (so called the “free streaming” regime). In this regime, the energy loss rate is proportional to the axion-nucleon coupling squared, and one can obtain the limit $F_a \gtrsim 4 \times 10^8 \text{GeV}$ [115]. On the other hand, for a large value of the coupling, axions are “trapped” inside the SN core. In this regime, by requiring that the axion emission should not have a significant effect on the neutrino burst, one can obtain another bound $F_a \lesssim \mathcal{O}(1) \times 10^6 \text{GeV}$ [116]. However, in this “trapped” regime, it was argued that the strongly-coupled axions with $F_a \lesssim \mathcal{O}(1) \times 10^5 \text{GeV}$ would have produced an unacceptably large signal at the Kamiokande detector, and hence they were ruled out [117].

White dwarfs

The axion-electron coupling is constrained by the observation of white-dwarfs. The cooling time of white-dwarfs due to the axion emission gives a bound $g_{aee} < 4 \times 10^{-13}$ [118]. Recently, it is reported that the fitting of the luminosity function of white-dwarfs is improved due to the axion cooling, which implies the axion-electron coupling $g_{aee} \simeq (0.6-1.7) \times 10^{-13}$ [119, 120]. Also, observed pulsation period of a ZZ Ceti star can be explained by means of the cooling due to the axion emission, if $g_{aee} \simeq (0.8-2.8) \times 10^{-13}$ [121, 122]. These observations might imply the existence of the meV mass axion, but require further discussions.

Telescopes

The axion with mass $m_a \sim \mathcal{O}(1)\text{eV}$ in galaxy clusters makes a line emission due to the decay into two photons, whose wavelength is $\lambda_a \simeq 24800\text{\AA}/[m_a/1\text{eV}]$. This line emission gives observable signature in telescopes [123, 124, 125]. Such a line has not been observed in any telescope searches, which excludes the mass range $3\text{eV} \lesssim m_a \lesssim 8\text{eV}$.

2.5.3 Cosmology

Hot dark matter

There is a parameter region around $F_a \sim 10^6\text{GeV}$, called the ‘‘hadronic axion window’’ [126], that is not excluded by observations. This occurs due to the ambiguity in light quark masses $Z = m_u/m_d$ which leads to the cancellation between E/A and $2(4 + Z)/3(1 + Z)$ in the axion-photon coupling (2.60) for the KSVZ model. In such a case, the astrophysical bounds on $g_{a\gamma\gamma}$ do not significantly constrain the value of F_a . However, in this parameter region, the axion becomes a candidate of hot dark matter [127], which can be constrained by observation of the large scale structure. The analysis in [128] gives a bound $m_a < 1.05\text{eV}$, which corresponds to $F_a > 5.7 \times 10^6\text{GeV}$. This bound is improved by using WMAP7 data in [129], pushing up to $m_a < 0.72\text{eV}$ or $F_a > 8.6 \times 10^6\text{GeV}$. Therefore, this hot dark matter scenario seems to be excluded.

Cold dark matter

In chapter 3, we will see that the invisible axion with a large value of F_a can be good candidate of cold dark matter. In this case, cosmological considerations place a limit on the axion density in the universe. The result of WMAP7 [6] implies the matter density of the present universe $\Omega_{\text{CDM}}h^2 = 0.11$ [see Eq. (A.8)]. By requiring that the present axion density $\Omega_a h^2 = \rho_a(t_0)h^2/\rho_{c,0}$ should not exceed the present matter abundance

$$\Omega_a h^2 \leq \Omega_{\text{CDM}} h^2 = 0.11, \quad (2.67)$$

we obtain the upper bound on the energy density of cosmic axions, or the axion decay constant F_a . The simple discussion gives $F_a \lesssim 10^{12}\text{GeV}$ [20, 21, 22]. We will give more extensive study in chapter 4.

2.5.4 Summary – The axion window

From various research activities, we have constrained the property of invisible axions. Aside from some numerical uncertainties in the coefficients such as $c_{a\gamma\gamma}$, all constraints would be translated into the bound on single parameter, the axion decay constant F_a , since all axion couplings are inversely proportional to F_a . The most stringent bound comes from the SN 1987A [115], which places the lower limit

$$F_a > 4 \times 10^8\text{GeV}. \quad (2.68)$$

If F_a is smaller than this value, the burst duration becomes inconsistent with the energy loss due to axions. Furthermore, if F_a is smaller than $F_a \simeq \mathcal{O}(1) \times 10^5 \text{GeV}$, SN axions would give too much signals in the Kamiokande detector, and hence it is ruled out [117]. The intermediate region $F_a \sim 10^6 \text{GeV}$ between these two bounds is not excluded from the observation of SN, but the globular cluster [112] gives another bound $g_{a\gamma\gamma} \lesssim 0.6 \times 10^{-10} \text{GeV}^{-1}$, which corresponds to $F_a/c_{a\gamma\gamma} \gtrsim 2 \times 10^7 \text{GeV}$. This bound might be avoided if we tune the value of $c_{a\gamma\gamma}$ [126, 127], but in this case the axion becomes hot dark matter, which is excluded by the observation of the large scale structure [128, 129]. Hence in the following we take Eq. (2.68) as an universal lower bound on F_a . Note that the estimation of the axion emission rate suffers from various numerical uncertainties which may modify the bound by a factor of $\mathcal{O}(1)$ [115].

Above the bound (2.68), the ADMX experiments [98] exclude the KSVZ axion in the region $1.9 \times 10^{-6} \text{eV} < m_a < 3.53 \times 10^{-6} \text{eV}$, which corresponds to $1.7 \times 10^{12} \text{GeV} < F_a < 3.2 \times 10^{12} \text{GeV}$. However, it is possible to avoid this constraint due to the uncertainty in the value of Z [99].

The cosmological axion density gives an upper bound on F_a [20, 21, 22]. Combined with the lower bound (2.68), we obtain the ‘‘classic axion window’’

$$4 \times 10^8 \text{GeV} < F_a < 10^{12} \text{GeV}. \quad (2.69)$$

However, this upper bound contains large uncertainties. The problem is that the value of $\Omega_a h^2$ in Eq. (2.67) strongly depends on the cosmological scenarios. In particular, the occurrence of the inflationary expanding stage and the formation of topological defects completely change the nature of the axion dark matter. The rest part of this thesis is devoted on this issue.

Chapter 3

Axion cosmology

Invisible axions are ideal candidates of dark matter, in the sense that they are stable and that their couplings with ordinary matters are extremely suppressed. Therefore, if the relic abundance of the invisible axions agrees with the present dark matter abundance, it is possible to explain the dark matter of the universe with axions. In order to discuss whether axions correctly explain the present abundance of the dark matter, we must investigate their production mechanisms in the early universe.

As mentioned in Chapter 1, cosmological scenario is different between the case where inflation has occurred after the PQ phase transition (scenario I) and the case where inflation has occurred before the PQ phase transition (scenario II). For scenario I, quantum fluctuations of axion field generated at the inflationary stage give a constraint on some model parameters. On the other hand, for scenario II, we must take account of the evolution of topological defects such as strings and domain walls. Since these topological defects produce additional population of axions, the composition of axion dark matter is different for each of scenarios. In this chapter, we mainly consider the cosmological aspects of axions produced by mechanisms other than topological defects. Implications of axions produced by topological defects are extensively studied in the next chapter.

The organization of this chapter is as follows. Two possible production mechanisms are introduced in Secs. 3.1 and 3.2. Section 3.1 is devoted to the estimation of the thermal production, while the non-thermal production is discussed in Sec 3.2. In that section, we give the standard expression for the relic abundance of the coherently oscillating axions. Finally, the constraint from isocurvature fluctuations is briefly described in Sec. 3.3.

3.1 Thermal production

If the temperature of the primordial plasma is sufficiently high, axions are produced from the thermal bath of the QCD plasma. The production of thermal axions is described by the standard freeze out scenario [130, 131, 132]. The number density of thermal axions n_a^{th} obeys the Boltzmann equation

$$\frac{dn_a^{\text{th}}}{dt} + 3Hn_a^{\text{th}} = \Gamma (n_a^{\text{eq}} - n_a^{\text{th}}), \quad (3.1)$$

where

$$\Gamma = \sum_i n_i \langle \sigma_i v \rangle, \quad (3.2)$$

is the interaction rate computed by summing over all processes involving axions $a + i \leftrightarrow 1 + 2$ ($i, 1,$ and 2 are other particles), n_i is the number density of i -th species, $\langle \sigma_i v \rangle$ is the thermal average of the cross section times relative velocity, and H is the Hubble parameter defined as Eq. (A.7). n_a^{eq} is the equilibrium number density of axions, which is obtained by using the Bose-Einstein distribution (A.13)

$$n_a^{\text{eq}} = \int_0^\infty \frac{4\pi g p^2 dp}{(2\pi)^3} \frac{1}{\exp(p/T) - 1} = \frac{\zeta(3)}{\pi^2} T^3, \quad (3.3)$$

where $\zeta(3) = 1.20206 \dots$ is the Riemann zeta function of 3, and we used $g = 1$ for axions.

Let us take a normalization

$$Y \equiv \frac{n_a^{\text{th}}}{s}, \quad (3.4)$$

where s is the entropy density given by Eq. (A.20)

$$s = \frac{2\pi^2}{45} g_{s*} T^3. \quad (3.5)$$

Equation (3.1) can be written as

$$x \frac{dY}{dx} = \frac{\Gamma}{H} (Y^{\text{eq}} - Y), \quad (3.6)$$

where $x = F_a/T$, and

$$Y^{\text{eq}} = \frac{n_a^{\text{eq}}}{s} \simeq \frac{0.27}{g_*}. \quad (3.7)$$

In the above equations, we used the approximation $g_{s*} \simeq g_* \simeq \text{constant}$, for simplicity.

The thermal average of the interaction rate Γ is calculated in Ref. [132] including the following three elementary processes

- (1) $a + g \leftrightarrow q + \bar{q}$
- (2) $a + q \leftrightarrow g + q$ and $a + \bar{q} \leftrightarrow g + \bar{q}$
- (3) $a + g \leftrightarrow g + g$,

where g is a gluon, and $q(\bar{q})$ is a light quark (anti-quark). Here, we quote the result of the analysis in [132]

$$\Gamma \simeq 7.1 \times 10^{-6} \frac{T^3}{F_a^2}, \quad (3.8)$$

which is obtained by using the value of the strong coupling constant $\alpha_s \equiv g^2/4\pi \simeq 1/35$ corresponding to the energy scale $E \simeq 10^{12} \text{GeV}$. Since $H \propto T^2$, the following quantity turns out to be constant

$$k \equiv x \frac{\Gamma}{H}. \quad (3.9)$$

Defining the quantity

$$y \equiv \frac{Y}{Y^{\text{eq}}}, \quad (3.10)$$

we reduce Eq. (3.6) into

$$x^2 \frac{dy}{dx} = k(1 - y), \quad (3.11)$$

which has a solution

$$y(x) = 1 - Ce^{k/x}, \quad (3.12)$$

where C is an integration constant. The axions decouple from the QCD plasma at $x = k$ ($\Gamma = H$). Afterwards, the number of axions becomes almost constant. The temperature at the decoupling T_D is obtained from the condition $x = k$, which gives

$$T_D \simeq 2 \times 10^{11} \text{GeV} \left(\frac{F_a}{10^{12} \text{GeV}} \right)^2. \quad (3.13)$$

The relic abundance of axions depends on the thermal history of the universe. For simplicity, let us assume that PQ symmetry is broken after inflation if $T_R > F_a$ is satisfied, where T_R is the reheating temperature after inflation.¹ We can consider the following possibilities: (i) $T_R > F_a > T_D$, (ii) $T_R > T_D > F_a$, (iii) $T_D > T_R > F_a$, (iv) $T_D > F_a > T_R$, (v) $F_a > T_D > T_R$, and (vi) $F_a > T_R > T_D$. These six domains are mapped into F_a - T_R plane, as shown in Fig 3.1.

For the case (i), Eq. (3.12) is rewritten as

$$y(x) = 1 - e^{k(1/x-1)}, \quad (3.14)$$

where we put the initial condition $y(x = 1) = 0$ such that axions do not exist at $T = F_a$. Requiring that the deviation from the thermal spectrum at the time of decoupling is less than 5%,

$$\frac{Y_D}{Y_{\text{eq}}} = y(x = k) = 1 - e^{k(1/k-1)} > 0.95,$$

where Y_D is the value of Y at the decoupling, we obtain

$$k = \frac{F_a}{T} \frac{\Gamma}{H} \simeq 5.0 \times \left(\frac{10^{12} \text{GeV}}{F_a} \right) > 4. \quad (3.15)$$

This corresponds to the condition [132]

$$F_a < 1.2 \times 10^{12} \text{GeV}. \quad (3.16)$$

In other words, if Eq. (3.16) is satisfied, axions enter into thermal equilibrium before they decouple from the plasma. On the other hand, for the cases (ii) and (iii), axions never enter into thermal equilibrium. Assuming the initial condition $y(x = 1) = 0$ at $T = F_a$, we obtain

$$y(\infty) = 1 - e^{-k}, \quad (3.17)$$

¹Note that there are some exceptions which invalidate this criterion. For example, if the highest temperature after inflation is greater than F_a , PQ symmetry is broken after inflation even if $T_R < F_a$ is satisfied. Furthermore, even though PQ symmetry is broken before inflation, it is restored during inflation if the amplitude of fluctuations of the axion field becomes larger than F_a , and hence it is broken again at the end of inflation. Here, we do not consider such cases since they depend on the detail of inflation models.

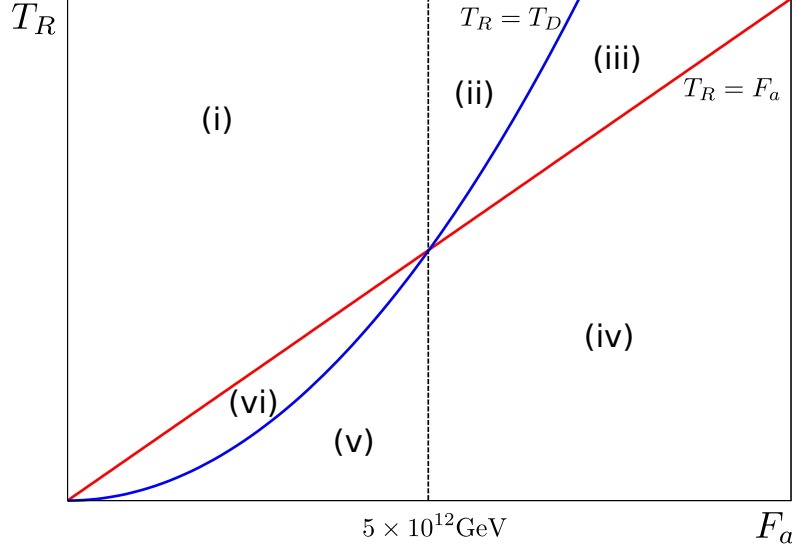


Figure 3.1: Six different domains (i) $T_R > F_a > T_D$, (ii) $T_R > T_D > F_a$, (iii) $T_D > T_R > F_a$, (iv) $T_D > F_a > T_R$, (v) $F_a > T_D > T_R$, and (vi) $F_a > T_R > T_D$ in the parameter space of F_a and T_R . These domains are divided by three lines, $T_R = F_a$ (red solid line), $T_R = T_D$ (blue solid line), and $F_a \simeq 5 \times 10^{12} \text{GeV}$ (dashed line) which corresponds to the condition $T_D = F_a$.

which implies that the final abundance of thermal axion is suppressed by a factor $1 - e^{-k}$.

Since PQ symmetry is broken before inflation for the cases (iv), (v), and (vi), we must use different initial condition from that used in Eq. (3.14). Here, we simply put the initial condition $y(x) = 0$ at $T = T_R$. This leads to the solution

$$y(x) = 1 - e^{k(1/x - 1/x_R)}, \quad (3.18)$$

where $x_R \equiv F_a/T_R$. For the cases (iv) and (v), axions never enter into thermal equilibrium, and we obtain

$$y(\infty) = 1 - e^{-k/x_R}, \quad (3.19)$$

where $k/x_R = T_R/T_D < 1$. On the other hand, for the case (vi), axions might enter into thermal equilibrium, but the condition for thermalization (3.15) is replaced by

$$\frac{k}{x_R} = \frac{T_R}{T_D} > 4. \quad (3.20)$$

Let us estimate the relic abundance of the thermal axions. For case (i) or (vi), if the condition (3.16) [for case (i)] or (3.20) [for case (vi)] is satisfied, the relic abundance is determined by the equilibrium number density (3.7) and it does not depend on the initial condition

$$n_a^{\text{th}}(t_0) = Y^{\text{eq}} s_0 = \frac{0.27}{g_*(T_D)} s_0 = 7.8 \text{cm}^{-3} \left(\frac{100}{g_*(T_D)} \right), \quad (3.21)$$

where s_0 is the entropy density at the present time, and $g_*(T_D)$ is the radiation degree of freedom at the time of decoupling. The present density of thermal axions is

$$\Omega_{a,\text{th}}h^2 = \frac{m_a n_a^{\text{th}}(t_0)}{\rho_{c,0}/h^2} = 4.44 \times 10^{-9} \left(\frac{100}{g_*(T_D)} \right) \left(\frac{10^{12}\text{GeV}}{F_a} \right), \quad (3.22)$$

where $\rho_{c,0}$ is the critical density today, and we used the expression for the axion mass (2.46). Note that we can use Eq. (3.22) only if the condition (3.16) [for case (i)] or (3.20) [for case (iv)] is satisfied. Otherwise we must multiply it by the suppression factor given by Eq. (3.17) or Eq. (3.19). It is clear that the population of thermal axions is too small to explain dark matter for the typical value of the decay constant $F_a \simeq 10^{9-12}\text{GeV}$.

3.2 Non-thermal production

3.2.1 Evolution of the axion field

The non-thermal production of axions is estimated by investigating the evolution of the background field. Let us consider the theory with the complex scalar field Φ (the PQ field) whose Lagrangian density is given by

$$\mathcal{L} = -\frac{1}{2}|\partial_\mu\Phi|^2 - V(\Phi), \quad (3.23)$$

where the potential $V(\Phi)$ is given by Eq. (2.41). When $U(1)_{\text{PQ}}$ is spontaneously broken, the axion field $a(x)$ is described by Eq. (2.65),

$$\langle\Phi\rangle = \eta e^{ia(x)/\eta}. \quad (3.24)$$

The evolution of the axion field in the expanding universe is described by

$$\ddot{a}(x) + 3H\dot{a}(x) - \frac{\nabla^2}{R^2(t)}a(x) + \frac{dV(a)}{da} = 0, \quad (3.25)$$

where $R(t)$ is the scale factor of the universe. Substituting the effective potential for the axion field (2.57) into $V(a)$ and assuming a is small compared with F_a , we obtain

$$\ddot{a}(x) + 3H\dot{a}(x) - \frac{\nabla^2}{R^2(t)}a(x) + m_a^2 a(x) = 0. \quad (3.26)$$

Let us define the time t_1 at which the following condition is satisfied

$$m_a(T_1) = 3H(t_1), \quad (3.27)$$

where T_1 is the temperature at the time t_1 , and $H(t_1)$ is the Hubble parameter at that time. Using the temperature dependence of $m_a(T)$ given in Eq. (2.47), we find

$$T_1 = 0.981\text{GeV} \left(\frac{g_{*,1}}{70} \right)^{-1/(4+n)} \left(\frac{F_a}{10^{12}\text{GeV}} \right)^{-2/(4+n)} \left(\frac{\Lambda_{\text{QCD}}}{400\text{MeV}} \right) \quad \text{for } T_1 \gtrsim 103\text{MeV}, \quad (3.28)$$

or

$$T_1 = 42.3\text{GeV} \left(\frac{g_{*,1}}{70}\right)^{-1/4} \left(\frac{F_a}{10^{12}\text{GeV}}\right)^{-1/2} \left(\frac{\Lambda_{\text{QCD}}}{400\text{MeV}}\right) \quad \text{for } T_1 \lesssim 103\text{MeV}, \quad (3.29)$$

where $g_{*,1}$ is the radiation degree of freedom at the time t_1 . Equation (3.28) is valid only for $T_1 \gtrsim 103\text{MeV}$, which corresponds to the case in which the condition given by Eq. (3.27) is satisfied before $m_a(T)$ becomes the zero-temperature value $m_a(0)$. We must use another expression (3.29) if $T_1 < 103\text{MeV}$. However, if we fix the values as $g_{*,1} = 70$ and $\Lambda_{\text{QCD}} = 400\text{MeV}$, this turnover occurs around the value $F_a \simeq 1.7 \times 10^{17}\text{GeV}$. Therefore, we can simply use Eq. (3.28) as long as we assume that $F_a < 1.7 \times 10^{17}$. The temperature given by Eq. (3.28) or Eq. (3.29) corresponds to the time

$$t_1 = 3.01 \times 10^{-7}\text{sec} \left(\frac{g_{*,1}}{70}\right)^{-n/2(4+n)} \left(\frac{F_a}{10^{12}\text{GeV}}\right)^{4/(4+n)} \left(\frac{\Lambda_{\text{QCD}}}{400\text{MeV}}\right)^{-2} \quad \text{for } T_1 \gtrsim 103\text{MeV}, \quad (3.30)$$

or

$$t_1 = 1.61 \times 10^{-10}\text{sec} \left(\frac{F_a}{10^{12}\text{GeV}}\right) \left(\frac{\Lambda_{\text{QCD}}}{400\text{MeV}}\right)^{-2} \quad \text{for } T_1 \lesssim 103\text{MeV}. \quad (3.31)$$

For $t < t_1$, we can ignore the mass term in Eq. (3.26) ($H \gg m_a$). Defining the Fourier component of the axion field

$$a(t, \mathbf{k}) = \int d^3\mathbf{x} e^{i\mathbf{k}\cdot\mathbf{x}} a(t, \mathbf{x}), \quad (3.32)$$

we obtain the following equation

$$\ddot{a}(t, \mathbf{k}) + 3H\dot{a}(t, \mathbf{k}) - \frac{k^2}{R^2}a(t, \mathbf{k}) = 0, \quad (3.33)$$

where $k = |\mathbf{k}|$. For the modes outside the horizon ($k/R \ll H$), the third term in the left hand side of Eq. (3.33) is dropped, and the solution is given by

$$a(t, \mathbf{k}) = C_1(\mathbf{k}) + C_2(\mathbf{k})t^{-1/2}, \quad (3.34)$$

where $C_1(\mathbf{k})$ and $C_2(\mathbf{k})$ are some \mathbf{k} -dependent constants. On the other hand, for modes inside the horizon ($k/R \gg H$), we cannot neglect the third term in the left hand side of Eq. (3.33). This leads to the solution oscillating with a frequency $\simeq k/R$, and the amplitude of the solution decreases with time as $\propto 1/R(t)$.

Every mode which is outside the horizon until $t \simeq t_1$ is frozen like Eq. (3.34). When the axion mass term becomes non-negligible ($t > t_1$), they begin to oscillate with a frequency $\simeq m_a$. We call these modes as zero modes and denote a_0 . Evolution of a_0 is described by

$$\ddot{a}_0 + 3H\dot{a}_0 + m_a^2 a_0 = 0. \quad (3.35)$$

Using the WKB approximation, we obtain the solution of this equation

$$a_0(t) \simeq a_0(t_1) \left(\frac{R(t_1)}{R(t)} \right)^{3/2} \cos \left(\int^t m_a dt \right). \quad (3.36)$$

This production mechanism of the zero modes is called the ‘‘misalignment mechanism’’. Note that, ‘‘zero’’ does not mean that the comoving momentum \mathbf{k} is exactly zero. In other words, all modes satisfying $k/R < H$ at $t > t_1$ can be described by Eq. (3.35) at least approximately.

3.2.2 Cold dark matter abundance

Let us estimate the contribution of zero modes to the cold dark matter abundance [20, 21, 22]. The crucial point of the misalignment mechanism is that the value of the axion field a_0 deviates from zero at the time of QCD phase transition. Since the axion mass vanishes at sufficiently high temperature, the value of a_0 is not necessarily zero at $t \lesssim t_1$. Then, a_0 begins to roll down to zero when the axion mass m_a is turned on. Subsequently, it oscillates around the minimum of the potential as described in Eq. (3.36). This oscillation energy density is interpreted as relic energy density of dark matter axions.

The energy density of zero modes is given by

$$\rho_{a,0}(t) = \frac{1}{2} \dot{a}_0^2(t) + \frac{1}{2} m_a^2(T) a_0^2(t). \quad (3.37)$$

Here, we include the temperature dependence of m_a , since the misalignment production occurs due to the emergence of the axion mass. For $H \ll m_a$, we can take time average over the period of the oscillation in Eq. (3.36), which gives the approximation $\rho_{a,0} \simeq \langle \dot{a}_0 \rangle \simeq m_a^2 \langle a_0^2 \rangle$. Then, from Eqs. (3.35) and (3.37) we obtain

$$\dot{\rho}_{a,0} = \left(\frac{\dot{m}_a}{m_a} - 3H \right) \rho_{a,0}, \quad (3.38)$$

which implies

$$\rho_{a,0} \propto \frac{m_a(T)}{R^3}. \quad (3.39)$$

Hence, the number of axions in the comoving volume $R^3 n_a = R^3 \rho_{a,0} / m_a$ is conserved. Noting this fact, we find the energy density of zero modes at the present time t_0

$$\rho_{a,0}(t_0) = \rho_{a,0}(t_1) \frac{m_a(0)}{m_a(T_1)} \left(\frac{R(t_1)}{R(t_0)} \right)^3, \quad (3.40)$$

where $\rho_{a,0}(t_1)$ is the energy density of zero modes at t_1

$$\rho_{a,0}(t_1) = \frac{1}{2} m_a(T_1)^2 (\bar{\theta}^{\text{mi}})^2 F_a^2, \quad (3.41)$$

and $\bar{\theta}^{\text{mi}} = a_0(t_1) / F_a$ is called the initial misalignment angle.

From the entropy conservation (A.23), it follows that

$$\left(\frac{R(t_1)}{R(t_0)}\right)^3 = \frac{s_0}{\frac{2\pi^2}{45}g_{*,1}T_1^3}, \quad (3.42)$$

where s_0 is the entropy density at the present time, and it satisfies

$$\frac{s_0 h^2}{\rho_{c,0}} = \frac{4}{3} \frac{g_{s*,0}}{g_{*,0}} \frac{\Omega_R h^2}{T_0}. \quad (3.43)$$

Here, $\rho_{c,0}$ is the critical density today, $g_{s*,0}$ and $g_{*,0}$ are the effective degrees of freedom for entropy density and energy density of radiations at the present time [see Eqs. (A.21) and (A.22)], T_0 is the temperature today, and $\Omega_R h^2 \equiv \rho_R(t_0)h^2/\rho_{c,0}$ is the density parameter of radiations. Using Eqs. (3.40) - (3.43) and the expression for T_1 given by Eq. (3.28), we find that the density parameter of the zero mode axions $\Omega_{a,0}h^2 = \rho_{a,0}(t_0)h^2/\rho_{c,0}$ becomes

$$\Omega_{a,0}h^2 = 0.095 \times (\bar{\theta}^{\text{ini}})^2 \left(\frac{g_{*,1}}{70}\right)^{-(n+2)/2(n+4)} \left(\frac{F_a}{10^{12}\text{GeV}}\right)^{(n+6)/(n+4)} \left(\frac{\Lambda_{\text{QCD}}}{400\text{MeV}}\right). \quad (3.44)$$

Strictly speaking, the above estimation is incorrect since we have used the following two approximations.

1. The form of the axion potential is assumed to be quadratic [i.e. the mass term in Eq. (3.37)], and other anharmonic terms are ignored.
2. It was assumed that the quantity $R^3 \rho_{a,0}/m_a$ becomes adiabatic invariant immediately after the time t_1 .

It was pointed out that the standard estimation (3.44) should be modified [77, 133, 78] if we take into account the deviation from above assumptions. There are two kinds of corrections corresponding to two conditions enumerated above. One is the anharmonic effect [77, 133] which gives a replacement $(\bar{\theta}^{\text{ini}})^2 \rightarrow f(\bar{\theta}^{\text{ini}})(\bar{\theta}^{\text{ini}})^2$ where $f(\bar{\theta}^{\text{ini}})$ is a function which converges into 1 for small $\bar{\theta}^{\text{ini}}$ but takes a value larger than 1 for large $\bar{\theta}^{\text{ini}}$. Another is the deviation from the adiabatic approximation at the initial time t_1 . It was shown that the adjustment in the initial stage, where the expansion rate H is not completely negligible, leads to larger energy density even though $\bar{\theta}^{\text{ini}}$ is small [78]. This correction makes $f(\bar{\theta}^{\text{ini}})(\bar{\theta}^{\text{ini}})^2$ larger than the previous estimations [77, 133] by a factor of 1.85. Taking account of these corrections, we rewrite Eq. (3.44) as

$$\Omega_{a,0}h^2 = 0.18 \times f(\bar{\theta}^{\text{ini}})(\bar{\theta}^{\text{ini}})^2 \left(\frac{g_{*,1}}{70}\right)^{-(n+2)/2(n+4)} \left(\frac{F_a}{10^{12}\text{GeV}}\right)^{(n+6)/(n+4)} \left(\frac{\Lambda_{\text{QCD}}}{400\text{MeV}}\right). \quad (3.45)$$

If PQ symmetry is broken after inflation (scenario II), it is expected that the value of $\bar{\theta}^{\text{ini}}$ spatially varies over the scale of the QCD horizon $\sim (R(t_1)/R(t_0))t_1$, which is smaller than the present horizon $\sim t_0$. Hence, we must replace $\bar{\theta}^{\text{ini}}$ by the root-mean square value

$$\langle (\bar{\theta}^{\text{ini}})^2 \rangle = \frac{1}{\pi} \int_0^\pi f(\bar{\theta}^{\text{ini}})(\bar{\theta}^{\text{ini}})^2 d\bar{\theta}^{\text{ini}}. \quad (3.46)$$

If the anharmonic correction is absent [$f(\bar{\theta}^{\text{ini}}) = 1$], it gives $\langle(\bar{\theta}^{\text{ini}})^2\rangle = \pi^2/3$. Turner [77] calculated the anharmonic effect numerically and obtained the correction factor 1.9-2.4. The origin of the uncertainty in this correction factor comes from the form of the temperature dependent axion mass. Later, Lyth [133] gave the extensive calculation and reported the agreement with Turner's result within a factor of 2.² Here, we take the magnitude of the correction as $\langle(\bar{\theta}^{\text{ini}})^2\rangle \rightarrow (1.9-2.4) \times \pi^2/3$. Substituting this value into Eq. (3.46), we finally obtain

$$\Omega_{a,0}h^2 = (1.10-1.39) \times \left(\frac{g_{*,1}}{70}\right)^{-(n+2)/2(n+4)} \left(\frac{F_a}{10^{12}\text{GeV}}\right)^{(n+6)/(n+4)} \left(\frac{\Lambda_{\text{QCD}}}{400\text{MeV}}\right)$$

for scenario II.

(3.47)

The requirement that $\Omega_{a,0}h^2 < \Omega_{\text{CDM}}h^2 = 0.11$ leads to the bound

$$F_a \lesssim (1.2-1.4) \times 10^{11}\text{GeV} \quad (3.48)$$

for $g_{*,1} = 70$ and $\Lambda_{\text{QCD}} = 400\text{MeV}$. This bound is more severe than that quoted in Eq. (2.69), due to the inclusion of two correction factors. The error in this expression is due to the uncertainty in the anharmonic correction factor, which might be caused by the uncertainty in the temperature dependence of the axion mass. Note that the above result is only applicable to scenario II. For scenario I, we must use different estimation, which will be described in Sec. 3.3.

So far we have considered the zero modes only, but there exist non-zero modes in scenario II. The non-zero modes, whose momenta satisfy $k/R \gg H$ at $t > t_1$, are produced from other mechanisms, namely the string decay and the domain wall decay. The estimation of the contributions of these non-zero modes will be performed in Chapter 4. We will see that the bound (3.48) becomes much more severe if we include the contributions from non-zero modes.

3.3 Axion isocurvature fluctuations

If PQ symmetry is broken before (during) inflation (scenario I), the axion exists as a massless scalar field during inflation, which induces some amount of quantum fluctuations. The scale of these fluctuations is stretched out beyond the horizon scale, and modes re-entering the horizon at the scale relevant to CMB observation can be measured precisely. There are two kinds of such fluctuations, called the adiabatic fluctuations and the isocurvature fluctuations. The adiabatic fluctuations are fluctuations in the total energy density $\delta\rho \neq 0$, but the number n does not fluctuate $\delta(n/s) = 0$, where s is the entropy density. On the other hand, the isocurvature fluctuations are characterized by $\delta\rho = 0$ and $\delta(n/s) \neq 0$, which means that there are no fluctuations in the total energy density. Each of them induces a

²In [133], it was assumed that inflation has occurred after PQ phase transition (scenario I), and the average (3.46) is not calculated. Hence we use Turner's estimation [77] for the anharmonic correction in scenario II.

distinctive spectrum in the anisotropy of CMB observed today. The difference between adiabatic fluctuations and isocurvature fluctuations becomes distinctive only when they are outside the horizon. Once they re-enter into the horizon, effects of microphysics become relevant, and isocurvature modes are converted into fluctuations in the total energy density. The magnitude of isocurvature fluctuations for a particle species i outside the horizon is characterized by the following quantity

$$S_i = \frac{\delta(n_i/s)}{n_i/s} = \frac{\delta n_i}{n_i} - 3 \frac{\delta T}{T}, \quad (3.49)$$

where n_i is the number density of species i , and we used $s \propto T^3$ in the second equality.

Fluctuations of the axion field induce isocurvature modes, but the recent observations prefer the adiabatic type, which might be created by the quantum fluctuations of the inflaton field [see e.g. [134]]. Therefore, the null observation of the isocurvature component gives a constraint on the axion models. Recently, several authors analyzed this isocurvature constraint using up-to-date observational data [135, 33, 34, 136, 137, 79, 138].

During the inflationary stage, the massless axion field has a quantum fluctuation whose spectrum is given by [see e.g. [139]]

$$\langle |\delta a(\mathbf{k})|^2 \rangle = \left(\frac{H_I}{2\pi} \right)^2 \frac{2\pi^2}{k^3}, \quad (3.50)$$

where H_I is the Hubble parameter during inflation. Let us use the abbreviation $\delta a^2 = (H_I/2\pi)^2$ representing this fact (δa is a typical amplitude of the fluctuations in the real space). These fluctuations of the axion field lead to fluctuations in the initial misalignment angle $\bar{\theta}^{\text{ini}}$ with the amplitude

$$\sigma_\theta^2 = \left(\frac{\delta a}{F_a} \right)^2 = \left(\frac{H_I}{2\pi F_a} \right)^2. \quad (3.51)$$

Since the value of the axion field becomes homogenized into a certain value of $\bar{\theta}^{\text{ini}}$ due to the inflationary expansion, we replace $\langle (\bar{\theta}^{\text{ini}})^2 \rangle \rightarrow (\bar{\theta}^{\text{ini}})^2 + \sigma_\theta^2$ in Eq. (3.45). Then, we obtain the relic abundance of axions

$$\Omega_{a,0} h^2 = 0.18 \times [(\bar{\theta}^{\text{ini}})^2 + \sigma_\theta^2] \left(\frac{g_{*,1}}{70} \right)^{-(n+2)/2(n+4)} \left(\frac{F_a}{10^{12} \text{GeV}} \right)^{(n+6)/(n+4)} \left(\frac{\Lambda_{\text{QCD}}}{400 \text{MeV}} \right) \quad (3.52)$$

for scenario I,

where we ignored the anharmonic correction $f(\bar{\theta}^{\text{ini}})$ for simplicity.

Fluctuations of the axion field are considered as isocurvature fluctuations, since the axion is massless before QCD phase transition, which means that $\delta\rho_a = 0$. When the axion acquires a mass after QCD phase transition, isocurvature fluctuations are arranged such that fluctuations in the sum of energy constituents vanish

$$\delta\rho = m_a \delta n_a + \sum_{j \neq a} m_j \delta n_j + 4\rho_R \frac{\delta T}{T} = 0, \quad (3.53)$$

where we included contributions of massive species j other than the axion. Assuming that fluctuations in the number density of species j are adiabatic, we obtain

$$S_j = \frac{\delta n_j}{n_j} - 3 \frac{\delta T}{T} = 0 \quad \text{for} \quad j \neq a. \quad (3.54)$$

From Eqs. (3.49), (3.53), and (3.54), we find

$$S_a = \frac{\delta n_a}{n_a} - 3 \frac{\delta T}{T}, \quad (3.55)$$

$$\frac{\delta T}{T} = -\frac{1}{4} S_a \left(\frac{\rho_a / \rho_R}{1 + 3\rho_M / 4\rho_R} \right), \quad (3.56)$$

where $\rho_M = m_a n_a + \sum_{j \neq a} m_j n_j$ is the total energy density of cold matters. In the early epoch ($\rho_R \gg \rho_M, \rho_a$), Eq. (3.56) implies that $\delta T/T \ll S_a$. Hence we ignore $\delta T/T$ in Eq. (3.55) and obtain

$$S_a \simeq \frac{\delta n_a}{n_a}. \quad (3.57)$$

Conventionally, the magnitude of isocurvature perturbations is parametrized as

$$\alpha(k_0) = \frac{\Delta_S^2(k_0)}{\Delta_{\mathcal{R}}^2(k_0) + \Delta_S^2(k_0)}, \quad (3.58)$$

where Δ_S^2 and $\Delta_{\mathcal{R}}^2$ are amplitudes of isocurvature fluctuations and adiabatic fluctuations, respectively, and $k_0 = 0.002 \text{Mpc}^{-1}$ is the pivot scale. The amplitude of the adiabatic fluctuations $\Delta_{\mathcal{R}}^2$ is measured by CMB observations as [6]

$$\Delta_{\mathcal{R}}^2(k_0) = 2.42 \times 10^{-9} \equiv A_{\mathcal{R}}. \quad (3.59)$$

Here, we assume that cold dark matter consists of axions and other particle species, and that only axions contribute to isocurvature fluctuations. In this case, the amplitude of cold dark matter isocurvature fluctuations is given by

$$\Delta_S^2(k_0) = \frac{\Omega_a^2}{\Omega_{\text{CDM}}^2} \Delta_a^2(k_0), \quad (3.60)$$

where Δ_a^2 is the amplitude of axion isocurvature fluctuations S_a .

Let us relate the amplitude of fluctuations in the axion field during inflation to the constraint on the magnitude of isocurvature fluctuations measured in CMB. Assuming that $\delta\bar{\theta}^{\text{ini}} \equiv \bar{\theta}^{\text{ini}} - \langle \bar{\theta}^{\text{ini}} \rangle$ obeys Gaussian distribution, we obtain

$$\Delta_a^2(k) = \langle |S_a(k)|^2 \rangle = \frac{2\sigma_\theta^2(2(\bar{\theta}^{\text{ini}})^2 + \sigma_\theta^2)}{((\bar{\theta}^{\text{ini}})^2 + \sigma_\theta^2)^2}. \quad (3.61)$$

where we used Eq. (3.57) with $n_a \propto (\bar{\theta}^{\text{ini}})^2$ and $\sigma_\theta^2 = \langle (\delta\bar{\theta}^{\text{ini}})^2 \rangle$. Combining Eqs. (3.58) - (3.61), we find

$$\alpha(k_0) \simeq \begin{cases} \frac{\Omega_a^2}{\Omega_{\text{CDM}}^2} \frac{4\sigma_\theta^2}{A_{\mathcal{R}}(\bar{\theta}^{\text{ini}})^2} & \text{for } (\bar{\theta}^{\text{ini}})^2 \gg \sigma_\theta^2 \\ \frac{\Omega_a^2}{\Omega_{\text{CDM}}^2} \frac{2}{A_{\mathcal{R}}} & \text{for } (\bar{\theta}^{\text{ini}})^2 \ll \sigma_\theta^2 \end{cases}, \quad (3.62)$$

where we assumed that $\Delta_S^2 \ll \Delta_{\mathcal{R}}^2$. The seven year observation of WMAP gives a bound [6]

$$\alpha(k_0) < 0.077. \quad (3.63)$$

Since $A_{\mathcal{R}} \sim 10^{-9}$, the case with $(\bar{\theta}^{\text{ini}})^2 \ll \sigma_{\theta}^2$ is inconsistent with this bound. Then, assuming that $(\bar{\theta}^{\text{ini}})^2 \gg \sigma_{\theta}^2$, and that axions give dominant contribution for cold dark matter abundance ($\Omega_{\text{CDM}} = \Omega_a$), from Eqs. (3.51), (3.62) and (3.63) we obtain

$$\frac{H_I}{\bar{\theta}^{\text{ini}} F_a} < 4.3 \times 10^{-5}. \quad (3.64)$$

Therefore, the isocurvature constraint gives an upper bound on the Hubble scale during inflation H_I , or a lower bound on the axion decay constant F_a . Note that, this isocurvature constraint is weakened if we assume that the contribution of axions for cold dark matter abundance is subdominant.

Defining the energy scale of inflation E_I as $H_I^2 = 8\pi G E_I^4/3$, we translate Eq. (3.64) into the bound on E_I

$$E_I < 1.3 \times 10^{13} \text{GeV} (\bar{\theta}^{\text{ini}})^{1/2} \left(\frac{F_a}{10^{12} \text{GeV}} \right)^{1/2}. \quad (3.65)$$

Assuming that axions give dominant contribution for cold dark matter abundance $\Omega_{\text{CDM}} h^2 = 0.11$, we relate $\bar{\theta}^{\text{ini}}$ with F_a such that

$$\Omega_{a,0} h^2 = 0.18 \times (\bar{\theta}^{\text{ini}})^2 \left(\frac{g_{*,1}}{70} \right)^{-(n+2)/2(n+4)} \left(\frac{F_a}{10^{12} \text{GeV}} \right)^{(n+6)/(n+4)} \left(\frac{\Lambda_{\text{QCD}}}{400 \text{MeV}} \right) = 0.11, \quad (3.66)$$

where we used $(\bar{\theta}^{\text{ini}})^2 \gg \sigma_{\theta}^2$ in Eq. (3.52). Then, Eq. (3.65) gives upper bound on $\bar{\theta}^{\text{ini}}$ or lower bound on F_a for a given value of inflationary scale E_I

$$\bar{\theta}^{\text{ini}} < 1.4 \times 10^{-3} \times \left(\frac{E_I}{10^{14} \text{GeV}} \right)^{-2.92} \left(\frac{g_{*,1}}{70} \right)^{1/2} \left(\frac{\Lambda_{\text{QCD}}}{400 \text{MeV}} \right)^{-1.23}, \quad (3.67)$$

$$F_a > 4.2 \times 10^{16} \text{GeV} \left(\frac{E_I}{10^{14} \text{GeV}} \right)^{4.92} \left(\frac{g_{*,1}}{70} \right)^{-1/2} \left(\frac{\Lambda_{\text{QCD}}}{400 \text{MeV}} \right)^{1.23}. \quad (3.68)$$

Therefore, there is a tension between high scale inflation models and axion isocurvature fluctuations. We can avoid this constraint by assuming the higher value of F_a , but in this case we must tune the initial value of the misalignment angle $\bar{\theta}^{\text{ini}}$ in order to explain the observed dark matter abundance. This region with $F_a \gg 10^{12} \text{GeV}$ and $\bar{\theta}^{\text{ini}} \ll 1$ is called the ‘‘anthropic axion window’’ [34, 137, 35] in contrast to the classic axion window discussed in Sec. 2.5.4. Note that this bound is not applicable if the reheating temperature T_R is high enough to satisfy $T_R \gg F_a$, since the PQ symmetry is restored after reheating. Also, the Hubble scale H_I should be smaller than F_a , otherwise the PQ symmetry is restored during inflation, and broken again at the end of inflation.

Chapter 4

Axion production from topological defects

So far, we have neglected the contribution of axions produced by topological defects. However, if inflation occurs before PQ phase transition (scenario II), we must take account of their effects. In scenario II, the total abundance of dark matter axions is given by the sum of three contributions: (i) coherent oscillation, (ii) string decay, and (iii) domain wall decay,

$$\Omega_{a,\text{tot}}h^2 = \Omega_{a,0}h^2 + \Omega_{a,\text{string}}h^2 + \Omega_{a,\text{dec}}h^2. \quad (4.1)$$

We already estimated the contribution from coherent oscillation $\Omega_{a,0}h^2$ [see Eq. (3.45) or (3.47)]. In this chapter, we will estimate the rest two contributions.

The contribution of the string decay has been studied by many authors [49, 50, 51, 52, 53, 54, 55, 56, 57], and there are some disagreements on the significance of $\Omega_{a,\text{string}}h^2$. The main uncertainty comes from the assumption of the energy spectrum of axions radiated from strings. The energy spectrum of radiated axions can be computed directly by performing numerical simulation of global strings, but the results may depend on the numerical methodologies or the approximations used in some analytical calculations. In this thesis, we estimate $\Omega_{a,\text{string}}h^2$ based on the result of recent numerical simulation executed by [58], where the contamination from the core of the string is excised carefully.

Compared with the string decay contribution $\Omega_{a,\text{string}}h^2$, the wall decay contribution $\Omega_{a,\text{dec}}h^2$ has received less attention in the literature. Perhaps the reason is that the decay process contains many uncertainties such as the time scale of the decay and the size of the defects at the decay time [48]. Some authors tried to estimate this contribution [140, 141, 38], but again their conclusions disagree with each other. The main purpose of this chapter is to resolve uncertainties on the estimation of $\Omega_{a,\text{dec}}h^2$ by performing field-theoretic lattice simulations. We will see that axions produced by the wall decay give a significant contribution to the relic dark matter abundance, and that the inclusion of the wall decay contribution $\Omega_{a,\text{dec}}h^2$ gives additional constraints on the axion models.¹

The organization of this chapter is as follows. First, the quantitative behavior of topological defects in the axion models and its cosmological implications are briefly reviewed

¹The contents of this chapter are based on the works with T. Hiramatsu, M. Kawasaki, and T. Sekiguchi [142, 143, 144].

in Sec. 4.1. In Sec. 4.2, the cosmological evolution of topological defects is investigated by means of numerical simulations. In Sec. 4.3, we shortly discuss on the estimation of the string decay contribution. The wall decay contribution is discussed in Secs. 4.4 and 4.5. As mentioned in chapter 1, there are two possible scenarios. One is the case with short-lived domain walls (scenario IIA), and another is the case with long-lived domain walls (scenario IIB). Section 4.4 is devoted to the investigation of scenario IIA, while Sec. 4.5 is devoted to the investigation of scenario IIB. Finally, using the results of numerical simulations, we give constraints for scenario IIA in Sec. 4.6 and for scenario IIB in Sec. 4.7. Properties of topological defects are reviewed in Appendices B.3, B.4, and B.5. The analysis methods for numerical simulations are summarized in Appendix C.

4.1 Formation and evolution of topological defects

In this section, we give an overview of the cosmological evolution of topological defects predicted in the axion models. Depending on the model parameters, these defects can become either stable or unstable.

4.1.1 Axionic string and axionic domain wall

We will follow the cosmological evolution of a complex scalar field Φ (the Peccei-Quinn field) with the Lagrangian density

$$\mathcal{L} = -\frac{1}{2}|\partial_\mu\Phi|^2 - V_{\text{eff}}(\Phi, T), \quad (4.2)$$

where $V_{\text{eff}}(\Phi, T)$ is the finite-temperature effective potential for the scalar field. At sufficiently high temperature ($T \gtrsim F_a$), we assume that Φ is in the thermal equilibrium, and the effective potential is given by [see Eq. (B.36)]

$$V_{\text{eff}}(\Phi, T) = \frac{\lambda}{4}(|\Phi|^2 - \eta^2)^2 + \frac{\lambda}{6}T^2|\Phi|^2, \quad (4.3)$$

where we neglect the couplings with other fields for simplicity. The effective potential (4.3) induces PQ phase transition, which occurs at the temperature given by Eq. (B.38)

$$T = T_c \equiv \sqrt{3}\eta. \quad (4.4)$$

After that, the scalar field gets vacuum expectation value $|\langle\phi\rangle|^2 = \eta^2$, and the $U(1)_{\text{PQ}}$ symmetry is spontaneously broken.

Since the axion field stays in a vacuum manifold of $U(1)_{\text{PQ}}$ after the spontaneous breaking of the PQ symmetry, linear topological objects called strings are formed. It is known that strings enter into the scaling regime, where the population of these strings in the Hubble volume tends to remain in the value of $\mathcal{O}(1)$ because of the causality [see e.g. [24]]. In order to satisfy this scaling property, long strings lose their energy by emitting closed loops of strings. These loops decay by radiating axion particles with the wavelength comparable

to the horizon size [47, 49, 50, 51, 57, 58]. The production of axions from decaying string loops continues until the time when the string networks disappear due to some mechanisms which we describe below.

When the temperature of the universe becomes comparable to the QCD scale ($\Lambda_{\text{QCD}} \sim \mathcal{O}(100)\text{MeV}$), the non-perturbative nature of QCD becomes relevant. We can describe this effect by adding the term (2.56) in the effective potential (4.3),

$$V(a) = m_a^2 F_a^2 \left\{ 1 - \cos \left(\frac{a}{F_a} \right) \right\}, \quad (4.5)$$

where a is the axion field which arises in the phase direction of the complex scalar field [see. Eq. (2.65)]

$$\Phi = |\Phi| \exp \left(i \frac{a}{\eta} \right). \quad (4.6)$$

The axion mass depends on the temperature T , which is described in Eqs. (2.47) and (2.48). When the temperature is high ($T \gg \Lambda_{\text{QCD}}$), axions can be regarded as massless particles. Later, their mass is turned on at the temperature $T \sim \Lambda_{\text{QCD}}$.

We note that there are two different energy scales in this model. One is the scale of the PQ symmetry breaking η , whose value is related to the axion decay constant through Eq. (2.66)

$$F_a = \frac{\eta}{N_{\text{DW}}}. \quad (4.7)$$

Phenomenologically, it takes a value $F_a \simeq 10^9\text{-}10^{12}\text{GeV}$ as we discussed in Chapter 2. Another is the QCD scale, $\Lambda_{\text{QCD}} \simeq \mathcal{O}(100)\text{MeV}$, which induces the potential (4.5). Since there is a large hierarchy between these two scales $F_a \gg \Lambda_{\text{QCD}}$, the height of the potential barrier of the first term in Eq. (4.3) ($\sim \eta^4$) is much larger than that of the term in Eq. (4.5) ($\sim \Lambda_{\text{QCD}}^4$).

Using Eq. (4.7), we can rewrite the potential (4.5) as

$$V(a) = \frac{m_a^2 \eta^2}{N_{\text{DW}}^2} \left\{ 1 - \cos \left(N_{\text{DW}} \frac{a}{\eta} \right) \right\}, \quad (4.8)$$

The existence of the QCD potential (4.8) explicitly breaks the original $U(1)_{\text{PQ}}$ symmetry down to its discrete subgroup $Z_{N_{\text{DW}}}$, in which the angular direction possesses the shift symmetry $a \rightarrow a + 2\pi\eta k/N_{\text{DW}}$ ($k = 0, 1, \dots, N_{\text{DW}} - 1$). This $Z_{N_{\text{DW}}}$ symmetry is also spontaneously broken because of the vacuum expectation value of the axion field. As a consequence, N_{DW} domain walls attached to strings are formed [25].

Because of the existence of the large hierarchy between η and Λ_{QCD} , the formation of strings occurs much earlier than the formation of domain walls. Once strings are formed, they evolve into the scaling regime. Subsequently, domain walls are formed when the Hubble parameter becomes comparable to the mass of the axion $H \sim m_a$. Shortly after that, the condition

$$\sigma_{\text{wall}} = \frac{\mu_{\text{string}}(t_2)}{t_2} \quad (4.9)$$

is satisfied at the time t_2 , where $\sigma_{\text{wall}} = 9.23m_a F_a^2$ is the surface mass density of domain walls [given by Eq. (B.67)], $\mu_{\text{string}}(t) \simeq \pi\eta^2 \ln(t/\delta_s\sqrt{\xi})$ is the mass energy of the strings per unit length [given by Eq. (B.56)], ξ is the length parameter of strings defined by Eq. (4.50), and $\delta_s \simeq 1/\sqrt{\lambda\eta}$ is the width of strings. From Eq. (4.9), we obtain

$$t_2 = 8.43 \times 10^{-7} \text{sec} \left(\frac{g_{*,2}}{70}\right)^{-n/2(n+4)} \left(\frac{F_a}{10^{12}\text{GeV}}\right)^{4/(n+4)} \left(\frac{\Lambda}{400\text{MeV}}\right)^{-2}$$

for $T_2 \gtrsim 103\text{MeV}$, (4.10)

or

$$t_2 = 2.53 \times 10^{-9} \text{sec} \left(\frac{F_a}{10^{12}\text{GeV}}\right) \left(\frac{\Lambda}{400\text{MeV}}\right)^{-2}$$

for $T_2 \lesssim 103\text{MeV}$, (4.11)

and the corresponding temperature

$$T_2 = 0.586\text{GeV} \left(\frac{g_{*,2}}{70}\right)^{-1/(n+4)} \left(\frac{F_a}{10^{12}\text{GeV}}\right)^{-2/(n+4)} \left(\frac{\Lambda}{400\text{MeV}}\right)$$

for $T_2 \gtrsim 103\text{MeV}$, (4.12)

or

$$T_2 = 10.7\text{GeV} \left(\frac{g_{*,2}}{70}\right)^{-1/4} \left(\frac{F_a}{10^{12}\text{GeV}}\right)^{-1/2} \left(\frac{\Lambda}{400\text{MeV}}\right)$$

for $T_2 \lesssim 103\text{MeV}$, (4.13)

where $g_{*,2}$ is the radiation degree of freedom at the time t_2 , and we substituted the typical value $\ln\left(\frac{t/\sqrt{\xi}}{\delta_s}\right) \approx 69$. After the time t_2 , the dynamics is dominated by the tension of domain walls.

The structure of domain walls depends on the number N_{DW} , and the fate of the string-wall networks is different between the case with $N_{\text{DW}} = 1$ and the case with $N_{\text{DW}} > 1$. If $N_{\text{DW}} = 1$ (scenario IIA), networks of domain walls are unstable, since the string is attached by only one domain wall. Such a piece of the domain wall bounded by string can easily chop the larger one, or shrink itself due to the tension of the domain wall [145]. Hence the networks of domain walls bounded by strings disappear immediately after the formation. We will discuss this scenario in Secs. 4.2.1, 4.4, and 4.6.

On the other hand, if $N_{\text{DW}} > 1$ (scenario IIB), N_{DW} domain walls are attached to strings. Such string-wall networks are stable, since the tension of walls acts on the string from N_{DW} different directions. Furthermore, it has been argued that domain walls also enter into the scaling regime, where the network of domain walls is characterized by one scale, the Hubble radius, and the averaged number of walls per Hubble volume remain the same in the evolution of the universe. Such a property is confirmed both numerically [146, 147, 148, 149] and analytically [150, 151, 152] for a simple model in which the domain

walls arise from the spontaneous breaking of Z_2 symmetry. Also, the numerical simulation performed in [153] indicates that this property is true for networks of N_{DW} domain walls attached to strings unless $N_{\text{DW}} = 1$.

If domain wall networks are in the scaling regime, the energy density of domain walls evolves as

$$\rho_{\text{wall}} \simeq \frac{\sigma_{\text{wall}}}{H^{-1}} \propto t^{-1}, \quad (4.14)$$

since the typical length scales of defects, such as the wall curvature radius and the distance of two neighboring walls, are given by the Hubble radius $H^{-1} = 2t$. This is equivalent to the fact

$$A/V \propto \tau^{-1}, \quad (4.15)$$

where A/V is the comoving area density occupied by domain walls, and τ is the conformal time. We will check this property in the numerical simulation described in the next section.

The scaling solution (4.14) implies that the energy density of domain wall decreases slower than that of cold matter $\rho_M \propto R^{-3}$ and radiations $\rho_R \propto R^{-4}$. Hence, it eventually dominates the energy density of the universe. If it occurs at sufficiently late time in the universe, it may conflict with standard cosmology [27]. This is called the axionic domain wall problem.

4.1.2 Domain wall problem and its solution

Now, let us look closer at the model with $N_{\text{DW}} > 1$. After the time t_2 given by Eq. (4.10) or (4.11), domain walls are straightened by their tension force up to the horizon scale. These networks of domain walls bounded by strings evolve into the scaling regime, whose energy density is given by Eq. (4.14). In the radiation dominated era, the energy density of the universe is given by $\rho_c(t) = (3/8\pi G)H^2 = 3/32\pi Gt^2$, where G is the Newton's gravitational constant. By equating $\rho_c(t)$ and $\rho_{\text{wall}} \simeq \sigma_{\text{wall}}/H^{-1} = \sigma_{\text{wall}}/2t$, we find that the wall domination occurs at the time

$$t_{\text{WD}} = \frac{3}{16\pi G\sigma_{\text{wall}}}. \quad (4.16)$$

For the axionic domain wall with $\sigma_{\text{wall}} = 9.23m_a F_a^2$ and $F_a \sim 10^{12}\text{GeV}$, this time t_{WD} corresponds to the temperature of the universe $T_{\text{WD}} \sim \mathcal{O}(10)\text{keV}$.

In order to avoid this overclosure problem, Sikivie [25] phenomenologically introduced a term

$$\delta V = -\Xi\eta^3(\Phi e^{-i\delta} + \text{h.c.}) \quad (4.17)$$

in the potential (4.8), where Ξ is a dimensionless parameter which is assumed to be much less than unity. This term, called a bias [36], explicitly breaks the discrete symmetry and lifts degenerate N_{DW} vacua. The bias term might correspond to the potential $V_{\text{grav}}(a)$ introduced in Eq. (2.57). The candidates of this term are the higher dimensional operators suppressed by the Planck mass M_P [44]. Instead of using such operators, however, we just use the form (4.17) treating Ξ as a free parameter, and give some constraints on the value of Ξ .

If this kind of term exists in the potential, it eventually annihilate domain walls. Let us estimate the typical time scale for the annihilation of walls. The energy difference between the neighboring vacua introduced by the $Z_{N_{\text{DW}}}$ breaking term (4.17) can be estimated as $\Delta V \sim \frac{2\pi}{N_{\text{DW}}} 2\Xi\eta^4$, which acts as a volume pressure p_V on the wall and accelerates it against the false vacuum regions:

$$p_V \sim \Delta V \sim 4\pi\Xi\eta^4/N_{\text{DW}}. \quad (4.18)$$

On the other hand, the surface tension p_T which straightens the wall up to the horizon scale can be estimated as

$$p_T \sim \sigma_{\text{wall}}/t. \quad (4.19)$$

The domain walls collapse when these two effects become comparable. From this fact, we can estimate the typical time of the decay of domain wall networks as

$$t_{\text{dec}} \sim \sigma_{\text{wall}}/\Delta V \sim \frac{m_a}{\Xi N_{\text{DW}}\eta^2}, \quad (4.20)$$

We will determine the precise value of the numerical coefficient in the formula (4.20) from the results of the numerical simulations in the next section. Requiring that the decay of walls occurs before the wall domination (i.e. $t_{\text{dec}} < t_{\text{WD}}$), we obtain a lower bound on Ξ

$$\Xi > \mathcal{O}(1) \times 10^{-59} \times N_{\text{DW}}^{-3} \left(\frac{m_a}{6 \times 10^{-4} \text{eV}} \right)^2. \quad (4.21)$$

Note that there are other ways to avoid the domain wall problem. First, we can simply assume that the PQ phase transition has occurred before inflation (scenario I). In this case, however, the isocurvature fluctuations give severe constraints on the model parameters, as was mentioned in Sec. 3.3. In particular, some high scale inflationary scenarios such as chaotic inflation models [154, 155] suffer from these kinds of problems. A more intricate solution is to embed the discrete subgroup $Z_{N_{\text{DW}}}$ of $U(1)_{\text{PQ}}$ in the center of another continuous group [156, 157, 158]. In this model, the degenerate vacua are connected to each other by another symmetry transformations, leading to the same cosmological property with the case for $N_{\text{DW}} = 1$. However, in this kind of model, one have to choose the symmetry group, Higgs representations and $U(1)_{\text{PQ}}$ charge judiciously [159]. Here, we do not consider such models, and simply assume that domain walls exist for a long time and annihilate due to the bias term which satisfies the condition (4.21). This biased domain wall scenario is investigated in Secs. 4.2.2, 4.5, and 4.7.

4.2 Evolution of string-wall networks

In this section, we show the results of numerical simulations of axionic string-wall networks. First, we consider the case with $N_{\text{DW}} = 1$ (scenario IIA) in Sec. 4.2.1. The formation and collapse of string-wall systems is investigated by performing three-dimensional lattice simulations. Next, in Sec. 4.2.2 we investigate the evolution of the long-lived string-wall networks in the case with $N_{\text{DW}} > 1$ (scenario IIB). In this case, we perform two-dimensional simulations in addition to three dimensional ones, since it is impossible to

estimate the decay time of domain wall networks in the limited dynamical ranges of three-dimensional simulations.

This section is devoted to the investigation of the evolution of defect networks. The production of axions from the decay of domain walls will be described in Secs. 4.4 and 4.5. The details of the analysis methods are described in Appendix C.

4.2.1 Short-lived networks

Let us consider $N_{\text{DW}} = 1$ axionic model model, with the effective potential given by

$$V_{\text{eff}}(\Phi, T) = \frac{\lambda}{4}(|\Phi|^2 - \eta^2)^2 + \frac{\lambda}{6}T^2|\Phi|^2 + m_a(T)^2\eta^2 \left\{ 1 - \frac{|\Phi|}{\eta} \cos(\text{Arg}(\Phi)) \right\}. \quad (4.22)$$

Note that the last term of Eq. (4.22) is different from the QCD potential (4.8). We find that the simulation becomes unstable when we use the potential given by Eq. (4.8) since this potential is not well defined at $|\Phi| = 0$. The modified potential given by Eq. (4.22) avoids this singularity since there is a factor $|\Phi|$ in front of the cosine term. The difference between Eqs. (4.22) and (4.8) is not important in the bulk region on which $|\Phi| = \eta$, and we observe that the quantitative behavior of topological defects such as time evolution of the length of strings is unchanged, except the existence of the numerical instability.

In the radiation-dominated universe, the time and temperature are related by the Friedmann equation

$$\frac{1}{4t^2} = H^2 = \frac{8\pi G}{3} \frac{\pi^2}{30} g_* T^4, \quad (4.23)$$

where g_* is the relativistic degree of freedom. For convenience in the numerical study, we introduce a dimensionless quantity

$$\zeta \equiv \sqrt{\frac{45}{16\pi^3 G g_*}} \frac{1}{\eta}. \quad (4.24)$$

Using this parameter, Eq. (4.23) can be written as

$$t = \frac{\zeta \eta}{T^2}. \quad (4.25)$$

In the simulation of the short-lived networks, we normalize all the dimensionful quantities in the unit of τ_c , which is the conformal time at which PQ phase transition occurs [cf. Eq. (4.4)],

$$\Phi \rightarrow \Phi \tau_c, \quad T \rightarrow T \tau_c, \quad x \rightarrow x / \tau_c, \quad \text{etc.} \quad (4.26)$$

Also, we introduce the normalized initial Hubble parameter as an input parameter of the numerical simulation

$$H(t = t_i) \rightarrow \tau_c H(t = t_i) \equiv \alpha, \quad (4.27)$$

and we set the scaling parameter at the initial time into unity

$$R(t_i) = 1. \quad (4.28)$$

Note the following relations:

$$R(\tau_c) = \tau_c/\tau_i = \alpha \quad \text{and} \quad \tau_c = \frac{2\zeta}{3\eta\alpha}. \quad (4.29)$$

By using Eq. (4.29), we can enumerate the various relations in the unit (4.26),

$$\tau_i = 1/\alpha, \quad R(\tau) = \alpha\tau, \quad T_i = \frac{2\zeta}{\sqrt{3}} \quad \text{and} \quad \eta = \frac{2\zeta}{3\alpha}. \quad (4.30)$$

The ratio between the axion mass (2.47) and the axion decay constant can be written as

$$m_a(T)^2/\eta^2 = c_T \kappa^{n+4} \left(\frac{T}{F_a} \right)^{-n}, \quad (4.31)$$

where κ is the ratio between the QCD scale and the PQ scale,

$$\kappa \equiv \Lambda_{\text{QCD}}/F_a = \Lambda_{\text{QCD}}/\eta. \quad (4.32)$$

We decompose the complex scalar field into its real and imaginary part, such that $\Phi = \phi_1 + i\phi_2$, where ϕ_1 and ϕ_2 are real variables. Assuming that Φ is in the thermal equilibrium at the high temperature, we give the initial conditions such that the two real scalar fields satisfy the equal-time correlation relations with temperature $\beta \equiv 1/T_i$,

$$\langle \beta | \phi_a(\mathbf{x}) \phi_b(\mathbf{y}) | \beta \rangle = \delta_{ab} \int \frac{d^3k}{(2\pi)^3} \frac{1}{2\omega_k} [1 + 2n_k] e^{i\mathbf{k}\cdot(\mathbf{x}-\mathbf{y})}, \quad (4.33)$$

$$\langle \beta | \dot{\phi}_a(\mathbf{x}) \dot{\phi}_b(\mathbf{y}) | \beta \rangle = \delta_{ab} \int \frac{d^3k}{(2\pi)^3} \frac{\omega_k}{2} [1 + 2n_k] e^{i\mathbf{k}\cdot(\mathbf{x}-\mathbf{y})}, \quad (4.34)$$

$$\langle \beta | \phi_a(\mathbf{x}) \dot{\phi}_b(\mathbf{y}) | \beta \rangle = 0, \quad (4.35)$$

where $\langle \beta | \dots | \beta \rangle \equiv \text{Tr}(\dots e^{-\beta\hat{H}})/\text{Tr}e^{-\beta\hat{H}}$ is the thermal average, and \hat{H} is the Hamiltonian of the system. Here, we used the following notations

$$n_k = \frac{1}{e^{\omega_k/T_i} - 1}, \quad \omega_k = \sqrt{k^2 + m_{\text{eff}}^2}, \quad (4.36)$$

and $m_{\text{eff}}^2 \equiv \partial^2 V_{\text{eff}}/\partial\Phi^* \partial\Phi|_{\Phi=0}$ is the effective mass of the scalar fields at the initial time. The first term in the bracket in Eqs. (4.33) and (4.34) corresponds to vacuum fluctuations, which contribute as a divergent term when we perform the integral over k . In numerical studies, we subtract these fluctuations and use the following renormalized correlation functions

$$\langle \phi_a(\mathbf{x}) \phi_b(\mathbf{y}) \rangle_{\text{ren.}} = \delta_{ab} \int \frac{d^3k}{(2\pi)^3} \frac{n_k}{\omega_k} e^{i\mathbf{k}\cdot(\mathbf{x}-\mathbf{y})}, \quad (4.37)$$

$$\langle \dot{\phi}_a(\mathbf{x}) \dot{\phi}_b(\mathbf{y}) \rangle_{\text{ren.}} = \delta_{ab} \int \frac{d^3k}{(2\pi)^3} \omega_k n_k e^{i\mathbf{k}\cdot(\mathbf{x}-\mathbf{y})}, \quad (4.38)$$

$$\langle \phi_a(\mathbf{x}) \dot{\phi}_b(\mathbf{y}) \rangle_{\text{ren.}} = 0. \quad (4.39)$$

In the momentum space, these correlation functions can be written as

$$\langle \phi_a(\mathbf{k})\phi_b(\mathbf{k}') \rangle_{\text{ren.}} = \delta_{ab} \frac{n_k}{\omega_k} (2\pi)^3 \delta^{(3)}(\mathbf{k} + \mathbf{k}'), \quad (4.40)$$

$$\langle \dot{\phi}_a(\mathbf{k})\dot{\phi}_b(\mathbf{k}') \rangle_{\text{ren.}} = \delta_{ab} \omega_k n_k (2\pi)^3 \delta^{(3)}(\mathbf{k} + \mathbf{k}'), \quad (4.41)$$

where $\phi_a(\mathbf{k})$ is the Fourier transform of $\phi_a(\mathbf{x})$. Since $\phi_a(\mathbf{k})$ and $\dot{\phi}_a(\mathbf{k})$ are uncorrelated in the momentum space, we generate $\phi_a(\mathbf{k})$ and $\dot{\phi}_a(\mathbf{k})$ in the momentum space randomly following the Gaussian distribution with

$$\langle |\phi_a(\mathbf{k})|^2 \rangle_{\text{sim.}} = \frac{n_k}{\omega_k} V, \quad \langle |\dot{\phi}_a(\mathbf{k})|^2 \rangle_{\text{sim.}} = n_k \omega_k V, \quad (4.42)$$

$$\text{and} \quad \langle \phi_a(\mathbf{k}) \rangle_{\text{sim.}} = \langle \dot{\phi}_a(\mathbf{k}) \rangle_{\text{sim.}} = 0, \quad (4.43)$$

for each $a = 1$ and 2 , where $\langle \dots \rangle_{\text{sim.}}$ represents the average over realizations of numerical simulations. Note that these conditions should be regarded as field configurations which mimic the conditions (4.40) and (4.41). We transform them into the configuration space and obtain the initial field configurations $\phi(\mathbf{x})$ and $\dot{\phi}(\mathbf{x})$. Here we used $(2\pi)^3 \delta^{(3)}(0) \simeq V$, where $V = L^3$ is the comoving volume of the simulation box and L is the size of the simulation box (in the unit of τ_c).

We solve the classical equations of motion for $\Phi = \phi_1 + i\phi_2$ (see Appendix C.1), with the potential (4.22) in the three-dimensional lattice with 512^3 points. In numerical simulations, we can vary four parameters λ , κ , ζ and α . We set $\alpha = 2.0$ which corresponds to the fact that $\tau_i = 0.5\tau_c$. Also, we choose the value of ζ as 3.0, which corresponds to the conditions $\eta = 1.23 \times 10^{17} \text{ GeV}$ and $g_* = 100$. It seems that this value of η may be too high and affect the small scale dynamics of the system. We will discuss this point in the end of this subsection. Note that, from Eq. (4.30) we see that $\eta = 1$ in the unit of τ_c^{-1} . Other parameters that we used are summarized in Table 4.1. The dynamical range of the simulation is estimated as $\tau_f/\tau_i = 24$.

We must keep the following conditions, in order to simulate the dynamics of the topological defects correctly.

- The width of global strings $\delta_s = 1/\eta\sqrt{\lambda}$ must be greater than the physical lattice spacing $\Delta x_{\text{phys}} = R(t)L/N$, where $N = 512$ is the number of grids, in order to maintain the resolution of the width of strings.
- The Hubble radius H^{-1} must be smaller than the box size $R(t)L$, to avoid the unphysical effect caused by the finiteness nature of the simulation box.

The physical scale of the Hubble radius and the width of strings divided by the physical lattice spacing are respectively

$$\frac{H^{-1}}{\Delta x_{\text{phys}}} = \frac{N}{L}\tau, \quad \text{and} \quad \frac{\delta_s}{\Delta x_{\text{phys}}} = \frac{3N}{2L\zeta\tau\sqrt{\lambda}}. \quad (4.44)$$

For the parameters given in table 4.1, we get $H^{-1}/\Delta x_{\text{phys}} \simeq 307$ and $\delta_s/\Delta x_{\text{phys}} \simeq 1.07$ at the end of the simulation $\tau = \tau_f$. Therefore, the conditions described above are satisfied even at the end of the simulation.

Table 4.1: Parameters used in numerical simulations for short-lived domain walls.

Grid size (N)	512
Box size (L)	20
Total number of steps	1150
Time interval ($\Delta\tau$)	0.01
λ	1.0
κ [Eq. (4.32)]	varying
ζ [Eq. (4.24)]	3.0
α [Eq. (4.27)]	2.0
c_T [Eq. (2.47)]	6.26
c_0 [Eq. (2.48)]	1.0
Initial time (τ_i)	0.5
Final time (τ_f)	12.0

We also treat c_T and c_0 defined in Eqs. (2.47) and (2.48) as free parameters in numerical simulations. In terms of these parameters, the time at which the value of $m_a(T)$ reaches the zero-temperature value $m_a(0)$ is written as

$$\tau_a = 1.73 \times \left(\frac{c_0}{c_T} \right)^{1/n} \kappa^{-1}. \quad (4.45)$$

Here we used the conformal time with the unit of $\tau_c = 1$. Also, the time t_1 given by Eq. (3.27) is rewritten as

$$\tau_1 = 1.52 \times \left(\frac{3.0}{\zeta} \right)^{2/(4+n)} c_T^{-1/(n+4)} \kappa^{-1}. \quad (4.46)$$

Choosing the values of three parameters c_0 , c_T and κ corresponds to the fact that we tune the values of τ_a , τ_1 , and $m_a(0)$ in the numerical simulations. Unfortunately, due to the limitation of the dynamical range, we cannot choose all parameters to be realistic values. One possible choice is to fix the ratio between τ_1 and τ_a so that

$$\tau_1/\tau_a = 0.88 \times \left(\frac{c_T}{c_0} \right)^{1/n} c_T^{-1/(n+4)} \left(\frac{3.0}{\zeta} \right)^{2/(n+4)} = 0.97 \times \left(\frac{3.0}{\zeta} \right)^{2/(n+4)}, \quad (4.47)$$

where the last equality follows from the realistic values $c_T = 1.68 \times 10^{-7}$ and $c_0 = 1.46 \times 10^{-3}$. In order to satisfy the condition (4.47), we must choose c_T and c_0 so that

$$c_T c_0^{-(n+4)/4} \simeq 6.26. \quad (4.48)$$

In numerical simulations, we use the values $c_0 = 1.0$ and $c_T = 6.26$ which satisfy the above condition. In this case the expression for τ_2 becomes

$$\tau_2 = 1.26 \times \left(\frac{3.0}{\zeta} \right)^{2/(4+n)} \left(\frac{\beta}{4} \right)^{2/(4+n)} \left(\frac{6.26}{c_T} \right)^{1/(4+n)} \kappa^{-1}, \quad (4.49)$$

which follows from Eq. (4.10). The expression (4.49) depends on $\beta \equiv \ln(t/\sqrt{\xi}\delta_s)$ which comes from μ_{string} in Eq. (4.9). Here we use the value $\beta \simeq 4$ obtained by using parameters which are used in numerical simulations. Both of the time scales τ_1 and τ_2 become comparable, but τ_2 is slightly shorter than τ_1 because of the small value of β . We summarize the typical time scales given by Eqs. (4.45), (4.46) and (4.49) in Table 4.2.

Table 4.2: Typical time scales for various values of κ .

κ	τ_2	τ_1	τ_a
0.4	3.15	3.20	3.29
0.35	3.59	3.65	3.76
0.3	4.19	4.27	4.38
0.25	5.03	5.12	5.26
0.2	6.29	6.40	6.57

Now, let us show the results of the simulations. Figure 4.1 shows the visualization of one realization of the simulation. We see that at the first stage of the simulation, strings evolve with keeping the scaling property. However, at late time they shrink because of the tension of domain walls. We also show the spatial distribution of the phase of the scalar field $\text{Arg}(\Phi)$ in Fig. 4.2. Note that the width of domain walls $\sim m_a^{-1}$ is much greater than that of strings $\sim (\sqrt{\lambda}\eta)^{-1}$, as shown in Fig. 4.2.

We performed 20 realizations for each choice of the parameter κ . For each realization, we calculated the length parameter of strings

$$\xi \equiv \frac{\rho_{\text{string}}}{\mu_{\text{string}}} t^2, \quad (4.50)$$

and the area parameter of domain walls

$$\mathcal{A} \equiv \frac{\rho_{\text{wall}}}{\sigma_{\text{wall}}} t, \quad (4.51)$$

where ρ_{string} and ρ_{wall} are energy densities of strings and domain walls, respectively. It is not straightforward to calculate μ_{string} and σ_{wall} exactly in numerical simulations, but it is possible to estimate ξ and \mathcal{A} indirectly by computing the length of strings and area of domain walls in the simulation box (see Appendix C.2.3).² These parameters take a constant value when the defect networks enter the scaling regime (i.e. $\rho_{\text{string}} \sim 1/t^2$ and $\rho_{\text{wall}} \sim 1/t$). Henceforth we refer to these parameters as the ‘‘scaling parameters’’. Figure 4.3 shows the time evolutions of ξ and \mathcal{A} for various values of κ . Comparing the plot of \mathcal{A} with Table 4.2, we see that the value of \mathcal{A} deviates from the scaling behavior

²We can roughly estimate ρ_{string} and ρ_{wall} by summing up the contributions of grid points located within the core of defects, as shown in Fig. 4.20. Here, instead of using ρ_{string} and ρ_{wall} directly, we simply compute ξ and \mathcal{A} by using Eq. (C.11).

($\mathcal{A} \simeq \text{constant}$) around $\tau = \tau_1$ and begins to fall off. Note that ξ starts to fall later than \mathcal{A} does. This can be interpreted as follows. Since domain walls are two-dimensional objects, they curve in various directions. This curvature gets stretched when the tension of walls becomes effective. The stretching process of walls reduces the value of \mathcal{A} , but might not affect the length of strings (i.e. the value of ξ). Later, stretched walls pull the strings attached on their boundaries, which causes the reduction of ξ .

We emphasize that there are ambiguities in the values of scaling parameters defined in Eqs. (4.50) and (4.51). Our result $\xi \simeq 0.5$, shown in Fig. 4.3, is somewhat lower than the value $\xi \simeq 0.8-1.3$ obtained in previous studies [57, 58, 160, 161, 162]. This might be caused by the different choice of the parameter ζ used as an input of the numerical simulations. Our choice $\zeta = 3.0$ is smaller than the values $\zeta = 8-10$ used in past numerical simulations [57, 160, 161, 162]. The parameter ζ controls the magnitude of the symmetry breaking scale η [see Eq. (4.30)], which determines the width of global strings $\delta_s \propto 1/\eta$. Therefore, different choice of ζ affects the emission rate of Nambu-Goldstone bosons from strings [24, 163] $\Gamma_{\text{NG}} = \tilde{\Gamma}/[2\pi L_s \ln(L_s/\delta_s)]$, where $\tilde{\Gamma}$ is a numerical factor of $\mathcal{O}(10-100)$ and $L_s \sim t$ is the characteristic length scale of strings. The simulation with small value of ζ corresponds to the simulation with thick strings, in which the global string networks lose their energy efficiently due to the emission of Nambu-Goldstone bosons, since the logarithmic correction to the emission rate $\Gamma_{\text{NG}} \propto 1/\ln(t/\delta_s)$ becomes large. This large emission rate of Nambu-Goldstone bosons reduces the energy density of global string networks and suppresses the value of ξ . However, it was argued that in the realistic case with $\ln(t/\delta_s) \approx 70$ the radiative effect becomes subdominant, and the value of ξ is purely determined by the formation rate of loops [162, 164]. Regarding this effect, the authors of Ref. [162] estimated the final value of scaling parameter as $\xi = 1.6 \pm 0.3$. Indeed, the results with smaller values of κ in Fig. 4.3 indicate that the value of ξ increases due to the change of emission rate $\Gamma_{\text{NG}} \propto 1/\ln(t/\delta_s)$ with time. We anticipate that the value of the length parameter gradually reaches the final value $\xi \approx 1$, which cannot be observed in the simulations with the limited dynamical range.

The reason why we choose smaller value of ζ is to improve the dynamical range of simulations by keeping the width of strings greater than the lattice spacing [see Eq. (4.44)]. This choice enables us to try to perform simulations with varying the values of κ but invalidates the estimation of ξ due to the large emission rate of Nambu-Goldstone bosons. However, we believe that this choice does not affect our main result about the radiated axions produced by domain walls, since the choice of the parameter ζ only controls the small scale properties such as the width of strings, while the population of axions is dominated by low momentum modes³ which are governed by the large scale physics with the wavelength comparable to the inverse of the axion mass.

The precise determination of the values of scaling parameters including the effect of back-reaction of Nambu-Goldstone boson emission is beyond the scope of this work. To be conservative, we use the rough estimate $\xi \simeq 1.0 \pm 0.5$ with 50% uncertainty when we calculate the abundance of cold axions in the subsequent sections. We also assume that the area parameter \mathcal{A} possesses similar uncertainty, and use the value $\mathcal{A} \simeq 0.50 \pm 0.25$ around

³We will confirm it in Sec. 4.4.

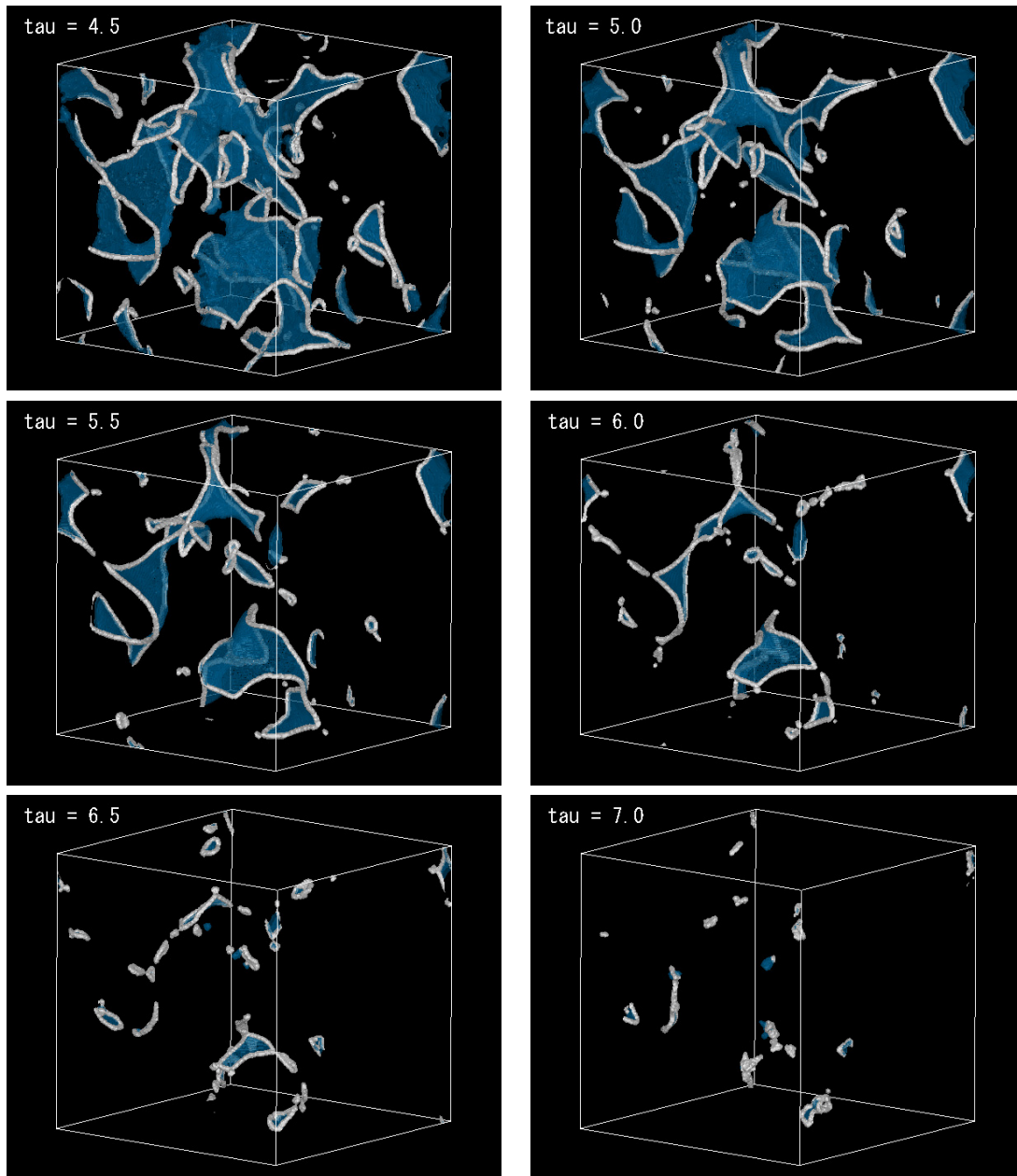


Figure 4.1: Visualization of one realization of the simulation. In this figure, we take the box size as $L = 15$ and $N = 256$, which is smaller than that shown in Table 4.1. Other parameters are fixed so that $\lambda = 1.0$, $\zeta = 3.0$, $\alpha = 2.0$ and $\kappa = 0.4$. The white lines correspond to the position of strings, while the blue surfaces correspond to the position of the center of domain walls.

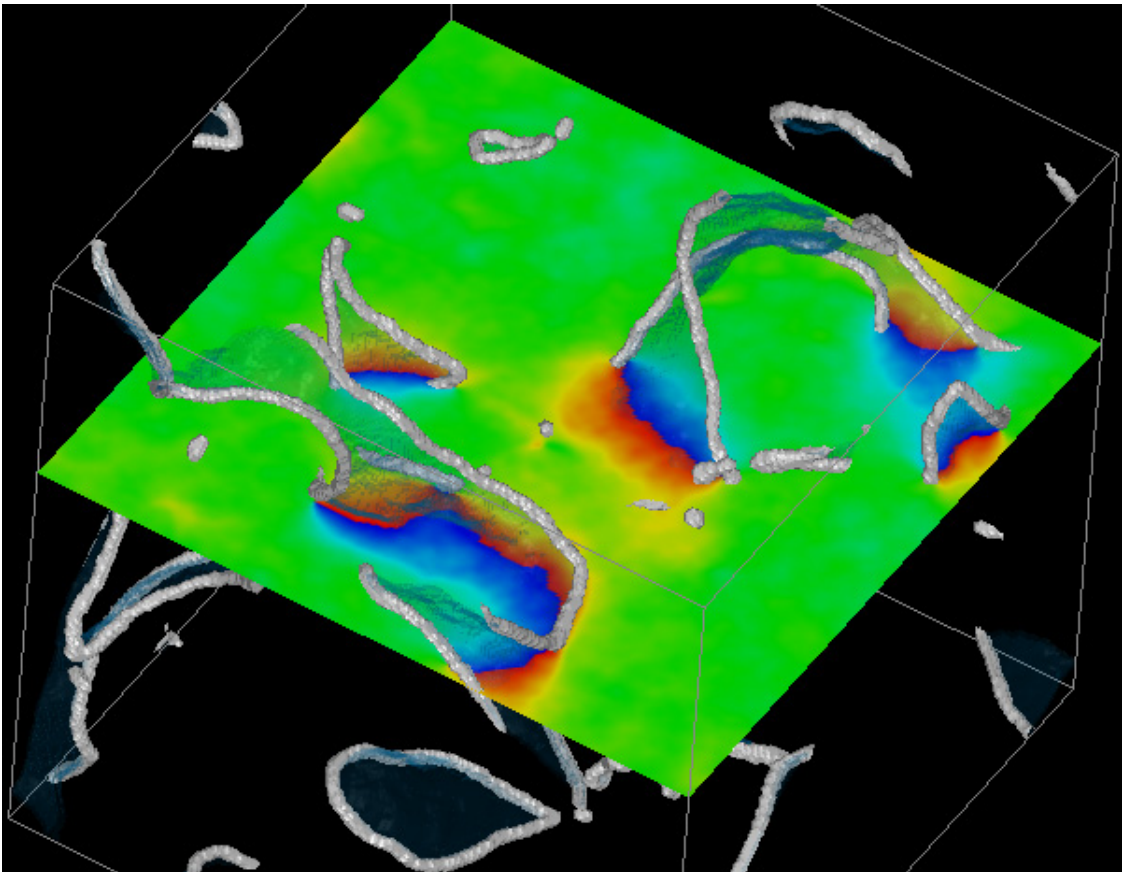


Figure 4.2: The distribution of the phase of the scalar field $\text{Arg}(\Phi)$ on the two-dimensional slice of the simulation box. In this figure, we used the same data that are used to visualize the result with $\tau = 5.0$ in Fig. 4.1. The value of $\text{Arg}(\Phi)$ varies from $-\pi$ (blue) to π (red). Domain walls are located around the region on which $\text{Arg}(\Phi)$ passes through the value $\pm\pi$, while the green region corresponds to the true vacuum [$\text{Arg}(\Phi) = 0$]. The length scale of the change of $\text{Arg}(\Phi)$ is roughly estimated as $\sim m_a^{-1}$, which gives the thickness of domain walls.

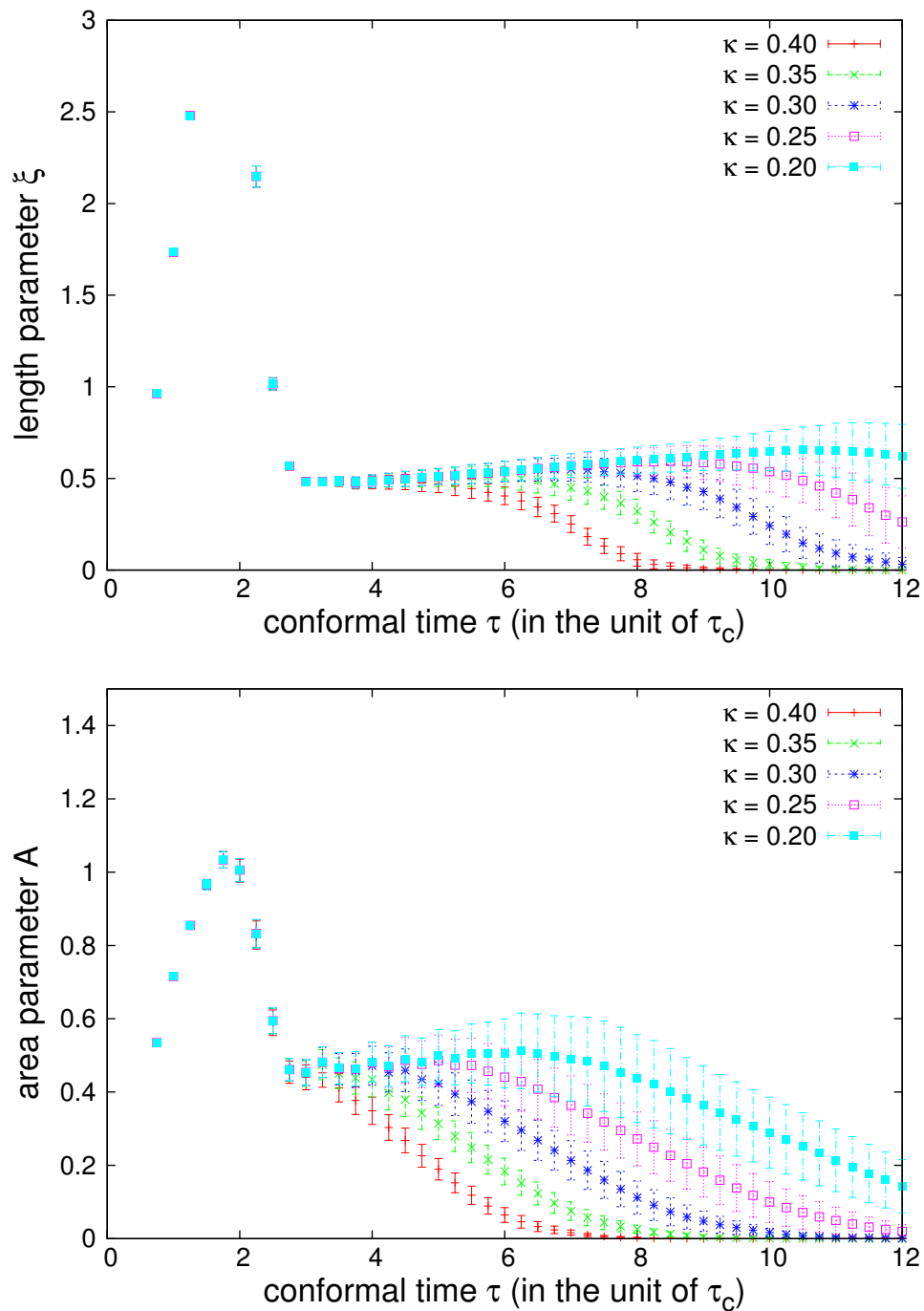


Figure 4.3: Time evolution of the length parameter ξ (top panel) and the area parameter \mathcal{A} (bottom panel) for various values of κ . Although walls do not exist before the time τ_1 , we can show the value of \mathcal{A} evaluated at the time $\tau < \tau_1$. This is because the value of \mathcal{A} is calculated from the number of grid points on which the phase of the scalar field passes the value $\theta = \pi$. In this sense, \mathcal{A} represents the area of domain walls only after the time τ_1 .

the time of the formation of domain walls.

4.2.2 Long-lived networks

Next, let us consider the models with $N_{\text{DW}} > 1$. In this case, we solve the classical equation of motion for Φ with the potential

$$V(\Phi) = \frac{\lambda}{4}(|\Phi|^2 - \eta^2)^2 + \frac{m_a^2 \eta^2}{N_{\text{DW}}^2} \left\{ 1 - \frac{|\Phi|}{\eta} \cos N_{\text{DW}} (\text{Arg}(\Phi)) \right\}. \quad (4.52)$$

Similarly to Eq. (4.22), the second term of Eq. (4.52) is modified from that of Eq. (4.8) in order to avoid the numerical instability.

Here, some formulations are different from that used in Sec. 4.2.1. In the simulation of the long-lived networks, we normalize all the dimensionful quantities in the unit of η ,

$$\Phi \rightarrow \Phi \eta, \quad x \rightarrow x \eta, \quad \text{etc}, \quad (4.53)$$

instead of using the time of the phase transition τ_c . The reason is as follows. In the case with $N_{\text{DW}} > 1$, domain walls exist for a long time, and decay at the time t_{dec} given by Eq. (4.20). However, because of the limitation of the dynamical range, it is difficult to follow the whole process including the formation of strings, that of domain walls, and decay of them, in the single realization of the simulation. Hence, in the simulation of long-lived networks, we just consider the late time evolution of them, ignoring the physics at the formation time τ_c . The normalization of the scale factor is the same with Eq. (4.28) [$R(\tau_i) = 1$].

For initial conditions, we treat $\phi_1 = \text{Re}(\Phi)$ and $\phi_2 = \text{Im}(\Phi)$ as two independent real scalar fields so that each of them has quantum fluctuations at the initial time with correlation function⁴ in the momentum space given by

$$\langle \phi_i(\mathbf{k}) \phi_i(\mathbf{k}') \rangle = \frac{1}{2k} (2\pi)^3 \delta^{(3)}(\mathbf{k} + \mathbf{k}'), \quad (4.54)$$

$$\langle \dot{\phi}_i(\mathbf{k}) \dot{\phi}_i(\mathbf{k}') \rangle = \frac{k}{2} (2\pi)^3 \delta^{(3)}(\mathbf{k} + \mathbf{k}'). \quad (i = 1, 2) \quad (4.55)$$

Since the effective squared masses of the fields quickly become negative at the initial time (i.e. on the top of the mexican hat potential), we used the massless fluctuations as the initial conditions, replacing the factor $\sqrt{k^2 + m^2}$ with k in the above formulae. We also put the momentum cutoff k_{cut} above which all fluctuations are set to zero in order to eliminate the unphysical noise which comes from high frequency modes in the field distributions. Here we set $k_{\text{cut}} = 1$ (in the unit of $\eta = 1$).

We generate initial conditions in momentum space as Gaussian random amplitudes satisfying Eqs. (4.54) and (4.55), then Fourier transform them into the configuration space to give the spatial distributions of the fields. We emphasize that this choice of initial conditions does not take account of the correct circumstances in the QCD epoch. However, we

⁴These correlation functions are evaluated at zero temperature, and different from the renormalized correlation functions used in Eqs. (4.40) and (4.41).

expect that the result at the late time of the simulations are qualitatively unchanged if we used the different initial conditions, since the evolution of defect networks in the scaling regime is not so much affected by the initial field configurations.

We also note that, in the simulation of the long-lived networks, the axion mass m_a is treated as a constant parameter. We do not use the temperature dependent expression (4.31) since we are interested in the late time evolution of domain walls where the axion mass is described as the zero-temperature value. In this case, m_a represents the ratio between the axion mass at the zero-temperature and PQ symmetry breaking scale η (recall that we use the unit of $\eta = 1$). With this normalization, the physical scale of the Hubble radius H^{-1} , the width of the wall $\delta_w = m_a^{-1}$, and the width of the string $\delta_s = \lambda^{-1/2}$ divided by the lattice spacing $\Delta x_{\text{phys}} = R(t)\Delta x = R(t)L/N$ are given by

$$\frac{H^{-1}}{\Delta x_{\text{phys}}} = \frac{N\tau}{L}, \quad \frac{\delta_w}{\Delta x_{\text{phys}}} = \frac{N}{Lm_a} \left(\frac{\tau_i}{\tau} \right), \quad \text{and} \quad \frac{\delta_s}{\Delta x_{\text{phys}}} = \frac{N}{L\lambda^{1/2}} \left(\frac{\tau_i}{\tau} \right). \quad (4.56)$$

Since the dynamical range of the numerical simulation is limited, we perform simulations both in two-dimensional and three-dimensional lattice. In two-dimensional simulations, we can improve dynamical range since the size of data is give by N^2 . Memory of the computer limits us to much smaller grid size and shorter dynamical range, if we perform three-dimensional simulations. In particular, the short dynamical range prevents us from following the evolution of string-wall networks until they decay due to the bias term in the three-dimensional simulations. Hence, first we perform two-dimensional lattice simulations by including a bias term (4.17) to investigate the annihilation of string-wall networks. Then, we calculate the spectrum of radiations produced by string-wall systems without a bias term by performing three-dimensional lattice simulations.⁵

2D

Here, we solve the evolution of Φ with the potential given by Eqs. (4.52) and (4.17) on the two-dimensional lattice with 4096^2 points. First, we present the evolution of unbiased domain walls (i.e. $\Xi = 0$) and check the consistency of the result with other existing numerical simulations. Next, we investigate the Ξ dependence of the results and estimate the lifetime of domain wall networks. The parameters used in the simulation are summarized in Table 4.3. We set the initial time as $\tau_i = 2.0$ and the final time as $\tau_f = 110.0$. The dynamical range of the simulation is therefore $\tau_f/\tau_i = 55$. At the end of the simulation $\tau_f = 110$, ratios given in Eq. (4.56) become $H^{-1}/\Delta x_{\text{phys}} \simeq 1959 < N$, $\delta_w/\Delta x_{\text{phys}} \simeq 3.2$, and $\delta_s/\Delta x_{\text{phys}} \simeq 1.02$.

The spatial distribution of the potential energy and the phase of the PQ field is shown in Fig. 4.4. We can see that the phase of the PQ field is indeed divided into N_{DW} domains and there is the core of strings attached by N_{DW} domain walls at the location where $\text{Arg}(\Phi)$ rotates by 2π . Since these are the results of two dimensional simulations, strings exist as a ‘‘point’’ in the two dimensional surface.

⁵It is impossible to calculate the gravitational waves properly in the two-dimensional field theoretic simulations. See Sec. 4.5.2.

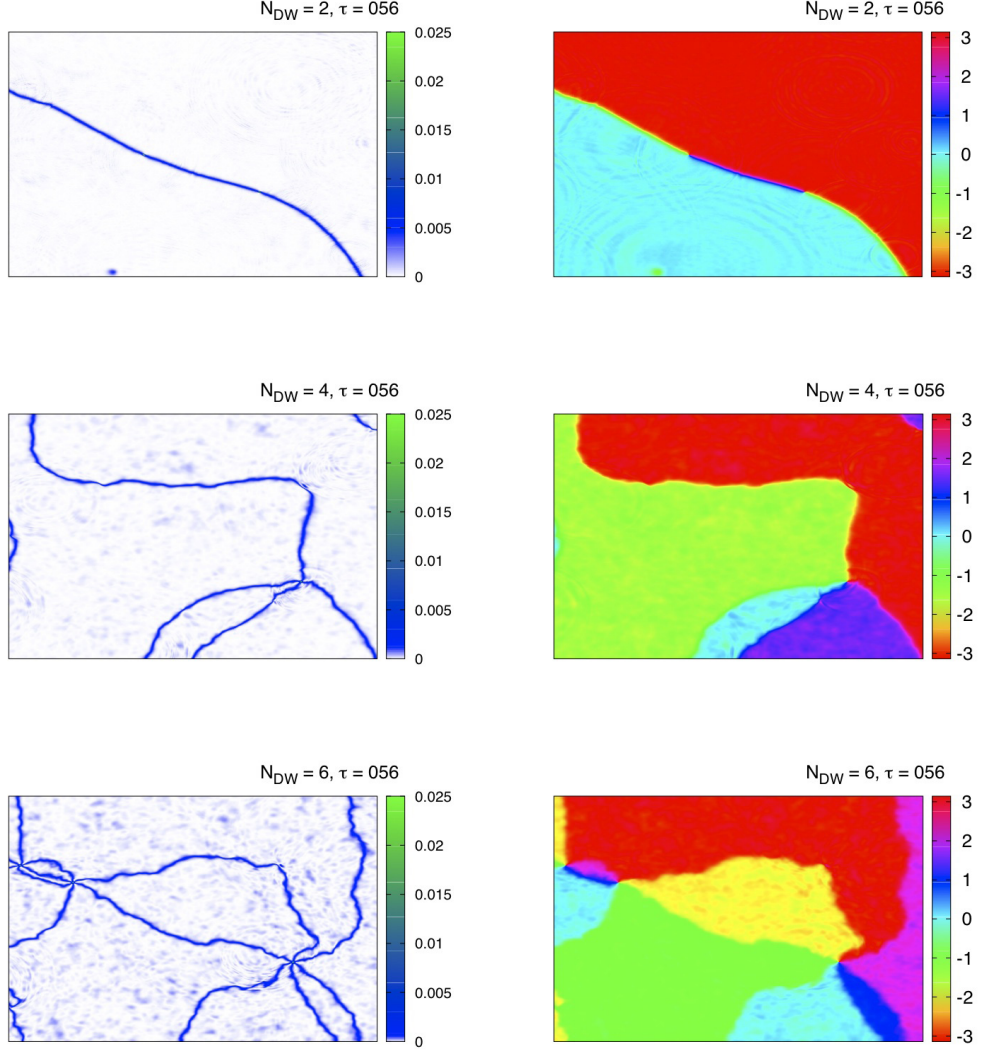


Figure 4.4: The distribution of the potential energy (left) and the phase of the PQ field $\text{Arg}(\Phi)$ (right) with the case $N_{\text{DW}} = 2$ (top), $N_{\text{DW}} = 4$ (middle), and $N_{\text{DW}} = 6$ (bottom) at the time $\tau = 56$. The size of these figures is set to be a quarter of the size of the simulation box. In the distribution of the energy density, the white region corresponds to the vacuum [$V(\Phi) \simeq 0$], the blue region corresponds to the domain wall [$V(\Phi) \simeq 2m_a^2\eta^2/N_{\text{DW}}^2$], and the green region corresponds to the string [$V(\Phi) \simeq \lambda\eta^4/4$], but the core of the string is too thin to see in this figure. We take the range of $\text{Arg}(\Phi)$ as $-\pi < \text{Arg}(\Phi) < \pi$ in the right panel.

Table 4.3: Parameters used in numerical simulations for long-lived domain walls (2D).

Grid size (N)	4096
Box size (L)	230
Total number of time steps	10800
Time interval ($\Delta\tau$)	0.01
λ	0.1
m_a	0.1
N_{DW}	varying
Initial time (τ_i)	2.0
Final time (τ_f)	110.0

We calculated the time evolution of the comoving area density of domain walls as shown in Fig. 4.5. In the case with $N_{\text{DW}} > 1$, the scaling regime in which the area density scales as τ^{-1} [see Eq. (4.15)] begins around $\tau \simeq 10$. On the other hand, if $N_{\text{DW}} = 1$, the area density falls off shortly after the beginning of the simulation. These properties are similar with that found in the past simulations [153].

Next we consider the effect of the term which explicitly breaks the discrete symmetry [i.e. Eq. (4.17)]. This effect is parameterized by two quantities: δ and Ξ . In general, δ can be defined relative to the phase in the quark mass matrix and have any value, but in the numerical simulation it only determines the location of the true minimum in the potential without affecting the results of the simulations. Therefore, we take $\delta = 0$ for simplicity.

We note that the lift of the degenerate vacua must be sufficiently small since we assume the circumstance in which the discrete symmetry is held approximately. We can understand this requirement more quantitatively as follows. If the lift of the degenerate vacua is large, the probability of choosing vacuum at the time of formation of domain walls is not uniform between different vacua. For example, assume that there are two vacua ($N_{\text{DW}} = 2$), and the energy density of one vacuum (false vacuum) is greater than that of another vacuum (true vacuum) due to the presence of the bias term δV . Then, let us denote the probability of having a scalar field fluctuation at the time of the formation of domain walls end up in true vacuum as p_t and in false vacuum as p_f . The ratio of these two probabilities is given by [165]

$$\frac{p_f}{p_t} = \exp\left(-\frac{\Delta V_{\text{bias}}}{\Delta V_{\text{pot}}}\right) \equiv \exp(-R), \quad (4.57)$$

where $\Delta V_{\text{pot}} \simeq 2m_a^2\eta^2/N_{\text{DW}}^2$ is the height of the axion potential, and $\Delta V_{\text{bias}} \simeq 2\Xi\eta^4$ is the difference of the energy density between two vacua. These probabilities are not uniform (i.e. $p_t = p_f = 0.5$) if $\Xi \neq 0$. It was shown that this non-uniform initial probability distribution also destabilizes domain walls [166, 37]. Let us define the parameter ϵ which represents the deviation from the uniform probability distribution as $p_t = 0.5 + \epsilon$. According to the numerical simulations [37], the time scale of the decay of domain walls $\tau_{\text{dec,prob}}$

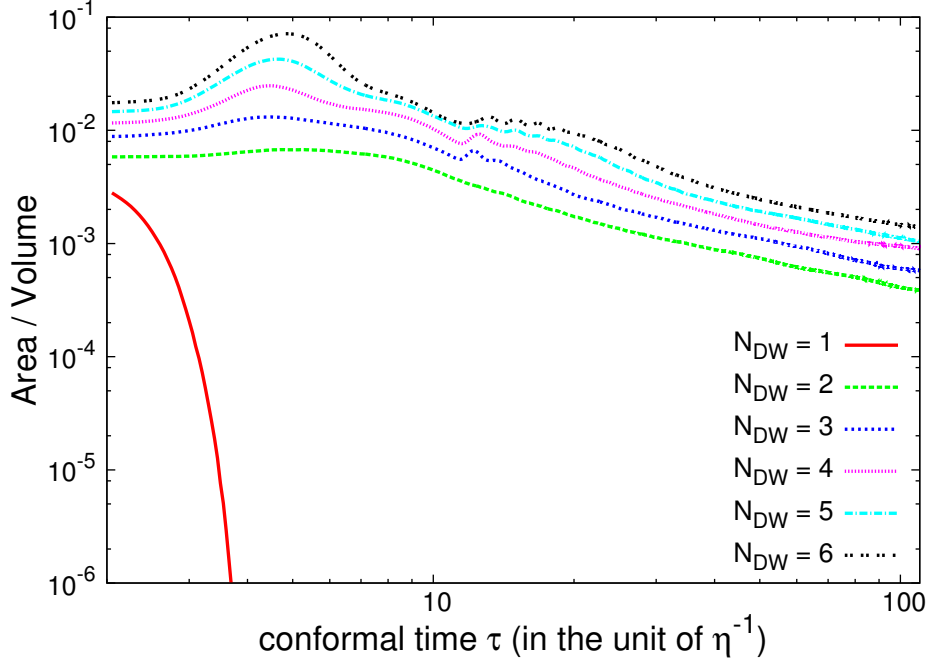


Figure 4.5: The time evolution of the comoving area density of domain walls for various values of N_{DW} .

(in conformal time) due to this effect is given by

$$\tau_{\text{dec,prob}}/\tau_{\text{form}} \simeq \epsilon^{-D/2}, \quad (4.58)$$

where τ_{form} is the time of the formation of domain walls, and D is the spatial dimension. We must require that this time scale should be greater than the simulation time scale ($\tau_{\text{dec,prob}} > \tau_f$), since we would like to check the effect of volume pressure [i.e. the relation given by Eq. (4.20)] as a decay mechanism of domain walls. This requirement leads the condition

$$R = \frac{\Xi \eta^2 N_{\text{DW}}^2}{m_a^2} < 0.4, \quad (4.59)$$

for $\tau_f = 110$ and $\tau_{\text{form}} \simeq 10$.

Note that this result is obtained for the case with $N_{\text{DW}} = 2$. It is not so straightforward to generalize above arguments for the case with multiple vacua. However, we guess that the condition for the case with $N_{\text{DW}} > 2$ might be less severe than that given by Eq. (4.59), since if N_{DW} is large, the relative probability of choosing true vacuum becomes small and less sensitive to R . Therefore, we take Eq. (4.59) as a criterion to ignore the effect of non-uniform initial probability distribution even for the case with $N_{\text{DW}} > 2$. It is difficult to satisfy this requirement for large N_{DW} in the numerical simulation, since the height of the axion potential is proportional to N_{DW}^{-2} and we have to choose small value of Ξ to make R satisfy the condition (4.59). Such an adjustment is forbidden because of the limitation

of the dynamical range (domain walls cannot decay in the simulation time scale). This restriction forbids us to perform the simulations with $N_{\text{DW}} = 5$ and 6.

We performed simulations for $N_{\text{DW}} = 2, 3, 4$, and Ξ satisfying the condition described above and calculated the time evolution of the area density of domain walls. The results are shown in Fig. 4.6. We confirmed that domain walls decay in the time scale which we naively expect as Eq. (4.20).

According to Eq. (4.20), the ratio

$$k_d \equiv \frac{\tau_{\text{dec}}}{\sqrt{m_a/(N_{\text{DW}}\Xi\eta^3)}} \quad (4.60)$$

is expected to have a constant value of $\mathcal{O}(1)$, where we translated Eq. (4.20) into the relation in conformal time. Here, we determine this coefficient based on the results of simulations. In numerical simulations, we define τ_{dec} as a conformal time when the value of A/V becomes 1% of that with $\Xi = 0$. Figure 4.7 shows the numerical results for k_d averaging over 5 realizations. Every result gives a value of $\mathcal{O}(1)$ for k_d , but some data points seem to be inconsistent with each other.

It should be noted that calculated values of k_d (or τ_{dec}) might be affected by unphysical nature of numerical simulations. First, if the value of Ξ is sufficiently small, domain walls tend to collapse around the final time of simulations where the Hubble radius (or typical distance between neighboring walls) is comparable with the size of the simulation box. In such a case, finiteness of the simulation box tends to promote walls to collapse faster, which gives smaller value of k_d than that obtained in simulations with larger values of Ξ .⁶ Furthermore, if the value of Ξ is sufficiently large, the criterion in Eq. (4.59) is marginally violated, which tends to collapse domain walls faster than the time scale estimated by Eq. (4.20) due to the non-uniform initial distribution. In order to resolve these effects, we must run simulations with higher spatial resolution (or larger simulation box), which is impossible in the current computational resources. For now, we estimate the value of k_d regarding large uncertainties observed in Fig. 4.7,

$$k_d \simeq 8.5 \pm 1.0. \quad (4.61)$$

In Sec. 4.7, we will use this value with the formula for t_{dec} in cosmic time

$$t_{\text{dec}} = \frac{k_d^2}{4} \left(\frac{m_a}{N_{\text{DW}}\Xi\eta^2} \right). \quad (4.62)$$

Finally, let us comment on the dependence of the decay time t_{dec} on the axion mass m_a . It is impossible to make the value of m_a arbitrarily small since we invalidate our assumption about the approximate discrete symmetry. Furthermore, m_a cannot be so large because the core size of the string δ_s must be smaller than the width of the domain wall δ_w for the formation of stable networks [38]: $\delta_s/\delta_w \simeq m_a/\sqrt{\lambda} \ll 1$.⁷ Therefore, the range of m_a , which we can choose in the actual numerical simulation, is narrow.

⁶A similar effect was observed in another numerical study [165].

⁷For the parameters we used in the simulations, $m_a/\sqrt{\lambda} \approx 0.32$.

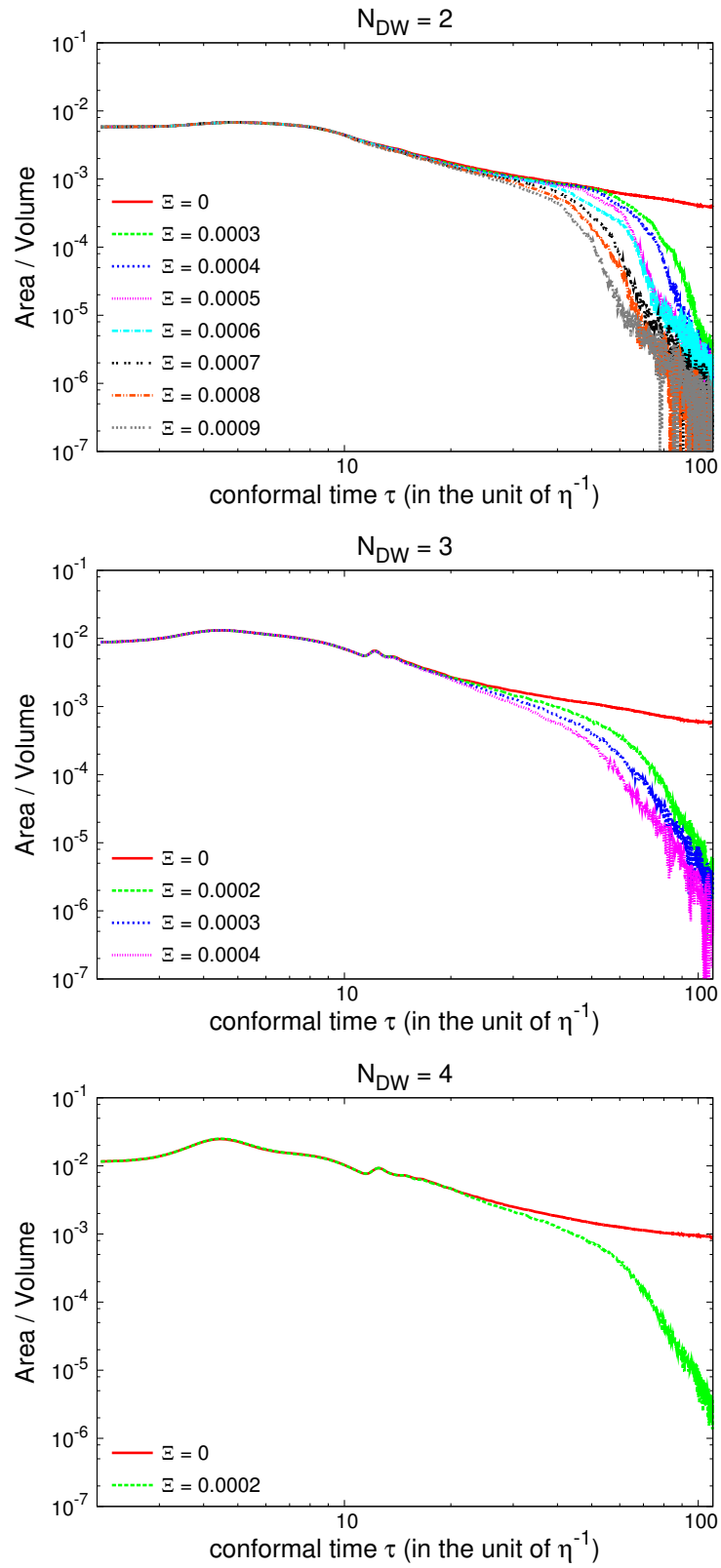


Figure 4.6: The time evolution of the comoving area density of domain walls for various values of Ξ with $N_{DW} = 2$ (top), $N_{DW} = 3$ (middle), and $N_{DW} = 4$ (bottom). In the case with $N_{DW} = 4$, we can choose only one parameter for Ξ because of the restriction given by Eq. (4.59).

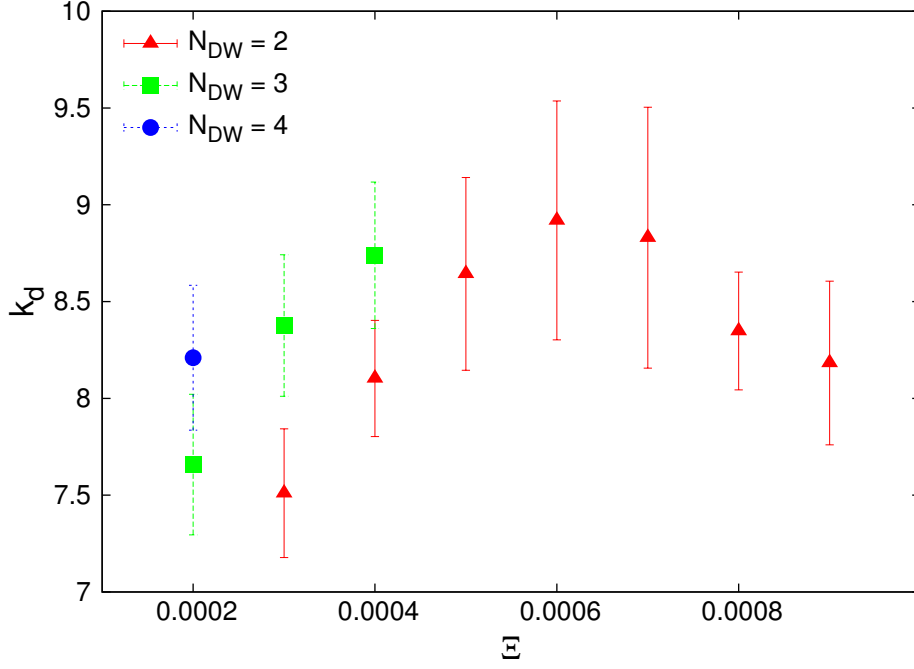


Figure 4.7: Results for k_d obtained from numerical simulations for various values of Ξ with $N_{\text{DW}} = 2$ (triangle), $N_{\text{DW}} = 3$ (square) and $N_{\text{DW}} = 4$ (circle).

Figure 4.8 shows the m_a dependence of the time evolution of the comoving area density of domain walls. Although the range of m_a is limited, from this figure we see that the decay time of domain walls (in conformal time) is proportional to $\sqrt{m_a}$, as we anticipated in Eq. (4.20). Therefore, we assume that this dependence on m_a is correct for other values of m_a , and use the relation (4.62) for the evaluation of the decay time of domain walls.

3D

In three-dimensional simulations, we simply use the potential (4.52) without including a bias term (4.17). The grid size is chosen as $N^3 = 512^3$. We set the initial time as $\tau_i = 2.0$ and the final time as $\tau_f = 40.0$. The dynamical range of the simulation is therefore $\tau_f/\tau_i = 20$. The other parameters are summarized in Table 4.4. At the end of the simulation $\tau_f = 40$, ratios given in Eq. (4.56) become $H^{-1}/\Delta x_{\text{phys}} \simeq 256 < N$, $\delta_w/\Delta x_{\text{phys}} \simeq 3.2$, and $\delta_s/\Delta x_{\text{phys}} \simeq 1.01$.

We naively guess that domain walls formed in the model with $N_{\text{DW}} = 2$ have a common property with that formed in the model of real scalar field with spontaneous breaking of a discrete Z_2 symmetry. Based on this observation, we also consider the real scalar field

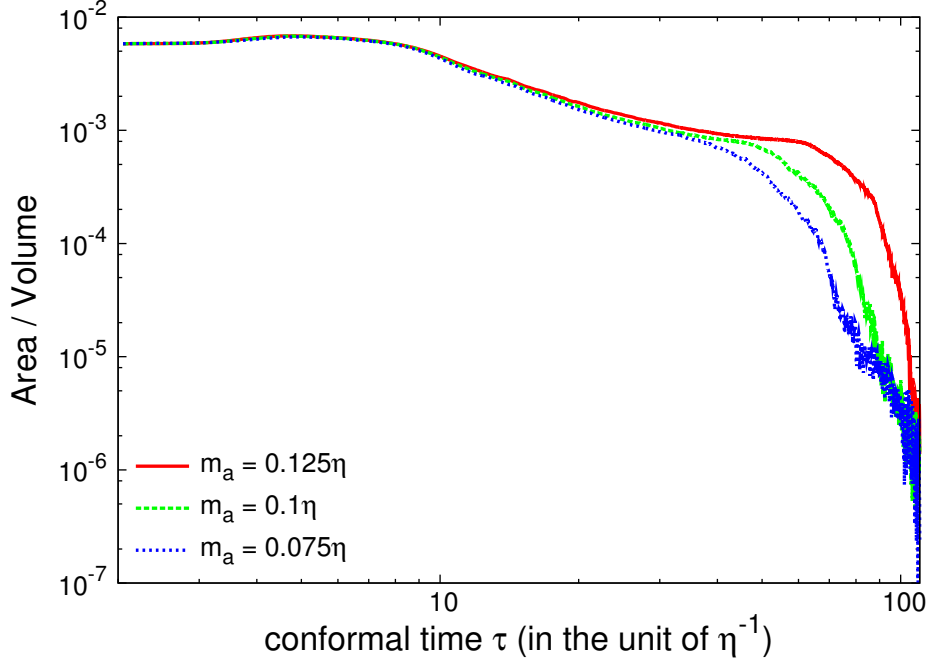


Figure 4.8: The time evolution of the comoving area density of domain walls for various values of m_a . Other parameters are fixed so that $\lambda = 0.1$, $N_{\text{DW}} = 2$, and $\Xi = 0.0004$.

theory with the Lagrangian density given by

$$\mathcal{L} = -\frac{1}{2}\partial_\mu\phi\partial^\mu\phi - V(\phi), \quad (4.63)$$

$$V(\phi) = \frac{m_a^2}{3\eta^2} \left(\phi^2 - \frac{3}{2}\eta^2 \right)^2, \quad (4.64)$$

where ϕ is the real scalar field. In Appendix B.5, it is shown that this model mimics the axionic model with $N_{\text{DW}} = 2$, in the sense that the surface mass density and the width of domain walls are same.

Figure 4.9 shows the visualization of one realization of the simulation. Using the identification scheme described in Appendix C.2, we confirmed that N_{DW} domain walls attached to strings are formed at late time of the simulations. The structure of defect networks becomes more complicated when we increase the number N_{DW} . Figure 4.10 shows the spatial distribution of the phase of the scalar field $\text{Arg}(\Phi)$ in the model with $N_{\text{DW}} = 3$ at selected time slices. Since we give the initial configuration of the scalar field as Gaussian random amplitude, the scalar field randomly oscillates around the minima $|\Phi|^2 = \eta^2$ of the potential, given by the first term of Eq. (4.52). Strings are formed when this initial random configuration becomes relaxed. Subsequently, the value of the phase of the scalar field $\text{Arg}(\Phi)$ is separated into $N_{\text{DW}} = 3$ domains. Domain walls are located around the boundaries of these domains.

In a similar way to the case of the short-lived networks, we compute the length param-

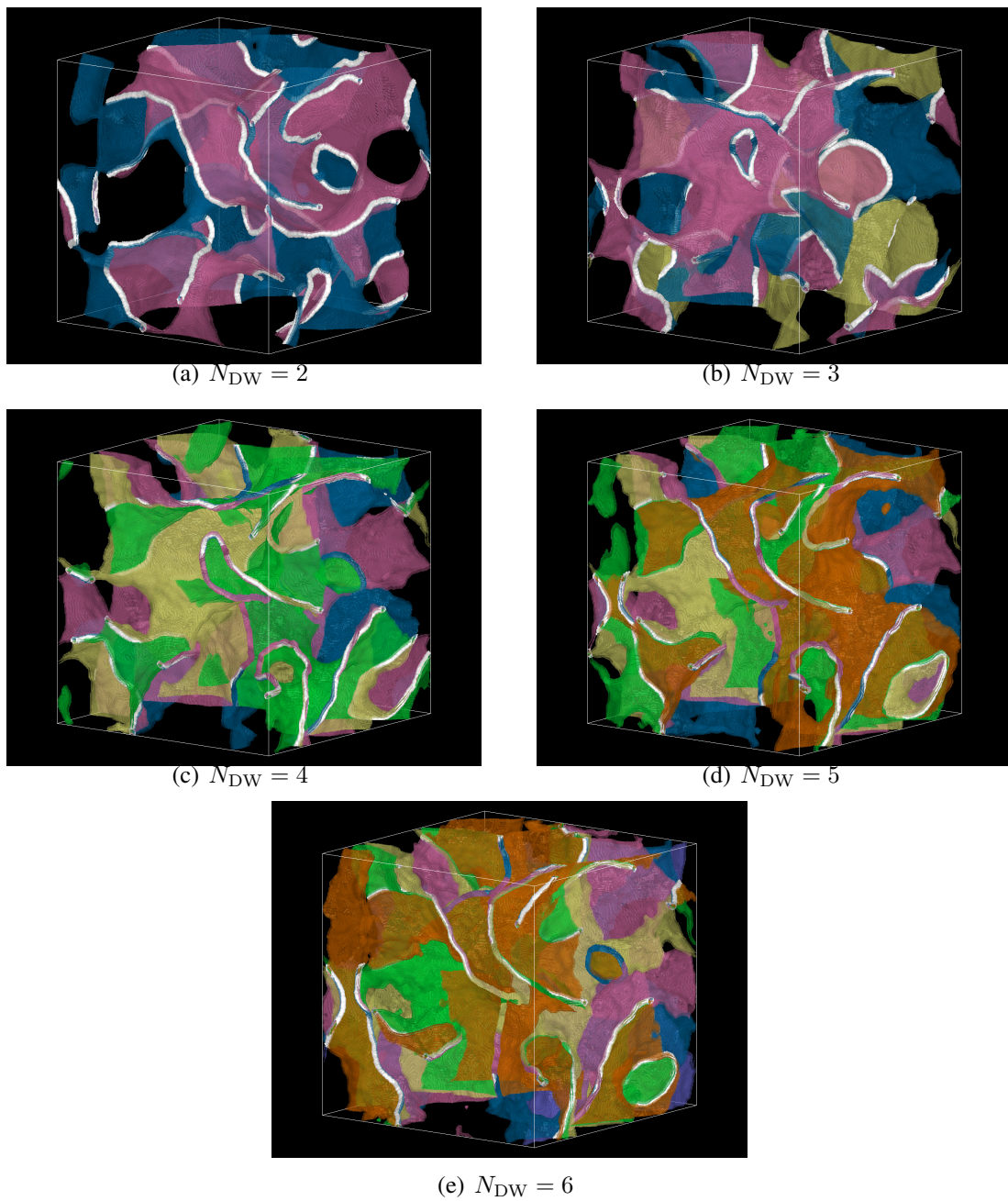


Figure 4.9: Visualization of the simulations with (a) $N_{\text{DW}} = 2$, (b) $N_{\text{DW}} = 3$, (c) $N_{\text{DW}} = 4$, (d) $N_{\text{DW}} = 5$, and (e) $N_{\text{DW}} = 6$. In this figure, we take the box size as $L = 60$ and $N = 256$, which is smaller than that shown in Table 4.4. Each figure shows the spatial configurations of topological defects at the time $\tau = 25$. The white lines correspond to the position of the core of strings, which is identified by using the method described in Appendix C.2.1. N_{DW} domain walls are represented by surfaces with various colors, which are identified by using the method described in Appendix C.2.2.

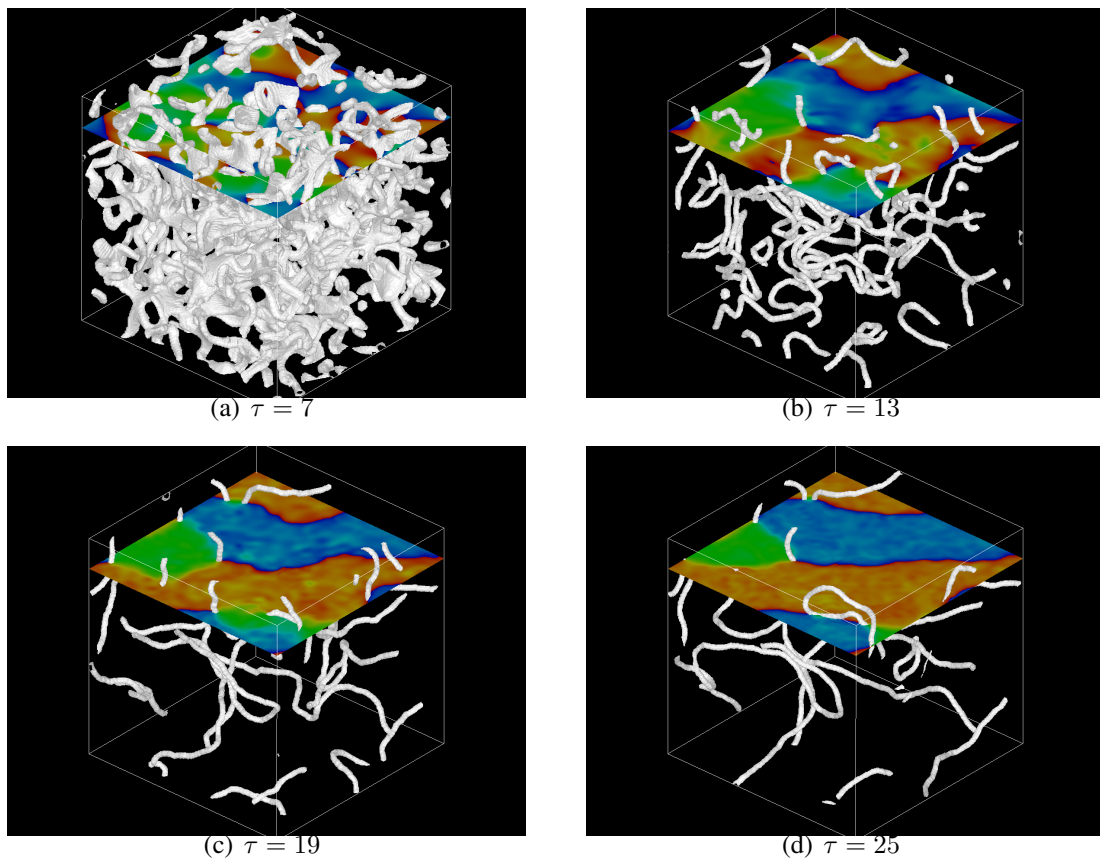


Figure 4.10: The distribution of the phase of the scalar field $\text{Arg}(\Phi)$ on the two-dimensional slice of the simulation box. Each figure shows the visualization at different times: (a) $\tau = 7$, (b) $\tau = 13$, (c) $\tau = 19$, and (d) $\tau = 25$. In these figures, we used the same data that are used to visualize the result with $N_{\text{DW}} = 3$ in Fig. 4.9. The value of $\text{Arg}(\Phi)$ varies from $-\pi$ (blue) to π (red). At late times, the value of $\text{Arg}(\Phi)$ is separated into three domains represented by blue, red, and green region. Domain walls are located around the boundary of these three regions, $\text{Arg}(\Phi) = \pi/3$, $\text{Arg}(\Phi) = -\pi/3$, and $\text{Arg}(\Phi) = \pm\pi$. Strings, which are represented by white lines, pass through the point where three regions meet each other.

Table 4.4: Parameters used in numerical simulations for long-lived domain walls (3D).

Grid size (N)	512
Box size (L)	80
Total number of time steps	1900
Time interval ($\Delta\tau$)	0.02
λ	0.1
m_a	0.1
N_{DW}	varying
Initial time (τ_i)	2.0
Final time (τ_f)	40.0

eter ξ of strings and the area parameter \mathcal{A} of domain walls given by Eqs. (4.50) and (4.51), respectively. The time evolution of these parameters is plotted in Fig. 4.11. From this figure, we see that the defect networks are in scaling regime in the time scale $\tau \gtrsim 15$. The length parameter ξ does not strongly depend on N_{DW} , and its value is consistent with that obtained in the simulations of short-lived networks (see Fig. 4.3). On the other hand, the value of the area parameter \mathcal{A} increases for large N_{DW} . This fact agrees with the intuitive argument that the number of domain walls increases proportionally to N_{DW} if the number of strings per simulation box is unchanged.

The bottom panel of Fig. 4.11 also implies that the area of domain walls in the real scalar field theory given by Eqs. (4.63) and (4.64) evolves similarly to the axionic model with $N_{\text{DW}} = 2$. This means that the behavior of the networks for the case with $N_{\text{DW}} = 2$ is similar to that produced by the model with Z_2 symmetry, except that they contain strings on the surface of walls. We note that the bump-like behavior of \mathcal{A} in the real scalar field model at the initial stage of the simulation should be regarded as a numerical fake. We identify the position of domain walls as the point on which scalar field changes its sign for the model with the real scalar field. This identification scheme is different from that used for the model with the complex scalar field (see Appendix C.2.2). These different identification schemes cause the different behavior of \mathcal{A} at the initial stage, where domain walls do not relax into the scaling regime.

4.3 Axion production from strings

Before going to the analysis of the axion production from string-wall systems, let us make a comment on the string decay contribution. Historically, there was long-term controversy on the estimation of string decay contribution. Davis [47] first recognized that axions emitted by strings give an additional cosmological abundance and found that this additional contribution dominates over the coherent oscillations, which gave more severe upper bound on the axion decay constant. This suggestion was supported by various analyti-

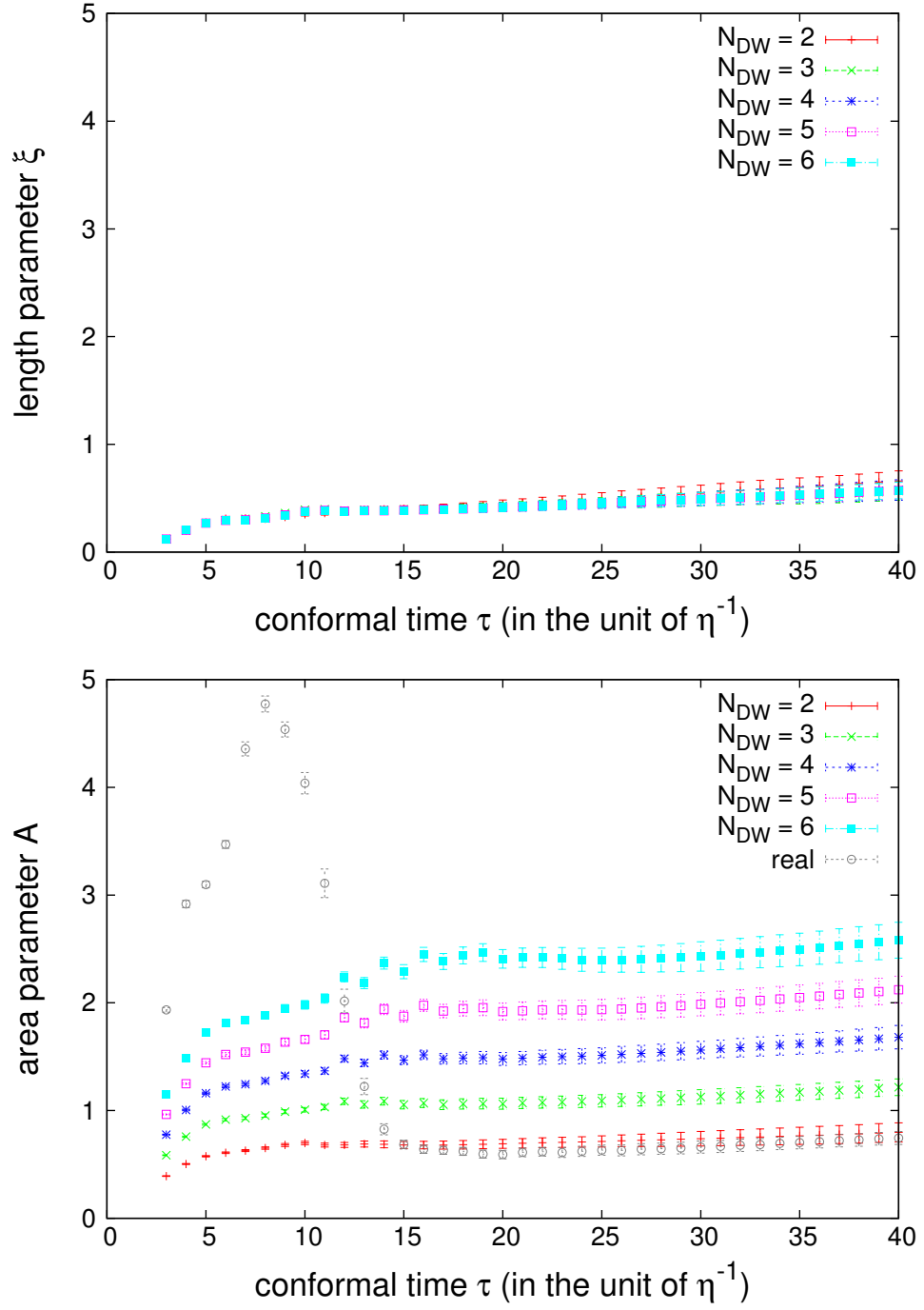


Figure 4.11: Time evolution of the length parameter ξ (top panel) and the area parameter \mathcal{A} (bottom panel) for various values of N_{DW} . The points denoted as “real” in the bottom panel show the evolution of \mathcal{A} in the model with real scalar field defined by Eqs. (4.63) and (4.64).

cal and numerical studies given by different authors [49, 50, 51, 52]. However, Harari and Sikivie [54] presented a different scenario which claims that the abundance of axions produced by strings do not exceed that of coherent oscillations, and gave a weaker upper bound on F_a . The subsequent numerical studies provided by [55, 56] supported this weaker bound.

This controversy about the contribution from strings arises from different assumptions on the spectrum of radiated axions, which determines the number of axions. From Eq. (4.50), the energy density of strings can be written as

$$\rho_{\text{string}}(t) = \frac{\mu_{\text{string}}\xi}{t^2}, \quad (4.65)$$

where μ_{string} is given by Eq. (B.56)

$$\mu_{\text{string}} = \pi\eta^2 \ln\left(\frac{t/\sqrt{\xi}}{\delta_s}\right). \quad (4.66)$$

Strings continue to radiate axions from the era of PQ phase transition t_c to the era of the QCD phase transition t_1 . For simplicity, let us assume that axions are exactly massless before QCD phase transition $t < t_1$.⁸ During this epoch, the evolution of energy densities of strings and axions is described by the following equations

$$\frac{d\rho_{\text{string}}}{dt} = -2H\rho_{\text{string}} - \left.\frac{d\rho_{\text{string}}}{dt}\right|_{\text{emission}}, \quad (4.67)$$

$$\frac{d\rho_a}{dt} = -4H\rho_a + \left.\frac{d\rho_{\text{string}}}{dt}\right|_{\text{emission}}, \quad (4.68)$$

where $(d\rho_{\text{string}}/dt)|_{\text{emission}}$ is the rate of radiation from strings. From Eqs. (4.65) and (4.67), we obtain

$$\left.\frac{d\rho_{\text{string}}}{dt}\right|_{\text{emission}} = \pi\eta^2 \frac{\xi}{t^3} \left[\ln\left(\frac{t/\sqrt{\xi}}{\delta_s}\right) - 1 \right]. \quad (4.69)$$

Let us define the comoving energy of radiated axions

$$E_{a,\text{string}}(t) = R^4(t)\rho_a(t). \quad (4.70)$$

Then, Eq. (4.68) reduces to

$$\frac{dE_{a,\text{string}}}{dt} = R^4(t) \left.\frac{d\rho_{\text{string}}}{dt}\right|_{\text{emission}}. \quad (4.71)$$

⁸Contribution of axions radiated by strings in $t > t_1$, where the axion mass becomes non-negligible, will be included in the wall decay contribution $\rho_{a,\text{dec}}$ in Secs. 4.6 and 4.7. In the realistic situation, however, the axion mass is continuously turned on around the time t_1 . Inclusion of such an effect might lead to a correction by a factor of $\mathcal{O}(1)$ in the estimation of the relic axion abundance similarly with the correction at the initial time t_1 of the coherent oscillation discussed in Sec. 3.2.2, but we will not include such a correction in the current analysis.

Therefore, the comoving number of radiated axions at the time $t > t_1$ is given by

$$\begin{aligned} N_{a,\text{string}}(t > t_1) &= \int_{t_c}^{t_1} dt' \frac{1}{R(t') \langle \omega_a(t') \rangle} \frac{dE_{a,\text{string}}}{dt} \\ &= \int_{t_c}^{t_1} dt' \frac{R^3(t')}{\langle \omega_a(t') \rangle} \pi \eta^2 \frac{\xi}{t'^3} \left[\ln \left(\frac{t'/\sqrt{\xi}}{\delta_s} \right) - 1 \right], \end{aligned} \quad (4.72)$$

where $\langle \omega_a(t) \rangle$ is the mean energy of radiated axions at time t . In order to estimate $N_{a,\text{string}}(t > t_1)$, we must know $\langle \omega_a(t) \rangle$, whose value depends on the interpretation of the spectrum of radiated axions.

In Refs. [47, 49, 50, 51, 52] it is assumed that the typical wavelength of radiated axions is given by the curvature size of global strings which is comparable to the size of the horizon, $k \sim 2\pi/t$, based on the result of [167, 168] which claims that closed loops or bent strings oscillate many times before they lose most of their energy. Let us call this case as case A. In this case, we can write $\langle \omega_a(t) \rangle$ as

$$\langle \omega_a(t) \rangle = \epsilon \frac{2\pi}{t}, \quad (4.73)$$

where ϵ is a factor whose value is determined from numerical simulations. Substituting Eq. (4.73) into Eq. (4.72), we obtain

$$N_{a,\text{string}}(t > t_1) = \frac{\eta^2 \xi}{\epsilon} \left[\frac{R^3(t')}{t'} \left(\ln \left(\frac{t'/\sqrt{\xi}}{\delta_s} \right) - 3 \right) \right]_{t_c}^{t_1}.$$

Hence, the present number density of axions produced by strings is given by

$$n_{a,\text{string}}(t_0) = \frac{N_{a,\text{string}}(t > t_1)}{R^3(t_0)} \simeq \left(\frac{R(t_1)}{R(t_0)} \right)^3 \frac{\eta^2 \xi}{t_1 \epsilon} \ln \left(\frac{t_1/\sqrt{\xi}}{\delta_s} \right), \quad (4.74)$$

In this scenario, the contribution from axions produced by strings becomes greater than that from coherent oscillations by a factor of $\ln(t_1/\sqrt{\xi}\delta_s) \sim 60$.

On the other hand, Refs. [54, 55, 56] suggest that the motion and decay of the global strings are more ‘‘turbulent’’. Let us call this as case B. In this case, strings lose their energy in one oscillation time, quickly decaying into small pieces. Therefore, whole scales between the largest scale $\sim t$ and the smallest scale $\sim \delta_s$ give the same contribution to the power spectrum of radiated axions, $dE/d \ln k \sim$ (independent on k), or

$$\left. \frac{d\rho_{\text{string}}}{dt dk} \right|_{\text{emission}} \sim \frac{1}{k}. \quad (4.75)$$

Integrating it between two length scales, we obtain

$$\left. \frac{d\rho_{\text{string}}}{dt} \right|_{\text{emission}} \sim \ln \left(\frac{t/\sqrt{\xi}}{\delta_s} \right). \quad (4.76)$$

In this case, the mean energy of radiated axions is given by

$$\frac{1}{\langle \omega_a(t) \rangle} = \frac{1}{(d\rho_{\text{string}}/dt)|_{\text{emission}}} \int \frac{dk}{k} \frac{d\rho_{\text{string}}}{dtdk} \Big|_{\text{emission}} \sim \left(\frac{t}{2\pi} \right) \frac{1}{\ln\left(\frac{t/\sqrt{\xi}}{\delta_s}\right)}. \quad (4.77)$$

Due to the the additional factor $\ln(t/\sqrt{\xi}\delta_s)$ in $\langle \omega_a(t) \rangle$, the contribution from strings is subdominant compared with that from coherent oscillations.

This discrepancy between two scenarios might be resolved by the field-theoretic global simulations including the cosmic expansion performed in [57, 58]. In [57, 58], it was concluded that the power spectrum of radiated axions has a sharp peak around the horizon scale $k_{\text{phys}} \sim 2\pi/t$, supporting case A. Here, we estimate $\Omega_{a,\text{string}}h^2$ by using their results. Noting that the energy density of axions today is given by $\rho_{a,\text{string}}(t_0) = m_a(0)n_{a,\text{string}}(t_0)$, where $n_{a,\text{string}}(t_0)$ is given by Eq. (4.74), we find the density parameter of axions radiated from strings

$$\Omega_{a,\text{string}}h^2 = 8.74 \times \frac{\xi}{\epsilon} \left(\frac{g_{*,1}}{70} \right)^{-(n+2)/2(n+4)} \left(\frac{F_a}{10^{12}\text{GeV}} \right)^{(n+6)/(n+4)} \left(\frac{\Lambda_{\text{QCD}}}{400\text{MeV}} \right). \quad (4.78)$$

In numerical simulations of Ref. [58], the value of ϵ is estimated as $\epsilon^{-1} = 0.23 \pm 0.02$. By using this value for ϵ and the rough estimation for the length parameter $\xi \simeq 1.0 \pm 0.5$, we obtain

$$\Omega_{a,\text{string}}h^2 = (2.0 \pm 1.0) \times \left(\frac{g_{*,1}}{70} \right)^{-(n+2)/2(n+4)} \left(\frac{F_a}{10^{12}\text{GeV}} \right)^{(n+6)/(n+4)} \left(\frac{\Lambda_{\text{QCD}}}{400\text{MeV}} \right). \quad (4.79)$$

It seems that the estimation of the contribution from domain walls is faced with the similar discrepancy about the spectrum of radiated axions. Nagasawa and Kawasaki [140, 141] found that axions produced by the collapse of domain walls are mildly relativistic, and this contribution can exceed that from strings. On the other hand, in the study given by Chang, Haggmann and Sikivie [38], the mean energy of axions produced by the decay of domain walls was estimated to be larger than that obtained in [140, 141] by a factor of 20. This leads to the conclusion that axions produced by the collapse of walls are subdominant compared with that produced by strings. The conclusion of [38] relies on the following reasoning. Since domain walls are bounded by strings, the wall energy is converted into the kinetic energy of strings. Then, if we assume that case B is correct, the spectrum of radiated axions becomes hard ($dE/dk \sim 1/k$). However, as we described above, the recent network simulation of global strings supports case A. Therefore it is not so clear whether the domain wall contribution is significant or not. We point out that this discrepancy on the domain wall contribution is also resolved by performing full field-theoretic network simulations. In the following two sections, we present the results of the analysis on the spectrum of axions radiated from domain walls.

4.4 Axion production from short-lived domain walls

Let us show the spectrum of axions produced from short-lived domain walls bounded by strings ($N_{\text{DW}} = 1$). From data of the scalar field obtained by numerical simulations de-

scribed in Sec. 4.2.1, we compute the power spectrum $P(k)$ of axions radiated by string-wall networks, which is defined by

$$\frac{1}{2} \langle \dot{a}(t, \mathbf{k})^* \dot{a}(t, \mathbf{k}') \rangle = \frac{(2\pi)^3}{k^2} \delta^{(3)}(\mathbf{k} - \mathbf{k}') P(k, t), \quad (4.80)$$

where $\dot{a}(t, \mathbf{k})$ is the Fourier component of the time derivative of the axion field, and $\langle \dots \rangle$ represents an ensemble average.

In general, the data of the scalar field Φ contain other components, which can be enumerated as follows:

1. *Initial fluctuations.* In numerical simulations, we give the initial conditions as Gaussian random fluctuations [see Eqs. (4.37), (4.38) and (4.39)]. These fluctuations are diluted away by the cosmic expansion, but might not be completely negligible even at the final time of the simulation, since the dynamical range of the numerical simulation is short. Therefore, they can contaminate the final form of the spectrum of radiated axions.
2. *Radiations from strings.* As we mentioned in Sec. 4.3, oscillating loops of strings radiate axions during the time between the string formation ($T = T_c$) and the domain wall formation ($T = T_1$). This contribution must be distinguished from the wall-decay contribution which is produced *after* the time t_1 .
3. *Core of defects.* In the core of strings, the energy density of the scalar field is higher than that of free axions. This can be regarded as another contamination on the spectrum of radiated axions.

Figure 4.12 shows the pipeline of removing these contaminations. To remove the contaminations from the core of strings, we mask the region near the position of the core of strings and estimate the power spectrum which contains only the contribution from free radiations. We calculate the power spectrum in two time slices, the time at which the mass of the axion becomes relevant ($t = t_1$) and the time at which the decay of string-wall networks completes ($t = t_d$). Then, we subtract the spectrum evaluated at t_1 from that evaluated at t_d in order to remove the contributions from initial fluctuations and strings, such that

$$P_{\text{dec}}(k, t_d) = P(k, t_d) - P_{\text{pre}}(k, t_d), \quad (4.81)$$

where $P_{\text{pre}}(k, t_d)$ is computed from $P(k, t_1)$ [see Eq. (C.38)]. We regard $P_{\text{dec}}(k, t_d)$ as the spectrum of radiations produced after the decay of domain walls. A more detailed description of these procedures is given in Appendix C.3.3.

Figure 4.13 shows the spectra of free axions evaluated at t_1 and t_d . The basic behavior of the spectrum evaluated at t_1 is similar to that obtained in Ref. [58]. This spectrum is dominated by the contribution of axions produced by strings. However, the population of axions with high momenta increases after the decay of domain walls ($t = t_d$). The final form of the spectrum, obtained by subtracting the components of radiations produced before t_1 , is shown in Fig. 4.14. The spectrum has a peak at the low momentum. This disagrees with the result of Chang, Haggmann and Sikivie [38], which claims that the radiated

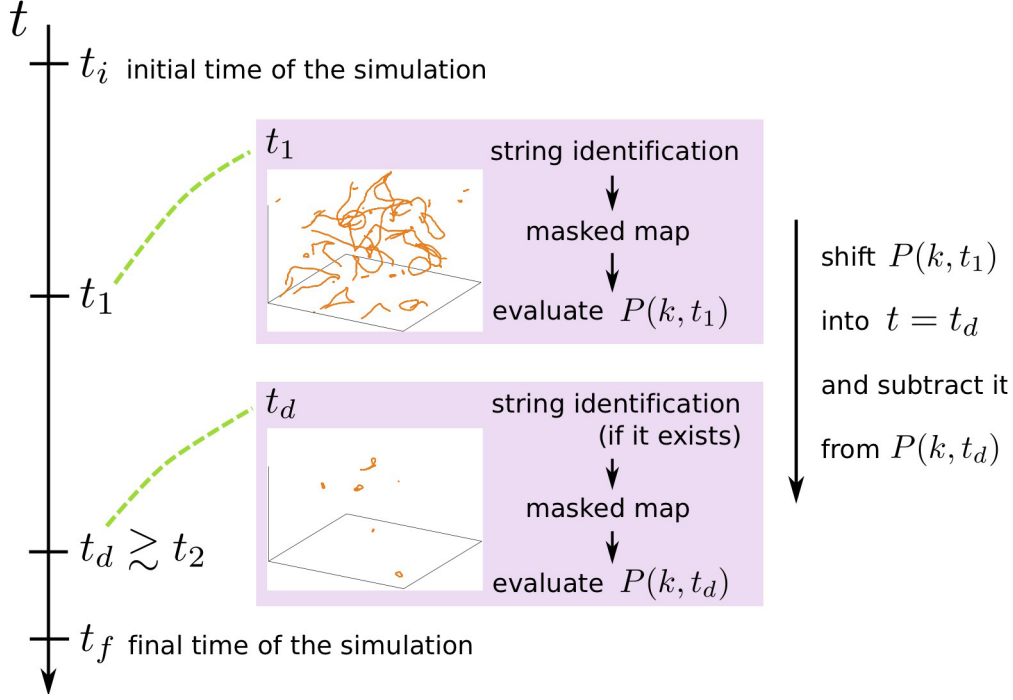


Figure 4.12: Schematics of the procedure to estimate the power spectrum of axions radiated from short-lived networks.

axions have a spectrum proportional to $1/k$. Note that, however, there is a high frequency tail in the spectrum, which has a cutoff at the momentum corresponding to (twice the size of) the width of strings $k \simeq (2\pi/2\delta_s)R(t_d) \simeq 64.4$ (for $\kappa = 0.3$). This feature might be interpreted in terms of the reasoning of [54, 55, 56, 38] (case B). Namely, there are various size of defects around the time $t = t_d$, and small scale defects can radiate axions with harder momentums. As we see in Fig. 4.14, the contribution from these hard axions is subdominant, and most axions have a momentum comparable to the mass of the axion $k/R(t_d) \sim m_a$.

Using the result of $P_{\text{dec}}(k, t_d)$, we compute the mean comoving momentum of radiated axions

$$\bar{k}(t_d) = \frac{\int \frac{dk}{2\pi} P_{\text{dec}}(k, t_d)}{\int \frac{dk}{2\pi} \frac{1}{k} P_{\text{dec}}(k, t_d)}. \quad (4.82)$$

Let us define the ratio of the physical momentum $\bar{k}/R(t_d)$ to the axion mass $m_a(t_d)$,

$$\epsilon_w \equiv \frac{\bar{k}(t_d)/R(t_d)}{m_a(t_d)}. \quad (4.83)$$

The value of ϵ_w will be determined from the results of numerical simulations.

Note that there are some ambiguities in this analysis. For instance, we choose the time t_d , at which the decay of networks completes, by hand. If we choose t_d as sufficiently late time (for example, the final time of the simulations), we would underestimate the

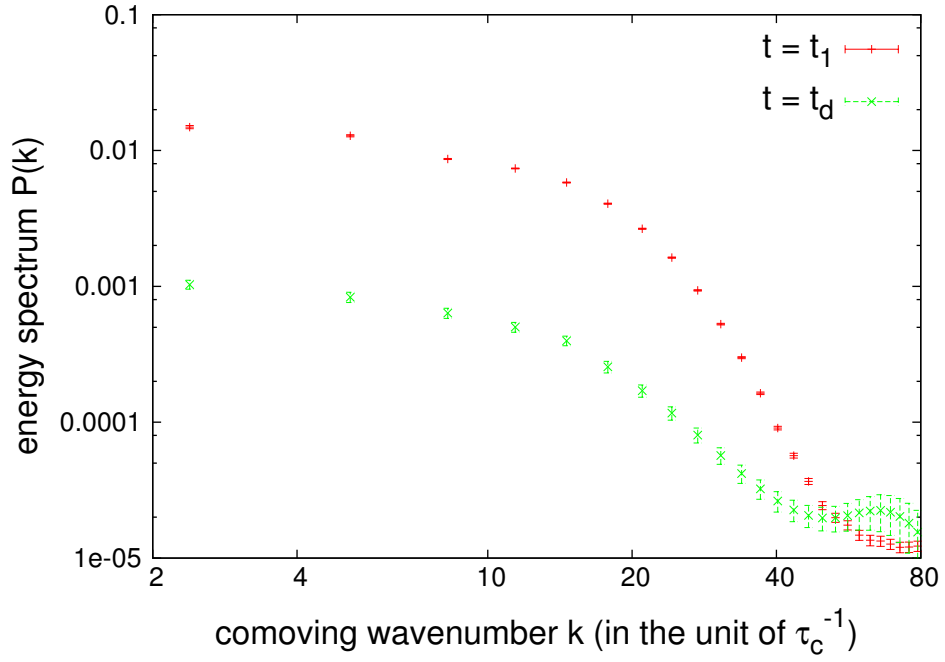


Figure 4.13: The power spectrum of free axions calculated by using Eq. (C.28) in the simulations with $\kappa = 0.3$. We plot the spectra evaluated at two different times t_1 and t_d . Note that the result of $P(k, t_1)$ shown here does not contain the numerical factor defined in Eq. (C.38). Here, we choose the number of bins $n_{\text{bin}} = 25$.

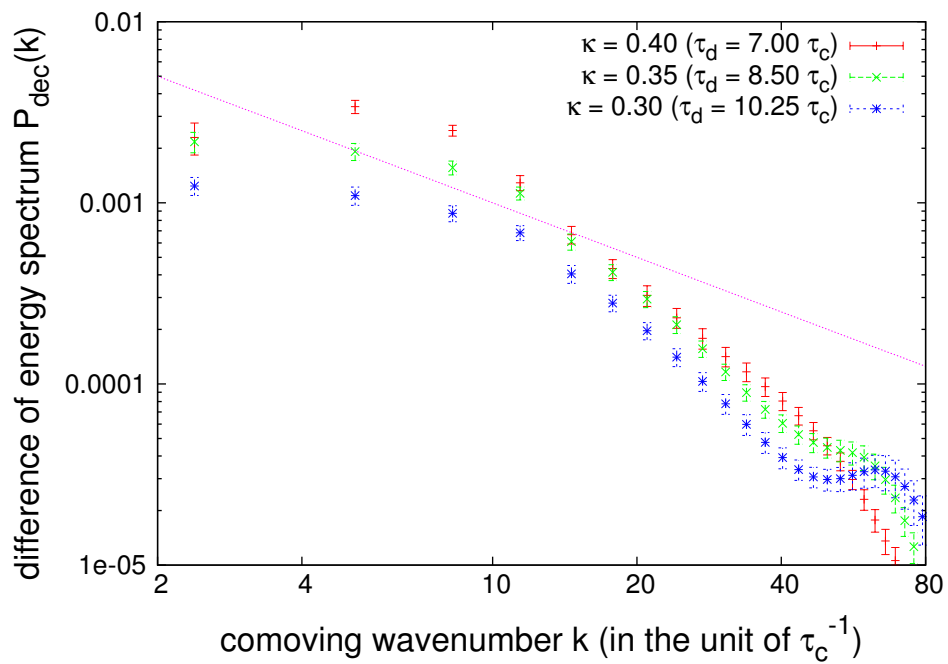


Figure 4.14: The spectrum of axions produced by the decay of networks, defined by Eq. (4.81). Note that the results with different value of κ are evaluated at different times (τ_d). The form of the spectra is different from the relation $P_{\text{dec}}(k) \propto 1/k$ which is indicated by the dotted line. Here, we choose the number of bins $n_{\text{bin}} = 25$.

mean momentum of radiated axions defined by Eqs. (4.82) and (4.83), since the physical momentum gets redshifted proportionally to $1/R(\tau_d)$. Figure 4.15 shows the results of the physical momentum $\bar{k}/R(\tau_d)$ for various choices of τ_d in the simulations with $\kappa = 0.3$. The value of $\bar{k}/R(\tau_d)$ begins to shift as $\propto 1/R$ at the result with $\tau_d = 10.25$. This value of τ_d corresponds to the time at which the area of domain walls becomes less than $\mathcal{O}(1)\%$ of the Hubble scale ($\mathcal{A} \lesssim 0.01$). Therefore, we choose τ_d as the time at which the value of \mathcal{A} falls below 0.01. We use this criterion to calculate the spectra with different values of κ shown in Fig. 4.14.

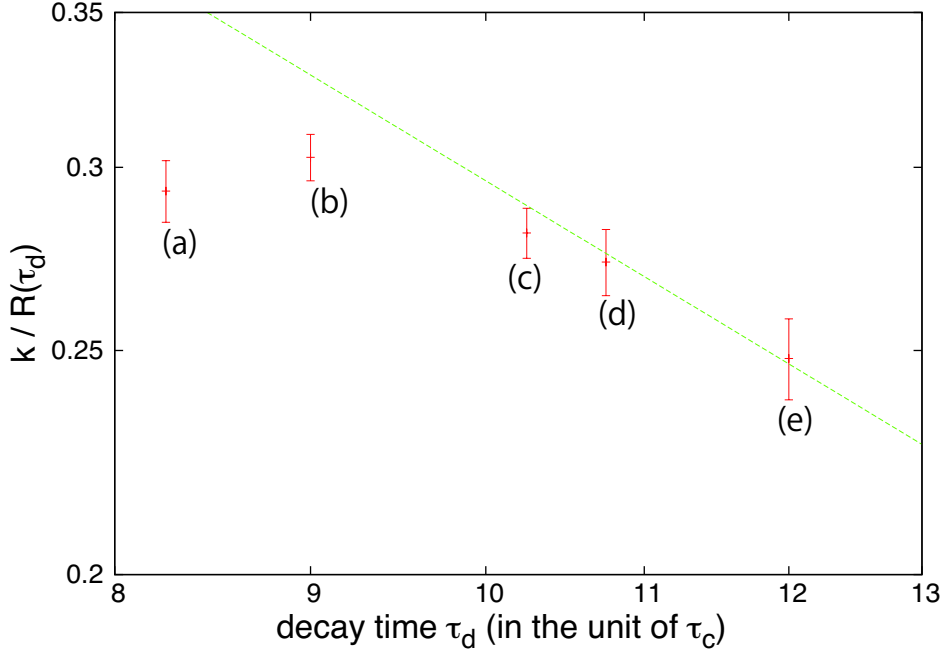


Figure 4.15: The value of the mean physical momentum of radiated axions $\bar{k}/R(\tau_d)$ and its dependence on the choice of τ_d . The dashed line represents the relation $\bar{k}/R(\tau_d) \propto 1/R(\tau_d) \propto 1/\tau_d$. The five points correspond to the results with the value of the area parameters (a) $\mathcal{A}(\tau_d) \lesssim 0.1$, (b) $\mathcal{A}(\tau_d) \lesssim 0.05$, (c) $\mathcal{A}(\tau_d) \lesssim 0.01$, (d) $\mathcal{A}(\tau_d) \lesssim 0.005$ and (e) $\mathcal{A}(\tau_d) \lesssim 0.001$.

Another subtlety is whether the results of numerical simulations are sensitive to the choice of $\kappa \equiv \Lambda_{\text{QCD}}/F_a$. There is a tremendous hierarchy between the QCD scale and the PQ scale, $\Lambda_{\text{QCD}}/F_a \simeq 100\text{MeV}/10^{10}\text{GeV} = 10^{-11}$, but we cannot perform simulations with such a small value of κ because of the limitation of the dynamical range. Nonetheless, we believe that the ratio between the mean momentum of the radiated axions and the typical momentum scale (such as m_a) is not so sensitive to the value of κ , since the power spectrum has a definite peak at the typical momentum scale as shown in Fig. 4.14.

However, in the present numerical results, the value of ϵ_w given by Eq. (4.83) might vary when we change the setup of simulations, which should be regarded as a systematic error in our numerical calculations. In order to clarify this uncertainty, we compute ϵ_w

by varying the value of κ and the number of bins n_{bin} over which the average (4.82) is computed. Here, n_{bin} is an integer which determines the total number of indices in the discretized power spectrum [see Eqs. (C.30)-(C.34)]. Figure 4.16 shows the spectrum of axions for $n_{\text{bin}} = 100$ with the same parameters as that used in Fig. 4.14, where we choose $n_{\text{bin}} = 25$. Comparing Fig. 4.16 with Fig. 4.14, we see that the resolution of the peak location improves if we choose a larger value of n_{bin} . Since there are only a few data points around the peak location in the spectrum with smaller value of n_{bin} , results for the mean momentum $\bar{k}(t_d)$ (or ϵ_w) will be overestimated if we use such coarse bins. The effect of the choice of n_{bin} is shown in Fig. 4.17, where we plotted the results for ϵ_w given by Eq. (4.83) for various values of κ and n_{bin} . We see that the value of ϵ_w changes by a factor of $\mathcal{O}(1)$ when we use a different value of n_{bin} for the evaluation of the mean momentum of radiated axions.

We note that the dependence of ϵ_w on κ is not serious, compared with the uncertainty caused by the choice of n_{bin} . The value of ϵ_w may become large if we use a small value of κ , but it is also regarded as a numerical fake due to the poor resolution of the peak location in the power spectrum. For a small value of κ (such as $\kappa = 0.3$), domain walls begin to collapse at the late time of the simulation, where the width of walls ($\sim m_a^{-1}$) is not sufficiently small compared with the size of the simulation box. Therefore, in the result with the small value of κ , the peak location is not fully resolved in the plot of the power spectrum, as we see in Fig. 4.16. This effect causes the overestimation of ϵ_w shown in Fig. 4.17.

In Fig. 4.17, we also plotted the results obtained by simulations with grid points $N^3 = 256^3$. These results provide another confirmation that the uncertainty in ϵ_w is caused by the resolution of the peak location in the power spectrum. In the simulation with a small value of spatial resolution N , the maximum value of the comoving wavenumber $k^{(\text{max})} = \pi N/L$ also becomes small. Hence the resolution of the power spectrum $\Delta k \equiv k^{(\text{max})}/n_{\text{bin}}$ is improved for a small value of N with a fixed value of n_{bin} . Indeed, data with $\kappa = 0.4$ plotted in Fig. 4.17 show that the value of ϵ_w becomes small for a fixed value of n_{bin} if we take $N = 256$ rather than $N = 512$.

Although we expect that the value of ϵ_w converges into a certain value for $n_{\text{bin}} \rightarrow \infty$, it cannot be confirmed in the current computational resources since the calculation with a large value of n_{bin} requires $\mathcal{O}(n_{\text{bin}}^2)$ arithmetics.⁹ Here, we estimate the systematic uncertainty as the range of ϵ_w observed in Fig. 4.17,

$$\epsilon_w \simeq 2 \pm 1. \quad (4.84)$$

This corresponds to the mean energy of radiated axions,

$$\langle \omega_a(t_d) \rangle / m_a(t_d) = \sqrt{1 + \epsilon_w^2} = 2.2 \pm 0.9. \quad (4.85)$$

We will use this result when we calculate the relic abundance of axions produced from collapse of string-wall systems in Sec. 4.6.

The limitation of the dynamical range of the simulation is provided by the conditions described above Eq. (4.44). Especially, the condition that the width of strings δ_s should be

⁹There are $\mathcal{O}(n_{\text{bin}}^2)$ arithmetics because we need to calculate matrices in Eq. (C.34).

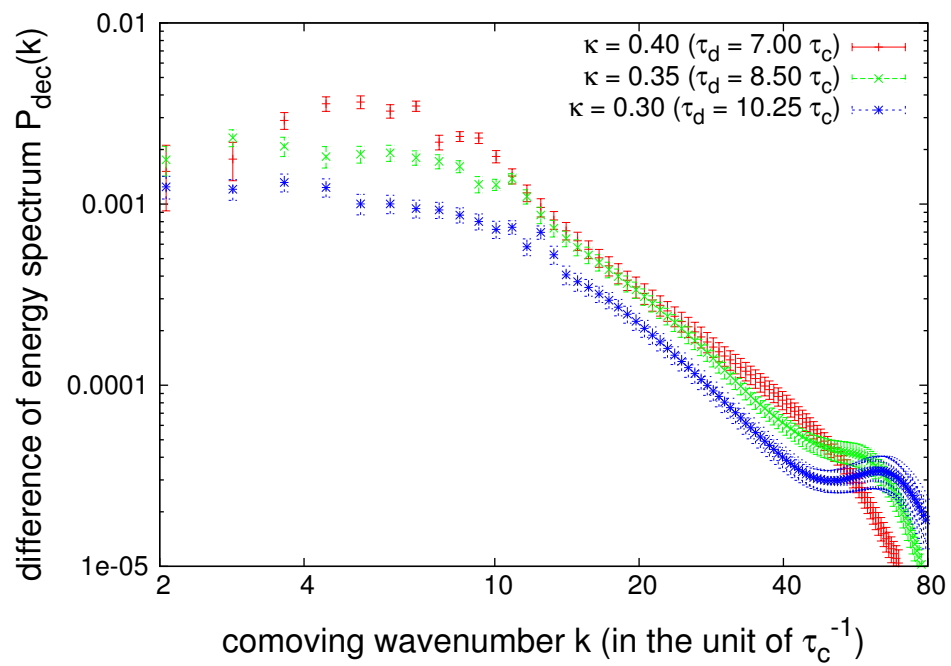


Figure 4.16: The spectrum of axions produced by the decay of networks, evaluated by choosing the number of bins as $n_{\text{bin}} = 100$. In this plot, all parameters are the same as that used in Fig. 4.14.

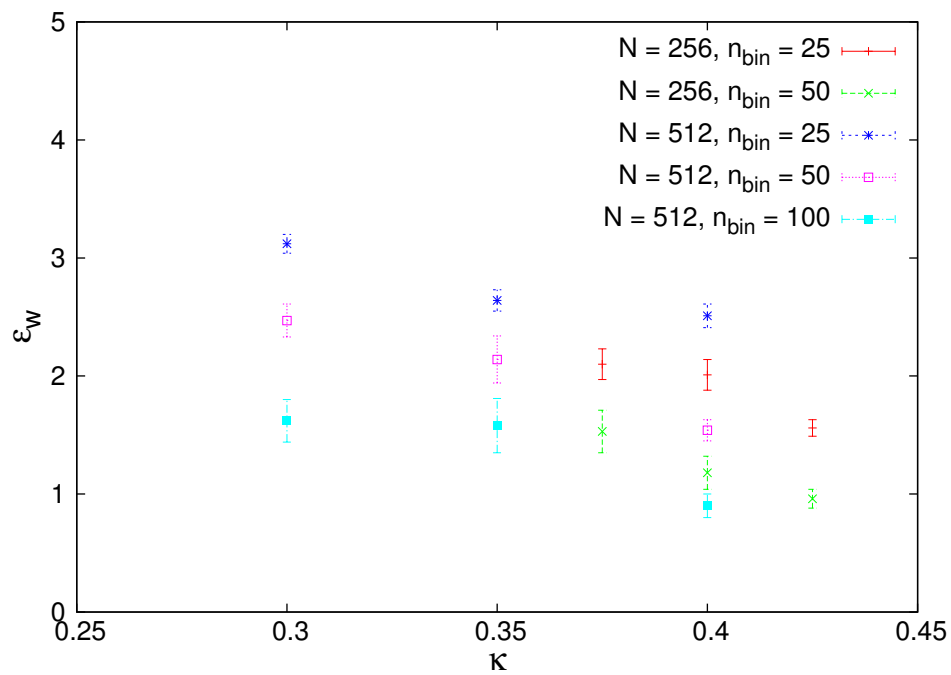


Figure 4.17: The numerical results of ϵ_w given by Eq. (4.83) for various values of κ , N , and n_{bin} . In the results with $N = 256$, we used the parameters $L = 15$, $\lambda = 1.0$, $\zeta = 3.0$, $\alpha = 2.0$, and $\tau_f = 8.0$.

grater than the lattice spacing Δx_{phys} might be marginally violated at the end of the simulation. It is not confident that our choice, $\delta_s/\Delta x_{\text{phys}} \simeq 1.07$ at the end of the simulation, is safe enough. To clarify this point, we performed the set of test simulations with smaller dynamical range and larger string width by tuning the grid size N and the box size L . We chose two set of parameters, $(N = 512, L = 10)$ and $(N = 256, L = 10)$, corresponding to the string width $\delta_s/\Delta x_{\text{phys}}|_{\tau=6} \simeq 4.27$ and 2.13 , respectively. Since the box size $L = 10$ is half of the full simulation with $L = 20$, we cannot run the simulation beyond the time $\tau = 6$, otherwise the condition on the Hubble radius described above Eq. (4.44) might be violated. In Fig. 4.18, we compare the results of these test simulations with the results found in simulations with larger dynamical range $(N = 512, L = 20)$. We confirmed that there is no dramatic change in results of the time evolution of scaling parameters, except that the error bars become slightly larger for the simulation with smaller dynamical range. This result quantitatively supports our supposition that the dynamical range does not much affect the results of the simulations. However, as we see in Fig. 4.18 (c), the result of the energy spectrum in the simulation with high resolution $(N = 512, L = 10)$ deviates from others at wavenumber $k \gtrsim 50$. This indicates that at wavenumber greater than $k \sim 50$ the result depends on the spatial resolution, but the result is robust at small wavenumber $k \lesssim 50$. We may overestimate the abundance of small scale modes, but it does not much affect the final results since their contribution is subdominant.

4.5 Axion production from long-lived domain walls

Next, let us consider the case with $N_{\text{DW}} > 1$. In this case, we also compute the spectrum of gravitational waves radiated from domain walls in addition to the spectrum of axions, since there is a speculation that long-lived domain walls lose their energy by radiating gravitational waves at the late time of their evolution [38, 142]. In Sec. 4.7, we will determine the amount of radiated axions and gravitational waves by using the spectra obtained in this section.

4.5.1 Production of axions

We computed the power spectrum of free axions from data of the scalar field obtained in three-dimensional simulations presented in Sec. 4.2.2. In the case with $N_{\text{DW}} > 1$, axions are continuously produced from stable domain walls in the scaling regime. Hence we must compute the spectrum of axions in the scaling regime, rather than that in the decay time t_d defined in the case with $N_{\text{DW}} = 1$.

Here, in order to compute the spectrum of axions produced from scaling domain wall networks, we modify some computational procedures from that used in the previous section. One modification is that we mask the position of the core of domain walls in addition to that of strings. This is because the core of domain walls becomes dominant source of contaminations for the spectrum of axions in the case with $N_{\text{DW}} > 1$. This situation is opposed to the case with $N_{\text{DW}} = 1$ (short-lived domain walls), where we did not mask the core of domain walls. The reason why we ignored the contamination from the core

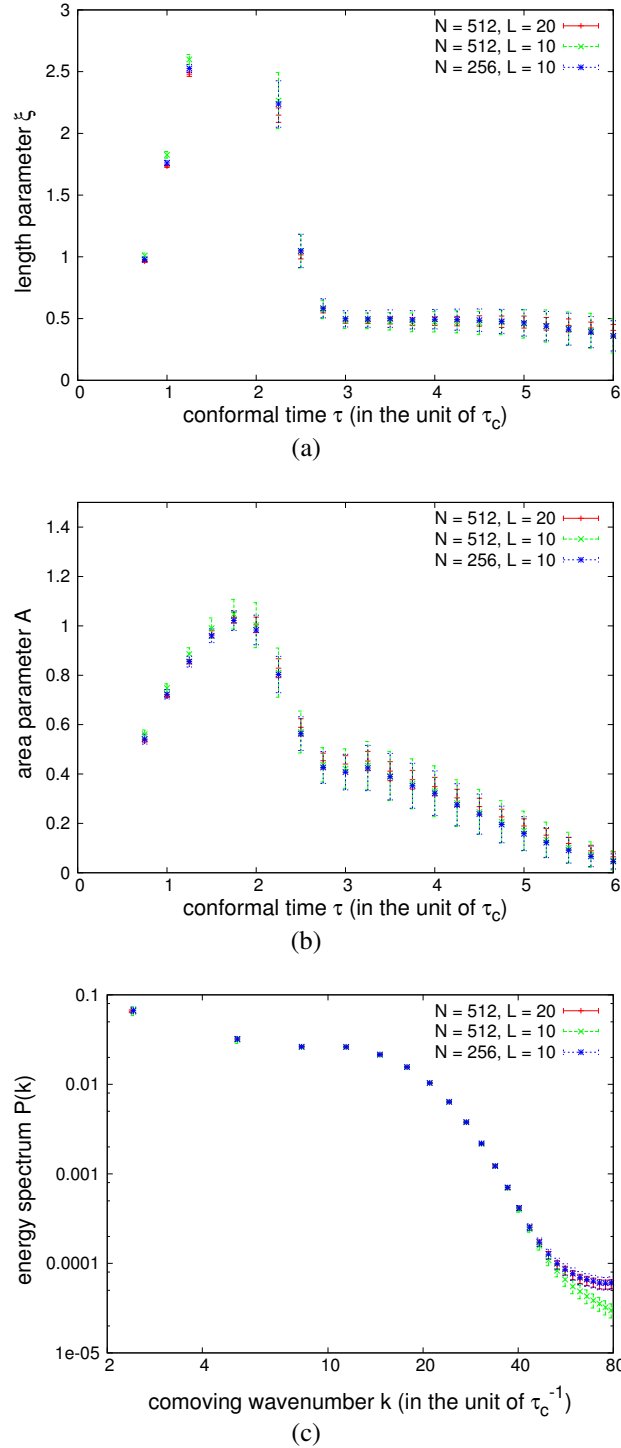


Figure 4.18: The comparison between simulations with larger dynamical range ($N = 512$, $L = 20$) and that with smaller dynamical range ($N = 512$, $L = 10$) and ($N = 256$, $L = 10$) on the result of (a) time evolution of the length parameter, (b) time evolution of the area parameter and (c) power spectrum of free axions evaluated at time t_1 with $n_{\text{bin}} = 25$. In these simulations, we choose the same set of parameters shown in Table 4.1 except that $\kappa = 0.4$. Note that we cannot calculate the difference of power spectrum $P_{\text{dec}}(k, t_d)$ and the mean momentum $\bar{k}(t_d)$, since the time t_d is beyond the final time in the simulation with smaller dynamical range.

of domain walls in the analysis of axion production from short-lived domain walls may be explained as follows. In the case with $N_{\text{DW}} = 1$, as described in the previous section, we compute the spectrum of radiated axions in two time slices t_1 and t_d . At $t = t_1$ (wall formation time), the energy of domain walls is smaller than that of strings, and hence the core of strings dominantly contaminates the power spectrum of axions. Furthermore, since the width of domain walls is comparable with the Hubble radius $\delta_w \simeq m_a^{-1} \sim t_1^{-1}$, it is impossible to identify domain walls as localized defect in this epoch. The effect of the core of domain walls is also ignored at $t = t_d$, since most of the walls disappeared at this time (recall that the decay time t_d was defined such that the area parameter of domain walls becomes less than $\mathcal{A} \lesssim 0.01$ at that time). On the other hand, in the case with $N_{\text{DW}} > 1$, the energy of walls becomes higher than that of strings at the late time of the simulation (we will explicitly confirm it later). At that time, the width of walls $\delta_w \simeq m_a^{-1}$ becomes sufficiently shorter than Hubble radius, and we can identify walls as localized defects. Therefore, the core of walls may contaminate the spectrum of radiated axions in the case with long-lived domain walls.

The other modification is that we compute the spectra at two time slices t_A and t_B where t_A and t_B are different from t_1 and t_d used in the analysis for the case with $N_{\text{DW}} = 1$, and subtract the spectrum obtained at t_A from that obtained at t_B in order to remove the contaminations from initial conditions. Since we are interested in the spectrum of axions radiated from domain walls in the scaling regime, we fix t_A at the time when the system begins to follow the scaling behavior. It is expected that the feature of the spectrum (such as the location of the peak) does not change once domain walls enter into the scaling regime, and the mean energy $\langle \omega_a \rangle$ of radiated axions does not depend on the choice of time t_B at which $\langle \omega_a \rangle$ is computed. We will confirm it by computing the spectra for various values of t_B .

Figure 4.19 shows the results for $P(k, t_f)$ for various values of N_{DW} evaluated at the final time of the simulation ($t_B = t_f$). We find that the spectrum has a peak around the momentum scale determined by the mass of the axion, $k/R(t_f) \sim m_a$, or $k \sim R(t_f)m_a \sim 2$. However, this peak does not seem to fall off, but makes a tail at higher momenta. This tail-like feature was also found in the spectrum of axions radiated from short-lived networks (see Fig. 4.14). Again, the appearance of this high-frequency tail can be understood in terms of the conjecture made in Refs. [54, 38, 55, 56]. The strings whose radius smaller than the horizon size quickly decay due to the tension of domain walls in the time scale comparable to (or less than) the Hubble time. This fast process does not change much the energy spectrum of the axion field composing the string configuration, which has a form $dE/dk \sim 1/k$ with a high-momentum cutoff of order δ_s^{-1} (the width of strings) and a low-momentum cutoff of order t^{-1} (the Hubble radius) [55]. This $1/k$ behavior makes a tail in the spectrum of radiated axions, as we see in Fig. 4.19. This argument cannot be applied for the spectrum of axions produced by global strings [57, 58], which has a sharp peak at the horizon scale since in the absence of domain walls the strings lose their energy in the time scale much longer than the Hubble time. The high-momentum cutoff which is given by the width of the string $\sim \delta_s^{-1}$ is not clearly shown in Fig. 4.19 because of the poor resolution at the final time of the simulation.

Note that the amplitude of the high-frequency tail becomes small if we increase the

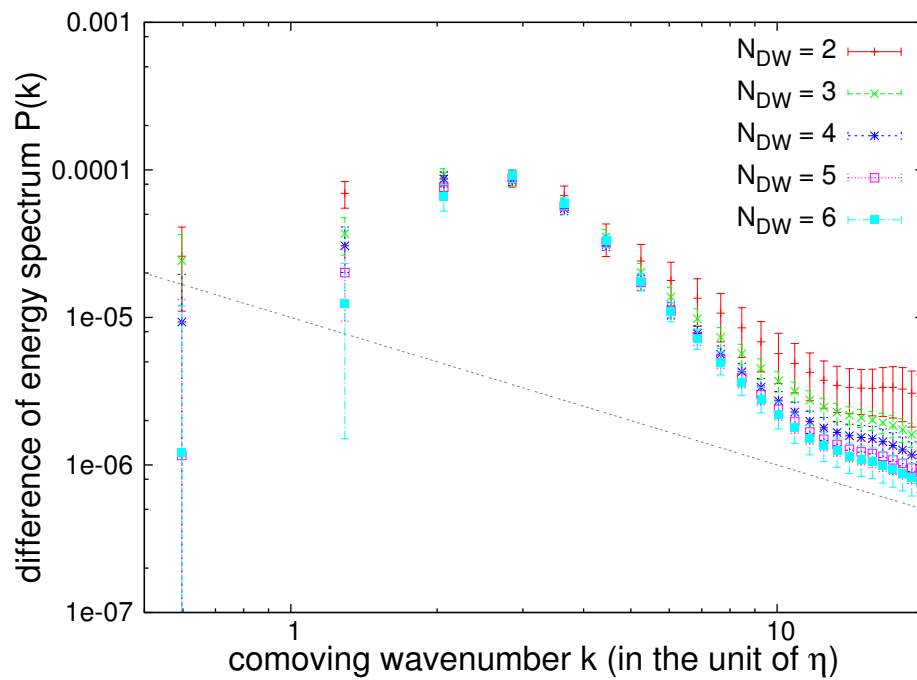


Figure 4.19: The spectra of axions produced by string-wall networks for various values of N_{DW} . These spectra are obtained by using the masking analysis method described in Appendix C.3. The dotted line represents the power law $P(k) \propto 1/k$. The spectrum shown in this figure is the difference of power spectra evaluated at two different time steps τ_A and τ_B [see Eqs. (C.38) and (C.39)]. Here, we choose $\tau_A = 14$ and $\tau_B = 40$.

domain wall number N_{DW} . In the case of large N_{DW} , the decay of loops of strings with small curvature radius might be “frustrated”, because of the tension of domain walls acting on the strings from various directions. Then, the radiation of hard axions with spectrum $\sim 1/k$ is suppressed, compared with the case of small N_{DW} .

We emphasize that our conclusion will be different from that made in [38] in support of [55, 56]. In Ref. [38] it was claimed that the spectrum of axions radiated by domain walls behaves as $\sim 1/k$ in the whole frequency domain, and hence the mean energy of radiated axions is proportional to $\ln(\sqrt{\lambda\eta}/m_a) \sim 60$, which suppresses the relic abundance of cold dark matter axions. Our result, however, shows that the spectrum does not behave like $\sim 1/k$ except for the high-frequency modes, and most axions are mildly relativistic, making a peak at the low frequency. This result supports the interpretation that most axions are produced by the self-interaction of domain walls whose width is given by the inverse of the mass of the axion $\sim m_a^{-1}$, which is different from the claim in [38] where axions are dominantly produced by the fast decay process of wall bounded by strings. Hence the mean energy of radiated axion is given by m_a , and there is no correction like $\ln(\sqrt{\lambda\eta}/m_a) \sim 60$. This fact implies that the relic abundance of axions becomes large compared with the result of [38] and leads to severe constraints on the axion models, as we will see in Sec. 4.7.

The above observation can be confirmed by estimating the energy of radiated axions. Roughly speaking, the product $P(k)k$ represents the fraction of the energy density of axions with comoving wavenumber k against the total energy of axions. Hence the ratio of the energy between hard axions which contribute to the tail of the power spectrum and the energy of axions which contribute to the peak of the power spectrum can be estimated as $\mathcal{E}_{\text{hard}}/\mathcal{E}_{\text{peak}} \sim [P(k_{\text{hard}})k_{\text{hard}}]/[P(k_{\text{peak}})k_{\text{peak}}] \sim [\mathcal{O}(10^{-6}) \times \mathcal{O}(10)]/[\mathcal{O}(10^{-4}) \times \mathcal{O}(1)] \sim 10^{-1}$. On the other hand, the ratio between the energy of domain walls and the energy of strings at the final time of the simulations becomes $\mathcal{E}_{\text{string}}/\mathcal{E}_{\text{wall}} \sim [t_f \mu_{\text{string}}]/[t_f^2 \sigma_{\text{wall}}] \sim 10^{-1}$. Therefore, strings have 10% of the energy of domain walls at the final time, which contributes to the hard component $\sim 1/k$ of the power spectrum of radiated axions. Since the fraction $\mathcal{E}_{\text{string}}/\mathcal{E}_{\text{wall}}$ decreases with time, we expect that the amplitude of the high-frequency tail would be negligible compared with the height of the peak of the spectrum if we follow the evolution for much larger dynamical ranges.

Since the population of the axions radiated by string-wall networks is dominated by low-momentum modes which has the frequency comparable to the mass of the axion m_a , we expect that the mean energy of radiated axions is determined by the parameter m_a . Here, using the result of $P(k, t_B)$, where t_B is chosen at the late time of the simulation [see Eq. (C.39)], we compute the mean comoving momentum of radiated axions

$$\bar{k}(t_B) \equiv \frac{\int \frac{dk}{2\pi^2} P(k, t_B)}{\int \frac{dk}{2\pi^2} \frac{1}{k} P(k, t_B)}, \quad (4.86)$$

and its ratio to the axion mass

$$\epsilon_a \equiv \frac{\bar{k}(t_B)/R(t_B)}{m_a}. \quad (4.87)$$

The results are shown in Table 4.5. We see that the value of the mean momentum is not strongly depend on the number N_{DW} . However, the uncertainty becomes large for the case

with large N_{DW} . This is because a large portion of the simulation box is masked when we evaluate the power spectrum, which causes a large systematic errors when we evaluate the spectrum in the large scale, as shown in Fig. 4.19.

Table 4.5: The values of mean comoving momentum \bar{k} and parameter ϵ_a defined in Eqs. (4.86) and (4.87) for various values of N_{DW} .

N_{DW}	\bar{k}	ϵ_a
2	2.38 ± 0.28	1.19 ± 0.14
3	2.38 ± 0.25	1.19 ± 0.12
4	2.63 ± 0.29	1.31 ± 0.15
5	2.97 ± 0.45	1.49 ± 0.22
6	3.07 ± 0.42	1.54 ± 0.21

The claim is that the parameter defined by Eq. (4.87) does not depend on the time t_B . To confirm it, we calculate the parameters \bar{k} and ϵ_a at different time steps, while fixing the reference time $\tau_A = 14$ in Eq. (C.39). The results are shown in table 4.6. We find that the value of \bar{k} changes proportionally to $R(t_B)$. On the other hand, the ratio ϵ_a between the *physical* momentum \bar{k}/R and the axion mass m_a remains constant. Therefore, we use the parameter ϵ_a as a constant of $\mathcal{O}(1)$ when we perform the analytic investigations in Sec. 4.7.

Table 4.6: The values of \bar{k} and ϵ_a evaluated at different times τ_B for the case with $N_{\text{DW}} = 3$.

τ_B	\bar{k}	ϵ_a
24	1.42 ± 0.22	1.19 ± 0.18
28	1.62 ± 0.13	1.15 ± 0.09
32	1.88 ± 0.19	1.18 ± 0.12
36	2.04 ± 0.22	1.13 ± 0.12
40	2.38 ± 0.25	1.19 ± 0.12

We close this subsection by showing Fig. 4.20, the time evolution of the total energy density of axions and topological defects in the simulation box. From this figure, we see that the domain wall networks evolve as $\rho_{\text{wall}} \sim 1/t$, or $\rho_{\text{wall}} \sim 1/\tau^2$ in conformal time. This behavior is expected from the property of the scaling solution, given by Eq. (4.14). We also find that the energy density of axions radiated by string-wall networks behaves similarly to that of topological defects at the late time. We will confirm this behavior in Sec. 4.7.1.

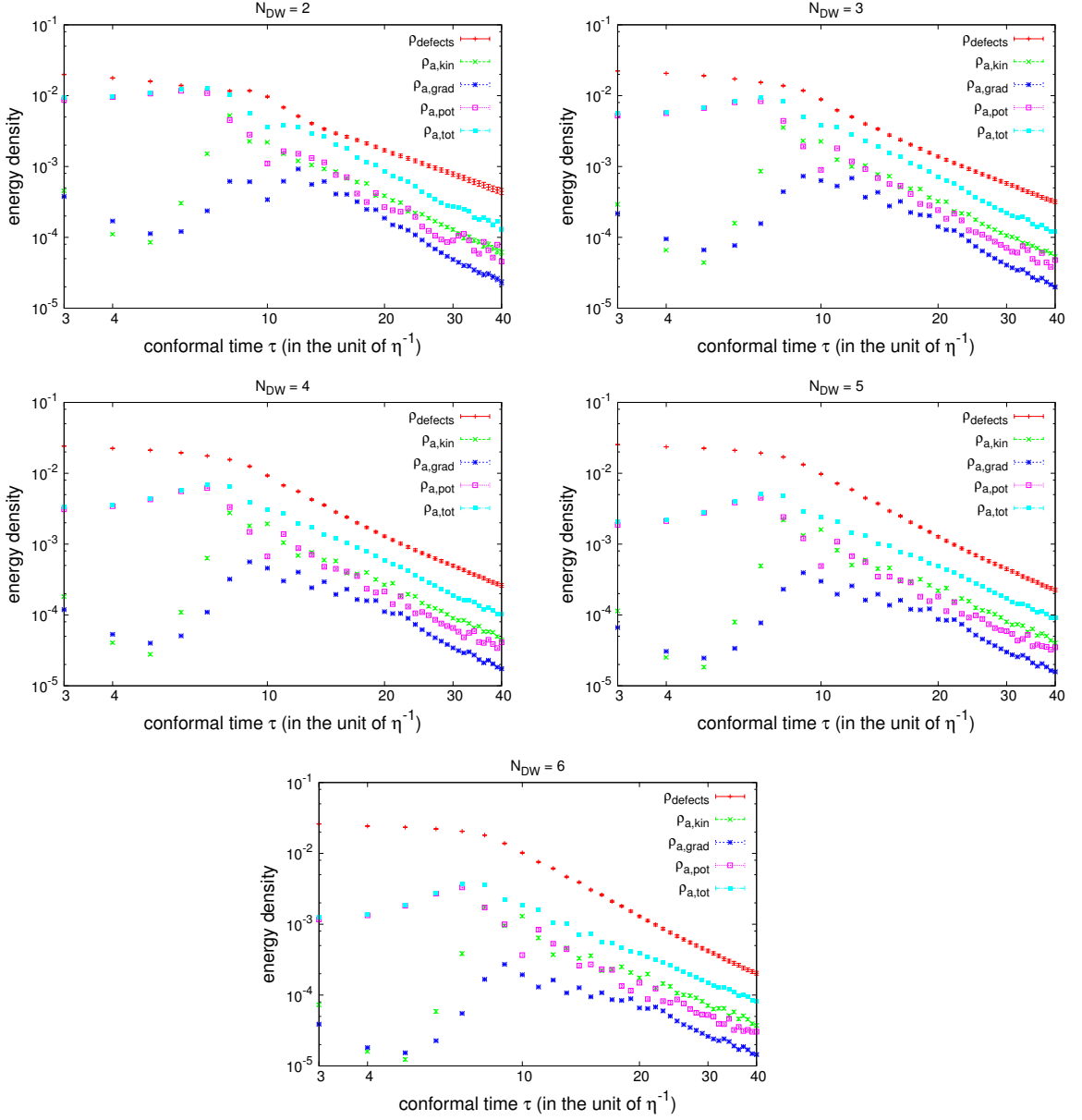


Figure 4.20: Time evolution of energy densities for various values of N_{DW} . ρ_{defects} represents the energy density of the string-wall networks which is evaluated by summing up the data of scalar field placed near the defects whose position is identified by using the algorithm described in Appendix C.2. $\rho_{a,\text{kin}}$, $\rho_{a,\text{grad}}$, and $\rho_{a,\text{pot}}$ are the kinetic, gradient, and potential energy density of radiated axions, respectively. $\rho_{a,\text{tot}}$ is the sum of $\rho_{a,\text{kin}}$, $\rho_{a,\text{grad}}$, and $\rho_{a,\text{pot}}$. These energy densities of axions are evaluated by subtracting the data of scalar field which contribute to ρ_{defects} .

4.5.2 Production of gravitational waves

Next, we investigate the production of gravitational waves from string-wall networks. The spectrum of gravitational waves is represented by the quantity

$$\Omega_{\text{gw}}(k, t) = \frac{1}{\rho_c(t)} \frac{d\rho_{\text{gw}}(k, t)}{d \ln k}, \quad (4.88)$$

where $\rho_c(t)$ is the critical density of the universe at the time t , and ρ_{gw} is the energy density of gravitational waves. We compute Ω_{gw} using the data of the scalar field Φ obtained from the numerical simulation. The method of the calculation is summarized in Appendix C.4.

Figure 4.21 shows the results for $\Omega_{\text{gw}}(k, t)$ for various values of N_{DW} . The slope of the spectrum changes at two characteristic scales. One is the Hubble radius ($k \sim 2\pi R(\tau_f)H(\tau_f) \sim 0.1$) and another is the width of the domain wall ($k \sim R(\tau_f)m_a \sim 2$). This result agrees with the general argument made in [169]. However, the amplitude of Ω_{gw} at high momenta is enhanced for the case with large N_{DW} . This can be interpreted as follows. Since the number of domain walls is large in the model with large N_{DW} , domain walls are “frustrated”, and there are many small scale configurations whose correlation length is shorter than the Hubble radius. Therefore, the small scale anisotropy becomes enhanced in the model with large domain wall number N_{DW} . We also plot the spectrum of gravitational waves produced by domain walls in the real scalar field theory given by Eqs. (4.63) and (4.64). Although the evolution of domain wall networks shown in Fig. 4.11 is similar between the model with $N_{\text{DW}} = 2$ and the model with real scalar field, the form of the spectrum of gravitational waves is slightly different between these two models at high momenta. This might be caused by the different form of the effective potential which determines the small scale structure of the defects.

As we see in Fig. 4.20, at the early times ($\tau \lesssim 15$) topological defects do not relax into the scaling regime. However, the nonlinear dynamics of scalar fields during this initial stage produces a “burst” of gravitational waves, which may contaminate the spectrum of gravitational waves produced at late times where the defect networks evolve along to the scaling solution. We subtract this contribution with the same manner that we used for the subtraction of axions produced at the initial stage [see Eq. (C.58)]. Figure 4.22 shows the time evolution of the spectrum of gravitational waves, where we compare the effect of this subtraction procedure. We see that the form of the spectrum is different at early times if we make a subtraction. In particular, there is a bump at the scale given by the Hubble radius $k/R \sim H$, and a plateau which falls off at the scale given by $k/R \sim m_a$. This form is different from that found in Refs. [165, 169], where a nearly “flat” spectrum extends between two characteristic scales. It seems that this difference in the form of spectra is caused by the contamination of radiations produced at the initial relaxation regime. We also note that the dynamical range of the past numerical studies ($\tau_f/\tau_i \simeq 12$) [165, 169] is shorter than that of the present studies ($\tau_f/\tau_i = 20$). Therefore, the bump-like feature is less apparent in the past numerical studies with shorter dynamical ranges. The form of the spectrum at the final time of the simulation is similar between the result with subtraction and that without subtraction, which indicates that contaminations of the initial stage are diluted due to the cosmic expansion.

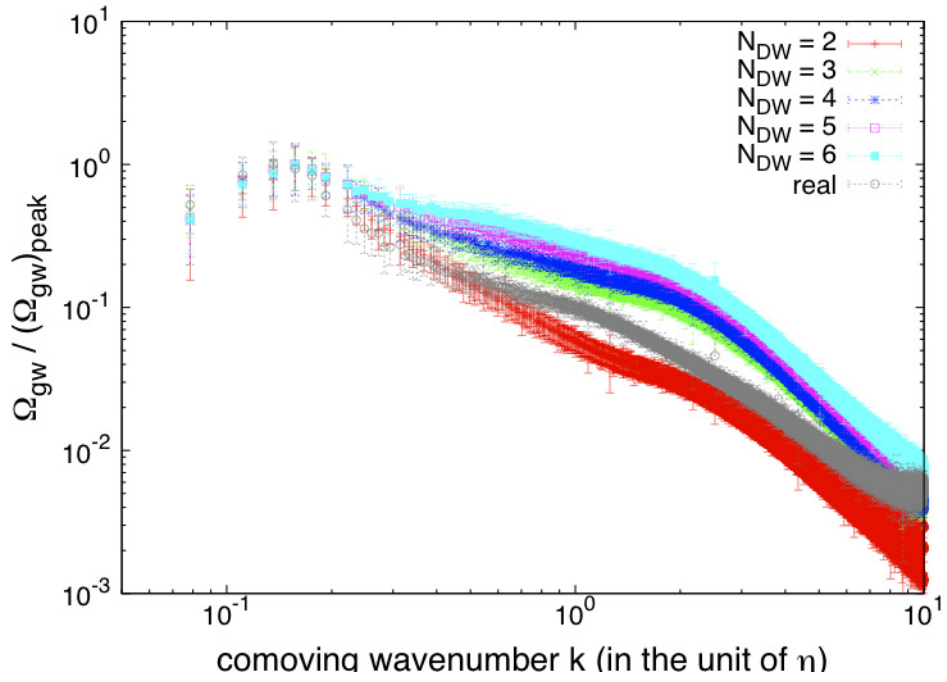


Figure 4.21: The spectra of gravitational waves for various values of N_{DW} . The plot denoted as “real” shows the spectrum of gravitational waves produced in the model with real scalar field defined by Eqs. (4.63) and (4.64). In this figure, we normalized the vertical axis by the amplitude at the peak momentum.

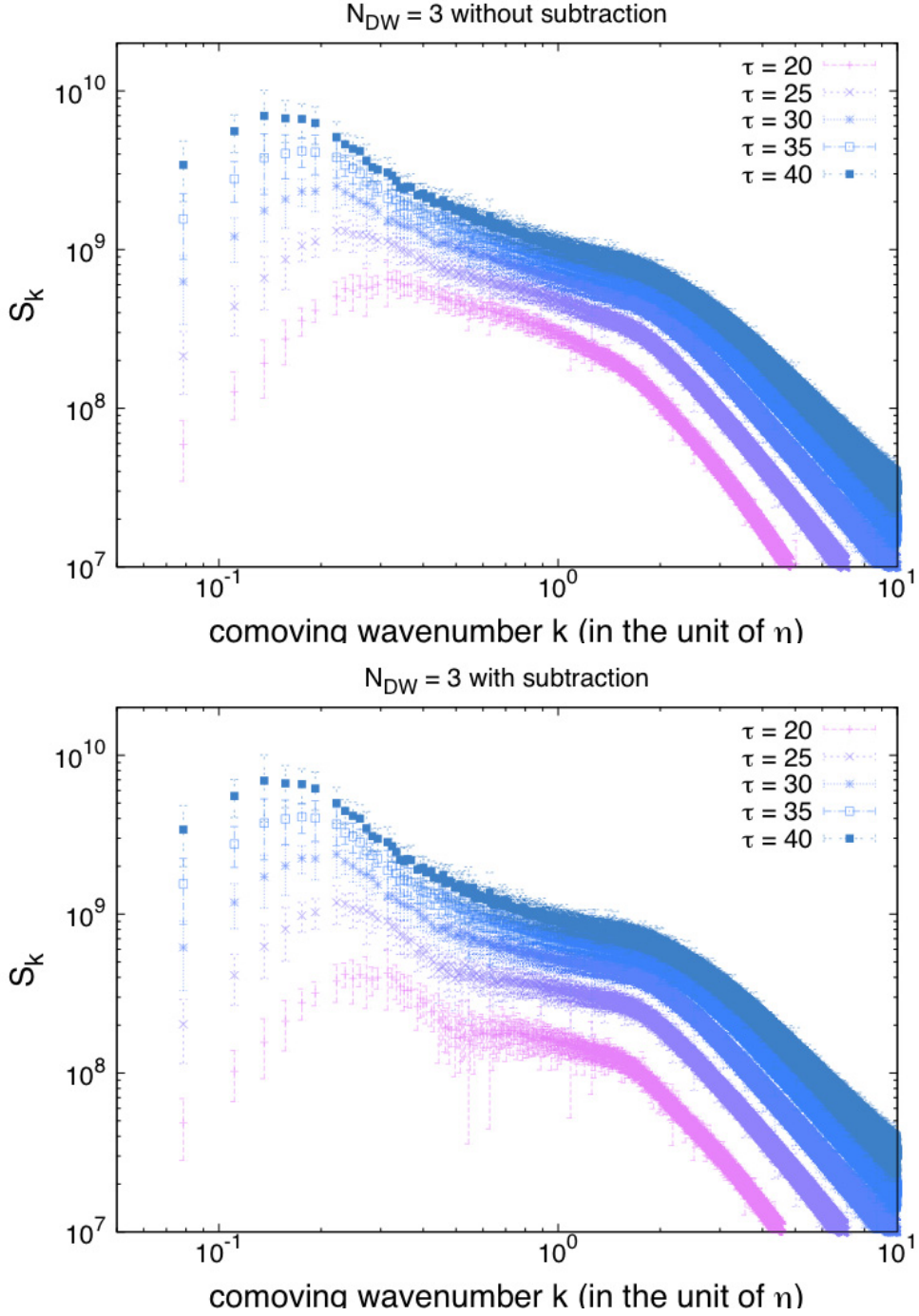


Figure 4.22: The time evolution of the spectrum of gravitational waves for the case with $N_{\text{DW}} = 3$. Here, we plot the function $S_k(\tau)$ defined by Eq. (C.56) (top panel) and $\Delta S_k(\tau)$ defined by Eq. (C.58) (bottom panel), which is proportional to Ω_{gw} in the radiation-dominated background. In the bottom panel, we subtract the contribution of gravitational waves produced before the time $\tau_g = 15$. The spectra are shown from the conformal time $\tau = 20$ (pink) to $\tau = 40$ (green) with the interval $\Delta\tau = 5$.

The spectrum shown in Fig. 4.21 is normalized in terms of the peak amplitude in order to give the relative form of the spectrum between different theoretical parameter N_{DW} . On the other hand, the total amplitude of gravitational waves is determined by the following arguments. Since the spectrum of gravitational waves has a peak at the momentum which is given by the Hubble scale, we regard that the most of the gravitational waves are generated at the length scale $\sim t$. Suppose that the radiation of gravitational waves occurs with the time scale comparable to the Hubble time. The power of gravitational waves radiated from domain walls is estimated by using the quadrupole formula [170]

$$P \sim G\ddot{Q}_{ij}\ddot{Q}_{ij}. \quad (4.89)$$

Here, $Q_{ij} \sim M_{\text{DW}}t^2$ is the quadrupole moment, and $M_{\text{DW}} \sim \rho_{\text{wall}}t^3 \sim \sigma_{\text{wall}}\mathcal{A}t^2$ is the mass energy of domain walls, where we used Eq. (4.51). The energy of gravitational waves is estimated as

$$E_{\text{gw}} \sim Pt \sim G\mathcal{A}^2\sigma_{\text{wall}}^2t^3. \quad (4.90)$$

We see that the energy density of gravitational waves does not depend on the time t

$$\rho_{\text{gw}} \sim E_{\text{gw}}/t^3 \sim G\mathcal{A}^2\sigma_{\text{wall}}^2. \quad (4.91)$$

Now, we define the efficiency ϵ_{gw} of gravitational waves

$$\rho_{\text{gw}}^{(\text{sim})} \equiv \epsilon_{\text{gw}}G\mathcal{A}^2\sigma_{\text{wall}}^2, \quad (4.92)$$

where $\rho_{\text{gw}}^{(\text{sim})}$ is the total energy density of gravitational waves computed from numerical simulations. We plot the time evolution of the parameter ϵ_{gw} in Fig. 4.23. Although the value of ϵ_{gw} does not remain in constant exactly, it seems to converge into a universal value of $\mathcal{O}(5-10)$.

We note that the time dependence of ϵ_{gw} is strongly affected by the choice of the time τ_g at which we subtract the contribution of gravitational waves produced in the initial relaxation regime [see Eq. (C.58)]. This is shown in Fig. 4.24, where we plot the time evolution of ϵ_{gw} for various values of τ_g . If we choose τ_g at an early time of the simulation, $\rho_{\text{gw}}^{(\text{sim})}$ contains the contribution of gravitational waves produced during the initial relaxation regime. Hence the behavior of $\rho_{\text{gw}}^{(\text{sim})}$ might be different from what we expect from Eq. (4.92), where we assumed that the energy density of domain walls is given by the scaling formula (4.51). This additional contribution is not negligible even at the late time of the simulations because the dynamical range of the numerical simulation is short. This constancy of ϵ_{gw} should be tested in future numerical studies with improved dynamical ranges. Since the time variation of ϵ_{gw} is small for the large value of τ_g , as shown in the plot of $\tau_g = 25$ in Fig. 4.24, we assume that ϵ_{gw} takes a constant value when string-wall networks enter into the scaling regime, and use the value $\epsilon_{\text{gw}} \simeq 5$ when we estimate the abundance of gravitational waves in Sec. 4.7.

4.6 Constraints for models with $N_{\text{DW}} = 1$

In this section, we calculate the abundance of dark matter axions produced from short-lived domain walls by using the result obtained in Sec. 4.4. Combining with other contributions,

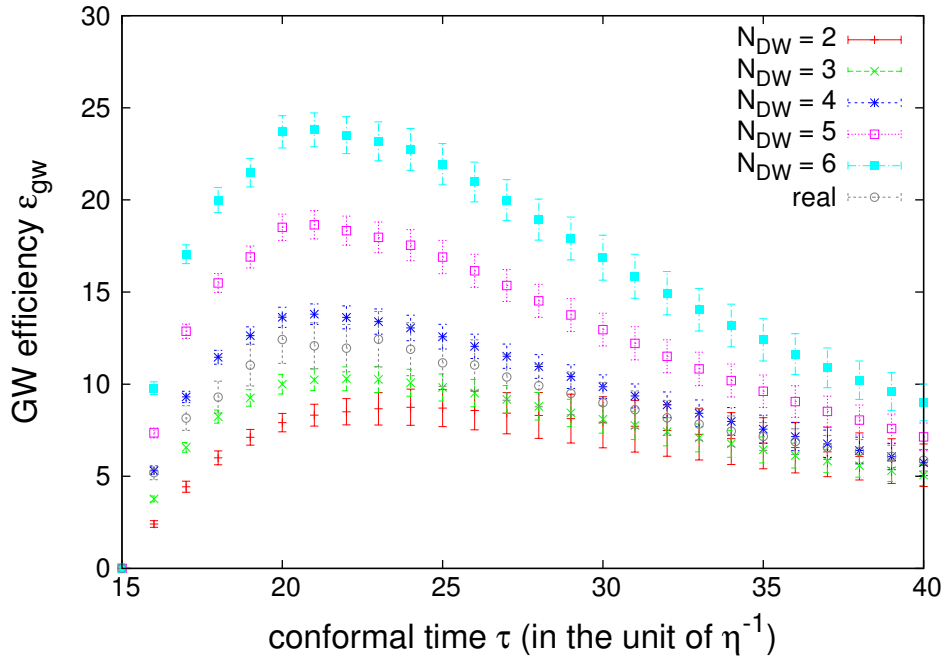


Figure 4.23: The time evolution of the efficiency parameter ϵ_{gw} defined by Eq. (4.92) for various values of N_{DW} . The points denoted as “real” show the evolution of ϵ_{gw} in the model with real scalar field defined by Eqs. (4.63) and (4.64). In this figure, we subtract the contribution of gravitational waves produced before the time $\tau_g = 15$.

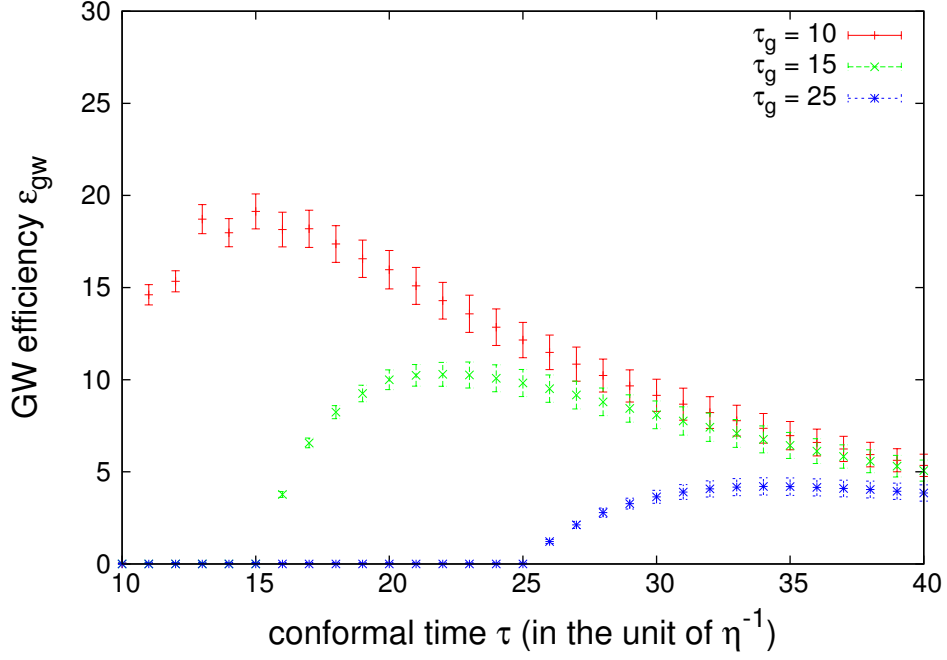


Figure 4.24: The time evolution of ϵ_{gw} and its dependence on the choice of τ_g . In this figure, we plot the result of the model with $N_{\text{DW}} = 3$.

we derive constraints for models with $N_{\text{DW}} = 1$ (scenario IIA).

Define the area parameter of domain walls at $t = t_1$

$$\mathcal{A}_1 \equiv \frac{\rho_{\text{wall}}(t_1)}{\sigma_{\text{wall}}(t_1)} t_1, \quad (4.93)$$

and the length parameter of strings at $t = t_1$

$$\xi_1 \equiv \frac{\rho_{\text{string}}(t_1)}{\mu_{\text{string}}(t_1)} t_1^2. \quad (4.94)$$

The string-wall networks begin to collapse around the time $t = t_1$. We simply assume that, after the time t_1 , the whole energy stored in these defects is diluted as $R^{-3}(t)$ due to the cosmic expansion

$$\rho_{\text{string-wall}}(t) = \left[\mathcal{A}_1 \frac{\sigma_{\text{wall}}(t_1)}{t_1} + \xi_1 \frac{\mu_{\text{string}}(t_1)}{t_1^2} \right] \left(\frac{R(t_1)}{R(t)} \right)^3 \quad \text{for } t > t_1. \quad (4.95)$$

Suppose that the decay completes at the time $t_d (> t_1)$. The number density of axions produced by the decay of string-wall networks is

$$\begin{aligned} n_{a,\text{dec}}(t) &= \frac{\rho_{\text{string-wall}}(t_d)}{\langle \omega_a \rangle} \left(\frac{R(t_d)}{R(t)} \right)^3 \\ &= \frac{1}{\sqrt{1 + \epsilon_w^2 m_a(t_d)}} \left[\mathcal{A}_1 \frac{\sigma_{\text{wall}}(t_1)}{t_1} + \xi_1 \frac{\mu_{\text{string}}(t_1)}{t_1^2} \right] \left(\frac{R(t_1)}{R(t)} \right)^3, \end{aligned} \quad (4.96)$$

where $\langle \omega_a \rangle = \sqrt{1 + \epsilon_w^2} m_a(t_d)$ is an average of the energy of radiated axions [see Eq. (4.85)].

The above expression does not depend on t_d except for the factor $1/m_a(t_d)$. Since the change in the mass of the axion can be negligible ($|\dot{m}_a/m_a^2| \simeq H/m_a < 1$) for $t > t_1$, we can approximate $m_a(t_d) \simeq m_a(t_1)$. Then, the present energy density of axions radiated after t_1 is given by

$$\rho_{a,\text{dec}}(t_0) = m_a(0)n_{a,\text{dec}}(t_0) = \frac{m_a(0)}{\sqrt{1 + \epsilon_w^2} m_a(t_1)} \left[\mathcal{A}_1 \frac{\sigma_{\text{wall}}(t_1)}{t_1} + \xi_1 \frac{\mu_{\text{string}}(t_1)}{t_1^2} \right] \left(\frac{R(t_1)}{R(t_0)} \right)^3. \quad (4.97)$$

The density parameter of axions radiated from the decay of defects is given by

$$\Omega_{a,\text{dec}} h^2 = 8.46 \times 10^{-2} \times \frac{13.8 \mathcal{A}_1 + 217 \xi_1}{\sqrt{1 + \epsilon_w^2}} \times \left(\frac{g_{*,1}}{70} \right)^{-(n+2)/2(n+4)} \left(\frac{F_a}{10^{12} \text{GeV}} \right)^{(n+6)/(n+4)} \left(\frac{\Lambda_{\text{QCD}}}{400 \text{MeV}} \right). \quad (4.98)$$

As we discussed in Sec. 4.2.1, we use the conservative estimations $\xi_1 \simeq 1.0 \pm 0.5$ and $\mathcal{A}_1 \simeq 0.50 \pm 0.25$. Also, discussion in Sec. 4.4 revealed that there are some ambiguities in the determination of ϵ_w . Here, we use the estimation $\epsilon_w \simeq 2 \pm 1$, taking account of various uncertainties in numerical calculations. Substituting these values, we finally obtain

$$\Omega_{a,\text{dec}} h^2 = (8.5 \pm 5.3) \times \left(\frac{g_{*,1}}{70} \right)^{-(n+2)/2(n+4)} \left(\frac{F_a}{10^{12} \text{GeV}} \right)^{(n+6)/(n+4)} \left(\frac{\Lambda_{\text{QCD}}}{400 \text{MeV}} \right). \quad (4.99)$$

Comparing Eq. (4.99) with Eqs. (3.47) and (4.79), we see that the contribution from domain wall decay is comparable with that from misalignment production and string decay. This result supports the conclusion of Refs. [48] and [140, 141].

The total abundance of cold dark matter axions is given by the sum of Eqs. (3.47), (4.79) and (4.99),

$$\begin{aligned} \Omega_{a,\text{tot}} h^2 &= \Omega_{a,0} h^2 + \Omega_{a,\text{string}} h^2 + \Omega_{a,\text{dec}} h^2 \\ &= (11.8 \pm 5.4) \times \left(\frac{g_{*,1}}{70} \right)^{-0.41} \left(\frac{F_a}{10^{12} \text{GeV}} \right)^{1.19} \left(\frac{\Lambda_{\text{QCD}}}{400 \text{MeV}} \right), \end{aligned} \quad (4.100)$$

where we used $n = 6.68$ according to [79]. The large uncertainty arises from the poor determination of the scaling parameter $\xi \simeq 1.0 \pm 0.5$ and the peak location in the spectrum of radiated axions $\epsilon_w \simeq 2 \pm 1$. The value of ξ might be fixed by developing the model of the evolution of global string networks, such as the study given by [163]. Also, future high-resolution simulations will resolve the uncertainty in ϵ_w . We require that $\Omega_{a,\text{tot}} h^2$ must not exceed the observed value of the abundance of the cold dark matter $\Omega_{\text{CDM}} h^2 = 0.11$ [6]. This gives an upper bound for the axion decay constant

$$F_a \lesssim (1.4\text{-}3.3) \times 10^{10} \text{GeV}, \quad (4.101)$$

if we take $g_{*,1} = 70$ and $\Lambda_{\text{QCD}} = 400 \text{MeV}$. This bound is severer than Eq. (3.48), which is obtained by considering only the contribution of coherent oscillations. We note that

the other group [79] already reported another bound $F_a \lesssim 3.2_{-2}^{+4} \times 10^{10} \text{GeV}$ as severe as obtained here, although they considered only the contribution of axionic strings. We believe that this severity would come from the larger scaling parameter $\xi \approx 13$ used in their analysis than our numerical prediction $\xi \approx 1$, which overestimates the relic abundance of axions radiated by strings. In this sense, we regard that the axion string constraint is milder than that indicated by Eq. (4.101).

As we mentioned in Sec. 2.5.4, there is a lower bound $F_a \gtrsim 10^9 \text{GeV}$ which comes from astrophysical observations. Combining this lower bound with the bound (4.101), we conclude that axion models are constrained into the narrow parameter region $F_a \simeq 10^9$ - 10^{10}GeV , which corresponds to the axion mass $m_a \simeq 10^{-3}$ - 10^{-2}eV .

4.7 Constraints for models with $N_{\text{DW}} > 1$

In this section, we give constraints on the parameters of axion models with long-lived domain walls (scenario IIB), using the results of numerical studies described in Secs. 4.2.2 and 4.5. First, we calculate the relic abundance of cold axions and gravitational waves produced by string-wall networks in Sec. 4.7.1. In Sec. 4.7.2, constraint on the magnitude of the bias parameter is described. In Sec. 4.7.3, we combine various observational constraints, and discuss their implications on the models with $N_{\text{DW}} > 1$. We find that the overabundance of the cold axions produced by domain walls gives a stringent bound on the model parameters, which excludes the most part of models, except for tiny loopholes. Finally we comment on some exceptions in Sec. 4.7.4.

4.7.1 Axion cold dark matter abundance

The relic abundance of axions produced from long-lived domain walls can be estimated similarly as to how we did with Sec. 4.3. Here we assume that the energy of strings becomes negligible compared with that of domain walls, and axions and gravitational waves are only produced by domain walls. In this approximation, the evolution of energy densities for domain walls, axions, and gravitational waves is described by the following coupled equations

$$\frac{d\rho_{\text{wall}}}{dt} = -H\rho_{\text{wall}} - \left. \frac{d\rho_{\text{wall}}}{dt} \right|_{\text{emission}}, \quad (4.102)$$

$$\frac{d\rho_a}{dt} = -3H\rho_a + \frac{d\rho_{w \rightarrow a}}{dt}, \quad (4.103)$$

$$\frac{d\rho_{\text{gw}}}{dt} = -4H\rho_{\text{gw}} + \frac{d\rho_{w \rightarrow g}}{dt}, \quad (4.104)$$

where

$$\left. \frac{d\rho_{\text{wall}}}{dt} \right|_{\text{emission}} = \frac{d\rho_{w \rightarrow a}}{dt} + \frac{d\rho_{w \rightarrow g}}{dt} \quad (4.105)$$

is the rate of radiation from domain walls. Following from Eqs. (4.51) and (4.92), we put an ansatz on the behavior of the energy densities of domain walls and gravitational waves

$$\rho_{\text{wall}} = \mathcal{A} \frac{\sigma_{\text{wall}}}{t}, \quad \text{and} \quad \rho_{\text{gw}} = \epsilon_{\text{gw}} G \mathcal{A}^2 \sigma_{\text{wall}}^2, \quad (4.106)$$

where \mathcal{A} and ϵ_{gw} are constants. Substituting these expressions to the above equations, we obtain

$$\left. \frac{d\rho_{\text{wall}}}{dt} \right|_{\text{emission}} = \mathcal{A} \frac{\sigma_{\text{wall}}}{2t^2}, \quad (4.107)$$

$$\frac{d\rho_{w \rightarrow g}}{dt} = 2\epsilon_{\text{gw}} \frac{G \mathcal{A}^2 \sigma_{\text{wall}}^2}{t}. \quad (4.108)$$

From Eqs. (4.105), (4.107), and (4.108), we find

$$\frac{d\rho_{w \rightarrow a}}{dt} = \mathcal{A} \frac{\sigma_{\text{wall}}}{2t^2} - 2\epsilon_{\text{gw}} \frac{G \mathcal{A}^2 \sigma_{\text{wall}}^2}{t}. \quad (4.109)$$

Note that the sign of the right hand side of this equation becomes negative for $t \gtrsim (G\sigma_{\text{wall}})^{-1}$. This is not problematic, since domain walls have to collapse before the time $t \sim (G\sigma_{\text{wall}})^{-1}$ otherwise they overclose the universe [see Eq. (4.16)].

Let us define the energy and number of axions per comoving box

$$E_{a,\text{dec}}(t) \equiv R^3(t) \rho_a(t), \quad (4.110)$$

$$N_{a,\text{dec}}(t) \equiv R^3(t) n_a(t), \quad (4.111)$$

where $n_a(t)$ is the number density of axions at the time t . Integrating Eqs. (4.103) and (4.109), we find

$$E_{a,\text{dec}}(t) = \int_{t_1}^t dt' R^3(t') \left[\frac{\mathcal{A} \sigma_{\text{wall}}}{2} t'^{-2} - 2\epsilon_{\text{gw}} G \sigma_{\text{wall}}^2 \mathcal{A}^2 t'^{-1} \right], \quad (4.112)$$

where t_1 is the time when domain walls begin to radiate axions, which might be chosen as the time of the QCD phase transition. In the regime $t \gg t_1$, it reduces to

$$E_{a,\text{dec}}(t) \simeq R^3(t) \left(\mathcal{A} \frac{\sigma_{\text{wall}}}{t} - \frac{4}{3} \epsilon_{\text{gw}} G \sigma_{\text{wall}}^2 \mathcal{A}^2 \right). \quad (4.113)$$

For sufficiently early times $t \ll (G\sigma_{\text{wall}})^{-1}$, the first term of Eq. (4.113) dominates over the second term, which leads to the behavior $\rho_a \propto 1/t$. This agrees with what we observed in numerical simulations, shown in Fig. 4.20. The ratio between $E_{a,\text{dec}}(t)$ and $N_{a,\text{dec}}(t)$ can be determined by the result of numerical simulations

$$\frac{E_{a,\text{dec}}(t)}{N_{a,\text{dec}}(t)} = \sqrt{1 + \epsilon_a^2} m_a, \quad (4.114)$$

where ϵ_a is defined by Eq. (4.87). Suppose that domain walls disappear at the time t_{dec} and the radiation of axions and gravitational waves is terminated at that time. In this case, the energy densities of axions and gravitational waves at the present time t_0 are given by

$$\begin{aligned}\rho_{a,\text{dec}}(t_0) &= \frac{m_a N_{a,\text{dec}}(t_{\text{dec}})}{R^3(t_0)} \\ &= \frac{1}{\sqrt{1 + \epsilon_a^2}} \left(\frac{R(t_{\text{dec}})}{R(t_0)} \right)^3 \left(\mathcal{A} \frac{\sigma_{\text{wall}}}{t_{\text{dec}}} - \frac{4}{3} \epsilon_{\text{gw}} G \sigma_{\text{wall}}^2 \mathcal{A}^2 \right),\end{aligned}\quad (4.115)$$

$$\rho_{\text{gw}}(t_0) = \left(\frac{R(t_{\text{dec}})}{R(t_0)} \right)^4 \epsilon_{\text{gw}} G \mathcal{A}^2 \sigma_{\text{wall}}^2. \quad (4.116)$$

The annihilation of domain walls occurs in the time scale estimated by Eq. (4.62)

$$t_{\text{dec}} = \frac{k_d^2}{4} \left(\frac{m_a}{N_{\text{DW}} \Xi \eta^2} \right), \quad (4.117)$$

where k_d is given by Eq. (4.61). Note that the relation

$$\frac{R(t_{\text{dec}})}{R(t_0)} = 6.43 \times 10^{-10} \times k_d N_{\text{DW}}^{-3/2} \left(\frac{10^{10} \text{GeV}}{F_a} \right)^{3/2} \left(\frac{10^{-58}}{\Xi} \right)^{1/2}. \quad (4.118)$$

Substituting Eqs. (4.117) and (4.118) into Eqs. (4.115) and (4.116), we obtain the density parameter of axions and gravitational waves

$$\begin{aligned}\Omega_{a,\text{dec}}(t_0) h^2 &= \frac{\rho_{a,\text{dec}}(t_0)}{\rho_c(t_0)/h^2} \\ &= 1.68 \times \frac{k_d^3 \mathcal{A}}{\sqrt{1 + \epsilon_a^2}} N_{\text{DW}}^{-3/2} \left(\frac{10^{-58}}{\Xi} \right)^{1/2} \left(\frac{10^{10} \text{GeV}}{F_a} \right)^{1/2} \\ &\quad \times \left[1 - 5.35 \times 10^{-3} \times \epsilon_{\text{gw}} \mathcal{A} N_{\text{DW}}^{-3} \left(\frac{10^{-58}}{\Xi} \right) \left(\frac{10^{10} \text{GeV}}{F_a} \right)^2 \right],\end{aligned}\quad (4.119)$$

$$\begin{aligned}\Omega_{\text{gw}}(t_0) h^2 &= \frac{\rho_{\text{gw}}(t_0)}{\rho_c(t_0)/h^2} \\ &= 4.33 \times 10^{-12} \times k_d^4 \epsilon_{\text{gw}} \mathcal{A}^2 N_{\text{DW}}^{-6} \left(\frac{10^{-58}}{\Xi} \right)^2 \left(\frac{10^{10} \text{GeV}}{F_a} \right)^4,\end{aligned}\quad (4.120)$$

We can fix the numerical values of k_d , \mathcal{A} , ϵ_a and ϵ_{gw} from the results of numerical simulations. Then, the relic abundance of axions and gravitational waves is determined by three theoretical parameters: N_{DW} , Ξ , and F_a . The second term in the square bracket in Eq. (4.119) represents the effect of gravitational radiation, which is negligible at early times but becomes relevant when domain walls survive for a long time. In particular, when domain wall survives enough time such that they overclose the universe, $t_{\text{dec}} \sim (G\sigma_{\text{wall}})^{-1}$, the contribution of the second term in the square bracket in Eq. (4.119) becomes $\mathcal{O}(1)$. In such a case, the gravitational field around walls cannot be regarded as a small perturbation [40], and we must use the full general relativistic treatment, which is out of the scope of

this work. Hence, the expression (4.119) is valid only for the time $t \ll t_{\text{WD}} \sim (G\sigma_{\text{wall}})^{-1}$. This condition is automatically satisfied as long as we consider the parameter region where domain walls do not overclose the universe.

The total abundance of cold dark matter axions is given by the sum of the coherent oscillation [Eq. (3.47)], the string decay [Eq. (4.79)] and the domain wall decay [Eq. (4.119)],

$$\Omega_{a,\text{tot}}h^2 = \Omega_{a,0}h^2 + \Omega_{a,\text{string}}h^2 + \Omega_{a,\text{dec}}h^2. \quad (4.121)$$

where

$$\Omega_{a,0}(t_0)h^2 \simeq 1.2 \times \left(\frac{F_a}{10^{12}\text{GeV}} \right)^{1.19}, \quad (4.122)$$

$$\Omega_{a,\text{string}}(t_0)h^2 \simeq 2.0 \times \left(\frac{F_a}{10^{12}\text{GeV}} \right)^{1.19}. \quad (4.123)$$

In the above expressions, we fixed the QCD scale such that $\Lambda_{\text{QCD}} = 400\text{MeV}$. Again, we require that $\Omega_{a,\text{tot}}h^2$ should not exceed the observed value of the abundance of cold dark matter $\Omega_{\text{CDM}}h^2 = 0.11$. This gives an upper bound on F_a and a lower bound on Ξ .

4.7.2 Neutron electric dipole moment

Next, we consider the effect of the Ξ term on the degree of strong CP-violation, following Refs. [42, 43, 45, 44]. As we described in Sec. 2.1, the recent experimental bound on the NEDM requires

$$\bar{\theta} < 0.7 \times 10^{-11}. \quad (4.124)$$

The original idea of Peccei and Quinn is to set $\bar{\theta} = 0$ by introducing a symmetry [11, 12]. However, if the additional term (4.17) exists in the effective potential, it shifts the CP-conserving minimum with a magnitude controlled by the parameters Ξ and δ .

Substituting the parametrization $\Phi = \eta e^{ia/\eta}$ into the effective potential given by Eqs. (4.8) and (4.17), and expanding for small a/η , we obtain the effective potential for a

$$V(a) \simeq \frac{1}{2}m_{\text{phys}}^2 a^2 - m_{\text{phys}}^2 F_a \bar{\theta} a, \quad (4.125)$$

where m_{phys} is the effective mass of the axion

$$m_{\text{phys}}^2 = m_a^2 + m_*^2 \equiv m^2 + 2\Xi N_{\text{DW}}^2 F_a^2 \cos \delta, \quad (4.126)$$

and $\bar{\theta}$ is the shifted minimum

$$\bar{\theta} = \frac{\langle a \rangle}{F_a} = \frac{2\Xi N_{\text{DW}}^3 F_a^2 \sin \delta}{m_a^2 + 2\Xi N_{\text{DW}}^2 F_a^2 \cos \delta}. \quad (4.127)$$

Requiring that this should not exceed the experimental bound (4.124), we obtain an upper bound for Ξ .

4.7.3 Implication for models

In Fig. 4.25, we plot the observational constraints described in the previous subsections. Based on the estimation given by Eq. (4.121), we find that the overabundance of cold axions gives a stringent lower bound on the bias parameter, $\Xi \gtrsim 10^{-50}-10^{-52}$. This lower bound is much stronger than that obtained from the overclosure of domain walls (4.21). Combined with the NEDM constraint, it completely excludes the parameter region if we assume that the phase δ of the bias term (4.17) is $\mathcal{O}(1)$. This bound might be weakened if we assume the extremely small value of δ , but this assumption spoils the genius of the original PQ solution to the strong CP problem. We must fine-tune δ in order to solve the fine-tuning problem of $\bar{\theta}$.

We find that the amplitude of gravitational waves produced by domain walls is weak $\Omega_{\text{gw}}h^2 \lesssim 10^{-20}$ in the parameter space considered above. This is irrelevant to any observations, since even the ultimate phase of DECIGO [171], which is a space-borne interferometer planned to launch in the future, will have a sensitivity $\Omega_{\text{gw}}h^2 \sim 10^{-18}$ [172]. The weakness of the signal of gravitational waves is due to the fact that domain walls annihilate in early epoch in order to avoid the overclosure of axions produced from them, and the dilution factor of cosmic expansion becomes large.

From the results shown in Fig. 4.25, we conclude that the axion models with $N_{\text{DW}} > 1$ are excluded if the PQ symmetry is broken after inflation. The exception is the case in which the value of δ is suppressed. Note that the degree of tuning in δ to avoid observational constraints is affected by uncertainty in k_d used in Eq. (4.119). As we discussed in Sec. 4.2.2, results for k_d vary due to unphysical nature of the numerical simulation. Taking into account of this uncertainty, we obtain critical value of δ as $\delta_{\text{crit}} = 0.023-0.006$ which corresponds to $k_d = 7.5-9.5$ [see Eq. (4.61)]. If δ is smaller than this value, there are still allowed regions in $F_a-\Xi$ parameter space. By using Eqs. (4.119) and (4.127), one can show that this degree of tuning does not strongly depend on the value of N_{DW} . Hence, about $\mathcal{O}(1-0.1)\%$ fine-tuning is required regardless of the value of N_{DW} .

4.7.4 Scenario with extremely small δ

Although there is no theoretical reason to consider the extremely small value of δ , it is possible, by accident or design of some fundamental physics, to yield δ whose value is small enough to avoid the NEDM bound. Let us comment on such a situation. In this case, the value of Ξ can take larger value than that we considered so far. In particular, if Ξ becomes as large as

$$\Xi > 2 \times 10^{-45} N_{\text{DW}}^{-2} \left(\frac{10^{10} \text{GeV}}{F_a} \right)^4, \quad (4.128)$$

the axion mass is not determined by QCD instanton effect, but by the correction term m_* [see Eq. (4.126) and also Ref. [44]]. Then, the cosmological history is significantly modified.

When the condition (4.128) is satisfied, the magnitude of the bias term (4.17) exceeds that of the QCD potential (4.8). Hence, ‘‘domain walls’’ with the tension $\sigma_{\text{wall}} \simeq 8m_*F_a^2$ are formed when the Hubble parameter becomes $H \simeq m_*$. The subsequent history is

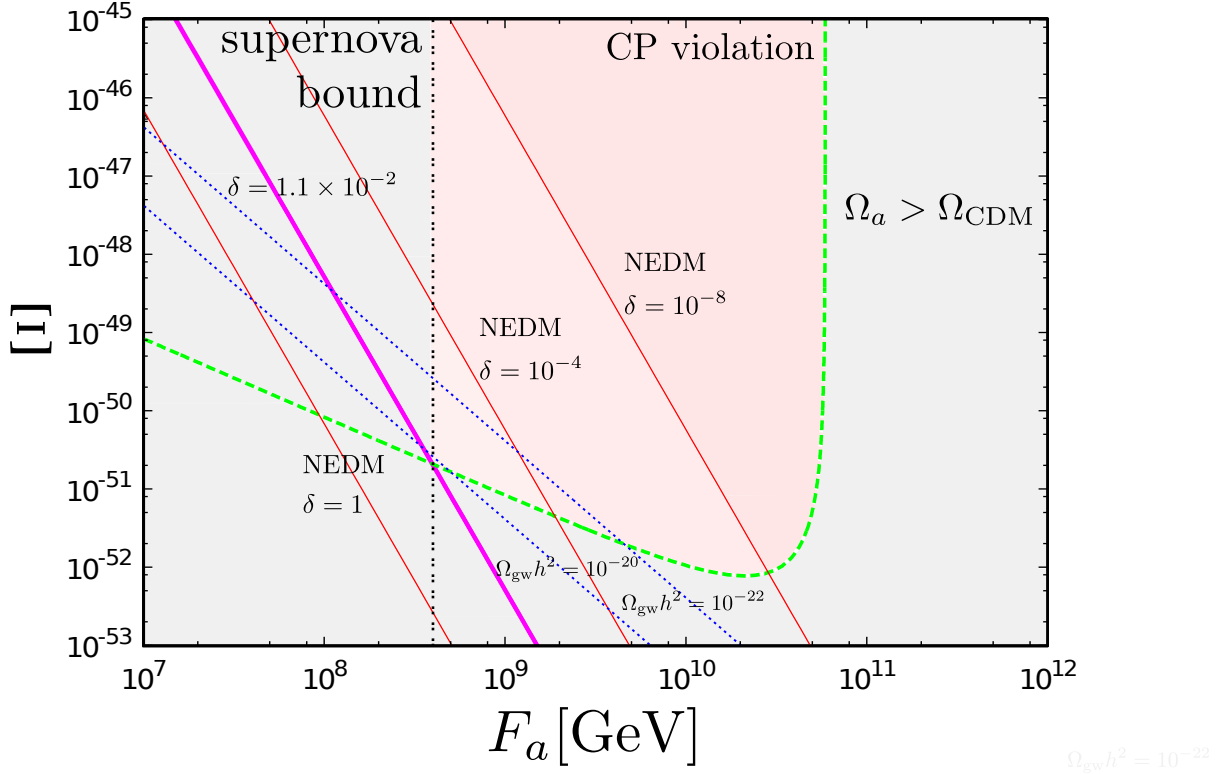


Figure 4.25: The various observational constraints in the parameter space of F_a and Ξ . The green dashed-line represents the parameter region estimated by Eq. (4.121) where $\Omega_a = \Omega_{\text{CDM}}$ is satisfied, and the region below this line is excluded since the relic abundance of axions exceeds the cold dark matter abundance observed today. The vertical dotted-line represents the bound given by Eq. (2.68) which comes from the observation of supernova 1987A. The red solid-lines represent the NEDM bound given by Eqs. (4.124) and (4.127) for $\delta = 1, 10^{-4}$, and 10^{-8} . The region above these lines is excluded since it leads to an experimentally unacceptable amount of CP-violation. The pink line represents the NEDM bound for the critical value $\delta_{\text{crit}} = 1.1 \times 10^{-2}$ for $k_d = 8.5$. There are still allowed regions if the value of δ is smaller than this critical value. The blue dotted-lines represent the parameter regions on which the amplitude of gravitational waves, given by Eq. (4.120), becomes $\Omega_{\text{gw}} h^2 = 10^{-20}$ and 10^{-22} . In this figure, we fixed other parameters as $N_{\text{DW}} = 6$, $k_d = 8.5$, $\epsilon_a = 1.5$, $\mathcal{A} = 2.6$, and $\epsilon_{\text{gw}} = 5$.

categorized into two possibilities, analogously to the scenarios described in Sec. 4.1. One possibility is that strings are get attached by domain walls at the time $t \sim m_*$, and they quickly disappear due to the tension of walls. Let us call this scenario case (a). On the other hand, if the structure of the term (4.17) is the form $\propto \Phi^n$, where n is an integer, n domain walls are attached to strings, and they survive for a long time. Let us call this scenario case (b). These string-wall networks annihilate due to the effect of a ‘‘bias’’ term which arises from the QCD instanton effect, $\delta V \sim \Lambda_{\text{QCD}}^4 \sim m_a^2 F_a^2$. This occurs at the time $t_{\text{dec},*} \sim \sigma_{\text{wall}}/\Lambda_{\text{QCD}}^4 \sim 8m_*/m_a^2$. Requiring that domain walls should disappear before the epoch of big bang nucleosynthesis (BBN), $t_{\text{dec},*} < t_{\text{BBN}} \sim 1\text{sec}$, we obtain

$$\Xi < 2 \times 10^{-23} \times N_{\text{DW}}^{-2} \left(\frac{F_a}{10^{10}\text{GeV}} \right)^{-6}. \quad (4.129)$$

In case (a), the abundance of axions is estimated in the usual way, as a sum of the coherent oscillation, strings, and decay of domain walls bounded by strings. The number of axions is fixed at $t \sim t_* \equiv m_*^{-1}$. At that time, the energy density of axions is given by $\rho_a(t_*) \sim 10 \times m_*^2 F_a^2$, where the factor 10 arises from the fact that the abundance of axions becomes larger by an order of magnitude if we include the contribution of strings and domain walls (see Sec. 4.6). The present energy density becomes $\rho_a(t_0) \sim 10(R(t_*)/R(t_0))^3 m_*^2 F_a^2$, which leads

$$\Omega_{a(\text{case (a)})}^{\text{nt}} h^2 \simeq 1.3 \times 10^{-5} \times N_{\text{DW}}^{1/2} \left(\frac{\Xi}{10^{-45}} \right)^{1/4} \left(\frac{F_a}{10^{10}\text{GeV}} \right)^{5/2}, \quad (4.130)$$

where the subscript ‘‘nt’’ indicates that they are produced non-thermally.

Axions are also produced from thermal bath of the primordial plasma (see Sec. 3.1). The difference from the usual scenario is that the axion mass is given by m_* so that their relic energy density can be large. The number of axions is fixed when their interactions with the thermal bath with the process mediated by gluons freeze out. Their number at the present time is given by $^{10} n_a^{\text{th}}(t_0) \simeq 7.8\text{cm}^{-3}$, which leads

$$\Omega_a^{\text{th}} h^2 \simeq 3.3 \times 10^{-7} \times N_{\text{DW}} \left(\frac{F_a}{10^{10}\text{GeV}} \right) \left(\frac{\Xi}{10^{-45}} \right)^{1/2}, \quad (4.131)$$

where the subscript ‘‘th’’ indicates that they are produced thermally. For sufficiently large value of Ξ , the contribution of thermal component (4.131) exceeds the non-thermal component (4.130). Requiring that it should not exceed the present cold dark matter abundance $\Omega_a^{\text{th}} h^2 < 0.11$, we obtain

$$\Xi < 1.1 \times 10^{-34} \times N_{\text{DW}}^{-2} \left(\frac{F_a}{10^{10}\text{GeV}} \right)^{-2} \quad \text{for case (a)}. \quad (4.132)$$

¹⁰Here, we assume that the interaction with gluons is determined by the $aG\tilde{G}$ vertex in the effective Lagrangian (2.28), while the axion mass is given by m_* . In this case, Eq. (3.21) can be applied. Note that this estimation is applicable only if the value of F_a satisfies the condition (3.16).

On the other hand, in case (b), axions are copiously produced from long-lived domain walls. The relic abundance of axions produced by domain walls can be estimated by using the argument analogous to that leads Eq. (4.119). Then we obtain

$$\Omega_{a(\text{case (b)})}^{\text{nt}} h^2 \simeq 9.1 \times 10^{-5} \times N_{\text{DW}}^{3/2} \left(\frac{\Xi}{10^{-45}} \right)^{3/4} \left(\frac{F_a}{10^{10} \text{GeV}} \right)^{9/2}. \quad (4.133)$$

In this case, the thermal component does not exceeds the non-thermal component. Requiring that $\Omega_{a(\text{case (b)})}^{\text{nt}} h^2 < 0.11$, we obtain

$$\Xi < 1.3 \times 10^{-41} \times N_{\text{DW}}^{-2} \left(\frac{F_a}{10^{10} \text{GeV}} \right)^{-6} \quad \text{for case (b)}. \quad (4.134)$$

This bound is more severe than that obtained from the lifetime of domain walls, given by Eq. (4.129).

However, if Ξ is much larger than the values considered above, axions become heavy and no longer stable. Their dominant decay channel is a decay into two photons. The lifetime is given by

$$\begin{aligned} t_\gamma &= \Gamma_\gamma^{-1} = \frac{64\pi}{m_*^3 g_{a\gamma\gamma}^2} \\ &= 1.1 \times 10^{41} \text{sec} \times N_{\text{DW}}^{-3} \left(\frac{\Xi}{10^{-45}} \right)^{-3/2} \left(\frac{10^{10} \text{GeV}}{F_a} \right), \end{aligned} \quad (4.135)$$

where Γ_γ is the decay rate of the process $a \rightarrow \gamma\gamma$, and we fixed the numerical coefficient $c_{a\gamma\gamma} = 1$ in the axion-photon coupling for simplicity. Since the axion mass is not given by m_a , we must treat m_* and $g_{a\gamma\gamma}$ as different parameters. Cosmological bounds on such models are investigated in [173]. The heavy axions which decay at early times lead to various effects on the cosmological observations, such as the distortion in the spectrum of CMB, and the disagreement of the theoretical prediction with the observed light element abundance. Each of the observations gives a severe constraints on the coupling $g_{a\gamma\gamma}$. In order to avoid these constraints, the lifetime of axions must be short enough to decay earlier than the onset of the BBN, $t_\gamma \lesssim 10^{-2} \text{sec}$. This requirement leads a bound

$$\Xi > 4.6 \times 10^{-17} \times N_{\text{DW}}^{-2} \left(\frac{F_a}{10^{10} \text{GeV}} \right)^{-2/3}. \quad (4.136)$$

In summary, if the value of Ξ is sufficiently large, the mass of axions is determined by the term proportional to Ξ , and this parameter is again constrained by various observational considerations. In order to avoid the observational bounds, axions should be light enough to avoid the overclosure of the universe, whose condition is given by Eq. (4.132) or (4.134), or heavy enough to decay before the BBN epoch, whose condition is given by Eq. (4.136).

Chapter 5

Conclusions and discussion

The axion possesses curious and distinctive properties, which emerge from the connection among particle physics, astronomy, and cosmology. Research on its properties leads to some clues to understand the origin of dark matter and the early history of the universe. In this thesis, we have investigated the production mechanisms of axions and their cosmological implications. The cosmological scenario depends on two theoretical parameters, the axion decay constant F_a (or the PQ symmetry breaking scale) and the domain wall number N_{DW} . Composition and behavior of dark matter axions differ in each scenario, which gives some constraints on the model parameters.

Cosmological domain wall problem leads to serious constraints on the axion models. Let us summarize its implications for each scenario.

- **Scenario I.** Inflation has occurred after the PQ phase transition. In this case, the dark matter abundance is dominated by the coherent oscillation of the axion field. The population of topological defects is wiped away beyond the horizon scale, and domain walls are not problematic. The axion decay constant F_a must take a high scale, which lies in the anthropic window. The observation of the isocurvature fluctuations in anisotropies of CMB gives constraints on the model parameters.
- **Scenario IIA.** Inflation has occurred before the PQ phase transition. Domain walls disappear shortly after their formation ($N_{\text{DW}} = 1$), and there is no cosmological problem. The dark matter abundance is dominated by axions produced from the decay of string-wall systems. The axion decay constant is constrained within the classic window.
- **Scenario IIB.** Inflation has occurred before the PQ phase transition. Domain walls lived for a long time ($N_{\text{DW}} > 1$), and the existence of Ξ term annihilates them. This possibility is almost excluded because of the overproduction of cold axions and the constraint from the observation of NEDM. The exception is the case where the phase δ of CP violating term is fine-tuned in an accuracy less than $\mathcal{O}(1-0.1)\%$. In this case, however, the value of Ξ is still constrained by cosmology, such as Eqs. (4.132), (4.134), and (4.136).

In this thesis, the spectrum of axions produced by string-wall systems is computed numerically. Two possibilities on the form of the spectrum of axions produced by topological defects have been argued in the literature. One possibility is that the spectrum has a peak at the typical scale such as the Hubble scale (for string decay) or the axion mass (for domain wall decay) and that the decay of topological defects gives significant contributions on the cold dark matter abundance (case A). Another possibility is that the spectrum becomes hard ($dE/dk \propto 1/k$), and that contributions on the cold dark matter abundance are subdominant (case B). The current numerical studies of defect networks support case A. Taking account of these results of numerical simulations, we expect that contributions of axions produced by the decay of topological defects can be comparable with that of axions produced by the misalignment mechanism in scenario IIA.

However, the results of current numerical simulations contain several uncertainties due to the limitation of computational resources or the usage of some approximations. Let us comment on the errors which should be taken into account in the estimation of axion cold dark matter abundance.

- On the estimation of the contribution of zero modes [see Eq. (3.47)], the main uncertainty comes from the calculation of anharmonic corrections. This might occur due to the form of the temperature dependent axion mass. In other words, this is the uncertainty in the determination of the time t_1 at which axions begin to coherently oscillate. Taking account of this uncertainty, we obtain the relic abundance of zero modes as

$$\Omega_{a,0}h^2 = (1.10-1.39) \times \left(\frac{g_{*,1}}{70}\right)^{-0.41} \left(\frac{F_a}{10^{12}\text{GeV}}\right)^{1.19} \left(\frac{\Lambda_{\text{QCD}}}{400\text{MeV}}\right). \quad (5.1)$$

- On the estimation of the contribution of the string decay [see Eq. (4.78)], the main uncertainty comes from the determination of the length parameter ξ of global strings. Regarding the fact that other numerical studies obtained various values of ξ , here we use a conservative estimation $\xi \simeq 1.0 \pm 0.5$. Using this value, we obtain the relic abundance of axions produced by the string decay

$$\Omega_{a,\text{string}}h^2 = (2.0 \pm 1.0) \times \left(\frac{g_{*,1}}{70}\right)^{-0.41} \left(\frac{F_a}{10^{12}\text{GeV}}\right)^{1.19} \left(\frac{\Lambda_{\text{QCD}}}{400\text{MeV}}\right). \quad (5.2)$$

- The wall decay contribution (4.98) depends on three parameters ξ_1 , \mathcal{A}_1 , and ϵ_w , which are determined by numerical simulations. The uncertainty of the area parameter \mathcal{A}_1 does not strongly affect the final result, since the energy of topological defects is dominated by that of strings at the decay time of them. For the same reason described above, the length parameter has a large uncertainty $\xi_1 \simeq 1.0 \pm 0.5$. Furthermore, the value of ϵ_w changes up to the choice of the setup of numerical calculation. However, it has been argued that this ambiguity is caused by the poor resolution of the peak location in the spectrum. For now, taking account of this ambiguity in the determination of ϵ_w , we estimate the uncertainty as $\epsilon_w \simeq 2 \pm 1$. For the estimation

of the relic abundance of axions produced by the decay of string-wall networks, we obtain

$$\Omega_{a,\text{dec}}h^2 = (8.5 \pm 4.1) \times \left(\frac{g_{*,1}}{70}\right)^{-0.41} \left(\frac{F_a}{10^{12}\text{GeV}}\right)^{1.19} \left(\frac{\Lambda_{\text{QCD}}}{400\text{MeV}}\right), \quad (5.3)$$

where we included uncertainties in ξ_1 and \mathcal{A}_1 , and used the value $\epsilon_w = 2$. On the other hand, if we include the uncertainty in ϵ_w , we obtain

$$\Omega_{a,\text{dec}}h^2 = (8.5 \pm 5.3) \times \left(\frac{g_{*,1}}{70}\right)^{-0.41} \left(\frac{F_a}{10^{12}\text{GeV}}\right)^{1.19} \left(\frac{\Lambda_{\text{QCD}}}{400\text{MeV}}\right). \quad (5.4)$$

Hence we conclude that the uncertainty in ϵ_w is as large as that in ξ , which strongly affects the final result of the relic dark matter abundance.

- In addition to ambiguities described above, there is subtlety in the behavior of string-wall networks around the time $t = t_1$. In this thesis, we used the approximation in which the axion is massless for $t < t_1$ and becomes massive for $t > t_1$. Then, contributions of axions produced at $t < t_1$ and $t > t_1$ are calculated separately in Eqs. (4.78) and (4.98). Furthermore, we used a naive argument that domain walls suddenly decay at $t_d \simeq t_1$ in the analytic estimation [see Eqs. (4.95)-(4.97)]. The effect of the continuous change in the axion mass at $t = t_1$ might give further corrections on the estimation of the relic axion abundance. We expect that this correction will be similar to that discussed in Sec. 3.2.2, where the relic axion density is corrected by a factor of $\mathcal{O}(1)$ due to the deviation from adiabaticity at the initial time t_1 of coherent oscillation. However, we did not include such corrections for the estimation of the abundance of axions produced by topological defects.

In the classic window (scenario IIA), if we consider the contribution from zero modes only, the upper bound on the axion decay constant, which explains the observed cold dark matter abundance, is given by $F_a \lesssim (1.2\text{-}1.4) \times 10^{11}\text{GeV}$ for $g_{*,1} = 70$ and $\Lambda_{\text{QCD}} = 400\text{MeV}$. This corresponds to the axion mass $m_a \gtrsim (4.3\text{-}5.0) \times 10^{-5}\text{eV}$. This bound might become more severe when we include the contributions of axions produced by strings and domain walls. If we use values of numerical parameters ξ , \mathcal{A} , and ϵ_w obtained by numerical simulations, the total abundance of dark matter axions in the classic window is given by

$$\begin{aligned} \Omega_{a,\text{tot}}h^2 &= \Omega_{a,0}h^2 + \Omega_{a,\text{string}}h^2 + \Omega_{a,\text{dec}}h^2 \\ &= (11.8 \pm 5.4) \times \left(\frac{g_{*,1}}{70}\right)^{-0.41} \left(\frac{F_a}{10^{12}\text{GeV}}\right)^{1.19} \left(\frac{\Lambda_{\text{QCD}}}{400\text{MeV}}\right). \end{aligned} \quad (5.5)$$

Then, for $g_{*,1} = 70$ and $\Lambda_{\text{QCD}} = 400\text{MeV}$, the upper bound on the axion decay constant becomes $F_a \lesssim (1.4\text{-}3.3) \times 10^{10}\text{GeV}$, which corresponds to the axion mass $m_a \gtrsim (1.8\text{-}4.2) \times 10^{-4}\text{eV}$.

Note that the contribution of zero modes already gives a bound $F_a \lesssim 10^{11}\text{GeV}$, which is more severe than the naive estimation $F_a \lesssim 10^{12}\text{GeV}$ used in the literature. Inclusion of contributions from the decay of topological defects might further constrain the value of

F_a , but there still remain various uncertainties which give corrections by a factor of $\mathcal{O}(1)$. Future simulations with higher resolutions will provide more precise bound on axions parameters. Combined with astrophysical and experimental researches, we will probe further into the property of axion dark matter.

Acknowledgments

I would like to thank Masahiro Kawasaki for his support of my Ph.D researches. Perhaps it is the best of luck for me to enter his research group. I have come to find a delight in studying particle cosmology, which might be influenced by his genius in research activities. His kindness helps me a lot, which leads to the current accomplishment of my academic research.

Takashi Hiramatsu helped me to solve various technical problems in the numerical study. The basic part of numerical schemes to solve the evolution of topological defects is developed by him. I would like to thank him.

Toyokazu Sekiguchi told me the analysis method to identify the topological defects and compute the power spectrum of axions. The precise computation of the spectrum of axions is achieved by use of the masking method introduced by him. I would also like to thank him.

I would like to thank Masahide Yamaguchi, Fuminobu Takahashi and Kazunori Nakayama for useful discussions on my dissertation researches. I also thank members of the theory group at the Institute of Cosmic Ray Research, the University of Tokyo. I have been inspired by wonderful discussions on particle physics and cosmology with them. Without their support, I would not have made the current achievement.

I also thank Takeo Moroi for careful review of the manuscript. His numerous suggestions lead to great improvements in the quality of this thesis.

Numerical computation in Chapter 4 was carried out at the Yukawa Institute Computer Facility. It was a great fortune for me to start my research on axionic domain walls at the year when the supercomputer system of that institute began to run.

I would like to acknowledge the financial support of the Japan Society for the Promotion of Science (JSPS). This program enabled me to concentrate on research activities in my graduate school and to have opportunities to go abroad and attend many exciting conferences.

I wish to give my best thank to my mother, Sayuri, father, Katsutoshi, and sister, Tomoko for supporting and encouraging me in my student life. Finally, I would like to thank my late grandparents, Kayoko Kudoh and Shigeru Kudoh. This thesis is dedicated to the memory of them.

Appendix A

Notes of standard cosmology

In this appendix, we summarize some basic formulae which are often used in discussions on cosmology. Our notations and discussions closely follow Refs. [174, 134].

A.1 The Friedmann Equation

It is reasonable, from the observational grounds, to assume that the universe is almost isotropic and homogeneous. Mathematically, such an isotropic and homogeneous universe is described by the Friedmann-Robertson-Walker (FRW) metric

$$ds^2 = -dt^2 + R^2(t) \left[d\mathbf{x}^2 + \frac{(\mathbf{x} \cdot d\mathbf{x})^2}{1 - K\mathbf{x}^2} \right], \quad (\text{A.1})$$

where K is the constant representing the geometry of the space, which takes $+1$, 0 , or -1 , corresponding to the closed, flat, or open universe, respectively.

The dynamics of the cosmic expansion is determined by the Einstein equation

$$R_{\mu\nu} - \frac{1}{2}g_{\mu\nu}R = 8\pi GT_{\mu\nu}, \quad (\text{A.2})$$

where $R_{\mu\nu}$ is the Ricci tensor, R is the Ricci scalar, G is Newton's gravitational constant, and $T_{\mu\nu}$ is the energy momentum tensor. Because of the assumption of the isotropy and homogeneity, the energy momentum tensor must take the form of the perfect fluids

$$T_{00} = \rho(t), \quad T_{i0} = 0, \quad \text{and} \quad T_{ij} = R^2(t)p(t) \left(\delta_{ij} + K \frac{x^i x^j}{1 - K\mathbf{x}^2} \right), \quad (\text{A.3})$$

where i and j run over the three spatial coordinate directions, and ρ and p are the energy density and pressure of fluids. Substituting the metric (A.1) into Eq. (A.2), we obtain the Friedmann equation

$$\left(\frac{\dot{R}}{R} \right)^2 + \frac{K}{R^2} = \frac{8\pi G}{3}\rho, \quad (\text{A.4})$$

and the conservation law

$$\dot{\rho} = -\frac{3\dot{R}}{R}(\rho + p). \quad (\text{A.5})$$

Various energy components contribute to the right hand side of Eq. (A.4), such as cold matter $\rho_M \propto R^{-3}$, radiations $\rho_R \propto R^{-4}$, and dark energy $\rho_\Lambda = \text{constant}$. Gathering these three contributions, we see that the energy density behaves as

$$\rho = \rho_{M,0} \left(\frac{R_0}{R}\right)^3 + \rho_{R,0} \left(\frac{R_0}{R}\right)^4 + \rho_\Lambda, \quad (\text{A.6})$$

where the subscript 0 represents the quantity at the present time. Let us define the Hubble parameter

$$H^2(t) \equiv \left(\frac{\dot{R}}{R}\right)^2, \quad (\text{A.7})$$

and the density parameters

$$\Omega_M \equiv \frac{\rho_{M,0}}{\rho_{c,0}}, \quad \Omega_R \equiv \frac{\rho_{R,0}}{\rho_{c,0}}, \quad \Omega_\Lambda \equiv \frac{\rho_{\Lambda,0}}{\rho_{c,0}}, \quad \Omega_K \equiv -\frac{K}{R_0^2 H_0^2}, \quad (\text{A.8})$$

where $\rho_{c,0} \equiv 3H_0^2/8\pi G$ is the critical density today, and $H_0 = 100h \text{ km sec}^{-1} \text{ Mpc}^{-1}$ is the Hubble parameter at the present time. h parameterizes the measures of the Hubble parameter and current measurements indicate $h \simeq 0.7$ [175]. Combining Eqs. (A.4), (A.6), (A.7) and (A.8), we obtain

$$\frac{H(t)^2}{H_0^2} = \Omega_M \left(\frac{R_0}{R}\right)^3 + \Omega_R \left(\frac{R_0}{R}\right)^4 + \Omega_\Lambda + \Omega_K \left(\frac{R_0}{R}\right)^2. \quad (\text{A.9})$$

The seven-year data from WMAP measurements indicates $\Omega_M h^2 = 0.1116^1$ and $\Omega_\Lambda = 0.729$ [6]. Also, from the observed temperature of the cosmic microwave background $T_0 = 2.725 \pm 0.002 \text{ K}$ [176], the density parameter of radiations is estimated as $\Omega_R h^2 = 4.15 \times 10^{-5}$. Using this result, the epoch of matter-radiation equality, where the energy density of matter becomes equal to that of radiations, is estimated as $R_{\text{eq}}/R_0 = 4.15 \times 10^{-5} (\Omega_M h^2)^{-1}$.

A.2 Thermodynamics in the expanding universe

In the early universe, various particle species contribute to the energy density of the universe as radiations. If the collision rate Γ_i of relativistic particle species i satisfies $\Gamma_i \gg H$, where H is the Hubble parameter, particles are in thermal equilibrium with each other, and we can define the equilibrium temperature T of the relativistic particles. Neglecting the chemical potential, we can describe the evolution of such system via thermodynamical functions such as the energy density $\rho(T)$, pressure $p(T)$, and entropy density $s(T)$, which depend on the temperature T alone.

¹In this thesis, we frequently use the notation Ω_{CDM} rather than Ω_M , emphasizing that it represents the density parameter of cold dark matter.

From the second law of thermodynamics, the change in the entropy is given by

$$d(s(T)V) = \frac{d(\rho(T)V) + p(T)dV}{T}, \quad (\text{A.10})$$

where V is volume of the system. Comparing the coefficient of dV and dT , we obtain

$$s = \frac{dp}{dT} = \frac{\rho + p}{T}, \quad (\text{A.11})$$

Using Eqs. (A.5) and (A.11), we see that the entropy of the universe is conserved

$$\frac{d(sR^3)}{dt} = 0. \quad (\text{A.12})$$

The number density of particle i with momentum p is given by the Bose-Einstein or Fermi-Dirac distributions

$$n_i(p, T)dp = \frac{4\pi g_i p^2 dp}{(2\pi)^3} \frac{1}{\exp(\sqrt{p^2 + m_i^2}/T) \pm 1}, \quad (\text{A.13})$$

where g_i is the degeneracy of the species, m_i is the mass of the species, and the sign is $+$ for fermions and $-$ for bosons. The energy density ρ_i and pressure p_i of a particle species i is given by

$$\rho_i(T) = \int_0^\infty \sqrt{p^2 + m_i^2} n_i(p, T) dp, \quad (\text{A.14})$$

$$p_i(T) = \int_0^\infty \frac{p^2}{3\sqrt{p^2 + m_i^2}} n_i(p, T) dp. \quad (\text{A.15})$$

In the ultrarelativistic limit $m_i \ll T$, they reduce to

$$\rho_i(T) = \begin{cases} \frac{\pi^2}{30} g_i T^4 & \text{for bosons} \\ \frac{7}{8} \frac{\pi^2}{30} g_i T^4 & \text{for fermions} \end{cases}, \quad (\text{A.16})$$

$$p_i(T) = \frac{1}{3} \rho_i(T) = \begin{cases} \frac{\pi^2}{90} g_i T^4 & \text{for bosons} \\ \frac{7}{8} \frac{\pi^2}{90} g_i T^4 & \text{for fermions} \end{cases} \quad (\text{A.17})$$

From Eq. (A.11), the entropy density is given by

$$s_i(T) = \frac{4\rho_i(T)}{3T} = \begin{cases} \frac{2\pi^2}{45} g_i T^3 & \text{for bosons} \\ \frac{7}{8} \frac{2\pi^2}{45} g_i T^3 & \text{for fermions} \end{cases} \quad (\text{A.18})$$

The total energy density and entropy density is given by the sum over whole contributions of relativistic particles

$$\rho_R(T) = \frac{\pi^2}{30} g_*(T) T^4, \quad (\text{A.19})$$

$$s(T) = \frac{2\pi^2}{45} g_{s*}(T) T^3, \quad (\text{A.20})$$

where g_* and g_{s*} are the total number of effectively massless degrees of freedom,

$$g_*(T) = \sum_{i=\text{bosons}} g_i \left(\frac{T_i}{T}\right)^4 + \sum_{i=\text{fermions}} \frac{7}{8} g_i \left(\frac{T_i}{T}\right)^4, \quad (\text{A.21})$$

$$g_{s*}(T) = \sum_{i=\text{bosons}} g_i \left(\frac{T_i}{T}\right)^3 + \sum_{i=\text{fermions}} \frac{7}{8} g_i \left(\frac{T_i}{T}\right)^3. \quad (\text{A.22})$$

Combining Eqs. (A.12) and (A.20), we obtain

$$g_{s*}(T)R^3T^3 = \text{constant}. \quad (\text{A.23})$$

As an application of this formula, let us estimate the temperature of neutrinos. Neutrinos are in thermal equilibrium with photons via the weak interaction until the temperature of photons cools down below $\approx 10^{10}\text{K}$. Before the decoupling, electrons (2 spin states), positrons (2), neutrinos (3 generations), anti-neutrinos (3), and photons (2 spin states) are contribute as relativistic degrees of freedom. Hence the value of Eq. (A.23) is estimated as

$$g_{s*}(T_1)R_1^3T_1^3 = [2 + (7/8)(2 + 2 + 3 + 3)](R_1T_1)^3, \quad (\text{A.24})$$

where T_1 is the common temperature before the decoupling and R_1 is the scale factor at that time. Soon after the decoupling of neutrinos, electrons and positrons annihilate into photons. After the annihilation, the value of Eq. (A.23) is given by

$$\left[2 \left(\frac{T_\gamma}{T_\nu}\right)^3 + \frac{7}{8}(3 + 3)\right] (R_2T_\nu)^3, \quad (\text{A.25})$$

where T_γ and T_ν are the photon and neutrino temperature after the annihilation, and R_2 is the scale factor at that time. Equating (A.24) and (A.25), and using $R_1T_1 = R_2T_\nu$ which follows from the fact that the neutrino temperature scales as R^{-1} , we find the ratio between the temperature of photons and neutrinos

$$\frac{T_\nu}{T_\gamma} = \left(\frac{4}{11}\right)^{1/3}. \quad (\text{A.26})$$

Substituting it into Eq. (A.21), we can estimate the effective degrees of freedom of radiations at the present time

$$g_{*,0} = 2 + \frac{7}{8}(3 + 3) \left(\frac{4}{11}\right)^{4/3} \simeq 3.36. \quad (\text{A.27})$$

In a similar way, from Eq. (A.22) we obtain

$$g_{s*,0} \simeq 3.91. \quad (\text{A.28})$$

A.3 Horizons

The maximum proper distances which can be reached by a light signal emitted in the past is called particle horizons. These length scales characterize the region of the universe which is in causal contact. Let us rewrite the FRW coordinate (A.1) by using spherical polar coordinates $dx^2 = dr^2 + r^2(d\theta^2 + \sin^2\theta d\phi^2)$ so that

$$ds^2 = -dt^2 + R^2(t) \left[\frac{dr^2}{1 - Kr^2} + r^2(d\theta^2 + \sin^2\theta d\phi^2) \right]. \quad (\text{A.29})$$

Then, when the greatest value of radial coordinate which is reached by a photon emitted at $t = 0$ (the beginning of the universe) is given by $r_{\max}(t)$, the particle horizon is defined as

$$d_H(t) = R(t) \int_0^{r_{\max}(t)} \frac{dr}{\sqrt{1 - Kr^2}} = R(t) \int_0^t \frac{dt'}{R(t')}. \quad (\text{A.30})$$

For example, in the radiation dominated universe we obtain $d_H(t) = 2t = 1/H(t)$, while in the matter dominated universe we obtain $d_H(t) = 3t = 2/H(t)$. From this fact, we see that the particle horizon is comparable to the Hubble radius H^{-1} in the radiation and matter dominated universe. Hence, in this thesis we do not make a distinction between $d_H(t)$ and H^{-1} , and simply call them horizons.

Appendix B

Extended field configurations

In this appendix, we review some non-perturbative results of quantum field theory. We especially consider instantons, strings, and domain walls, which are relevant to the discussion on axions and cosmology.

B.1 Classifications

Consider the following scalar field theory in $1 + 1$ dimensions

$$\mathcal{L} = -\frac{1}{2}\partial_\mu\phi\partial^\mu\phi - V(\phi), \quad \mu = 0, 1, \quad (\text{B.1})$$

where $x^0 = t$, $x^1 = x$, and the potential is given by

$$V(\phi) = \frac{\lambda}{4}(\phi^2 - \eta^2)^2. \quad (\text{B.2})$$

The field equation obtained from Eqs. (B.1) and (B.2) has a solution

$$\phi(x) = \eta \tanh\left(\sqrt{\frac{\lambda}{2}}\eta x\right). \quad (\text{B.3})$$

This solution describes a kink-like configuration localized at $x = 0$, which interpolates between $\phi = -\eta$ at $x = -\infty$ and $\phi = \eta$ at $x = +\infty$. It can be shown that this solution is stable under small perturbations [177].

The classical stability of this field configuration is a consequence of the topology of the vacuum manifold. The finiteness of the energy requires that the value of the field ϕ at the spatial infinity must be zeros of the potential $V(\phi)$. There are distinct configurations which satisfy such conditions. A non-trivial one is the configuration which takes $\phi(-\infty) = -\eta$ and $\phi(\infty) = \eta$, similar to the solution given by Eq. (B.3). It is impossible to continuously change this solution into a trivial one such as $\phi(x) = \eta$ without the infinite cost of lifting the field at the spatial infinity. In this case, the classical stability of the field configuration arises from the fact that the vacuum manifold is disconnected.

Since the topological nature of the classical stability is related to the continuous deformation of the field configurations, we can easily extend the discussion on the stability of time-independent, localized solutions into arbitrary spatial dimensions. Consider a theory of a gauge field A_a^μ in D spatial dimensions, with a scalar field ϕ which transforms as a linear representation of the gauge group. The energy of a localized solution $(\phi(\mathbf{x}), A_a^i(\mathbf{x}))$ is given by

$$\begin{aligned} E &= \int d^D x \left[\frac{1}{2} (D_i \phi)^2 + \frac{1}{4} F_{aij} F_a^{ij} + V(\phi) \right] \\ &\equiv I_{K_S} + I_{K_A} + I_V, \end{aligned} \quad (\text{B.4})$$

where $I_{K_S} \equiv \int d^D x \frac{1}{2} (D_i \phi)^2$, $I_{K_A} \equiv \int d^D x \frac{1}{4} F_{aij} F_a^{ij}$, $I_V \equiv \int d^D x V(\phi)$, and D_i is the usual gauge covariant derivative. Here, we consider the gauge field in temporal gauge, in which $A_a^0 = 0$. We assume that the potential energy is chosen such that $V \geq 0$, and hence

$$I_{K_S} \geq 0, \quad I_{K_A} \geq 0, \quad I_V \geq 0. \quad (\text{B.5})$$

Suppose that $(\phi(\mathbf{x}), A_a^i(\mathbf{x}))$ is a set of time-independent, localized solution. Define the transformation of $(\phi(\mathbf{x}), A_a^i(\mathbf{x}))$ as $\phi(\mathbf{x}) \rightarrow \phi(\lambda \mathbf{x})$ and $A_a^i(\mathbf{x}) \rightarrow \lambda A_a^i(\lambda \mathbf{x})$ where λ is a positive parameter. Then, the energy of the new configuration becomes

$$E_\lambda = \lambda^{2-D} I_{K_S} + \lambda^{4-D} I_{K_A} + \lambda^{-D} I_V. \quad (\text{B.6})$$

Requiring that this must be stationary at $\lambda = 1$, we find

$$(2 - D)I_{K_S} + (4 - D)I_{K_A} - DI_V = 0. \quad (\text{B.7})$$

In the absence of the gauge field ($I_{K_A} = 0$), we see that the stable solution for the scalar field exists only if $D = 1$ [Derrick's theorem [178]]. This corresponds to the solution given by Eq. (B.3), which will be investigated further in Sec. B.5. On the other hand, in the absence of the scalar field ($I_{K_S} = 0$ and $I_V = 0$), the stable solution for the gauge field exists only if $D = 4$. The topologically non-trivial gauge field solutions for $D = 4$ is called *instantons*, which we will discuss in the next section.

In the mathematical point of view, whether non-trivial solutions exist is related to the study of homotopy theory.¹ As we saw in the above example, finite energy configurations are determined by the field value in the spatial infinity. Then, field configurations which can be deformed into each other with keeping their energy E finite are regarded as topologically equivalent. In general, for a field theory with D dimensions, a finite energy configuration $\phi(\mathbf{x})$ [and $A_a^i(\mathbf{x})$ if there exists a gauge field] which is restricted by a condition at the spatial infinity represents a mapping from the D -dimensional space with the infinity $|\mathbf{x}| = \infty$ taken as a single point, into the vacuum manifold \mathcal{M} . Since a D -dimensional space with the infinity identified as a single point is topologically identical to the $(D - 1)$ -dimensional sphere S_{D-1} , the field configuration $\phi(\mathbf{x})$ defines a continuous mapping from S_{D-1} into the manifold \mathcal{M} ,

$$\phi : S_{D-1} \rightarrow \mathcal{M}. \quad (\text{B.8})$$

¹See e.g. [177, 179] for more comprehensive reviews.

The set of mappings which are topologically equivalent to each other defines a equivalence class, which is called the homotopy class. It is known that the mappings which are distinguished according to the homotopy class define a group. Such a group is called the $(D - 1)$ th homotopy group of the manifold \mathcal{M} and denoted as $\pi_{D-1}(\mathcal{M})$.

The elements of $\pi_{D-1}(\mathcal{M})$ which can be continuously changed into the configuration ϕ which takes the same value (say $\phi = \eta$) in the whole region of the space are called trivial. The physical interest arises if there exist non-trivial elements, which describe localized finite energy configurations. A homotopy group which consists of just a trivial element is called the trivial homotopy group, and is denoted as $\pi_{D-1}(\mathcal{M}) = I$. Then, non-trivial field configurations are possible if $\pi_{D-1}(\mathcal{M}) \neq I$.

Suppose that ϕ represents a Higgs field which causes spontaneous breaking of a certain symmetry group G into its subgroup H . In such a case, zeros of the potential of ϕ correspond to the coset space G/H . Hence, whether non-trivial configurations exist is determined by the structure of the manifold $\mathcal{M} = G/H$. In other words, when a symmetry breaking $G \rightarrow H$ occurs, non-trivial configurations arise if $\pi_{D-1}(G/H) \neq I$. For example, in one-dimensional theory defined by Eqs. (B.1) and (B.2), a Z_2 symmetry in which the scalar field transforms as $\phi \rightarrow -\phi$ is broken down to the trivial subgroup I . Non-trivial configurations exist since $\pi_0(G/H) \neq I$ where $G = Z_2$ and $H = I$.

From the viewpoint of physical interests, there are two kinds of extended field configurations which affect real phenomena in the universe. One is event-like field configurations whose effect arises as correction terms in path integrals, and another is lump-like field configurations which appear as components of actual physical states. We will describe the former case in the next section. The later case contains string-like configurations called *strings*, and sheet-like configurations called *domain walls*, which will be described in Secs. B.4 and B.5 with a focus on the axionic models.

B.2 Instantons

In Eq. (B.7) we see that there exist non-trivial localized configurations in a pure gauge field theory with $D = 4$ spatial dimensions. To derive this result, we assumed temporal gauge ($A_a^0 = 0$) in $(D + 1)$ -dimensional Minkowski spacetime. However, this result is also applicable to pure gauge field theories in $D = 4$ -dimensional Euclidean spacetime. Indeed, such 4-dimensional Euclidean gauge theories describe the actual physics of elementary particles such as QCD, since quantum field theory may be rigorously formulated in terms of Feynmann amplitudes in Euclidean spacetime [180].

Henceforth we consider a pure gauge theory in which the Lagrangian is invariant under transformations of a non-abelian gauge group G , with the action given by

$$S = \int d^4x \frac{1}{4} F_{\mu\nu}^a F_{\mu\nu}^a, \quad (\text{B.9})$$

where we work in a Euclidean spacetime with $x^4 = x_4 = ix^0$ and $A^{a4} = A_4^a = iA_0^a$. The Euclidean field strength is defined in the same way as the Minkowski space

$$F_{\mu\nu}^a = \partial_\mu A_\nu^a - \partial_\nu A_\mu^a + gf^{abc} A_\mu^b A_\nu^c, \quad (\text{B.10})$$

where g is the gauge coupling constant, and f^{abc} is the structure constants of the gauge group G , which is defined by the commutator between generators T^a of the gauge group, $[T^a, T^b] = if^{abc}T^c$. For matrices of the gauge group, we choose the normalization so that

$$\text{Tr}[T^a T^b] = C_r \delta^{ab}. \quad (\text{B.11})$$

where C_r is a constant depending on the representation, which takes $C_r = 1/2$ for fundamental representation of $SU(N)$. We also define abbreviate notations

$$A_\mu = T^a A_\mu^a, \quad F_{\mu\nu} = T^a F_{\mu\nu}^a. \quad (\text{B.12})$$

The gauge transformation yields

$$A_\mu \rightarrow U A_\mu U^{-1} - \frac{i}{g} (\partial_\mu U) U^{-1}, \quad (\text{B.13})$$

$$F_{\mu\nu} \rightarrow U F_{\mu\nu} U^{-1}, \quad (\text{B.14})$$

where U is an element of the gauge group G

$$U(x) = \exp(iT^a \Lambda^a(x)), \quad (\text{B.15})$$

and $\Lambda^a(x)$ is a set of real functions.

In the path integral formulation of the quantum field theory, we construct a perturbation theory by integrating over fluctuations on a field configuration for which the Euclidean action is finite. Hence we must consider gauge field configurations which make the Euclidean action (B.9) finite. In order for the action to be finite, the field strength $F_{\mu\nu}^a$ must vanish at $|\mathbf{x}| \rightarrow \infty$.² This can be achieved when the gauge field approaches a pure gauge

$$A_\mu(\mathbf{x}) \rightarrow \frac{i}{g} (\partial_\mu U(\hat{\mathbf{x}})) U^{-1}(\hat{\mathbf{x}}) \quad \text{for} \quad |\mathbf{x}| \rightarrow \infty, \quad (\text{B.16})$$

where $U(\hat{\mathbf{x}})$ is an element of the gauge group G , which depends only on the direction of \mathbf{x} . Eq. (B.16) maps one direction of 4-dimensional Euclidean space $\hat{\mathbf{x}}$ into one element of the gauge group G . Hence this condition defines a mapping from the unit sphere $|\hat{\mathbf{x}}| = 1$ (3-dimensional sphere S_3) to the group manifold G . Classes of such mappings are topologically distinguishable, and define the third homotopy group of the group manifold G , $\pi_3(G)$. For QCD with $G = SU(3)$, it is known that this homotopy group is non-trivial

$$\pi_3(SU(3)) = \mathbb{Z}. \quad (\text{B.17})$$

This implies that the vacuum of QCD is topologically distinguishable, labeled by an integer number which is an element of \mathbb{Z} .

The remarkable fact is that non-trivial configurations exist even though there are no spontaneous breaking of the gauge symmetry G . This is inevitable consequence of pure

²In this section we use the notation in which \mathbf{x} represents 4-dimensional Euclidean vector $\mathbf{x} = (x^1, x^2, x^3, x^4)$ and $|\mathbf{x}| = \sqrt{(x^1)^2 + (x^2)^2 + (x^3)^2 + (x^4)^2}$. The Greek indices take components of the 4-dimensional Euclidean vector $\mu = 1, 2, 3, 4$.

QCD in 4-dimensional space. Since these solutions are localized in 4-dimensional Euclidean space,³ they correspond to the configurations localized both in space and time in Minkowski space. Such time-localized nature of these configurations motivates their naming, instantons.

It is known that the topologically distinguishable vacuum of the gauge field theory is characterized by a topologically invariant quantity which is written as an integral over the manifold

$$\nu = \frac{1}{48\pi^2 C_r} \int d\theta^1 d\theta^2 d\theta^3 \epsilon^{ijk} \text{Tr} \left[U^{-1}(\theta) \frac{\partial U(\theta)}{\partial \theta^i} U^{-1}(\theta) \frac{\partial U(\theta)}{\partial \theta^j} U^{-1}(\theta) \frac{\partial U(\theta)}{\partial \theta^k} \right], \quad (\text{B.18})$$

where θ^i with $i = 1, 2, 3$ are coordinates of the 3-sphere S_3 , ϵ^{ijk} is the totally antisymmetric quantity with $\epsilon^{123} = 1$, and C_r is a normalization constant defined by Eq. (B.11). The quantity (B.18) is indeed a topologically invariant, in the sense that it is independent of the choice of the coordinate system θ^i , and that it is invariant under a small deformation of the group element U . Furthermore, the value ν is additive, in the sense that if $U = U_a U_b$ where U_a and U_b are other elements of G , then $\nu = \nu_a + \nu_b$ where ν_a and ν_b are obtained by substituting U_a and U_b into Eq. (B.18), respectively. Hence any mapping $S^3 \rightarrow G$ is characterized by ν , and it is called the winding number. Substituting Eq. (B.16) into Eq. (B.18), we find

$$\nu = \frac{ig^3}{48\pi^2 C_r} \lim_{r \rightarrow \infty} r^3 \int d\theta^1 d\theta^2 d\theta^3 \epsilon^{ijk} \frac{\partial \hat{x}^\mu}{\partial \theta^i} \frac{\partial \hat{x}^\rho}{\partial \theta^j} \frac{\partial \hat{x}^\sigma}{\partial \theta^k} \text{Tr} [A_\mu A_\rho A_\sigma], \quad (\text{B.19})$$

where $r = |\mathbf{x}|$ is the radius of 3-sphere.

To evaluate this integral, we define a quantity

$$K_\mu \equiv C_r^{-1} \epsilon_{\mu\nu\rho\sigma} \text{Tr} \left(A_\nu F_{\rho\sigma} + \frac{2i}{3} g A_\nu A_\rho A_\sigma \right), \quad (\text{B.20})$$

where $\epsilon_{\mu\nu\rho\sigma}$ is the totally antisymmetric tensor with $\epsilon_{1234} = 1$. The divergence of this quantity can be written as

$$\partial_\mu K_\mu = F_{\mu\nu}^a \tilde{F}_{\mu\nu}^a, \quad (\text{B.21})$$

where $\tilde{F}_{\mu\nu}^a$ is the dual of $F_{\mu\nu}^a$, defined by

$$\tilde{F}_{\mu\nu}^a = \frac{1}{2} \epsilon_{\mu\nu\rho\sigma} F_{\rho\sigma}^a. \quad (\text{B.22})$$

Since the field strength vanishes in the limit $r \rightarrow \infty$, we obtain

$$K_\mu \rightarrow C_r^{-1} \frac{2i}{3} g \epsilon_{\mu\nu\rho\sigma} \text{Tr} [A_\nu A_\rho A_\sigma] \quad \text{for } r \rightarrow \infty. \quad (\text{B.23})$$

³Here, we consider a gauge field theory in 4-dimensional Euclidean spacetime, rather than that in $(D+1)$ -dimensional Minkowski spacetime assumed in Eq. (B.7). Hence the ‘‘energy’’ E in Eq. (B.4) should be replaced by the Euclidean action, and instantons are non-trivial configurations which keep the Euclidean action finite.

Using Gauss's theorem and Eq. (B.23), we reduce the surface integral in Eq. (B.19) into the form

$$\nu = \frac{g^2}{32\pi^2} \int_{S^3} dS n_\mu K_\mu = \frac{g^2}{32\pi^2} \int_{E^4} d^4x \partial_\mu K_\mu \quad (\text{B.24})$$

where $\int_{S^3} dS$ represents the integration over the surface of 3-sphere, $\int_{E^4} d^4x$ represents the integration over 4-dimensional Euclidean space, and n_μ is a unit vector normal to the surface of S^3 . Then, using Eq. (B.21) we obtain

$$\nu = \frac{g^2}{32\pi^2} \int_{E^4} d^4x F_{\mu\nu}^a \tilde{F}_{\mu\nu}^a. \quad (\text{B.25})$$

This quantity is called the Pontryagin index.

An explicit form of the solution which satisfies the boundary condition (B.16) was found by [181],

$$\begin{aligned} A_\mu(x) &= \frac{i}{g} \left(\frac{r^2}{r^2 + \rho^2} \right) (\partial_\mu U_1(\hat{\mathbf{x}})) U_1^{-1}(\hat{\mathbf{x}}), \\ U_1(\hat{\mathbf{x}}) &= \frac{x_4 + i(x_1\sigma_1 + x_2\sigma_2 + x_3\sigma_3)}{r}, \end{aligned} \quad (\text{B.26})$$

where ρ is an arbitrary parameter which represents the instanton size, and

$$\sigma_1 = \begin{pmatrix} 0 & 1 \\ 1 & 0 \end{pmatrix}, \quad \sigma_2 = \begin{pmatrix} 0 & -i \\ i & 0 \end{pmatrix}, \quad \sigma_3 = \begin{pmatrix} 1 & 0 \\ 0 & -1 \end{pmatrix}. \quad (\text{B.27})$$

It can be shown that this configuration leads $\nu = 1$. Also, this configuration is self-dual, so that

$$F_{\mu\nu}^a = \tilde{F}_{\mu\nu}^a. \quad (\text{B.28})$$

From Eqs. (B.25) and (B.28), and the fact that $\nu = 1$, we see that the value of Euclidean action (B.9) becomes

$$S = \frac{8\pi^2}{g^2}. \quad (\text{B.29})$$

To make a physical interpretation of instantons, let us consider a cylindrical surface along to x_4 -axis shown in Fig. B.1, which is obtained by deforming the boundary S^3 of the Euclidean spacetime. Since the quantity ν in Eq. (B.24) does not depend on the gauge, here we choose a gauge such that $A_4 = 0$. In this gauge K_1 , K_2 , and K_3 vanish since they contain at least one factor of A_4 , according to Eq. (B.23). Therefore, the contribution to the integral (B.24) only comes from the upper and lower hypersurfaces $x_4 = \pm\infty$ of the cylinder

$$\nu = \frac{g^2}{32\pi^2} \int d^3x K_4 \Big|_{x_4=-\infty}^{x_4=\infty}, \quad (\text{B.30})$$

where $\int d^3x$ represents the integration over 3-dimensional hypersurface at $x_4 = \pm\infty$. This implies that, for a vacuum at $x_4 = -\infty$ with a winding number n , the existence of the instanton with $\nu = 1$ makes a transition into another vacuum with the winding number $n + 1$ at $x_4 = +\infty$. This situation is sketched in Fig. B.1.

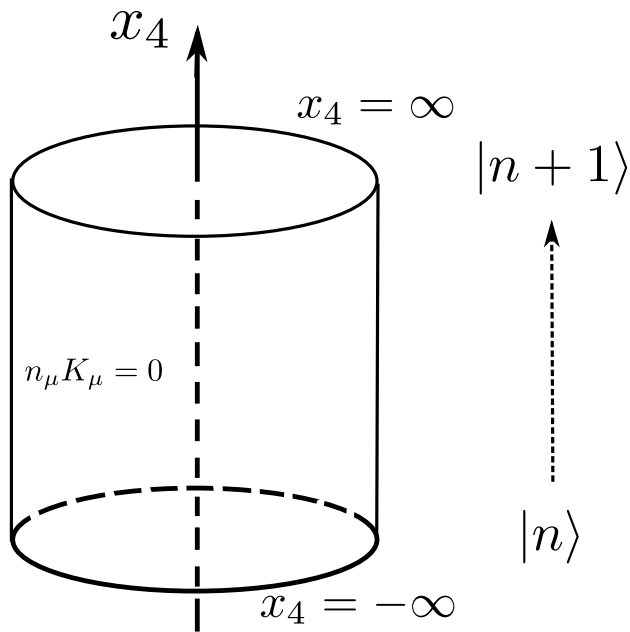


Figure B.1: Schematics of the cylindrical surface which is chosen in order to evaluate the winding number in 4-dimensional Euclidean space. The upper and lower bases correspond to the 3-dimensional hypersurfaces at $x_4 = \infty$ and $x_4 = -\infty$, respectively. On the side of the cylinder, the contribution to the integral (B.24) vanishes since $n_\mu K_\mu = 0$. When an instanton with $\nu = 1$ exists, the winding number n at $x_4 = -\infty$ changes into $n + 1$ at $x_4 = \infty$.

B.3 Symmetry restoration and phase transitions

In the following sections we describe another kind of extended field configurations, called topological defect, which might be created when some symmetry is spontaneously broken. Before going to the discussion on particular solutions, let us discuss how such defects are created in the early universe.

Let us consider a spontaneous symmetry breaking which caused by a complex scalar field Φ acquiring the non-zero vacuum expectation value due to the dynamics of the classical scalar potential $V(\Phi)$. In the early universe, the field Φ couples with light degrees of freedom in the thermal bath with the temperature T . Such couplings induce correction terms in the effective potential at high temperature. The leading contribution is given by [182, 183]

$$\begin{aligned} V_{\text{eff}}(\Phi, T) &= V(\Phi) + \text{Tr} \left[\frac{T^4}{2\pi^2} J_B(M_s^2/T^2) - \frac{T^4}{2\pi^2} J_F(M_f^\dagger M_f/T^2) + \frac{3T^4}{2\pi^2} J_B(M_g^2/T^2) \right], \\ J_B(m^2/T^2) &= \int_0^\infty dx x^2 \ln \left[1 - e^{-\sqrt{x^2+m^2}/T} \right], \\ J_F(m^2/T^2) &= \int_0^\infty dx x^2 \ln \left[1 + e^{-\sqrt{x^2+m^2}/T} \right], \quad m = M_s, M_f, \text{ or } M_g, \end{aligned} \quad (\text{B.31})$$

where M_s , M_f , and M_g are mass matrices for scalar fields, fermions, and gauge bosons which couple to the field Φ , respectively, and “Tr” takes the trace over the mass matrices. These contributions are exponentially suppressed at low temperature $T \ll m$. On the other hand, at sufficiently high temperature $T \gg m$, we can expand Eq. (B.31) in terms of m^2/T^2 , and obtain

$$V_{\text{eff}}(\Phi, T) = V(\Phi) + \frac{1}{24} \mathcal{M}^2 T^2 - \frac{\pi^2}{90} g T^4 + \dots, \quad (\text{B.32})$$

where dots represent the contributions with higher order in m^2/T^2 , $g = g_B + 7g_F/8$ is the sum of the number of bosonic states g_B and fermionic states g_F with a weighting factor $7/8$, and \mathcal{M}^2 is given by

$$\mathcal{M}^2 = \text{Tr} M_s^2 + 3\text{Tr} M_g^2 + \frac{1}{2} \text{Tr} M_f^\dagger M_f. \quad (\text{B.33})$$

For simplicity, here we assume that the field Φ has no coupling with fermions and gauge bosons, and only has a self coupling, which is given by the bare potential

$$V(\Phi) = \frac{\lambda}{4} (|\Phi|^2 - \eta^2)^2. \quad (\text{B.34})$$

By using the decomposition $\Phi = \phi_1 + i\phi_2$ where ϕ_1 and ϕ_2 are real scalar fields,⁴ we find the scalar mass matrix

$$(M_s^2)_{ij} = \frac{\partial^2 V}{\partial \phi_i \partial \phi_j} = \lambda (|\Phi|^2 - \eta^2) \delta_{ij} + 2\lambda \phi_i \phi_j, \quad (\text{B.35})$$

⁴We assume that the kinetic term of the complex scalar field takes the form $\mathcal{L}_{\text{kin}} = -\frac{1}{2} |\partial_\mu \Phi|^2$, and hence ϕ_1 and ϕ_2 are canonically normalized.

where $i, j = 1, 2$. Then, the effective potential reduces to

$$V_{\text{eff}}(\Phi, T) \simeq \frac{\lambda}{4}(|\Phi|^2 - \eta^2)^2 + \frac{\lambda}{6}T^2|\Phi|^2 - \frac{\pi^2}{45}T^4. \quad (\text{B.36})$$

From this expression, we find that the scalar field has a temperature-dependent mass

$$m^2(T) = \frac{\lambda}{3}(T^2 - 3\eta^2). \quad (\text{B.37})$$

When the temperature is sufficiently high, the mass squared $m^2(T)$ is positive, and the scalar field takes the equilibrium value $|\langle\Phi\rangle| = 0$. After T falls below the critical temperature

$$T_c = \sqrt{3}\eta, \quad (\text{B.38})$$

$m^2(T)$ becomes negative, and the equilibrium field value is given by

$$|\langle\Phi\rangle|(T) = \frac{1}{\sqrt{3}}(T_c^2 - T^2)^{1/2}. \quad (\text{B.39})$$

In axion models, we identify Eq. (B.36) as the potential for PQ field which induces the spontaneous breaking of the global U(1) symmetry. Since the field value vanishes for $T > T_c$, the global symmetry is restored at high temperature. Then, at $T = T_c$ this global symmetry is broken, and the magnitude of the scalar field takes a finite value (B.39). Such transition is called the second-order phase transition, as the order parameter $|\langle\Phi\rangle|$ grows continuously from zero.

Although the magnitude of Φ is determined by Eq. (B.39), the phase α of Φ is undetermined solely from the dynamics described by the effective potential (B.36). Just after the phase transition, α takes different values in different positions in space. However, since the free energy of the system is minimized by the configuration where Φ takes a homogeneous value, these spatial fluctuations in α will eventually die out as the temperature decreases.

The amplitude of the field fluctuations can be estimated from the following naive arguments [24]. Let us define the correlation length l_c above which the values of α are different. We estimate that l_c is given by the typical microscopic scale at the epoch of the phase transition, which is comparable to the inverse of the effective mass of Φ

$$l_c \sim |m(T)|^{-1} \sim |\lambda^{1/2}\langle\Phi\rangle(T)|^{-1}, \quad (\text{B.40})$$

where $|\langle\Phi\rangle|(T)$ is given by Eq. (B.39). Since the fluctuation in the energy induced by the fluctuation of the scalar field $\delta\Phi$ is comparable to $m^2(T)|\Phi\delta\Phi|$, the typical energy of the fluctuation in the region with the length scale l_c is estimated as

$$l_c^3 m^2(T) |\Phi\delta\Phi| \sim T. \quad (\text{B.41})$$

From Eqs. (B.40) and (B.41), we find

$$\left| \frac{\delta\Phi}{\Phi} \right| \sim \frac{\lambda T}{m(T)}. \quad (\text{B.42})$$

Therefore, the amplitude of fluctuations of Φ becomes less than the equilibrium value when $\lambda T/|m(T)| < 1$ is satisfied. The temperature T_G at which $\lambda T/|m(T)| \sim 1$ is satisfied is called the Ginzburg temperature. From Eq. (B.37) we find

$$T_c - T_G \sim \lambda T_c. \quad (\text{B.43})$$

Below the Ginzburg temperature T_G , the fluctuations of Φ do not have enough kinetic energy to go up the potential between different minima, and hence the field configurations “freeze-out”. Afterwards the correlation length l_c begins to grow with time. However, the causality requires that l_c must not exceed the horizon scale

$$l_c(t) \lesssim d_H(t) \sim t, \quad (\text{B.44})$$

where we assumed a power law expansion in which $d_H \sim t$ [see Eq. (A.30)]. This fact indicates that the values of Φ are uncorrelated above the horizon scale of the universe, and that there exist regions on which the value of Φ (or α) transits from one minimum to another minimum. Topological defects are expected to form around such regions. Since the causal region is bound inside the finite length scale in the universe, the formation of topological defects is inevitable consequence of cosmological phase transitions. Such an unavoidable production mechanism of topological defects is called the Kibble mechanism [184].

B.4 Cosmic strings

When a continuous symmetry G is spontaneously broken into its subgroup H , formation of strings occurs if $\pi_1(G/H) \neq I$ is satisfied. Such configurations are considered as finite energy solutions in a field theory with $D = 2$ spatial dimensions. In the actual (3+1)-dimensional spacetime, they are tube-like configurations, which correspond to sequences of field configurations localized in 2-dimensional slice.

In Sec. B.1 we see that there is no stable localized finite energy solution for $D = 2$ field theory in the absence of the gauge field, but such a solution still exists in the field theory which contains both scalar and gauge fields. A well known example is the abelian-Higgs model, which describes a spontaneous breaking of a local $U(1)$ symmetry, and contains a gauge field A_μ and a complex scalar field Φ . In such a model, finite energy solutions correspond to the configurations which satisfy $D_\mu \Phi \rightarrow 0$ and $F_{\mu\nu} \rightarrow 0$ in the spatial infinity, where $F_{\mu\nu} = \partial_\mu A_\nu - \partial_\nu A_\mu$ is the gauge field strength, and $D_\mu \Phi$ is the gauge covariant derivative. It is necessary to include the gauge field in order to guarantee $D_\mu \Phi \rightarrow 0$, since the contribution from A_μ cancels the positive contribution which comes from the spatial derivative of Φ .

In the axion models, there is no gauge field which compensates the spatial variation of Φ , since the $U(1)_{PQ}$ symmetry is global symmetry. However, it is known that stable string solutions exist even in the model which describes a spontaneous breaking of a global $U(1)$ symmetry. This does not conflict with the above discussion on the local $U(1)$ symmetry based on Derrick’s theorem, since such configurations are *global* in the sense that their energy is logarithmically divergent, as we will see below, and they evade the condition of

locality which we assumed in the proof of Derrick's theorem. Such non-localized solutions are called global strings.

Let us consider the model with the complex scalar field (the PQ field) Φ whose potential is given by Eq. (B.34). To describe the global string solution, we take an ansatz

$$\Phi = \Phi(r, \varphi), \quad (\text{B.45})$$

which represents a straight string lying along the z-axis in the cylindrical coordinates (r, φ, z) . Equation of motion for Φ in the flat Minkowski background becomes

$$\frac{1}{r} \frac{\partial}{\partial r} \left(r \frac{\partial \Phi}{\partial r} \right) + \frac{1}{r^2} \frac{\partial^2 \Phi}{\partial \varphi^2} - \lambda \Phi (|\Phi|^2 - \eta^2) = 0. \quad (\text{B.46})$$

Assuming the form of the solution

$$\Phi(r, \varphi) = \eta f(r) e^{i\varphi}, \quad (\text{B.47})$$

Eq. (B.46) reduces to

$$\frac{\partial^2 f}{\partial y^2} + \frac{1}{y} \frac{\partial f}{\partial y} - \frac{f}{y^2} - f(f^2 - 1) = 0, \quad (\text{B.48})$$

where $y = \sqrt{\lambda} \eta r$. We seek the solution which satisfies the boundary condition

$$f(y) \rightarrow \begin{cases} 1, & y \rightarrow \infty \\ 0, & y \rightarrow 0 \end{cases}. \quad (\text{B.49})$$

Explicit form for f which satisfies (B.49) is not known. However, we can find approximate solution in the limit $r \rightarrow 0$ by linearizing Eq. (B.48)

$$f(y) \simeq J_1(y) = J_1(\sqrt{\lambda} \eta r) \quad \text{for } y \ll 1, \quad (\text{B.50})$$

where $J_n(y)$ is the Bessel function of the first kind. We see that $f(r)$ deviates from zero for a length scale $r \simeq (\sqrt{\lambda} \eta)^{-1}$, which can be interpreted as the core width of the string

$$\delta_s \simeq (\sqrt{\lambda} \eta)^{-1}. \quad (\text{B.51})$$

Also, the numerical solution of Eq. (B.48) shows that $1 - f(r)$ decays with a power law for large r [24].

For length scales much larger than the core width δ_s of strings, we can ignore the internal structure of the string. In such cases, we can define an effective energy-momentum tensor for a straight string lying along the z-axis in the Cartesian coordinates (x, y, z) ,

$$\tilde{T}_\mu^\nu = \delta(x) \delta(y) \int T_\mu^\nu dx dy. \quad (\text{B.52})$$

It can be shown that all components of \tilde{T}_μ^ν vanishes except for $\tilde{T}_0^0 = \tilde{T}_3^3$ from the requirement of symmetry and the conservation law of T_μ^ν [40]. Then, the energy-momentum tensor of the string takes the form

$$\tilde{T}_\nu^\mu = -\mu_{\text{string}} \delta(x) \delta(y) \text{diag}(1, 0, 0, 1), \quad (\text{B.53})$$

where

$$\mu_{\text{string}} = - \int dx dy T_0^0 = \int dx dy T_{00} \quad (\text{B.54})$$

is the mass energy of the string per unit length.⁵ Note that the magnitude of the pressure \tilde{T}_{33} on the string is equal to the energy density, but its sign is negative. This implies that the string has a large tension.

Substituting the solution (B.47) and assuming that $f(r)$ suddenly changes from 0 to 1 at $r \sim \delta_s$, we find

$$\begin{aligned} \mu_{\text{string}} &= - \int r dr d\varphi \mathcal{L} = \int_0^R \int_0^{2\pi} r dr d\varphi \left[\frac{1}{2} \left| \frac{\partial \Phi}{\partial r} \right|^2 + \frac{1}{2} \left| \frac{1}{r} \frac{\partial \Phi}{\partial \varphi} \right|^2 + V(\Phi) \right] \\ &\approx \frac{\pi}{4} \eta^2 + \int_{\delta_s}^R \frac{1}{2} \left| \frac{1}{r} \frac{\partial \Phi}{\partial \varphi} \right|^2 2\pi r dr \\ &\approx \pi \eta^2 \ln \left(\frac{R}{\delta_s} \right), \end{aligned} \quad (\text{B.55})$$

where R is a cutoff radius, and in the third line we neglected the contribution from the core $\pi \eta^2/4$ assuming that $\ln(R/\delta_s) \gg 1$. We see that the energy of the string is logarithmically divergent at large distance $R \rightarrow \infty$. This logarithmic factor arises due to the long-range force between strings mediated by the Goldstone boson field. As a consequence, the energy of global strings does not localize around the core, but extends over a long distance R . This does not occur in the case of local string, since the existence of the gauge field screens the contribution of the gradient energy of the scalar field.

The cutoff radius R is not infinity, but it is given by the curvature radius of the string or by the distance between neighboring strings. As shown in Eq. (B.44), we expect that the distance R is comparable to the horizon scale of the universe $R \sim t$. Indeed, various numerical studies indicate there is the scaling regime where R takes the value comparable to the horizon radius t [57, 160, 185, 164, 161, 162, 58]. Therefore, we estimate the mass energy of the string per unit length as

$$\mu_{\text{string}} \simeq \pi \eta^2 \ln \left(\frac{t/\sqrt{\xi}}{\delta_s} \right), \quad (\text{B.56})$$

where ξ is a numerical factor of $\mathcal{O}(1)$ [see Eq. (4.50)].

B.5 Domain walls

Domain walls arise when a discrete symmetry is spontaneously broken. This corresponds to the condition $\pi_0(G/H) \neq I$. The simplest example is given by the (1+1)-dimensional scalar field theory defined by Eqs. (B.1) and (B.2). Although this example describes a field theory with one spatial dimension, it is possible to consider the theory with the same

⁵The sign of Eq. (B.53) is different from that of [40] since we use different sign conventions with $\eta_{\mu\nu} = (-, +, +, +)$.

scalar potential in the actual (3+1)-dimensional spacetime. In this case, the kink-like solution (B.3) represents a planar wall orthogonal to one coordinate axis (say z-axis)

$$\phi(z) = \eta \tanh \left[\sqrt{\frac{\lambda}{2}} \eta z \right]. \quad (\text{B.57})$$

From this form of the solution, the thickness of the wall is estimated as

$$\delta_w \simeq \left(\sqrt{\lambda/2} \eta \right)^{-1}. \quad (\text{B.58})$$

For a planer solution $\phi = \phi(z)$, the equation of motion yields

$$\frac{1}{2} \left(\frac{d\phi}{dz} \right)^2 - V(\phi) = 0. \quad (\text{B.59})$$

With this relation, the energy-momentum tensor of the wall takes the form

$$\begin{aligned} T_{\mu\nu} &= \partial_\mu \phi \partial_\nu \phi + g_{\mu\nu} \mathcal{L} \\ &= \left(\frac{d\phi}{dz} \right)^2 \text{diag}(+1, -1, -1, 0). \end{aligned} \quad (\text{B.60})$$

The surface mass density of the wall is given by

$$\sigma_{\text{wall}} = \int_{-\infty}^{\infty} dz T_{00} = \int dz \left(\frac{d\phi}{dz} \right)^2 = \frac{4}{3} \sqrt{\frac{\lambda}{2}} \eta^3. \quad (\text{B.61})$$

From Eq. (B.60), we find that the magnitude of the pressure in the two tangential directions is identical to its surface mass density

$$\int dz T_{11} = \int dz T_{22} = -\sigma_{\text{wall}}, \quad (\text{B.62})$$

where the minus sign indicates that this pressure force is the tension, which straightens the wall up to the horizon scale.

Next, let us consider the axionic model with the PQ field Φ whose potential is given by Eq. (4.52). If we restrict ourselves to low energy configurations at the QCD scale, we can put $\Phi = \eta e^{i\alpha}$, which gives the effective potential for α

$$\mathcal{L}_\alpha = \frac{\eta^2}{2} (\partial_\mu \alpha)^2 + \frac{m_a^2 \eta^2}{N_{\text{DW}}^2} (1 - \cos N_{\text{DW}} \alpha). \quad (\text{B.63})$$

In this model, the discrete $Z_{N_{\text{DW}}}$ symmetry is spontaneously broken, and the classical field equation in the Minkowski background again yields a planer solution perpendicular to the z-axis

$$\alpha(z) = \frac{2\pi k}{N_{\text{DW}}} + \frac{4}{N_{\text{DW}}} \tan^{-1} \exp(m_a z), \quad k = 0, 1, \dots, N_{\text{DW}} - 1. \quad (\text{B.64})$$

From this form of the solution, the thickness of the wall is estimated as

$$\delta_w \simeq m_a^{-1}. \quad (\text{B.65})$$

Integrating out the energy density, we obtain the surface mass density of the domain wall

$$\sigma_{\text{wall}} = \int_{-\infty}^{\infty} dz \eta^2 \left(\frac{d\alpha}{dz} \right)^2 = \frac{8m_a \eta^2}{N_{\text{DW}}^2}. \quad (\text{B.66})$$

Comparing Eqs. (B.61) and (B.66), the values of σ_{wall} coincide between these two models if we set $\lambda \rightarrow 4m_a^2/3\eta^2$, $\eta \rightarrow (3/2)^{1/2}\eta$, and $N_{\text{DW}} = 2$. Also, the width of domain walls becomes the same order $\delta_w \simeq (\lambda/2)^{-1/2}\eta^{-1} \rightarrow m_a^{-1}$. Substituting these replacements of λ and η into Eq. (B.2), we obtain the potential given by Eq. (4.64).

We note that the surface mass density of axionic domain wall, given by Eq. (B.66) should be modified if we include the structure of the neutral pion field which varies inside the wall. In this case, the surface mass density is given by [186]

$$\sigma_{\text{wall}} = 4.32F_\pi m_\pi \eta / N_{\text{DW}} \simeq 9.23m_a \eta^2 / N_{\text{DW}}^2, \quad (\text{B.67})$$

where F_π is the pion decay constant, and m_π is the mass of the pion. In the second equality, we used $m_u/m_d \simeq 0.48$ [14], where m_u and m_d are the mass of up quark and down quark, respectively.

Appendix C

Lattice simulation

In chapter 4, we see that axions produced by the decay of topological defects give a significant contribution to the dark matter abundance. Since topological defects obey non-linear evolution equations, we must investigate the process numerically in order to study how they evolve with time and how they produce particle radiations. In this appendix, we describe the analysis method to compute the spectrum of axions produced by topological defects. Our numerical code is the combined version of that used in [58, 187].

C.1 Formulation

Consider the following equation of motion for a real scalar field ϕ in FRW background

$$\ddot{\phi} + 3H\dot{\phi} - \frac{\nabla^2}{R^2(t)}\phi + \frac{\partial V}{\partial\phi} = 0. \quad (\text{C.1})$$

If we use the conformal time τ [$d\tau = dt/R(t)$], the above equation becomes

$$f'' - \nabla^2 f + R^3(\tau)\frac{\partial V}{\partial\phi} = 0, \quad (\text{C.2})$$

where $f \equiv R\phi$, and a prime denotes a derivative with respect to the conformal time τ . Here, we assume $R'' = 0$ which is satisfied in the radiation dominated background.

We would like to ask how the classical field configuration $\phi(\mathbf{x}, t)$ evolve with time, given an initial configuration $\phi_{\text{ini}}(\mathbf{x}, t_0)$ at some fixed time t_0 . If the scalar potential $V(\phi)$ contains non-linear terms, it cannot be solved analytically and we are forced to use numerical analysis. We solve it numerically by imposing discrete spatial coordinates

$$\begin{aligned} \mathbf{x} &\rightarrow (i, j, k), \\ f(\mathbf{x}) &\rightarrow f_{i,j,k}, \end{aligned} \quad (\text{C.3})$$

where $i, j, k = 0, 1, 2, \dots, N - 1$ and N is the total number of grids. The Laplacian is

given by using the finite difference approximation

$$(\nabla^2 f)_{i,j,k} = \frac{1}{12(\Delta x)^2} [16(f_{i+1,j,k} + f_{i-1,j,k} + f_{i,j+1,k} + f_{i,j-1,k} + f_{i,j,k+1} + f_{i,j,k-1}) - (f_{i+2,j,k} + f_{i-2,j,k} + f_{i,j+2,k} + f_{i,j-2,k} + f_{i,j,k+2} + f_{i,j,k-2}) - 90f_{i,j,k}], \quad (\text{C.4})$$

where $\Delta x = L/N$ is the grid spacing, and L is the comoving size of the simulation box. This formula has fourth-order accuracy in Δx . Here, we imposed the periodic boundary condition on the boundaries of the simulation box (i.e. $f_{N,j,k} = f_{0,j,k}$, etc.).

To execute the time evolution which follows from Eq. (C.2), we used the symplectic integration scheme developed in [188]. In this numerical scheme the (implicit) Hamiltonian of the system is exactly conserved and there is no secular growth of the conserved quantity. In practice, we compute the following sequence of mappings,

$$f(\tau, \mathbf{x}) \rightarrow f(\tau + c_r \Delta\tau, \mathbf{x}) = f(\tau, \mathbf{x}) + c_r \Delta\tau f'(\tau, \mathbf{x}), \quad (\text{C.5})$$

$$f'(\tau, \mathbf{x}) \rightarrow f'(\tau + d_r \Delta\tau, \mathbf{x}) = f'(\tau, \mathbf{x}) + d_r \Delta\tau f''(\tau, \mathbf{x}), \quad (\text{C.6})$$

from $r = 1$ to $r = 4$, in each time step. The values of coefficients c_r and d_r are given by [188]

$$c_1 = c_4 = \frac{1}{2(2 - 2^{1/3})}, \quad c_2 = c_3 = \frac{1 - 2^{1/3}}{2(2 - 2^{1/3})}, \\ d_1 = d_3 = \frac{1}{2 - 2^{1/3}}, \quad d_2 = -\frac{2^{1/3}}{2 - 2^{1/3}}, \quad d_4 = 0. \quad (\text{C.7})$$

It turns out that this integration scheme has fourth-order accuracy in time.

Here, our aim is to follow the cosmological evolution of a complex scalar field Φ (the Peccei-Quinn field). The evolution equation for Φ can be obtained by varying the Lagrangian density given by

$$\mathcal{L} = -\frac{1}{2}|\partial_\mu \Phi|^2 - V(\Phi).$$

We decompose the complex scalar field into its real and imaginary part, such that

$$\Phi = \phi_1 + i\phi_2, \quad (\text{C.8})$$

where ϕ_1 and ϕ_2 are real variables. From the equation of motion for Φ , we can obtain two equations of motion for two real scalar fields ϕ_1 and ϕ_2 . Then, we follow the evolution of Φ by applying the numerical formulation described above to each of two real scalar fields ϕ_1 and ϕ_2 .

C.2 Identification of topological defects

Using the lattice algorithm described in the previous section, we can solve the time evolution of two real scalar fields $\phi_1(t, \mathbf{x})$ and $\phi_2(t, \mathbf{x})$ in the comoving simulation box. From

these data of scalar fields, we estimate various physical quantities, such as the length of strings, the area of domain walls, and the spectra of axions and gravitational waves radiated by defect networks. In order to calculate such physical quantities, we have to identify the position of topological defects in the simulation box. Here we summarize our identification method of topological defects, and describe how to calculate scaling parameters of strings ξ and domain walls \mathcal{A} defined in Eqs. (4.50) and (4.51).

C.2.1 Identification of strings

We used the method developed in [58] to identify the position of strings. Consider a quadrature which consists of four neighboring grids in the simulation box (see points A, B, C, and D in Fig. C.1). At each vertex point, we estimate the phase of the complex scalar field α from the data of two real scalar fields ϕ_1 and ϕ_2 . Then, we obtain a mapping from the quadrature in the real space to the phase distribution in the field space, as shown in Fig. C.1. Let us denote the minimum range of the phase which contains all the images of four vertices as $\Delta\alpha$. The string exists within the quadrature if $\Delta\alpha > \pi$ is satisfied, as long as the value of the phase changes continuously around the core of strings.

We can also determine the position at which a string penetrates the quadrature. At the boundary of the quadrature, we determine the positions of points on which $\phi_1 = 0$ or $\phi_2 = 0$ is satisfied, by using linear interpolation of the values of ϕ_1 and ϕ_2 . If the string correctly penetrates the quadrature, there are two points with $\phi_1 = 0$ and two points with $\phi_2 = 0$ on the boundary of the quadrature. Then we determine the position of the string as the point at which the line connecting two points with $\phi_1 = 0$ intersects with the line connecting two points with $\phi_2 = 0$ (see left-hand panel of Fig. C.1).

This simple criterion breaks down when the quadrature is penetrated by more than two strings. However, we observed that such region is at most 1% of the whole simulation box when the system relaxes into the scaling regime. Therefore, this scheme enables us to determine the position of strings with at least 99% accuracy.

C.2.2 Identification of domain walls

The identification of domain walls is simpler than that of strings. We separate the region of the phase of Φ , $0 \leq \alpha < 2\pi$, into N_{DW} domains. For example, if $N_{\text{DW}} = 3$, we obtain three domains with $0 \leq \alpha < \pi/3$ and $5\pi/3 \leq \alpha < 2\pi$ (vac. 1), $\pi/3 \leq \alpha < \pi$ (vac. 2), and $\pi \leq \alpha < 5\pi/3$ (vac. 3), as shown in Fig. C.1. At each grid point, we compute the phase of the scalar field and assign the number of the vacuum domain (i.e. vac. 1, vac. 2, or vac. 3) which contains that point. Let us call the neighboring grid points that differ by a unit lattice spacing $\Delta x = L/N$ as the ‘‘link’’. We identify that the domain wall intersects the link if the number of vacuum is different between the two ends of the link.

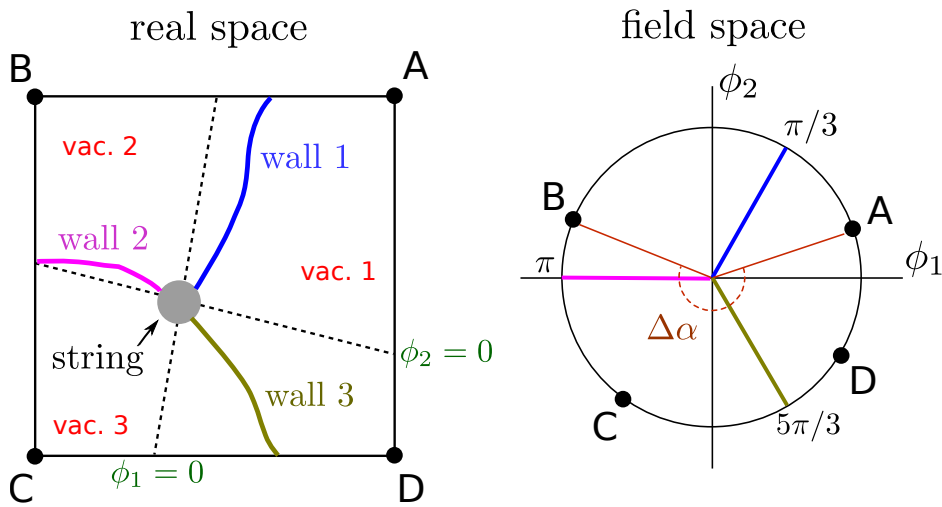


Figure C.1: Schematics of the identification method of topological defects. Left panel shows a quadrangle with four vertex points (A, B, C, and D) penetrated by a string and domain walls in the real space. Right panel shows a mapping of them in the field space. In this figure, we assume the model with $N_{\text{DW}} = 3$. Hence, there are three domain walls attached to the string. The blue (wall 1), pink (wall 2), and yellow (wall 3) lines represent the locations of the center of domain walls, which correspond to $\alpha = \pi/3$, $\alpha = \pi$, and $\alpha = 5\pi/3$, respectively, in the field space. The region is separated into three domains, vac. 1, vac. 2, and vac. 3, which are surrounded by domain walls on the boundaries. The dashed lines correspond to the loci of $\phi_1 = 0$ and $\phi_2 = 0$, which intersect on the core of the string. In the field space, we define $\Delta\alpha$ as the minimum range of the phase which contains all the images of four vertices. A string penetrates the quadrangle if the condition $\Delta\alpha > \pi$ is satisfied.

C.2.3 Calculation of scaling parameters

The scaling parameters of strings and domain walls are given by

$$\xi = \frac{\rho_{\text{string}} t^2}{\mu_{\text{string}}} \quad \text{and} \quad \mathcal{A} = \frac{\rho_{\text{wall}}}{\sigma_{\text{wall}}} t, \quad (\text{C.9})$$

where ρ_{string} is the energy density of strings, ρ_{wall} is the energy density of domain walls, μ_{string} is the mass energy of strings per unit length, and σ_{wall} is the surface mass density of domain walls. It might be difficult to determine the values of μ_{string} and σ_{wall} directly from the data of scalar fields since they are quantities obtained by integrating ρ_{string} and ρ_{wall} over the coordinates which are perpendicular to the direction along which the defects extend. Instead of estimating μ_{string} and σ_{wall} , we calculate the length l of strings and area A of domain walls in the comoving coordinates, such that

$$\rho_{\text{string}} = \frac{\mu_{\text{string}} l}{R^2(t)V} \quad \text{and} \quad \rho_{\text{wall}} = \frac{\sigma_{\text{wall}} A}{R(t)V}, \quad (\text{C.10})$$

where $V = L^3$ is the comoving volume of the simulation box. Then, the scaling parameters are given by

$$\xi = \frac{lt^2}{R^2(t)V} \quad \text{and} \quad \mathcal{A} = \frac{At}{R(t)V}. \quad (\text{C.11})$$

The length of strings l can be computed by connecting the loci of strings identified by the method described in the previous subsection. The computation of the area of domain walls A is not so straightforward, since it depends on the way how we define the segment of A in each lattice. Here, we use the simple algorithm introduced by Press, Ryden, and Spergel [146]. Define the quantity δ_{\pm} which takes the value 1 if the number of vacuum is different between the two ends of the link, and the value 0 otherwise. We sum up δ_{\pm} for each of the links with the weighting factor

$$A = \Delta A \sum_{\text{links}} \delta_{\pm} \frac{|\nabla\alpha|}{|\alpha_{,x}| + |\alpha_{,y}| + |\alpha_{,z}|}, \quad (\text{C.12})$$

where $\Delta A = (\Delta x)^2$ is the area of one grid surface, and $\alpha_{,x}$, etc. is a derivative of $\alpha(\mathbf{x})$ with respect to x . The weighting factor given by the function of $\nabla\alpha$ gives the average number of links per area segment. This method takes account of the orientation of the surface of walls in the lattice. See [146] for details.

C.3 Calculation of power spectrum of radiated axions

In this section, we describe the method to calculate the spectrum of axions produced by the string-wall networks. Our aim is to extract the pure component of the axion field produced by collapse of the networks, from simulated data of the scalar field Φ . In general, the data of Φ contain other components, that are regarded as contamination on the spectrum of radiated axions. One of such contaminations is the initial fluctuation of the scalar fields.

In numerical simulations, we give the initial conditions as Gaussian random fluctuations. These fluctuations are diluted away by the cosmic expansion, but might not be completely negligible even at the final time of the simulation, since the dynamical range of the numerical simulation is short. Therefore, they can contaminate the final form of the spectrum of radiated axions. Another kind of the contamination is the core of topological defects. In the core of defects, the energy density of the scalar field is higher than that of free axions. Hence we would overestimate the amplitude of the power spectrum if we include the contribution of the field near the core of defects.

To remove the contaminations from the core of defects, we mask the region near the position of the core of strings or domain walls, and estimate the power spectrum which contains only the contribution from free radiations. Also, in order to remove the contributions which come from initial fluctuations, we calculate the power spectrum in two time slices t_A and t_B , and subtract the spectrum evaluated at t_A from that evaluated at t_B . We will give a more detailed description of these procedures in the following subsections.

C.3.1 Energy spectrum of axions

We calculate the power spectrum of axion radiations $P(k, t)$ defined by

$$\frac{1}{2} \langle \dot{a}(t, \mathbf{k})^* \dot{a}(t, \mathbf{k}') \rangle = \frac{(2\pi)^3}{k^2} \delta^{(3)}(\mathbf{k} - \mathbf{k}') P(k, t), \quad (\text{C.13})$$

where $\langle \dots \rangle$ represents an ensemble average and $\dot{a}(t, \mathbf{k})$ is the Fourier component of the time derivative of the axion field

$$\dot{a}(t, \mathbf{k}) = \int d^3 \mathbf{x} e^{i\mathbf{k} \cdot \mathbf{x}} \dot{a}(t, \mathbf{x}). \quad (\text{C.14})$$

The value of $\dot{a}(t, \mathbf{x})$ can be obtained from the simulated data of Φ and $\dot{\Phi}$

$$\dot{a}(t, \mathbf{x}) = \text{Im} \left[\frac{\dot{\Phi}}{\Phi}(t, \mathbf{x}) \right]. \quad (\text{C.15})$$

The averaged kinetic energy of axions can be written as

$$\rho_{a,\text{kin}}(t) = \left\langle \frac{1}{2} \dot{a}(t, \mathbf{x})^2 \right\rangle = \int \frac{dk}{2\pi^2} P(k, t). \quad (\text{C.16})$$

On the other hand, the total energy density of axions is given by

$$\rho_{a,\text{tot}}(t) = \rho_{a,\text{kin}}(t) + \rho_{a,\text{grad}}(t) + \rho_{a,\text{mass}}(t), \quad (\text{C.17})$$

where $\rho_{a,\text{grad}}(t)$ is the averaged gradient energy of axions and $\rho_{a,\text{mass}}(t)$ is the averaged mass energy of axions

$$\rho_{a,\text{grad}}(t) = \left\langle \frac{1}{2} |\nabla a(t, \mathbf{x})|^2 \right\rangle, \quad \rho_{a,\text{mass}}(t) = \left\langle \frac{1}{2} m_a^2 a(t, \mathbf{x})^2 \right\rangle. \quad (\text{C.18})$$

One can easily show that, if $a(t, \mathbf{x})$ is a free field,

$$\rho_{a,\text{kin}}(t) = \rho_{a,\text{grad}}(t) + \rho_{a,\text{mass}}(t). \quad (\text{C.19})$$

Therefore, $P(k, t)$ can be regarded as the energy spectrum of axions

$$\rho_{a,\text{tot}}(t) = 2\rho_{a,\text{kin}}(t) = 2 \int \frac{dk}{2\pi^2} P(k, t). \quad (\text{C.20})$$

C.3.2 Pseudo-power spectrum estimator

If strings or domain walls exist, the data of $\dot{a}(t, \mathbf{x})$ obtained by numerical simulations contain field values around moving defects,

$$\dot{a}(t, \mathbf{x}) = \dot{a}_{\text{free}}(t, \mathbf{x}) + (\text{contamination from defects}), \quad (\text{C.21})$$

where $\dot{a}_{\text{free}}(t, \mathbf{x})$ is the contribution from free axion radiations. This moving defect contribution can contaminate the spectrum of the axion radiations. In order to subtract the contamination from the core of defects, we use the pseudo power spectrum estimator (PPSE) [189] introduced in [58].

We mask the contribution from the axion field near defects by introducing a window function

$$W(\mathbf{x}) = \begin{cases} 0 & (\text{near defects}) \\ 1 & (\text{elsewhere}) \end{cases}. \quad (\text{C.22})$$

Here, we mask the field data over grid points within a distance d_{width} from the position of the core of defects which we identified by using the methods described in Appendix C.2. The critical distance is chosen as $d_{\text{width}} = n_{\text{width}}\delta_s = n_{\text{width}}\lambda^{-1/2}\eta^{-1}$ for strings and $d_{\text{width}} = n_{\text{width}}\delta_w = n_{\text{width}}m_a^{-1}$ for walls, where δ_s and δ_w are widths of strings and domain walls, respectively, and n_{width} is an arbitrary number which we will specify later. Multiplying $W(\mathbf{x})$, we obtain the masked axion field

$$\tilde{\dot{a}}(\mathbf{x}) \equiv W(\mathbf{x})\dot{a}(\mathbf{x}) = W(\mathbf{x})\dot{a}_{\text{free}}(\mathbf{x}), \quad (\text{C.23})$$

or, in the Fourier space,

$$\tilde{\dot{a}}(\mathbf{k}) = \int \frac{d^3\mathbf{k}'}{(2\pi)^3} W(\mathbf{k} - \mathbf{k}')\dot{a}(\mathbf{k}'). \quad (\text{C.24})$$

We can compute the power spectrum by using the masked field in a simulation box,

$$\tilde{P}(k) \equiv \frac{k^2}{V} \int \frac{d\Omega_k}{4\pi} \frac{1}{2} |\tilde{\dot{a}}(\mathbf{k})|^2, \quad (\text{C.25})$$

where V is the comoving volume of the simulation box and Ω_k is a unit vector representing the direction of \mathbf{k} . However, this masked spectrum is not equivalent to the spectrum of radiated axions, $\langle \tilde{P}(k) \rangle \neq P_{\text{free}}$, where $P_{\text{free}}(k)$ is defined by

$$\frac{1}{2} \langle \dot{a}_{\text{free}}(t, \mathbf{k})^* \dot{a}_{\text{free}}(t, \mathbf{k}') \rangle = \frac{(2\pi)^3}{k^2} \delta^{(3)}(\mathbf{k} - \mathbf{k}') P_{\text{free}}(k, t). \quad (\text{C.26})$$

We can resolve this discrepancy by introducing a window weight matrix,

$$M(k, k') \equiv \frac{1}{V^2} \int \frac{d\Omega_{\mathbf{k}}}{4\pi} \frac{d\Omega_{\mathbf{k}'}}{4\pi} |W(\mathbf{k} - \mathbf{k}')|^2, \quad (\text{C.27})$$

and defining the PPSE of $P_{\text{free}}(k)$,

$$P_{\text{PPSE}}(k) \equiv \frac{k^2}{V} \int \frac{dk'}{2\pi^2} M^{-1}(k, k') \tilde{P}(k'), \quad (\text{C.28})$$

with $M^{-1}(k, k')$ satisfying

$$\int \frac{k'^2 dk'}{2\pi^2} M^{-1}(k, k') M(k', k'') = \frac{2\pi^2}{k^2} \delta(k - k''). \quad (\text{C.29})$$

Then, it can be shown that $\langle P_{\text{PPSE}}(k) \rangle = P_{\text{free}}(k)$ [58].

In the actual numerical calculation, we divide the domain of the comoving wavenumber k into plural bins, which is defined by

$$F_i = \left\{ \mathbf{k} \left| k_i^{(\min)} \leq |\mathbf{k}| < k_i^{(\max)} \right. \right\}, \quad \text{for } i = 1, 2, \dots, n_{\text{bin}}, \quad (\text{C.30})$$

where $k_1^{(\min)} = 0$, $k_{n_{\text{bin}}}^{(\max)} = k^{(\max)} \equiv \pi N/L$, $k_i^{(\max)} = (i/n_{\text{bin}})k^{(\max)}$, and n_{bin} is number of bins. Then, the masked power spectrum (C.25) is replaced with the average over i -th bin

$$\tilde{P}_i = \frac{1}{V} \frac{\sum_{\mathbf{k} \in F_i} \frac{k^2}{2} |\tilde{a}(\mathbf{k})|^2}{N_i}, \quad (\text{C.31})$$

where

$$N_i \equiv \sum_{\mathbf{k} \in F_i} 1. \quad (\text{C.32})$$

The window weight matrix (C.27) is also replaced with¹

$$M_{ij} = \frac{1}{V^2} \frac{\sum_{\mathbf{k} \in F_i} \sum_{\mathbf{k}' \in F_j} |W(\mathbf{k} - \mathbf{k}')|^2}{\sum_{\mathbf{k} \in F_i} \sum_{\mathbf{k}' \in F_j} 1}. \quad (\text{C.33})$$

The final form of the power spectrum (C.28) is obtained as

$$P_{\text{PPSE},i} = \frac{1}{N_i} \sum_j M_{ij}^{-1} \tilde{P}_j. \quad (\text{C.34})$$

¹It takes quite a lot of time to compute double integral in M_{ij} . However, we can improve the arithmetics by using some approximations for $M(k, k')$ [see Ref. [144]].

C.3.3 Subtraction of preexisting radiations

The power spectrum $P_{\text{PPSE}}(k, t)$ contains the contributions of axions produced before the time t . This means that it contains the contributions of axions radiated at initial epoch, which can be regarded as a contamination on the spectrum of radiated axions. In order to extract the spectrum of axions radiated from the decay of string-wall networks, we must subtract the contribution of these preexisting radiations. This can be achieved by evaluating the power spectra for selected time steps t_A and $t_B > t_A$, and subtracting the spectrum obtained at t_B from that obtained at t_A [143]. The radiations created at t_A are diluted due to the cosmic expansion, and we evaluate this redshift factor before we perform the subtraction. Note that the axion mass becomes non-negligible around the time of the decay of domain walls. Hence, we cannot subtract the spectrum simply assuming that the spectrum is diluted as R^{-4} , which is only applicable to massless particles.

From Eq. (C.20), the total energy density of axions can be written as

$$\rho_a(t) = \int \frac{d^3\mathbf{k}}{(2\pi)^3} \omega_a(k, t) n_a(k, t), \quad (\text{C.35})$$

where

$$\omega_a(k, t) = \sqrt{m_a^2 + k^2/R(t)^2} \quad (\text{C.36})$$

is the energy of axions with momentum $k/R(t)$, and we define

$$n_a(k, t) \equiv 2 \frac{P(k, t)}{\omega_a(k, t) k^2}. \quad (\text{C.37})$$

We can regard $n_a(k, t) d^3\mathbf{k}/(2\pi)^3$ as the number density of axions which have comoving momentum within the range from k to $k + dk$. Therefore, we expect that $n_a(k, t)$ scales as $R(t)^{-3}$, if there are no changes in the number of axions. By using the fact that $n_a(k, t) \propto R(t)^{-3}$ and Eq. (C.37), we find the form of the spectrum of pre-existing radiations produced before t_A , at the time t_B ,

$$P_{\text{pre}}(k, t_B) = P(k, t_A) \frac{\omega_a(k, t_B)}{\omega_a(k, t_A)} \left(\frac{R(t_A)}{R(t_B)} \right)^3, \quad (\text{C.38})$$

where $P(k, t_A)$ is the spectrum evaluated at t_A . Subtracting the contribution $P_{\text{pre}}(k, t_B)$ from the whole spectrum $P(k, t_B)$ evaluated at t_B , we obtain the spectrum of radiations produced after t_A

$$\Delta P(k, t_B) = P(k, t_B) - P_{\text{pre}}(k, t_B). \quad (\text{C.39})$$

In the simulation for the short-lived networks ($N_{\text{DW}} = 1$), we choose $\tau_A = \tau_1$ and $\tau_B = \tau_d$, where τ_1 is given by Eq. (4.46) and τ_d is the decay time of domain walls described in Sec. 4.4. In the simulation for the long-lived networks ($N_{\text{DW}} > 1$), we use $\tau_A = 14$ as the subtraction time, at which the system begins to follow the scaling regime, and vary the value of τ_B .

Figure C.2 shows the effect of this subtraction procedure. We see that the position of the peak is falsified, and the amplitude of the spectrum is overestimated if we do not

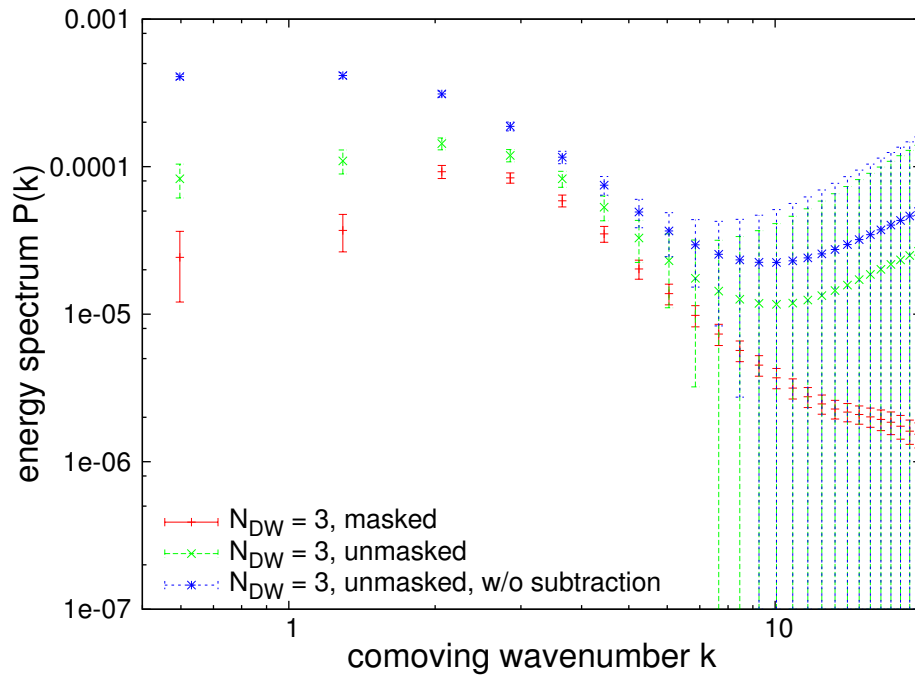


Figure C.2: The power spectrum of axions evaluated at the time $\tau_B = 40$ for the case $N_{DW} = 3$. The red plot shows the spectrum evaluated with masking the contamination of the core of topological defects and subtracting the contribution of axions produced at initial stage ($\tau \leq 14$). The green plot shows the spectrum obtained by the same model without masking the contamination of defects. The blue plot shows the spectrum evaluated without masking and subtraction.

perform the subtraction. Figure C.2 also shows that the spectrum is overestimated at higher momentum scale when we do not mask the data near the position of topological defects.

We note that the form of the power spectrum is affected by the choice of the region where the masking takes place. The masked region is determined such that the grid points within the distance d_{width} from the core of defects are excised, where $d_{\text{width}} = n_{\text{width}}\delta_s$ for strings and $d_{\text{width}} = n_{\text{width}}\delta_w$ for domain walls. Figure C.3 shows the power spectrum for various values of n_{width} . We see that the power spectrum in large k is overestimated when we use the smaller value of n_{width} . Since the spectra agree within the error bars for the results with $n_{\text{width}} \geq 2$, we use $n_{\text{width}} = 2$ for numerical analysis presented in the text.

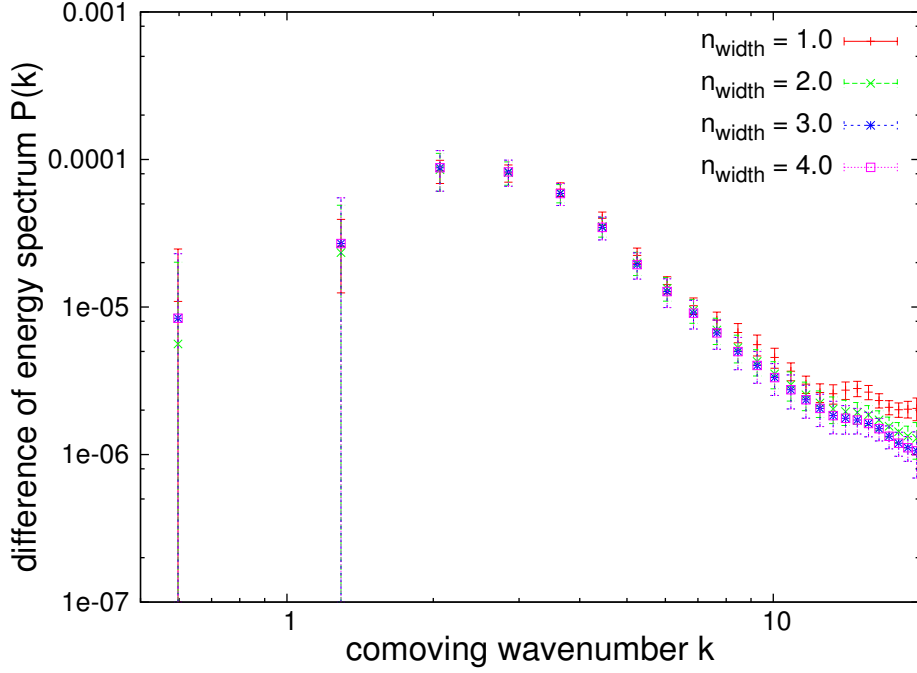


Figure C.3: The spectra of axions for various values of n_{width} . In these plots, we used the same parameters as those used in Fig. 4.19 for $N_{\text{DW}} = 3$.

C.4 Calculation of gravitational waves

For the model with long-lived domain walls, we also investigate the production of gravitational waves from defect networks. To calculate the spectrum of gravitational waves, we use the method introduced in [190]. The evolution of gravitational waves is described by spatial metric perturbations h_{ij} around the FRW background

$$ds^2 = -dt^2 + R^2(t)(\delta_{ij} + h_{ij})dx^i dx^j. \quad (\text{C.40})$$

Let us define the proper fluctuations as

$$\chi_{ij}(\mathbf{x}, \tau) \equiv R(\tau)h_{ij}(\mathbf{x}, \tau), \quad (\text{C.41})$$

and denote their Fourier components as

$$\tilde{\chi}_{ij}(\mathbf{k}, \tau) = \int d^3\mathbf{x} e^{i\mathbf{k}\cdot\mathbf{x}} \chi_{ij}(\mathbf{x}, \tau). \quad (\text{C.42})$$

In the Fourier space, the equations of motion for metric perturbations reduce to the form [169]

$$\left[\frac{\partial^2}{\partial y^2} + 1 \right] \tilde{\chi}_{ij} = \frac{S_{ij}}{k^2}, \quad (\text{C.43})$$

where we defined the variable $y \equiv k\tau$ and the source

$$S_{ij}(\mathbf{k}, \tau) \equiv 16\pi G R(\tau) T_{ij}^{\text{TT}}(\mathbf{k}, \tau). \quad (\text{C.44})$$

The transverse traceless (TT) part of the stress-energy tensor is computed by applying the projection operator

$$\begin{aligned} T_{ij}^{\text{TT}}(\mathbf{k}, \tau) &= \Lambda_{ij,kl}(\hat{k}) T_{ij}(\mathbf{k}, \tau) \\ &= \Lambda_{ij,kl}(\hat{k}) \{ \partial_k \Phi^* \partial_l \Phi \}(\mathbf{k}, \tau), \end{aligned} \quad (\text{C.45})$$

$$\Lambda_{ij,kl}(\hat{k}) = P_{ik}(\hat{k}) P_{jl}(\hat{k}) - \frac{1}{2} P_{ij}(\hat{k}) P_{kl}(\hat{k}), \quad (\text{C.46})$$

$$P_{ij}(\hat{k}) = \delta_{ij} - \hat{k}_i \hat{k}_j, \quad (\text{C.47})$$

where $\hat{k} = \mathbf{k}/|\mathbf{k}|$, and $\{ \partial_k \Phi^* \partial_l \Phi \}(\mathbf{k}, \tau)$ is the Fourier transform of $\partial_k \Phi^*(\mathbf{x}, \tau) \partial_l \Phi(\mathbf{x}, \tau)$.

There are two homogeneous solutions of Eq. (C.43), $\cos y$ and $\sin y$. The special solution is given by the time integral of the source term convoluted with two homogeneous solutions

$$\tilde{\chi}_{ij}(\mathbf{k}, \tau) = C_{ij}^{(1)}(\mathbf{k}, \tau) \cos k\tau + C_{ij}^{(2)}(\mathbf{k}, \tau) \sin k\tau, \quad (\text{C.48})$$

where

$$C_{ij}^{(1)}(\mathbf{k}, \tau) = - \int_{y_i}^y dy' \sin k\tau' \frac{S_{ij}(\mathbf{k}, \tau')}{k^2} \equiv \frac{16\pi G}{k^2} \bar{C}_{ij}^{(1)}(\mathbf{k}, \tau), \quad (\text{C.49})$$

and

$$C_{ij}^{(2)}(\mathbf{k}, \tau) = \int_{y_i}^y dy' \cos k\tau' \frac{S_{ij}(\mathbf{k}, \tau')}{k^2} \equiv \frac{16\pi G}{k^2} \bar{C}_{ij}^{(2)}(\mathbf{k}, \tau). \quad (\text{C.50})$$

The energy density of the gravitational waves is given by

$$\rho_{\text{gw}}(\tau) = \frac{1}{32\pi G R^4} \langle \chi'_{ij}(\mathbf{x}, \tau) \chi'_{ij}(\mathbf{x}, \tau) \rangle, \quad (\text{C.51})$$

where a prime denotes a derivative with respect to conformal time τ . We replace the ensemble average in Eq. (C.51) by an average over a volume V of the comoving simulation box,

$$\rho_{\text{gw}}(\tau) = \frac{1}{32\pi G R^4} \frac{1}{V} \int \frac{d^3\mathbf{k}}{(2\pi)^3} \chi'_{ij}(\mathbf{k}, \tau) \chi'^*_{ij}(\mathbf{k}, \tau). \quad (\text{C.52})$$

Substituting the solution given by Eq. (C.48), and ignoring the terms with higher order in RH , we obtain

$$\rho_{\text{gw}}(\tau) = \frac{4\pi G}{R^4 V} \int \frac{d^3 \mathbf{k}}{(2\pi)^3} \frac{1}{k^2} \sum_{ij} \left(\left| \bar{C}_{ij}^{(1)} \right|^2 + \left| \bar{C}_{ij}^{(2)} \right|^2 \right), \quad (\text{C.53})$$

where we averaged over a period of the oscillation of $\chi_{ij}(\mathbf{k}, \tau)$ with time. The spectrum of gravitational waves is given by

$$\frac{d\rho_{\text{gw}}}{d \ln k} = \frac{Gk}{2\pi^2 V R^4} \int d\Omega_k \sum_{ij} \left(\left| \bar{C}_{ij}^{(1)} \right|^2 + \left| \bar{C}_{ij}^{(2)} \right|^2 \right). \quad (\text{C.54})$$

We define the dimensionless energy spectrum of gravitational waves

$$\Omega_{\text{gw}}(k, \tau) \equiv \frac{d\rho_{\text{gw}}/d \ln k}{\rho_c(\tau)} = \frac{4}{3\pi V} \frac{G^2}{R^4 H^2} S_k(\tau), \quad (\text{C.55})$$

where

$$S_k(\tau) \equiv k \int d\Omega_k \sum_{ij} \left(\left| \bar{C}_{ij}^{(1)} \right|^2 + \left| \bar{C}_{ij}^{(2)} \right|^2 \right), \quad (\text{C.56})$$

and $\rho_c(\tau)$ is the critical density of the universe at conformal time τ

$$\rho_c(\tau) = \frac{3H^2}{8\pi G}. \quad (\text{C.57})$$

In radiation dominated background, we expect that $\Omega_{\text{gw}}(k, \tau) \propto S_k(\tau)$, since $R^4 H^2$ remains constant. Therefore, we calculate $S_k(\tau)$ in the numerical studies. Note that $\Omega_{\text{gw}}(k, \tau)$ given by Eq. (C.55) does not correspond to the spectrum observed today. The spectrum of gravitational waves observed today is obtained by multiplying $\Omega_{\text{gw}}(k, \tau)$ with a damping factor which arises from the following matter-dominated epoch.

We subtract the contribution of gravitational waves produced at the initial epoch where the defects do not relax into the scaling regime. This subtraction can be executed as follows. Since the energy density of gravitational waves shifts as $\propto R^{-4}$, the quantity $S_k(\tau) \propto R(\tau)^4 d\rho_{\text{gw}}(\tau)/d \ln k$ is proportional to the number of gravitons with the momentum k per comoving volume. Therefore, the difference of the spectral function

$$\Delta S_k(\tau) \equiv S_k(\tau) - S_k(\tau_g) \quad (\text{C.58})$$

gives the spectrum of gravitational waves produced during the time interval $[\tau_g, \tau]$. Here τ_g is a reference time which we treat as a free parameter in the numerical simulations.

Bibliography

- [1] **Supernova Cosmology Project** Collaboration, S. Perlmutter *et. al.*, *Measurements of Omega and Lambda from 42 high redshift supernovae*, *Astrophys.J.* **517** (1999) 565–586 [astro-ph/9812133].
- [2] **Supernova Search Team** Collaboration, A. G. Riess *et. al.*, *Observational evidence from supernovae for an accelerating universe and a cosmological constant*, *Astron.J.* **116** (1998) 1009–1038 [astro-ph/9805201].
- [3] S. Weinberg, *The Cosmological Constant Problem*, *Rev.Mod.Phys.* **61** (1989) 1–23.
- [4] S. Schindler, *Omega_m - different ways to determine the matter density of the universe*, astro-ph/0107028.
- [5] D. Kirkman, D. Tytler, N. Suzuki, J. M. O’Meara and D. Lubin, *The Cosmological baryon density from the deuterium to hydrogen ratio towards QSO absorption systems: D/H towards Q1243+3047*, *Astrophys.J.Suppl.* **149** (2003) 1 [astro-ph/0302006].
- [6] **WMAP Collaboration** Collaboration, E. Komatsu *et. al.*, *Seven-Year Wilkinson Microwave Anisotropy Probe (WMAP) Observations: Cosmological Interpretation*, *Astrophys.J.Suppl.* **192** (2011) 18 [1001.4538].
- [7] D. Clowe, M. Bradac, A. H. Gonzalez, M. Markevitch, S. W. Randall *et. al.*, *A direct empirical proof of the existence of dark matter*, *Astrophys.J.* **648** (2006) L109–L113 [astro-ph/0608407].
- [8] G. Bertone, D. Hooper and J. Silk, *Particle dark matter: Evidence, candidates and constraints*, *Phys.Rept.* **405** (2005) 279–390 [hep-ph/0404175].
- [9] S. Weinberg, *A New Light Boson?*, *Phys.Rev.Lett.* **40** (1978) 223–226.
- [10] F. Wilczek, *Problem of Strong p and t Invariance in the Presence of Instantons*, *Phys.Rev.Lett.* **40** (1978) 279–282.
- [11] R. Peccei and H. R. Quinn, *CP Conservation in the Presence of Instantons*, *Phys.Rev.Lett.* **38** (1977) 1440–1443.
- [12] R. Peccei and H. R. Quinn, *Constraints Imposed by CP Conservation in the Presence of Instantons*, *Phys.Rev.* **D16** (1977) 1791–1797.

- [13] J. E. Kim, *Light Pseudoscalars, Particle Physics and Cosmology*, *Phys.Rept.* **150** (1987) 1–177.
- [14] J. E. Kim and G. Carosi, *Axions and the Strong CP Problem*, *Rev.Mod.Phys.* **82** (2010) 557–602 [0807.3125].
- [15] T. Donnelly, S. Freedman, R. Lytel, R. Peccei and M. Schwartz, *Do Axions Exist?*, *Phys.Rev.* **D18** (1978) 1607.
- [16] J. E. Kim, *Weak Interaction Singlet and Strong CP Invariance*, *Phys.Rev.Lett.* **43** (1979) 103.
- [17] M. A. Shifman, A. Vainshtein and V. I. Zakharov, *Can Confinement Ensure Natural CP Invariance of Strong Interactions?*, *Nucl.Phys.* **B166** (1980) 493.
- [18] M. Dine, W. Fischler and M. Srednicki, *A Simple Solution to the Strong CP Problem with a Harmless Axion*, *Phys.Lett.* **B104** (1981) 199.
- [19] A. Zhitnitsky, *On Possible Suppression of the Axion Hadron Interactions. (In Russian)*, *Sov.J.Nucl.Phys.* **31** (1980) 260.
- [20] J. Preskill, M. B. Wise and F. Wilczek, *Cosmology of the Invisible Axion*, *Phys.Lett.* **B120** (1983) 127–132.
- [21] L. Abbott and P. Sikivie, *A Cosmological Bound on the Invisible Axion*, *Phys.Lett.* **B120** (1983) 133–136.
- [22] M. Dine and W. Fischler, *The Not So Harmless Axion*, *Phys.Lett.* **B120** (1983) 137–141.
- [23] G. R. Blumenthal, S. Faber, J. R. Primack and M. J. Rees, *Formation of Galaxies and Large Scale Structure with Cold Dark Matter*, *Nature* **311** (1984) 517–525.
- [24] A. Vilenkin and E. P. S. Shellard, *Cosmic Strings and Other Topological Defects*. Cambridge University Press, 2000.
- [25] P. Sikivie, *Of Axions, Domain Walls and the Early Universe*, *Phys.Rev.Lett.* **48** (1982) 1156–1159.
- [26] H. Georgi and M. B. Wise, *Hiding the invisible axion*, *Phys.Lett.* **B116** (1982) 123.
- [27] Y. Zeldovich, I. Y. Kobzarev and L. Okun, *Cosmological Consequences of the Spontaneous Breakdown of Discrete Symmetry*, *Zh.Eksp.Teor.Fiz.* **67** (1974) 3–11.
- [28] A. H. Guth, *The Inflationary Universe: A Possible Solution to the Horizon and Flatness Problems*, *Phys.Rev.* **D23** (1981) 347–356.
- [29] K. Sato, *First Order Phase Transition of a Vacuum and Expansion of the Universe*, *Mon.Not.Roy.Astron.Soc.* **195** (1981) 467–479.

- [30] D. H. Lyth, *A limit on the inflationary energy density from axion isocurvature fluctuations*, *Phys.Lett.* **B236** (1990) 408.
- [31] M. S. Turner and F. Wilczek, *Inflationary axion cosmology*, *Phys.Rev.Lett.* **66** (1991) 5–8.
- [32] A. D. Linde, *Axions in inflationary cosmology*, *Phys.Lett.* **B259** (1991) 38–47.
- [33] M. Kawasaki and T. Sekiguchi, *Cosmological Constraints on Isocurvature and Tensor Perturbations*, *Prog.Theor.Phys.* **120** (2008) 995–1016 [0705.2853].
- [34] M. P. Hertzberg, M. Tegmark and F. Wilczek, *Axion Cosmology and the Energy Scale of Inflation*, *Phys.Rev.* **D78** (2008) 083507 [0807.1726].
- [35] K. J. Mack, *Axions, Inflation and the Anthropic Principle*, *JCAP* **1107** (2011) 021 [0911.0421].
- [36] G. B. Gelmini, M. Gleiser and E. W. Kolb, *Cosmology of Biased Discrete Symmetry Breaking*, *Phys.Rev.* **D39** (1989) 1558.
- [37] S. E. Larsson, S. Sarkar and P. L. White, *Evading the cosmological domain wall problem*, *Phys.Rev.* **D55** (1997) 5129–5135 [hep-ph/9608319].
- [38] S. Chang, C. Hagmann and P. Sikivie, *Studies of the motion and decay of axion walls bounded by strings*, *Phys.Rev.* **D59** (1999) 023505 [hep-ph/9807374].
- [39] P. Sikivie, *Axion Cosmology*, *Lect.Notes Phys.* **741** (2008) 19–50 [astro-ph/0610440].
- [40] A. Vilenkin, *Gravitational Field of Vacuum Domain Walls and Strings*, *Phys.Rev.* **D23** (1981) 852–857.
- [41] B. Rai and G. Senjanovic, *Gravity and domain wall problem*, *Phys.Rev.* **D49** (1994) 2729–2733 [hep-ph/9301240].
- [42] M. Kamionkowski and J. March-Russell, *Planck scale physics and the Peccei-Quinn mechanism*, *Phys.Lett.* **B282** (1992) 137–141 [hep-th/9202003].
- [43] R. Holman, S. D. Hsu, T. W. Kephart, E. W. Kolb, R. Watkins *et. al.*, *Solutions to the strong CP problem in a world with gravity*, *Phys.Lett.* **B282** (1992) 132–136 [hep-ph/9203206].
- [44] S. M. Barr and D. Seckel, *Planck scale corrections to axion models*, *Phys.Rev.* **D46** (1992) 539–549.
- [45] B. A. Dobrescu, *The Strong CP problem versus Planck scale physics*, *Phys.Rev.* **D55** (1997) 5826–5833 [hep-ph/9609221].
- [46] M. Dine, *Problems of naturalness: Some lessons from string theory*, hep-th/9207045.

- [47] R. L. Davis, *Cosmic Axions from Cosmic Strings*, *Phys.Lett.* **B180** (1986) 225.
- [48] D. H. Lyth, *Estimates of the cosmological axion density*, *Phys.Lett.* **B275** (1992) 279–283.
- [49] R. Davis and E. Shellard, *Do axions need inflation?*, *Nucl.Phys.* **B324** (1989) 167.
- [50] A. Dabholkar and J. M. Quashnock, *Pinning down the axion*, *Nucl.Phys.* **B333** (1990) 815.
- [51] R. Battye and E. Shellard, *Global string radiation*, *Nucl.Phys.* **B423** (1994) 260–304 [astro-ph/9311017].
- [52] R. Battye and E. Shellard, *Axion string constraints*, *Phys.Rev.Lett.* **73** (1994) 2954–2957 [astro-ph/9403018].
- [53] E. Shellard and R. Battye, *Cosmic axions*, astro-ph/9802216.
- [54] D. Harari and P. Sikivie, *On the Evolution of Global Strings in the Early Universe*, *Phys.Lett.* **B195** (1987) 361.
- [55] C. Hagmann and P. Sikivie, *Computer simulations of the motion and decay of global strings*, *Nucl.Phys.* **B363** (1991) 247–280.
- [56] C. Hagmann, S. Chang and P. Sikivie, *Axion radiation from strings*, *Phys.Rev.* **D63** (2001) 125018 [hep-ph/0012361].
- [57] M. Yamaguchi, M. Kawasaki and J. Yokoyama, *Evolution of axionic strings and spectrum of axions radiated from them*, *Phys.Rev.Lett.* **82** (1999) 4578–4581 [hep-ph/9811311].
- [58] T. Hiramatsu, M. Kawasaki, T. Sekiguchi, M. Yamaguchi and J. Yokoyama, *Improved estimation of radiated axions from cosmological axionic strings*, *Phys.Rev.* **D83** (2011) 123531 [1012.5502].
- [59] G. 't Hooft, *Computation of the Quantum Effects Due to a Four-Dimensional Pseudoparticle*, *Phys.Rev.* **D14** (1976) 3432–3450.
- [60] G. 't Hooft, *How Instantons Solve the U(1) Problem*, *Phys.Rept.* **142** (1986) 357–387.
- [61] S. Weinberg, *The U(1) Problem*, *Phys.Rev.* **D11** (1975) 3583–3593.
- [62] K. Fujikawa, *Path Integral Measure for Gauge Invariant Fermion Theories*, *Phys.Rev.Lett.* **42** (1979) 1195.
- [63] K. Fujikawa, *Path Integral for Gauge Theories with Fermions*, *Phys.Rev.* **D21** (1980) 2848.

- [64] M. Pospelov and A. Ritz, *Electric dipole moments as probes of new physics*, *Annals Phys.* **318** (2005) 119–169 [hep-ph/0504231].
- [65] C. Baker, D. Doyle, P. Geltenbort, K. Green, M. van der Grinten *et. al.*, *An Improved experimental limit on the electric dipole moment of the neutron*, *Phys.Rev.Lett.* **97** (2006) 131801 [hep-ex/0602020].
- [66] C. Vafa and E. Witten, *Parity Conservation in QCD*, *Phys.Rev.Lett.* **53** (1984) 535.
- [67] W. A. Bardeen and S.-H. Tye, *Current Algebra Applied to Properties of the Light Higgs Boson*, *Phys.Lett.* **B74** (1978) 229.
- [68] W. A. Bardeen, R. Peccei and T. Yanagida, *Constraints on variant axion models*, *Nucl.Phys.* **B279** (1987) 401.
- [69] M. Sivertz, J. Lee-Franzini, J. Horstkotte, C. Klopfenstein, R. D. Schamberger *et. al.*, *Upper limit for axion production in radiative epsilon decay*, *Phys.Rev.* **D26** (1982) 717–719.
- [70] Y. Asano, E. Kikutani, S. Kurokawa, T. Miyachi, M. Miyajima *et. al.*, *Search for a Rare Decay Mode $K^+ \rightarrow \pi^+ \text{ Neutrino anti-neutrino}$ and Axion*, *Phys.Lett.* **B107** (1981) 159.
- [71] R. Peccei, T. T. Wu and T. Yanagida, *A viable axion model*, *Phys.Lett.* **B172** (1986) 435.
- [72] L. M. Krauss and F. Wilczek, *A shortlived axion variant*, *Phys.Lett.* **B173** (1986) 189–192.
- [73] **SINDRUM Collaboration** Collaboration, R. Eichler *et. al.*, *Limits for shortlived neutral particles emitted mu+ or pi+ decay*, *Phys.Lett.* **B175** (1986) 101.
- [74] M. Davier, J. Jeanjean and H. Nguyen Ngoc, *Search for axions in electron bremsstrahlung*, *Phys.Lett.* **B180** (1986) 295.
- [75] D. B. Kaplan, *Opening the Axion Window*, *Nucl.Phys.* **B260** (1985) 215.
- [76] D. J. Gross, R. D. Pisarski and L. G. Yaffe, *QCD and Instantons at Finite Temperature*, *Rev.Mod.Phys.* **53** (1981) 43.
- [77] M. S. Turner, *Cosmic and Local Mass Density of Invisible Axions*, *Phys.Rev.* **D33** (1986) 889–896.
- [78] K. J. Bae, J.-H. Huh and J. E. Kim, *Update of axion CDM energy*, *JCAP* **0809** (2008) 005 [0806.0497].
- [79] O. Wantz and E. Shellard, *Axion Cosmology Revisited*, *Phys.Rev.* **D82** (2010) 123508 [0910.1066].

- [80] O. Wantz and E. Shellard, *The Topological susceptibility from grand canonical simulations in the interacting instanton liquid model: Chiral phase transition and axion mass*, *Nucl.Phys.* **B829** (2010) 110–160 [0908.0324].
- [81] O. Wantz, *The Topological susceptibility from grand canonical simulations in the interacting instanton liquid model: Zero temperature calibrations and numerical framework*, *Nucl.Phys.* **B829** (2010) 48–90 [0907.3506].
- [82] J. Christenson, J. Cronin, V. Fitch and R. Turlay, *Evidence for the 2π Decay of the $k(2)0$ Meson*, *Phys.Rev.Lett.* **13** (1964) 138–140.
- [83] H. Georgi and L. Randall, *Flavor Conserving CP Violation in Invisible Axion Models*, *Nucl.Phys.* **B276** (1986) 241.
- [84] R. Kallosh, A. D. Linde, D. A. Linde and L. Susskind, *Gravity and global symmetries*, *Phys.Rev.* **D52** (1995) 912–935 [hep-th/9502069].
- [85] M. Srednicki, *Axion Couplings to Matter. I. CP Conserving Parts*, *Nucl.Phys.* **B260** (1985) 689.
- [86] S. Cheng, C. Geng and W. Ni, *Axion - photon couplings in invisible axion models*, *Phys.Rev.* **D52** (1995) 3132–3135 [hep-ph/9506295].
- [87] R. Mayle, J. R. Wilson, J. R. Ellis, K. A. Olive, D. N. Schramm *et. al.*, *Constraints on Axions from SN 1987a*, *Phys.Lett.* **B203** (1988) 188.
- [88] R. Mayle, J. R. Wilson, J. R. Ellis, K. A. Olive, D. N. Schramm *et. al.*, *Updated Constraints on Axions from SN 1987a*, *Phys.Lett.* **B219** (1989) 515.
- [89] S. Moriyama, M. Minowa, T. Namba, Y. Inoue, Y. Takasu *et. al.*, *Direct search for solar axions by using strong magnetic field and x-ray detectors*, *Phys.Lett.* **B434** (1998) 147 [hep-ex/9805026].
- [90] Y. Inoue, Y. Akimoto, R. Ohta, T. Mizumoto, A. Yamamoto *et. al.*, *Search for solar axions with mass around 1 eV using coherent conversion of axions into photons*, *Phys.Lett.* **B668** (2008) 93–97 [0806.2230].
- [91] **CAST Collaboration** Collaboration, S. Andriamonje *et. al.*, *An Improved limit on the axion-photon coupling from the CAST experiment*, *JCAP* **0704** (2007) 010 [hep-ex/0702006].
- [92] **CAST Collaboration** Collaboration, E. Arik *et. al.*, *Probing eV-scale axions with CAST*, *JCAP* **0902** (2009) 008 [0810.4482].
- [93] I. Irastorza, F. Avignone, S. Caspi, J. Carmona, T. Dafni *et. al.*, *Towards a new generation axion helioscope*, *JCAP* **1106** (2011) 013 [1103.5334].
- [94] **IAXO Collaboration** Collaboration, I. Irastorza *et. al.*, *The International Axion Observatory (IAXO)*, 1201.3849.

- [95] P. Sikivie, *Experimental Tests of the Invisible Axion*, *Phys.Rev.Lett.* **51** (1983) 1415.
- [96] P. Sikivie, *Detection rates for ‘invisible’ axion searches*, *Phys.Rev.* **D32** (1985) 2988.
- [97] R. Bradley, J. Clarke, D. Kinion, L. Rosenberg, K. van Bibber *et. al.*, *Microwave cavity searches for dark-matter axions*, *Rev.Mod.Phys.* **75** (2003) 777–817.
- [98] **ADMX Collaboration** Collaboration, S. Asztalos *et. al.*, *A SQUID-based microwave cavity search for dark-matter axions*, *Phys.Rev.Lett.* **104** (2010) 041301 [0910.5914].
- [99] M. R. Buckley and H. Murayama, *Quark mass uncertainties revive Kim-Shifman-Vainshtein-Zakharov axion dark matter*, *JCAP* **0707** (2007) 012 [0705.0542].
- [100] E. Paschos and K. Zioutas, *A Proposal for solar axion detection via Bragg scattering*, *Phys.Lett.* **B323** (1994) 367–372.
- [101] **COSME Collaboration** Collaboration, A. Morales *et. al.*, *Particle dark matter and solar axion searches with a small germanium detector at the Canfranc Underground Laboratory*, *Astropart.Phys.* **16** (2002) 325–332 [hep-ex/0101037].
- [102] **SOLAX Collaboration** Collaboration, I. Avignone, F.T. *et. al.*, *Experimental search for solar axions via coherent Primakoff conversion in a germanium spectrometer*, *Phys.Rev.Lett.* **81** (1998) 5068–5071 [astro-ph/9708008].
- [103] **TEXONO Collaboration** Collaboration, H. Chang *et. al.*, *Search of axions at the Kuo-Sheng nuclear power station with a high-purity germanium detector*, *Phys.Rev.* **D75** (2007) 052004 [hep-ex/0609001].
- [104] R. Bernabei, P. Belli, R. Cerulli, F. Montecchia, F. Nozzoli *et. al.*, *Search for solar axions by Primakoff effect in NaI crystals*, *Phys.Lett.* **B515** (2001) 6–12.
- [105] J. Redondo and A. Ringwald, *Light shining through walls*, *Contemp.Phys.* **52** (2011) 211–236 [1011.3741].
- [106] **PVLAS Collaboration** Collaboration, E. Zavattini *et. al.*, *Experimental observation of optical rotation generated in vacuum by a magnetic field*, *Phys.Rev.Lett.* **96** (2006) 110406 [hep-ex/0507107].
- [107] C. Robilliard, R. Battesti, M. Fouche, J. Mauchain, A.-M. Sautivet *et. al.*, *No light shining through a wall*, *Phys.Rev.Lett.* **99** (2007) 190403 [0707.1296].
- [108] **GammeV (T-969) Collaboration** Collaboration, A. S. Chou *et. al.*, *Search for axion-like particles using a variable baseline photon regeneration technique*, *Phys.Rev.Lett.* **100** (2008) 080402 [0710.3783].

- [109] K. Ehret, M. Frede, S. Ghazaryan, M. Hildebrandt, E.-A. Knabbe *et. al.*, *New ALPS Results on Hidden-Sector Lightweights*, *Phys.Lett.* **B689** (2010) 149–155 [1004.1313].
- [110] H. Schlattl, A. Weiss and G. Raffelt, *Helioseismological constraint on solar axion emission*, *Astropart.Phys.* **10** (1999) 353–359 [hep-ph/9807476].
- [111] P. Gondolo and G. Raffelt, *Solar neutrino limit on axions and keV-mass bosons*, *Phys.Rev.* **D79** (2009) 107301 [0807.2926].
- [112] G. G. Raffelt, *Particle physics from stars*, *Ann.Rev.Nucl.Part.Sci.* **49** (1999) 163–216 [hep-ph/9903472].
- [113] G. Raffelt and A. Weiss, *Red giant bound on the axion - electron coupling revisited*, *Phys.Rev.* **D51** (1995) 1495–1498 [hep-ph/9410205].
- [114] G. G. Raffelt, *Astrophysical methods to constrain axions and other novel particle phenomena*, *Phys.Rept.* **198** (1990) 1–113.
- [115] G. G. Raffelt, *Astrophysical axion bounds*, *Lect.Notes Phys.* **741** (2008) 51–71 [hep-ph/0611350].
- [116] A. Burrows, M. T. Ressell and M. S. Turner, *Axions and SN1987A: Axion trapping*, *Phys.Rev.* **D42** (1990) 3297–3309.
- [117] J. Engel, D. Seckel and A. Hayes, *Emission and detectability of hadronic axions from SN1987A*, *Phys.Rev.Lett.* **65** (1990) 960–963.
- [118] G. G. Raffelt, *Axion constraints from white dwarf cooling times*, *Phys.Lett.* **B166** (1986) 402.
- [119] J. Isern, E. Garcia-Berro, S. Torres and S. Catalan, *Axions and the cooling of white dwarf stars*, 0806.2807.
- [120] J. Isern, S. Catalan, E. Garcia-Berro and S. Torres, *Axions and the white dwarf luminosity function*, *J.Phys.Conf.Ser.* **172** (2009) 012005 [0812.3043].
- [121] J. Isern, M. Hernanz and E. Garcia-Berro, *Axion cooling of white dwarfs*, *Astrophys. J.* **392** (1992) L23.
- [122] J. Isern, E. Garcia-Berro, L. Althaus and A. Corsico, *Axions and the pulsation periods of variable white dwarfs revisited*, 1001.5248.
- [123] M. A. Bershadsky, M. T. Ressell and M. S. Turner, *Telescope search for multi-eV axions*, *Phys.Rev.Lett.* **66** (1991) 1398–1401.
- [124] M. T. Ressell, *Limits to the radiative decay of the axion*, *Phys.Rev.* **D44** (1991) 3001–3020.

- [125] D. Grin, G. Covone, J.-P. Kneib, M. Kamionkowski, A. Blain *et. al.*, *A Telescope Search for Decaying Relic Axions*, *Phys.Rev.* **D75** (2007) 105018 [astro-ph/0611502].
- [126] S. Chang and K. Choi, *Hadronic axion window and the big bang nucleosynthesis*, *Phys.Lett.* **B316** (1993) 51–56 [hep-ph/9306216].
- [127] T. Moroi and H. Murayama, *Axionic hot dark matter in the hadronic axion window*, *Phys.Lett.* **B440** (1998) 69–76 [hep-ph/9804291].
- [128] S. Hannestad, A. Mirizzi and G. Raffelt, *New cosmological mass limit on thermal relic axions*, *JCAP* **0507** (2005) 002 [hep-ph/0504059].
- [129] S. Hannestad, A. Mirizzi, G. G. Raffelt and Y. Y. Wong, *Neutrino and axion hot dark matter bounds after WMAP-7*, *JCAP* **1008** (2010) 001 [1004.0695].
- [130] E. W. Kolb and M. S. Turner, *The Early universe*. Westview Press, 1990.
- [131] M. S. Turner, *Thermal Production of Not SO Invisible Axions in the Early Universe*, *Phys.Rev.Lett.* **59** (1987) 2489.
- [132] E. Masso, F. Rota and G. Zsembinszki, *On axion thermalization in the early universe*, *Phys.Rev.* **D66** (2002) 023004 [hep-ph/0203221].
- [133] D. Lyth, *Axions and inflation: Sitting in the vacuum*, *Phys.Rev.* **D45** (1992) 3394–3404.
- [134] S. Weinberg, *Cosmology*. Oxford University Press, 2008.
- [135] M. Beltran, J. Garcia-Bellido and J. Lesgourgues, *Isocurvature bounds on axions revisited*, *Phys.Rev.* **D75** (2007) 103507 [hep-ph/0606107].
- [136] L. Visinelli and P. Gondolo, *Dark Matter Axions Revisited*, *Phys.Rev.* **D80** (2009) 035024 [0903.4377].
- [137] J. Hamann, S. Hannestad, G. G. Raffelt and Y. Y. Wong, *Isocurvature forecast in the anthropic axion window*, *JCAP* **0906** (2009) 022 [0904.0647].
- [138] C. Hikage, M. Kawasaki, T. Sekiguchi and T. Takahashi, *CMB constraint on non-Gaussianity in isocurvature perturbations*, 1211.1095.
- [139] A. R. Liddle and D. Lyth, *Cosmological inflation and large scale structure*. Cambridge University Press, 2000.
- [140] M. Nagasawa and M. Kawasaki, *Collapse of axionic domain wall and axion emission*, *Phys.Rev.* **D50** (1994) 4821–4826 [astro-ph/9402066].
- [141] M. Nagasawa and M. Kawasaki, *Cold dark matter generation by axionic domain wall collapses*, *Nucl.Phys.Proc.Suppl.* **43** (1995) 82–85.

- [142] T. Hiramatsu, M. Kawasaki and K. Saikawa, *Evolution of String-Wall Networks and Axionic Domain Wall Problem*, *JCAP* **1108** (2011) 030 [1012 . 4558].
- [143] T. Hiramatsu, M. Kawasaki, K. Saikawa and T. Sekiguchi, *Production of dark matter axions from collapse of string-wall systems*, *Phys. Rev.* **D85** (2012) 105020 [1202 . 5851].
- [144] T. Hiramatsu, M. Kawasaki, K. Saikawa and T. Sekiguchi, *Axion cosmology with long-lived domain walls*, *JCAP* **1301** (2013) 001 [1207 . 3166].
- [145] S. M. Barr, K. Choi and J. E. Kim, *Axion cosmology in superstring models*, *Nucl.Phys.* **B283** (1987) 591.
- [146] W. H. Press, B. S. Ryden and D. N. Spergel, *Dynamical evolution of domain walls in an expanding universe*, *Astrophys.J.* **347** (1989) 590–604.
- [147] T. Garagounis and M. Hindmarsh, *Scaling in numerical simulations of domain walls*, *Phys.Rev.* **D68** (2003) 103506 [hep-ph/0212359].
- [148] P. Avelino, J. Oliveira and C. Martins, *Understanding domain wall network evolution*, *Phys.Lett.* **B610** (2005) 1–8 [hep-th/0503226].
- [149] J. Oliveira, C. Martins and P. Avelino, *The Cosmological evolution of domain wall networks*, *Phys.Rev.* **D71** (2005) 083509 [hep-ph/0410356].
- [150] M. Hindmarsh, *Analytic scaling solutions for cosmic domain walls*, *Phys.Rev.Lett.* **77** (1996) 4495–4498 [hep-ph/9605332].
- [151] M. Hindmarsh, *Level set method for the evolution of defect and brane networks*, *Phys.Rev.* **D68** (2003) 043510 [hep-ph/0207267].
- [152] P. Avelino, C. Martins and J. Oliveira, *One-scale model for domain wall network evolution*, *Phys.Rev.* **D72** (2005) 083506 [hep-ph/0507272].
- [153] B. S. Ryden, W. H. Press and D. N. Spergel, *The evolution of networks of domain walls and cosmic strings*, *Astrophys. J.* **357** (1990) 293–300.
- [154] S. Kasuya, M. Kawasaki and T. Yanagida, *Cosmological axion problem in chaotic inflationary universe*, *Phys.Lett.* **B409** (1997) 94–100 [hep-ph/9608405].
- [155] S. Kasuya, M. Kawasaki and T. Yanagida, *Domain wall problem of axion and isocurvature fluctuations in chaotic inflation models*, *Phys.Lett.* **B415** (1997) 117–121 [hep-ph/9709202].
- [156] G. Lazarides and Q. Shafi, *Axion Models with No Domain Wall Problem*, *Phys.Lett.* **B115** (1982) 21.
- [157] S. M. Barr, X. Gao and D. Reiss, *Peccei-Quinn symmetries without domains*, *Phys.Rev.* **D26** (1982) 2176.

- [158] K. Choi and J. E. Kim, *Domain walls in superstring models*, *Phys.Rev.Lett.* **55** (1985) 2637.
- [159] S. M. Barr, D. Reiss and A. Zee, *Families, the invisible axion, and domain walls*, *Phys.Lett.* **B116** (1982) 227.
- [160] M. Yamaguchi, *Scaling property of the global string in the radiation dominated universe*, *Phys.Rev.* **D60** (1999) 103511 [hep-ph/9907506].
- [161] M. Yamaguchi and J. Yokoyama, *Lagrangian evolution of global strings*, *Phys.Rev.* **D66** (2002) 121303 [hep-ph/0205308].
- [162] M. Yamaguchi and J. Yokoyama, *Quantitative evolution of global strings from the Lagrangian view point*, *Phys.Rev.* **D67** (2003) 103514 [hep-ph/0210343].
- [163] C. Martins and E. Shellard, *Extending the velocity dependent one scale string evolution model*, *Phys.Rev.* **D65** (2002) 043514 [hep-ph/0003298].
- [164] J. Moore, E. Shellard and C. Martins, *On the evolution of Abelian-Higgs string networks*, *Phys.Rev.* **D65** (2002) 023503 [hep-ph/0107171].
- [165] T. Hiramatsu, M. Kawasaki and K. Saikawa, *Gravitational Waves from Collapsing Domain Walls*, *JCAP* **1005** (2010) 032 [1002.1555].
- [166] D. Coulson, Z. Lalak and B. A. Ovrut, *Biased domain walls*, *Phys.Rev.* **D53** (1996) 4237–4246.
- [167] R. L. Davis, *Goldstone bosons in string models of galaxy formation*, *Phys.Rev.* **D32** (1985) 3172.
- [168] A. Vilenkin and T. Vachaspati, *Radiation of Goldstone bosons from cosmic strings*, *Phys.Rev.* **D35** (1987) 1138.
- [169] M. Kawasaki and K. Saikawa, *Study of gravitational radiation from cosmic domain walls*, *JCAP* **1109** (2011) 008 [1102.5628].
- [170] M. Maggiore, *Gravitational Waves. Vol. 1: Theory and Experiments*. Oxford University Press, 2007.
- [171] N. Seto, S. Kawamura and T. Nakamura, *Possibility of direct measurement of the acceleration of the universe using 0.1-Hz band laser interferometer gravitational wave antenna in space*, *Phys.Rev.Lett.* **87** (2001) 221103 [astro-ph/0108011].
- [172] H. Kudoh, A. Taruya, T. Hiramatsu and Y. Himemoto, *Detecting a gravitational-wave background with next-generation space interferometers*, *Phys.Rev.* **D73** (2006) 064006 [gr-qc/0511145].
- [173] D. Cadamuro and J. Redondo, *Cosmological bounds on pseudo Nambu-Goldstone bosons*, *JCAP* **1202** (2012) 032 [1110.2895].

- [174] S. Dodelson, *Modern cosmology*. Academic Press, 2003.
- [175] **HST Collaboration** Collaboration, W. Freedman *et. al.*, *Final results from the Hubble Space Telescope key project to measure the Hubble constant*, *Astrophys.J.* **553** (2001) 47–72 [astro-ph/0012376].
- [176] J. C. Mather, D. Fixsen, R. Shafer, C. Mosier and D. Wilkinson, *Calibrator design for the COBE far infrared absolute spectrophotometer (FIRAS)*, *Astrophys.J.* **512** (1999) 511–520 [astro-ph/9810373].
- [177] S. Coleman, *Aspects of Symmetry*. Cambridge University Press, 1988.
- [178] G. Derrick, *Comments on nonlinear wave equations as models for elementary particles*, *J.Math.Phys.* **5** (1964) 1252–1254.
- [179] S. Weinberg, *The quantum theory of fields. Vol. 2: Modern applications*. Cambridge University Press, 1996.
- [180] S. Weinberg, *The Quantum theory of fields. Vol. 1: Foundations*. Cambridge University Press, 1995.
- [181] A. Belavin, A. M. Polyakov, A. Schwartz and Y. Tyupkin, *Pseudoparticle Solutions of the Yang-Mills Equations*, *Phys.Lett.* **B59** (1975) 85–87.
- [182] L. Dolan and R. Jackiw, *Symmetry Behavior at Finite Temperature*, *Phys.Rev.* **D9** (1974) 3320–3341.
- [183] S. Weinberg, *Gauge and Global Symmetries at High Temperature*, *Phys.Rev.* **D9** (1974) 3357–3378.
- [184] T. Kibble, *Topology of Cosmic Domains and Strings*, *J.Phys.A* **A9** (1976) 1387–1398.
- [185] M. Yamaguchi, J. Yokoyama and M. Kawasaki, *Evolution of a global string network in a matter dominated universe*, *Phys.Rev.* **D61** (2000) 061301 [hep-ph/9910352].
- [186] M. Huang and P. Sikivie, *The structure of axionic domain walls*, *Phys.Rev.* **D32** (1985) 1560.
- [187] T. Hiramatsu, M. Kawasaki and F. Takahashi, *Numerical study of Q-ball formation in gravity mediation*, *JCAP* **1006** (2010) 008 [1003.1779].
- [188] H. Yoshida, *Construction of higher order symplectic integrators*, *Phys.Lett.* **A150** (1990) 262–268.
- [189] E. Hivon, K. Gorski, C. Netterfield, B. Crill, S. Prunet *et. al.*, *Master of the cosmic microwave background anisotropy power spectrum: a fast method for statistical analysis of large and complex cosmic microwave background data sets*, *Astrophys.J.* **567** (2002) 2 [astro-ph/0105302].

- [190] J. F. Dufaux, A. Bergman, G. N. Felder, L. Kofman and J.-P. Uzan, *Theory and Numerics of Gravitational Waves from Preheating after Inflation*, *Phys.Rev.* **D76** (2007) 123517 [0707.0875].